Université Claude Bernard Lyon 1

Mémoire pour l'obtention de
l'Habilitation à Diriger les Recherches

présenté et soutenu publiquement par

Simon Rit

le 27 novembre 2020

Fourth dimensions of computed tomography: motion corrected CT, spectral CT and multi-variate proton CT

Composition du Jury

Mme.	Irène Buvat	Directrice de Recherche (CNRS)	Rapporteur
M.	Johan Nuyts	Professeur (KU Leuven)	Rapporteur
M.	Thomas Rodet	Professeur (ENS Cachan)	Rapporteur
M.	Loïc Boussel	Professeur (Université Claude Bernard Lyon 1)	Examinateur
M.	Charles Soussen	Professeur (CentraleSupélec)	Examinateur

Preface

This *habilitation à diriger les recherches* (HDR) aims at presenting my scientific contributions since I have been appointed as a researcher of the *Centre National de la Recherche Scientifique* (CNRS) in 2010, within the *Centre de Recherche En Acquisition et Traitement de l'Image pour la Santé* (CREATIS), team *Tomographic imaging and therapy with radiation*, either performing the investigations myself or, more often, as a supervisor of PhD and postodoctoral fellows. All the works presented here have already been published and this HDR aims at giving an overview of these publications. They cover a broad scope of topics, from tomographic reconstruction to deformable registration, and the brief presentation will necessarily be incomplete, but the reader can refer to the original publications for more details (three are included as appendices). All the references I have co-signed can easily be identified with the prefix letter (J for journal articles, B for book chapters, etc.). After my curriculum vitæ, the manuscript is divided in three parts, corresponding to the fields I have explored in the past 10 years: motion in cone-beam computed tomography (CT), spectral CT and proton CT. The conclusion finally outlines future research topics and my motivation for being habilitated.

Contents

Preface **3**

Contents **5**

Curriculum vitæ **9**

Acronyms **15**

I Motion in cone-beam computed tomography **19**

1 Introduction **21**

1.1 Computed tomography 21
1.2 Cone-beam CT 21
1.3 Motion in CT 22
1.3.1 Reconstruction with a periodic motion prior 23
1.3.2 Motion-compensated cone-beam CT 23

2 Breathing motion estimation for motion-compensated cone-beam CT reconstruction **25**

2.1 Spatiotemporal motion estimation 25
2.2 Pleural sliding 26
2.3 Motion estimation from cone-beam projections 28
2.4 Conclusions 29

3 Regularized iterative four-dimensional (4D) cone-beam CT **31**

3.1 Cardiac C-arm CT 31
3.2 Cone-beam CT for image-guided radiotherapy 32
3.3 Conclusions 33

4 Region-of-interest reconstruction in the presence of motion **35**

4.1 Differentiated backprojection 35
4.2 ROI reconstruction with motion in the fan-beam 36
4.3 ROI reconstruction with piecewise linear translations 36
4.4 Conclusions 36

5 Motion estimation and geometric calibration using data consistency conditions (DCC) **39**

5.1 Motion detection 39
5.2 Geometric calibration 39
5.3 Conclusions 41

II Spectral computed tomography **43**

6 Image formation in spectral CT **45**

6.1 Forward problem . . . 45
6.2 Projection-based two-step reconstruction . . . 46
6.3 One-step reconstruction . . . 48
6.4 Scatter correction in spectral CT . . . 48
6.5 Conclusions . . . 49

7 Spectral CT for ion therapy **51**

7.1 Dual-energy CT parameters for proton therapy . . . 52
7.2 Comparison between projection-based and image-based spectral decomposition . 53
7.3 Dual-layer CT for relative stopping power (RSP) estimation . . . 53
7.4 Conclusion . . . 54

III Proton computed tomography **57**

8 Energy-loss proton CT **59**

8.1 Most likely path of protons . . . 60
8.2 Distance-driven binning . . . 60
8.3 Two-step reconstruction based on differentiated backprojection . . . 62
8.4 Oblique ramp filtering . . . 62
8.5 Comparison between reconstruction algorithms . . . 63
8.6 Calibration of x-ray CT numbers to RSP using proton radiography . . . 63
8.7 Mean excitation energy map from energy loss proton CT and dual-energy x-ray CT 64
8.8 Assessment of the clinical relevance of proton CT using Monte Carlo simulations 65
8.9 Conclusion . . . 66

9 Other proton CT modalities **67**

9.1 Attenuation proton CT . . . 67
9.2 Scattering proton CT . . . 70
9.3 Conclusion . . . 70

10 Outlook for the future **71**

10.1 Motion correction in tomography . . . 71
10.2 Region-of-interest CT . . . 73
10.3 Ion CT . . . 74
10.4 Spectral CT . . . 75
10.5 International and local positioning . . . 76

Conclusion **79**

References **81**

Personal references . . . 81
Other references . . . 96

Appendices **105**

A Article illustrating Part I Motion in cone-beam computed tomography **105**

B Book chapter illustrating Part II Spectral computed tomography **129**

C Article illustrating Part III Proton computed tomography **147**

D Résumé français **157**

Curriculum vitæ

Simon Rit

105, cours Berriat
38000 Grenoble, France

+33 (0)6 01 74 26 85
simon.rit@creatis.insa-lyon.fr

French

Education

2004 – 2007	**PhD in computer science** with highest honors - Research Center for Images and Intelligent Information Systems (LIRIS) / Léon Bérard anticancer Center / Lumière University, Lyon, France
2004	**Masters of computer science** - Research Center for Images and Intelligent Information Systems (LIRIS) / National Institute of Applied Sciences (INSA), Lyon, France
1999 – 2004	**Masters in computer science engineering** National Institute of Applied Sciences (INSA), Lyon, France
1999	**Baccalauréat Scientifique majoring in Maths and Physics** *passed with distinction* Lycée Aristide Briand, Gap, France

Professional Academic Experience

2010 –	**Research Scientist** - CNRS / CREATIS / CLB, Lyon, France
2007 – 2009	**Postdoc** - Nederlands Kanker Instituut, Amsterdam, The Netherlands
2004 – 2007	**PhD** - LIRIS/Elekta, Lyon, France

Honors

2009	**HPIR best paper award** - Fully 3D - Beijing, China
2008	**MICCAI Young scientist award** - New York, USA

Publications

3 book chapters (2 as first author, 1 as last author)
67 refereed journal articles (7 as first author, 21 as last author)
5 conference invitations
48 conference proceedings articles (12 as first author, 13 as last author)
1 patent

Available online: `https://www.creatis.insa-lyon.fr/~srit`

PhD supervision

2020 – 2023	**Mathurin Charles** - Virtual Cone-Beam Approach for 3D Region-of-Interest CT - Ministry grant ED MSTII - Co-supervision with Rolf Clackdoyle
2019 – 2022	**Mélanie Mouchet** - Breathing motion correction in CT using data consistency conditions - Siemens Healthineers - Co-supervision with Jean Michel Létang
2018 – 2021	**Antoine Robert** - Breathing motion correction in SPECT quantitation - CIFRE Kitware - Co-supervision with David Sarrut
2018 – 2021	**Aurélien Coussat** - Region-of-interest CT reconstruction for dose reduction - ANR ROIdoré - Co-supervision with Jean Michel Létang

2017 – 2020	**Feriel Khellaf** - List-mode proton CT reconstruction - Fondation pour la recherche médicale - Co-supervision with Jean Michel Létang
2016 – 2019	**Odran Pivot** - Scatter correction for spectral tomographic imaging - CEA and Labex PRIMES - Co-supervision with Jean Michel Létang
2014 – 2017	**Gloria Vilches-Freixas** - Dual-energy cone-beam CT for protontherapy - ANR DEXTER - Co-supervision with Jean Michel Létang
2013 – 2016	**Catherine Therese Quiñones** - Proton CT reconstruction - Ministry grant ED EEA - Co-supervision with Jean Michel Létang
2013 – 2016	**Jan Hoskovec** - Dynamic region-of-interest cone-beam CT reconstruction for radiotherapy - ARC6 of the Rhone-Alpes region - Co-supervision with Rolf Clackdoyle
2010 – 2013	**Vivien Delmon** - Deformable registration of cone-beam CT projection images - CIFRE with the Elekta company - Co-supervision with David Sarrut

Postdoc supervision

2019 – 2020	**Nils Krah** - Proton CT reconstruction - Fondation pour la recherche médicale
2018 – 2019	**Pierre-Antoine Rodesch** - Material decomposition and tomographic reconstruction for spectral CT - PhysiCancer SPEDIV - H2020 SPCCT
2018 – 2019	**Ahmad Addoum** - Proton CT reconstruction - Fondation pour la recherche médicale
2017 – 2019	**Nils Krah** - Proton CT reconstruction with a Cone Beam CT prior - Marie Skłodowska-Curie Individual Fellowship
2017 – 2019	**Olga Kochebina** - Monte Carlo simulations of SPECT imaging - PhysiCancer SPEDIV
2016 – 2018	**Cyril Mory** - Sparsity-promoting iterative reconstruction for spectral photon-counting CT - H2020 SPCCT
2015 – 2017	**Thomas Cajgfinger** - Towards an hybrid deterministic-stochastic module in GATE simulations - ANR tGate
2014 – 2016	**Cyril Mory** - Sparsity-promoting cone-beam CT - ImagX project
2013 – 2015	**François Smekens** - Monte-Carlo simulations for low energy photon beam - PhysiCancer MC-SMART
2013 – 2014	**Nicolas Arbor** - Clinical interest of proton CT and investigation of instrumentation developments - Labex PRIMES
2012 – 2015	**Benoit Presles** - Ultra-Sound guided prostate radiation therapy treatments - Centre Léon Bérard
2012 – 2014	**Edward Romero** - Simulation of cone-beam CT - ImagX project
2012	**Georgios Dedes** - Proton computed tomography - PhysiCancer ProTom
2012 – 2014	**Rémi Blanc and Dominik Spinczyk** - Respiratory motion management for extracorporeal HIFU treatment of liver carcinoma - Siric LYRIC

Conference Organization

2019	**Second ion imaging workshop.** `http://ionimaging.sciencesconf.org/` - Manchester, United Kingdom
2018	**Proton imaging workshop.** `http://protonimaging.sciencesconf.org/` - Lyon, France
2017	**DROITE workshop on tomography: mathematics and applications.** `http://droite.imag.fr/doku.php?id=workshops` - Grenoble, France
2016	**Sixth International Workshop on Pulmonary Image Analysis** `http://www.lungworkshop.org/2016/` - MICCAI, Athens, Greece
2015	**ICART: Imaging and Computer Assistance in Radiation Therapy** `https://hal.archives-ouvertes.fr/hal-01264358` - MICCAI, Munich, Germany
2014	**Workshop on Numerical Modeling and Simulation of Inverse Problems in Medical Imaging** `http://tinyurl.com/mnu8ptt` - Lyon, France
2013	**Fifth International Workshop on Pulmonary Image Analysis** `http://www.lungworkshop.org/2013/` - MICCAI, Nagoya, Japan

2013	**Workshop on Numerical Modeling and Simulation of Inverse Problems in Medical Imaging** `http://tinyurl.com/njjvsze` - Grenoble, France
2012	**Image-Guidance and Multimodal Dose Planning in Radiation Therapy** `https://hal.archives-ouvertes.fr/hal-00755222v1` - MICCAI, Nice, France
2011	**Fourth International Workshop on Pulmonary Image Analysis** `http://www.lungworkshop.org/2011/` - MICCAI, Toronto, Canada

Teaching

2019	**Summer school ATTIRE** `http://attire.sciencesconf.org/` - 12h, hands-on sessions - Yenne, France
2016 – 2019	**X-ray tomography** - 32h (8h per year), 3rd year biomedical engineering - Polytech Lyon, France
2016 – 2019	**Image registration** - 24h (6h per year), Master MISS - Polytech Lyon, France
2016	**Image registration** - 2h, master in medical physics - Univ. Grenoble, France
2015 – 2017	**RTK training** - 28h (7h per session) - Lyon, France
2015	**Reconstruction and registration for IGRT** - 2h, EPU IGRT - Marseille, France
2015	**Imaging physics, simulation and biomedical applications - Hands on the simulation of x-ray imaging** - 4h, Summer School - Lyon, France
2013 – 2017	**Radiotherapy and Imaging** - 8h (2h per year), Master IMAVI - INSA Lyon, France
2011 – 2015	**Image registration** - 30h (6h per year), Master EEAP - INSA Lyon, France
2013	**Reconstruction and registration for IGRT** - 2h, EPU IGRT - Nantes, France
2011	**Image-Guided Radiotherapy** - 4h, Master IMA - Univ. Paris VI, France
2005 – 2007	**Probabilities and Statistics** - 58h, Graduate level - Univ. Lyon 1, France
2006	**C-ANSI** - 56h, Graduate level - IUT A, Lyon, France
2006	**Industrial Vision** - 24h, Post-graduate level - INSA Lyon, France
2005	**Office software** - 36h, Graduate level - Univ. Lyon 2, France

Research projects

Principal investigator of the project

2017 – 2021	**Computational methods to optimize proton radiography and tomography for improved proton therapy** - Fondation pour la recherche médicale
2014 – 2017	**Dual-Energy X-ray imaging for TargEting Radiotherapy (DEXTER)** - ANR Blanc SIMI3

Principal investigator of the CREATIS partner

2020 – 2021	**Small animal respiration-correlated cone-beam CT** - French - Bavarian cooperation center
2017 – 2022	**ROI tomography and dose reduction (ROIdoré)** - ANR generic call for proposals 2017
2016 – 2017	**High quality CBCT imaging for proton therapy** - French - Bavarian cooperation center
2014 – 2015	**Clinical relevance of proton computed tomography in proton therapy** - French - Bavarian cooperation center
2014 – 2015	**Sparsity-promoting dynamic cone-beam CT** - Public-private partnership ImagX2 between the IBA company and the université catholique de Louvain
2013 – 2017	**Dynamic and Region Of Interest Tomography, Theory and Experiments (DROITE)** - ANR Blanc SIMI1
2012 – 2014	**Monte Carlo cone-beam CT reconstruction** - Public-private partnership ImagX between the IBA company and the université catholique de Louvain

Co-investigator

2019 – 2022	**Nuclear medicine imaging with motion (NADIAM)** - Pack ambition recherche - Région Auvergne-Rhône-Alpes
2019 – 2022	**Deep Learning for dose monitoring in EBRT of pelvic cancers (DELPEL)** - PhysiCancer MIC 2019
2019 – 2022	**Personalized Optimization of Prognostic and thErapeutic protocols with Lu-177 for MNETs, through the development of advanced computational tools and a portable detection sYstEm (POPEYE)** - ERA PerMed
2018 – 2020	**1D and 2D QA dosimetric systems based on prompt- radioluminescence transduction for MRI guided stereotactic radiation therapy (QASys)** - Physicancer 2018
2018 – 2023	**LYon Recherche Innovation contre le CANcer (LYRICAN), WP3** - Labellisation de Sites de Recherche Intégrée sur le Cancer - SIRIC
2017 – 2021	**Ultra-Fast Timing for Online Control of Particle Therapy: CLaRyS-UFT** - PhysiCancer 2017
2016 – 2021	**In Vivo Spectral Photon Counting CT Molecular Imaging in Cardio and Neuro-Vascular Diseases (SPCCT)** - H2020 european project
2016 – 2019	**Single Photon Emission and Detection for In-Vivo Nanoparticles Quantification (SPEDIV)** - PhysiCancer 2016
2014 – 2018	**t-GATE: a unique integrative simulation platform for theranostics modeling** - Appel Generique ANR
2014	**Dose measure in radiotherapy using x-ray acoustic imaging (PHOTOX)** - DEFI Instrumentation aux limites (CNRS)
2013 – 2016	**Scientific animation: Modelling and numerical simulation in inverse problems for medical imaging** - ARC6 of the Rhone-Alpes region
2013 – 2015	**Monte Carlo – SMall Animal Radiation Therapy (MC SMART)** - PhysiCancer 2012
2012	**ProTom: Proton beam computed tomography applied to treatment planning in protontherapy** - PhysiCancer 2011
2012 – 2024	**Labex Physique, Radiobiologie, Imagerie Médicale et Simulation (PRIMES), WP4 and WP5** , Initiative d'excellence (IDEX) Lyon-Saint-Etienne
2012 – 2017	**LYon Recherche Intégrée en Cancérologie (LYRIC), WP4** - Labellisation de Sites de Recherche Intégrée sur le Cancer - SIRIC
2011 – 2014	**Implementation and clinical evaluation of a new strategy for image-guided radiotherapy of the lungs** - Funded by the Elekta company

Open-source software

RTK	**Reconstruction Toolkit** `http://www.openrtk.org/` - Creator, developer and maintainer
ITK	**Insight Toolkit** `https://itk.org/` - Occasional contributor
Gate	**Monte-Carlo simulation toolkit for medical physics applications** `http://www.opengatecollaboration.org/` - Developer

Acronyms

1D One-dimensional

2D Two-dimensional

3D Three-dimensional

4D Four-dimensional

5D Five-dimensional

CEA Commissariat à l'énergie atomique et aux énergies alternatives

CG Conjugate gradient

CLaRyS-UFT Ultra-Fast Timing for Online Control of Particle

CLB Centre Léon Bérard

CNRS Centre National de la Recherche Scientifique

CREATIS Centre de Recherche En Acquisition et Traitement de l'Image pour la Santé

CT Computed tomography

DBP Differentiated backprojection

DCC Data consistency conditions

DEXTER Dual-Energy X-ray imaging for TargEting Radiotherapy

DRR Digitally reconstructed radiography

ECG Electrocardiogram

ESRF European Synchrotron Radiation Facility

ETOILE Espace de Traitement Oncologique par Ions Légers Européen

FBP Filtered backprojection

FDK Felkamp, David, Kress

FRM Fondation pour la Recherche Médicale

HDR Habilitation à diriger les recherches

ICRP International Commission on Radiological Protection

ITK Insight toolkit

LETI Laboratoire d'électronique des technologies de l'information

LHC Laboratoire Hubert Curien

LMU Ludwig Maximilians university

MA-ROOSTER Motion-aware RecOnstructiOn using Spatial and TEmporal Regularization (ROOSTER)

MCFDK Motion-compensated FDK

MCS Multiple Coulomb scattering

MGH Massachussets General Hospital

MLP Most likely path

NADIAM NucleAr meDicine ImAging with Motion

NKI Nederlands Kanker Instituut

PET Positron emission tomography

PICCS Prior image constrained compressed sensing

PRIMES Physics, Radiobiology, Imaging and Simulation

RED Relative electron density

ROI Region-of-interest

ROIdoré Region-of-interest and dose reduction

ROOSTER RecOnstructiOn using Spatial and TEmporal Regularization

RSP Relative stopping power

RTK Reconstruction toolkit

SLP Straight-line path

SPARE Sparse view reconstruction

SPCCT Spectral Photon Counting CT

SPECT Single photon emission computed tomography

SVD Singular value decomposition

TDM Tomodensitométrie

TIMC Techniques de l'Ingénierie Médicale et de la Complexité

TRE Target registration error

TV Total variation

UCL University college London

WEPL Water-equivalent path length

XVI X-ray volume imaging

Part I

Motion in cone-beam computed tomography

1 Introduction

The purpose of this chapter is to outline the problem of motion in x-ray CT and to introduce two classes of solutions. The other chapters of the section will then summarize my scientific contributions to this field. Most of the investigations in this part have contributed to the development of the reconstruction toolkit (RTK) [C29], an open-source software for cone-beam CT (http://www.openrtk.org) which has greatly contributed to my international visibility.

1.1 Computed tomography

X-ray CT is a two-step imaging technique. First, x-ray projections are acquired around the scanned object. The measured quantity in each sample of the projection is assumed to be proportional to the flux of photons such that the measured fluxes with and without object, respectively noted Φ and Φ_0, can be linked to a line integral through the linear attenuation coefficient of the object according to the Beer-Lambert law

$$\Phi = \Phi_0 \exp\left(-\int_0^L \mu\left(\boldsymbol{s} + l\boldsymbol{\xi}\right) \mathrm{d}l\right) \tag{1.1}$$

with $\boldsymbol{s}$ the three-dimensional (3D) source position, $\boldsymbol{\xi}$ the 3D unit direction vector of the measured line, L the source-to-sample distance and μ the map of the attenuation coefficient of the object at a given energy. This relation only holds for monoenergetic x-ray beams, but it is assumed to be true for a polychromatic clinical source in this chapter, see Part II for a discussion on CT and polychromatism.

Second, the function μ is computed from its line integrals using a tomographic reconstruction algorithm. Several books on 3D CT reconstruction are available in the literature and I would suggest, as entry points, [1] for a beginner's overview, [2] for the mathematical aspects and [3] for an implementation guide of basic algorithms.

1.2 Cone-beam CT

The acquisition of tomographic projections can be realized in many manners. The *acquisition geometry* is the description of both the geometry of the x-ray source emission (parallel, point, etc.) and the geometry of the x-ray detector (flat detector, cylindrical detector, etc.). Here, cone-beam CT will be limited to a circular source trajectory of radius R, which I will parameterize by the angle θ, i.e. $\boldsymbol{s}_\theta = (-R\sin\theta, R\cos\theta, 0)$, and a flat panel detector. Figure 1.1 illustrates several systems with such a geometry and with which x-ray projections have been acquired and used in my co-authored publications. We denote with g_θ one two-dimensional (2D) projection image acquired at source position θ.

Figure 1.1: Cone-beam CT scanners with a circular source trajectory and a flat panel detector which I have used in my research: Elekta XVI used in [T1, 4, S6] (top left), medPhoton ImagingRing used in [S3] (top right), Philips C-arm used in [S5] (bottom left) and Photonic Science table top system used in [J31] (bottom right).

1.3 Motion in CT

Tomographic reconstruction generally assumes that the scanned object was static during the acquisition of the x-ray projections. Under this assumption, the reconstruction algorithm will produce a 3D CT of the static object. Patient motion cannot always be controlled: for examples, heart beating cannot be stopped and breath can only be held for a short time (a few seconds). The effect of motion on image quality can be observed in Figure 1.2: breathing motion causes blur around the moving structure, here mainly around the diaphragm and in the lungs, and along streaks which follow x-rays tangent to moving structures. Note that blur around the mediastinum in both images is likely caused by cardiac motion.

When there is motion during the acquisition, the sought image is a four-dimensional (4D) CT of the dynamic patient, which is sometimes referred to as a dynamic tomography. Let μ_t be the map of the attenuation coefficient of the object at time t. We limit ourselves to acquisitions with one revolution and there is a bijective relation between t and θ. The map μ_θ will refer to the map of the attenuation coefficient at the time when the x-ray source position is at angle θ along its circular trajectory.

The motion of the patient during the tomographic acquisition is generally not known. Reconstructing the 4D function of the patient attenuation coefficients is then a difficult problem. In its most general form, μ_θ is different at each source position θ and one would then have to reconstruct μ_θ from only one projection g_θ. This is obviously not possible without some *a priori* information about μ_θ, and more specifically about the motion of the patient during the acquisition. Several solutions have been proposed and I summarize two of them which I had already explored during my PhD investigations [T1]: a periodic motion prior and full motion knowledge. The landscape of the available solutions for breathing motion in cone-beam CT has

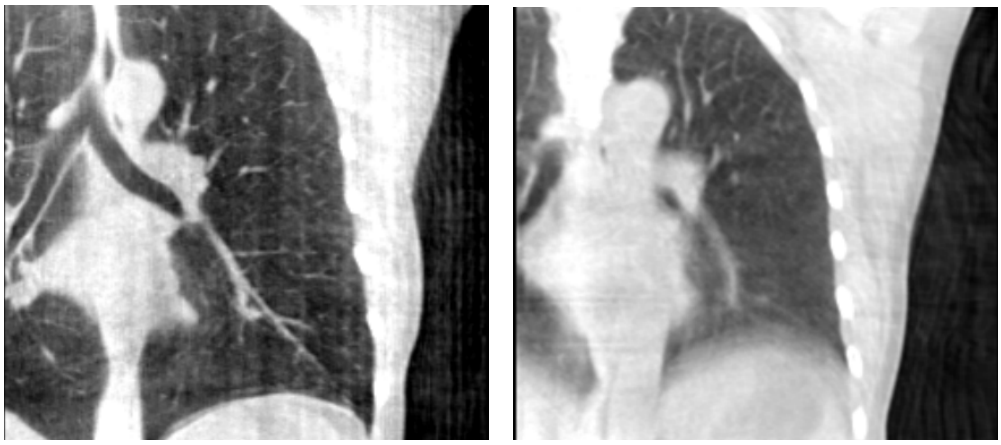

Figure 1.2: Cone-beam CT images of the same patient using static cone-beam CT image reconstruction. Reconstruction from breath-hold acquisition of 95 projection images (left) and from free-breathing acquisition of 670 projection images (right). Figure re-printed from [B3].

been summarized in [B3].

1.3.1 Reconstruction with a periodic motion prior

An overview of respiratory motion models is available in [5]. The simplest and most intuitive patient model is one-dimensional (1D): a signal describes the periodic position of the patient in a cyclic motion. This model has been used for cardiac and respiratory motions. The position in the cycle is called the phase, generally expressed in percentage although some use an angle to outline the periodic nature of this quantity. It can be obtained with an external sensor, e.g., an electrocardiogram (ECG) or a spirometer. In cone-beam CT, one x-ray projection captures a large part of the patient body and it has been shown that the breathing signal can be extracted from the x-ray projections [6, 7, C48].

The signal can then be used to *bin* the x-ray projections in a discrete set of positions according to their position in the cyclic motion. Each bin of projections is used to reconstruct one 3D CT image, and the resulting sequence of 3D CT images is the sought 4D CT. The early works on *gated* cone-beam CT are [8] for breathing motion and [9, 10] for cardiac motion. The difficulty of this technique is the small amount of x-ray projections available to reconstruct each 3D cone-beam CT image. When possible, the amount of x-ray projections per breathing phase can be increased by slowing down the scanner rotation as suggested by [8]. Otherwise, several works have investigated regularization techniques to cope with the lack of x-ray projections. The PhD and postdoc investigations of Cyril Mory have chosen this approach of cardiac and respiratory motions and will be presented in chapter 3.

1.3.2 Motion-compensated cone-beam CT

Another option to avoid the oversampling of the acquisition is to estimate the breathing motion during the acquisition of the x-ray projections. We then further assume that the motion only deforms the map of attenuation coefficients, without changing its values, i.e.,

$$\mu_{\text{ref}}(\boldsymbol{x}) = \mu_\theta(\Phi_\theta(\boldsymbol{x})) \tag{1.2}$$

with Φ_θ the 3D mapping describing the spatial deformation of the patient from each time point θ to a reference position at time ref. Estimating Φ_θ is a first problem which Jef Vandemeulebroucke [4] and Vivien Delmon [S6] have investigated using a prior CT image of the same patient. These works will be described in chapter 2. Another option is to estimate a rigid motion from

the x-ray projections using data consistency conditions (DCC), a topic investigated by both Jan Hoskovec and Jérôme Lesaint and covered by chapter 5.

Reconstructing μ_{ref} from all projections g_θ and the corresponding Φ_θ is the separate problem of motion-compensated cone-beam CT. Analytic solutions to this problem only exist for a limited class of deformations Φ_θ which includes affine motion [11] and other deformations for which the measured sinogram can be rebinned to a motion-free sinogram of the patient at time ref [12]. Such analytical solutions have been further explored in combination with region-of-interest (ROI) CT by Jan Hoskovec and will be presented in chapter 4. There is no analytical solution for breathing and cardiac motions, and these non-rigid anatomical motions are compensated heuristically during the backprojection of filtered backprojection (FBP) [13]. The motion-compensated FDK (MCFDK) algorithm is based on the Felkamp, David, Kress (FDK) algorithm [14], the standard FBP algorithm for circular cone-beam CT. It has been used for cardiac [9] and breathing [15] motions. Since this algorithm is used throughout this HDR thesis, we recall the formula

$$\mu_{\text{MCFDK}}(\boldsymbol{x}) = \int_0^{2\pi} \frac{1}{U^2} \int_{\mathbb{R}} \frac{D}{\sqrt{u^{*2} + v^{*2} + D^2}} \frac{R}{D} g_\theta(u, v^*) h(u^* - u) \,\mathrm{d}u \,\mathrm{d}\theta \tag{1.3}$$

with $U = [R + \Phi_\theta(\boldsymbol{x}) \cdot (-\sin\theta, \cos\theta, 0)]/D$ the inverse magnification factor at point $\Phi_\theta(\boldsymbol{x})$, D the source-to-detector distance, $u^* = \Phi(\boldsymbol{x}) \cdot (\cos\theta, \sin\theta, 0)/U$ and $v^* = \Phi(\boldsymbol{x}) \cdot (0, 0, 1)/U$ the detector coordinates of point $\Phi_\theta(\boldsymbol{x})$ at source position θ, and

$$h(u) = \int_{\mathbb{R}} |k_u| \exp(2\pi i u k_u) \,\mathrm{d}k_u \tag{1.4}$$

the kernel of the ramp filter. The FBP algorithm derived from this formula has three steps: (1) weight the projections g_θ, (2) ramp-filter the weighted projections and (3) backproject with a spatially varying weight each ramp-filtered projection along the x-rays warped from the acquisition time θ to the reference time ref. Note that when there is no motion, i.e., when $\Phi(\boldsymbol{x}) = \boldsymbol{x}$, the algorithm becomes the conventional FDK algorithm. I have proposed an adaptation of the FDK algorithm for cone-beam CT scanners where the source and the detector can rotate independently such as the ImagingRing shown in Figure 1.1 [J41]. It will not be detailed here because it is very similar. FDK and MCFDK are approximate, but they have proven efficient in practice. My experience on real data is that other uncorrected effects, particularly scatter, have more impact on image quality and mask the approximations of these reconstruction algorithms. Alternatively, similar adaptations can also be made to 3D iterative algorithms and I have investigated iterative motion-compensated cone-beam CT during my PhD investigations [T1, J65].

Motion-compensated CT reconstruction produces one 3D image. I differentiate these techniques from the use of an estimate of the motion Φ_θ to better regularize 4D cone-beam CT reconstruction in the temporal direction such as the one described in chapter 3. These differences will be emphasized in chapter 3 after chapter 2 on motion estimation for motion-compensated cone-beam CT.

2

Breathing motion estimation for motion-compensated cone-beam CT reconstruction

Non-rigid registration was a "hot topic" in the field of medical image processing when I started my PhD fellowship and it has been increasingly investigated since with radiotherapy being one of the applications motivating this boom [B2, J27]. The research group I joined at the *Centre Léon Bérard* (CLB) comprised Vlad Boldea, a PhD student (co-supervised by David Sarrut and Serge Miguet, like me), who was investigating non-rigid estimation for breathing motion from multiple breathholds and 4D CT images [16]. I have used the result of their investigations to estimate a prior model of the breathing motion on 4D CT correlated with the x-ray projections using a breathing signal [T1, J65]. During my postdoc at the *Nederlands Kanker Instituut* (NKI), I used another software for the same purpose [C43, J66] developed by Jochem Wolthaus [17] based on [18]. Therefore, my first experience of non-rigid registration is from a user perspective.

When I joined the *Centre de Recherche En Acquisition et Traitement de l'Image pour la Santé* (CREATIS), Jef Vandemeulebroucke was finishing his PhD fellowship under the co-supervision of Patrick Clarysse and David Sarrut. We have collaborated on two topics: spatio-temporal regularization [J64] and automated detection of the interface where sliding motion occurs [J59]. This latter topic was taken over by Vivien Delmon, a PhD student co-supervised by David Sarrut and me, to account for the sliding interface in a B-spline registration algorithm [J58]. Both Jef Vandemeulebroucke and Vivien Delmon used their motion models for breathing motion estimation from cone-beam CT projections. This chapter summarizes all these contributions.

2.1 Spatiotemporal motion estimation

Non-rigid registration is an inverse problem which requires regularization [19, B2]. For example, regularization is crucial in the estimation of breathing motion on 4D CT images which suffer from severe artefacts due to irregular breathing [20, C28].

Registration of 4D CT images can be realized by registering pairs of 3D frames [16, 21, 22]. However, only spatial smoothness can be enforced then, either by penalizing non-smooth solutions in the cost function which is minimized iteratively and/or by limiting the search space to smooth deformations only, e.g., using free-form deformations based on B-splines [23]. There are then no constraints on the smoothness of the deformation in time.

Adding a temporal regularization seems natural and we have investigated the extension of 3D free-form deformations based on B-splines to 4D [J64]. We first analyzed traces of the cranio-caudal position of one of the two diaphragm domes on cone-beam CT projections which were extracted in one of my postdoc studies [J61]. We observed in these traces a discontinuity in the first derivative of motion (the velocity) and deduced that the temporal model should account for this discontinuity. Two B-spline models were therefore investigated and compared with the model $\mathcal{T}_{\mathrm{s}}$ with spatial regularization only: one fully cyclic B-spline model $\mathcal{T}_{\mathrm{st}}$, with the same

trajectory smoothness at any point along the cycle, and one cyclic B-spline model $\mathcal{T}_{\mathrm{st}}^{*}$ with a speed discontinuity at end-inhale, where we had observed a sudden change of direction of breathing. This is illustrated on projected 3D trajectories in Figure 2.1.

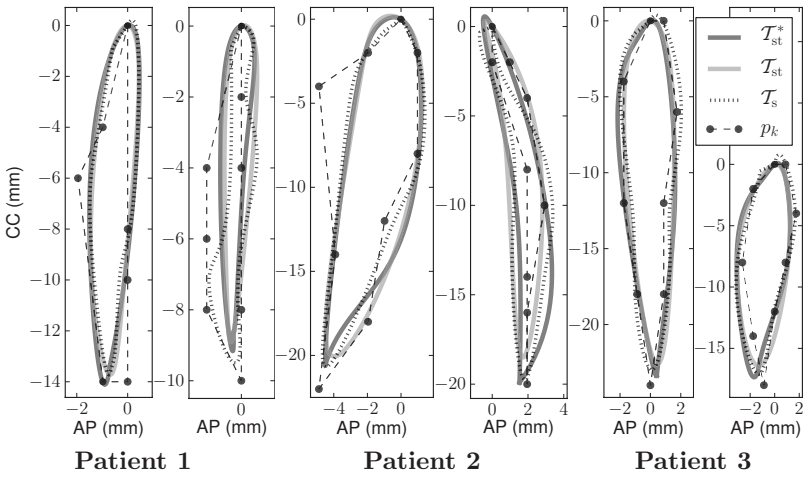

Figure 2.1: Examples of 3D trajectories projected on the sagittal plane without temporal regularization ($\mathcal{T}_{\mathrm{s}}$) and with the two models of temporal regularization, fully smooth ($\mathcal{T}_{\mathrm{st}}$) or with a discontinuity of the speed ($\mathcal{T}_{\mathrm{st}}^{*}$). The black dots p_k are the spatial landmarks identified by an expert on each frame of the 4D CT. Figure re-printed from [J64].

There was no doubt in our opinion that constraining the registration based on a more realistic modeling of breathing motion was desirable, but it turned out to be difficult to evaluate, as is often the case with non-rigid registration. The accepted reference on real data are manually identified landmarks on each registered image, as shown in Figure 2.1. However, this reference for evaluation is, like deformable registration, limited by image artifacts. In [J64], the evaluation of the above-described temporal constraints based on landmarks registration show poorer results, with a slightly larger target registration error (TRE) evaluated on 300 landmarks placed on end-inhale and end-exhale CT images of 6 patients: on average 1.38 mm, 1.57 mm and 1.46 mm for $\mathcal{T}_{\mathrm{s}}$, $\mathcal{T}_{\mathrm{st}}$ and $\mathcal{T}_{\mathrm{st}}^{*}$, respectively. However, if one evaluates the ability of the spatiotemporal registration to overcome image artifacts in one of the frames of the 4D CT, the temporal regularization can help to overcome the image artifacts, as visually illustrated in Figure 2.2 on simulated (top) and real (bottom) CT images. We therefore argue that spatio-temporal registration is preferable because it provides a more realistic estimate of the breathing motion, but we acknowledge that we did not have the means to validate its accuracy on real data.

2.2 Pleural sliding

The group at the CLB has also investigated the modeling of another characteristic of breathing motion which goes against conventional spatial regularization: sliding of the lungs along the rib cage realized by the pleural cavity (Figure 2.3). The effect of this sliding on the sought motion is visible in Figure 2.2: the ribs on the left are nearly static whereas the adjacent lungs and diaphragm dome have large motion.

The investigations on this topic started during a collaboration between the Massachussets General Hospital (MGH) (Boston) and the CLB. The *motion mask* was identified as the interface between the moving region (lungs, mediastinum, upper-abomen) and the less moving region (the rest, e.g., the rib cage). In this first work [24], the motion mask was manually identified and accounted for in the registration by performing two independent registrations, one estimating

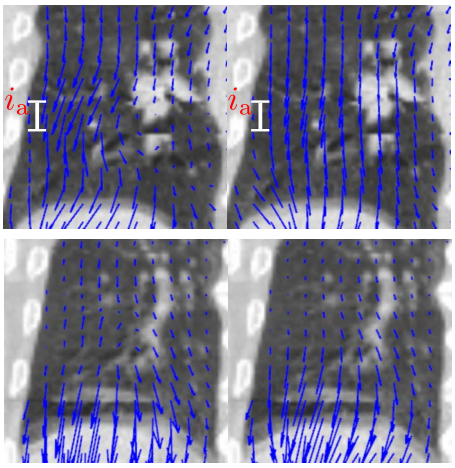

Figure 2.2: Motion vector fields (blue) estimated with spatial only (left) and spatiotemporal (right) regularizations on simulated (top) and real (bottom) CT images with artifacts due to irregular breathing. The range i_a indicates the height where artifacts were simulated. Figures adapted from [J64].

motion in the moving region by setting the voxel values of the less moving region to a constant and conversely for estimating motion in the less moving region.

Jef Vandemeulebroucke improved the usability of this solution by automating the segmentation of this motion mask [J59]. The segmentation is based on the segmentation of anatomical features: the bones, the lungs and the patient envelope. These features are clearly visible on CT images and, therefore, relatively easy to segment automatically. From these, the motion mask is obtained using a monitored level set which maximizes the coverage of the lungs without overlapping bones and until it reaches a point in front of the patient abdomen. The extracted motion masks were validated like in [24], by evaluating the registration accuracy with the same two-step registration procedure, which was significantly better than without mask, from 4.8 mm to 2.6 mm for all points within 10 mm of the chest wall (757 landmarks manually annotated in 8 patients). This work also shows that allowing a discontinuity for sliding motion along the motion mask enables to increase the regularity elsewhere with little impact on the TRE, which is not the case without motion mask (see, e.g., Figure 6 of [J59]).

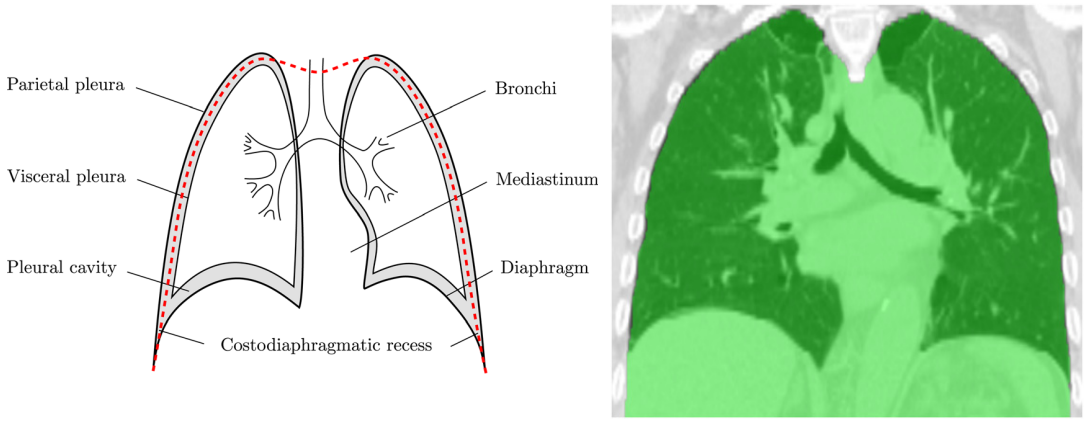

Figure 2.3: Schematic representation of the anatomy of the thorax focused on the pleural cavity (left) and an example of motion mask (green) overlaid on a coronal slice of a patient CT image. Figures adapted from [J59] (left) and [J58] (right).

Use of the motion mask in non-rigid registration was further investigated by Vivien Delmon

in [J58]. The goal of this work was to replace the above-described two-step registration of pairs of images by a single registration while accounting for the motion mask. To this end, the motion was decomposed in a fully smooth motion orthogonal to the sliding interface, represented by B-splines, and the rest, which is smooth everywhere except along the motion mask, represented by two sets of B-splines for each side of the interface (Figure 2.4). Without going into the details of the implementation, the number of parameters (i.e., of B-spline coefficients) actually used to build the spatial transformation is the same as usual except for control points adjacent to the motion mask (the nearest ones for order zero B-splines, the two nearest ones for order one B-splines, etc.) for which they are doubled for the non-orthogonal directions. The resulting algorithm has several advantages, the main ones being that : (1) enforcing a smooth deformation in the direction orthogonal is a better representation of sliding and (2) when registering a pair of images, only the mask of the fixed image is required, therefore removing the risk of inconsistent masks. Similarly to the constraints imposed by a smooth spatiotemporal registration (section 2.1), the sliding constraint did not improve the TRE: on 16 pairs of end-exhale and end-inhale CT images of two open datasets [25] the TRE increased from 1.43 mm with the two-step registration to 1.49 mm with the new method. But the plausibility of the registration was improved with a better consistency of the motion mask warped with the inner and the outer spatial transformations (37% less gaps and overlaps with the new method).

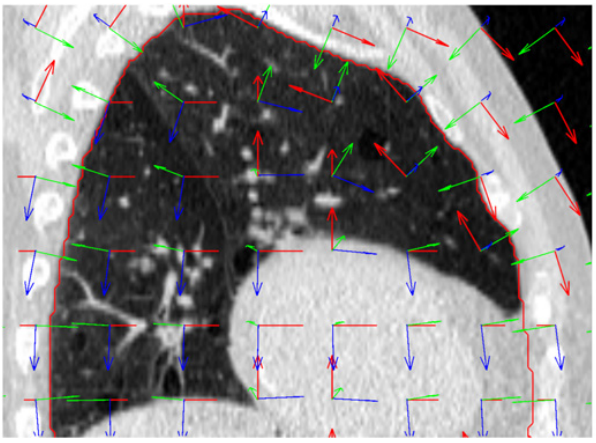

Figure 2.4: Illustration of local bases used by [J58] for registering pairs of images in one step while accounting for sliding. Motion is the linear combination of a smooth motion in the direction of the green arrows and discontinuous motion along the motion mask (but smooth elsewhere) along the blue and the red arrows. Figure adapted from [J58].

2.3 Motion estimation from cone-beam projections

Interestingly, the main goal of Jef Vandemeulebroucke and Vivien Delmon during their PhD fellowships was to estimate non-rigid breathing motion from 2D cone-beam projections using a prior 3D CT (a breathhold CT image or a frame of a 4D CT image). Instead, both have mainly contributed to improving the modeling of breathing motion first and have finalized their work with some preliminary results on 2D/3D registration which were never published in international journals. Their contribution has only been published in a conference paper [C27] and in their PhD theses [4, S6]. The forward problem they address is a classical registration problem which can be easily described by Jamie McClelland's framework [26]

$$\hat{\boldsymbol{p}} = \arg\min_{\boldsymbol{p}} \sum_{\theta} C(\mu_{\text{prior}}, g_\theta, \Phi_\theta) \tag{2.1}$$

where $\boldsymbol{p}$ are the parameters of the motion model which allow to compute the 3D patient motion Φ_θ between the prior 3D CT image μ_{prior} to time θ in combination with a breathing signal (extracted from the projections using [7], see subsection 1.3.1), C is the correlation coefficient used as a similarity metric to compare the measured cone-beam projections g_θ and the digitally reconstructed radiography (DRR) of μ_{prior} (Equation 1.1) and the other notations are described in subsection 1.3.2. Jef Vandemeulebroucke has derived the gradient of this cost function with respect to the sought parameters $\boldsymbol{p}$. His preliminary results have been further validated on simulated and real data by Vivien Delmon. On real data, the validation is even more challenging than with regular 3D/3D non-rigid registration because it is difficult to annotate landmarks on cone-beam projections. In our opinion, a convincing proof of accurate motion estimation is to integrate the estimated motion in motion-compensated reconstruction Equation 1.3. We have seen in patients which had changed their breathing motion cycles during the cone-beam acquisition an improvement in image quality (e.g., sharpness of moving structures) when re-estimating the motion instead of using the same cyclic motion as the one obtained from the prior (subsection 1.3.2), as illustrated in Figure 2.5.

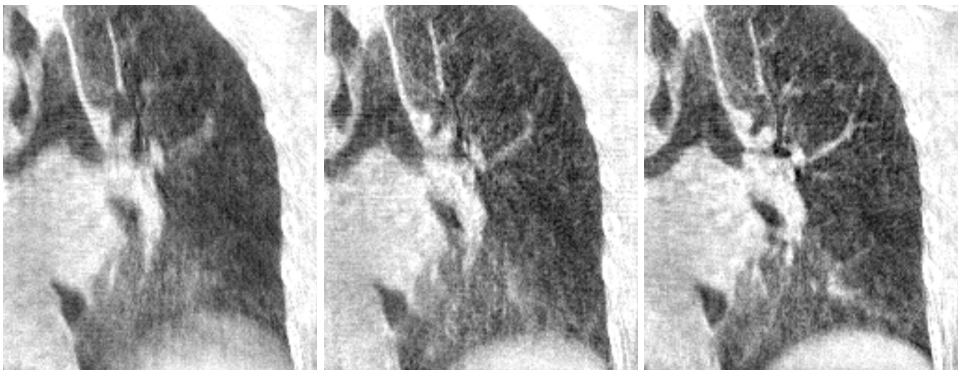

Figure 2.5: Cone-beam CT images of the patient with different FDK reconstructions: without motion compensation (left), with a prior motion model of the breathing cycle (middle) and with an estimate of the breathing cycle estimated by registering 2D cone-beam projections on a prior 3D CT image. Figure re-printed from [C27].

The developments on this 2D/3D registration have been further developed by Pauline Mouches [M2] under the co-supervision of Cyril Mory of CREATIS, Jamie McClelland of University college London (UCL) and me. She has used a more elaborate model [27] which uses the phase and the derivative of the breathing signals to account for breathing irregularities during the acquisition. Our first results were encouraging and the investigations are still on-going in collaboration with this group [A7].

2.4 Conclusions

My early investigations of motion-compensated cone-beam CT have led to investigations at CREATIS on breathing motion modeling and estimation. I have reviewed our developments on motion modeling and outlined the challenges in validating non-rigid registration. The problem of 2D/3D registration bridges non-rigid registration with a tomographic problem. Including the estimated motion in MCFDK is a good motivation for image quality improvement and Jamie McClelland *et al* have recently published a "framework unifying image registration and respiratory motion models and incorporating image reconstruction" [26]. I am hopeful that these developments will move forward, e.g., in collaboration with this group.

3

Regularized iterative 4D cone-beam CT

The solution explored in the previous chapter, MCFDK (Equation 1.3), is not truly a 4D cone-beam CT reconstruction method. It corrects for motion artifacts from an estimate of this motion. Under the strong assumption that motion only deforms the spatial distribution (Equation 1.2), one can reconstruct the 3D cone-beam CT image of the patient at the reference position, not a 4D cone-beam CT image. To obtain the 4D cone-beam CT image of the patient after reconstruction, one can simply warp the images using the motion estimate. Therefore, it cannot capture changes in the linear attenuation coefficients of the patient tissues during the acquisition. In some situations, this solution is not applicable.

An alternative is to handle the problem without prior image or motion, using the respiratory signal only and assuming periodicity. If one simply sorts the acquired projections in a few bins according to the breathing phase, the difficulty is the reconstruction of each 3D frame of a 4D cone-beam CT image from each bin of projections. This few-view reconstruction problem is probably as old as CT, but it has seen a renewed interest in the past decade inspired by compressive sensing [28], e.g., for 4D cone-beam CT [29]. The key challenge here is to obtain 4D cone-beam CT images from acquisitions designed for 3D cone-beam CT, i.e., with a number of projections insufficient for reconstructing with a conventional FBP algorithm such as FDK [14]. This chapter reviews the contributions of Cyril Mory on this topic during his PhD, co-supervised by Françoise Peyrin, Philippe Douek, Loïc Boussel, Vincent Auvray and me, and postdoc fellowships, under my supervision.

3.1 Cardiac C-arm CT

The PhD thesis of Cyril Mory [S5], funded by Philips, dealt with cardiac motion during cone-beam CT acquisitions with a C-arm scanner (Figure 1.1). This device is used by surgeons in emergency situations (e.g., an infarctus) in a planar mode. Tomographic acquisitions are not the standard of care, but it is foreseen that a cone-beam CT image acquired during or after the intervention could be useful, e.g., to segment the infarcted region of the myocardium using late enhancement [30]. However, cardiac motion is detrimental to image quality. In the mentioned emergency situations, there is generally no prior image on which motion could be estimated, preventing the use of motion-compensated cone-beam CT.

The work of Cyril Mory was initially inspired by the PhD thesis of Fabien Momey [31] who reformulated the problem as a 4D iterative reconstruction problem with a smooth approximation of a 4D total variation (TV) constraint. Briefly, TV is the L1 norm of the gradient's magnitude [32] and adding a TV constraint during minimization of nD signals (with $n > 1$) promotes solutions which are piecewise constant, i.e., solutions which have mainly null spatial gradient. TV (or smooth approximations of TV) has become the most widely used regularization in iterative CT reconstruction.

Cyril Mory's investigations led to the development of a new algorithm that he named RecOnstructiOn using Spatial and TEmporal Regularization (ROOSTER), which alternates between the minimization of a data attachment term (using a least squares conjugate gradient minimization) and four regularization steps: positivity, averaging time in pre-identified static parts of the anatomy, 3D TV denoising in space and 1D TV denoising in time. One can express the problem with a single cost function [33], but alternating between steps proved to be more practical with faster convergence and easier tuning of the regularization parameters. Convergence is not proven, but the article demonstrates that "if the algorithm has at least one fixed point, it converges to one of its fixed points". The resulting algorithm gave better image quality than state-of-the-art algorithms, e.g., prior image constrained compressed sensing (PICCS) [34], as illustrated in Figure 3.1.

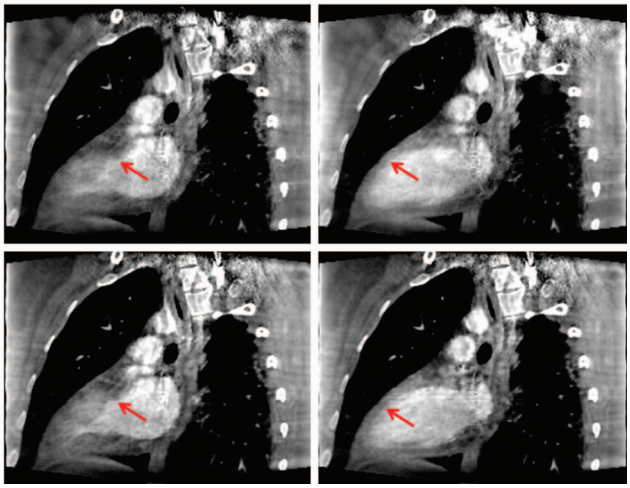

Figure 3.1: Long axis cut of the left ventricle of the end systole (left) and end diastole (right) frames of 4D cone-beam CT images reconstructed with PICCS [34] (top) and ROOSTER (bottom) from projections acquired on a C-arm cone-beam CT scanner. Figure adapted from [J51].

3.2 Cone-beam CT for image-guided radiotherapy

A natural application of the ROOSTER algorithm is image-guided radiotherapy for which respiration-correlated 4D cone-beam CT was initially developped [8]. Cyril Mory investigated this application in a postdoctoral fellowship funded by a public-private partnership between the IBA company and the Université Catholique de Louvain-La-Neuve. Compared to MCFDK, ROOSTER has the advantage of avoiding the need for a prior motion model and to provide the variations of the linear attenuation coefficients in time. However, the temporal regularization rapidly proved to be more detrimental to image quality than in cardiac imaging, probably because the contrast between anatomical structures is larger in the lungs than in the heart. This problem lead to the development of a new reconstruction algorithm, motion-aware ROOSTER (MA-ROOSTER) [J37].

MA-ROOSTER also makes use of a prior motion model to modify the temporal TV regularization of ROOSTER: the 4D cone-beam CT image is warped before temporal regularization and warped back after regularization. If the prior model perfectly compensates for the motion of 4D cone-beam CT, each voxel of the motion-compensated image contains the same tissue and displays only the temporal variations of its linear attenuation coefficient. This is equivalent to regularizing in time along the trajectories of the tissues instead of regularizing in time along the same spatial positions, which we know do not contain the same tissues due to breathing motion. MA-ROOSTER is therefore an intermediate algorithm between ROOSTER and MCFDK. MA-

ROOSTER clearly improved the image quality of ROOSTER and other unregularized iterative 4D cone-beam CT reconstruction algorithms (Figure 3.2).

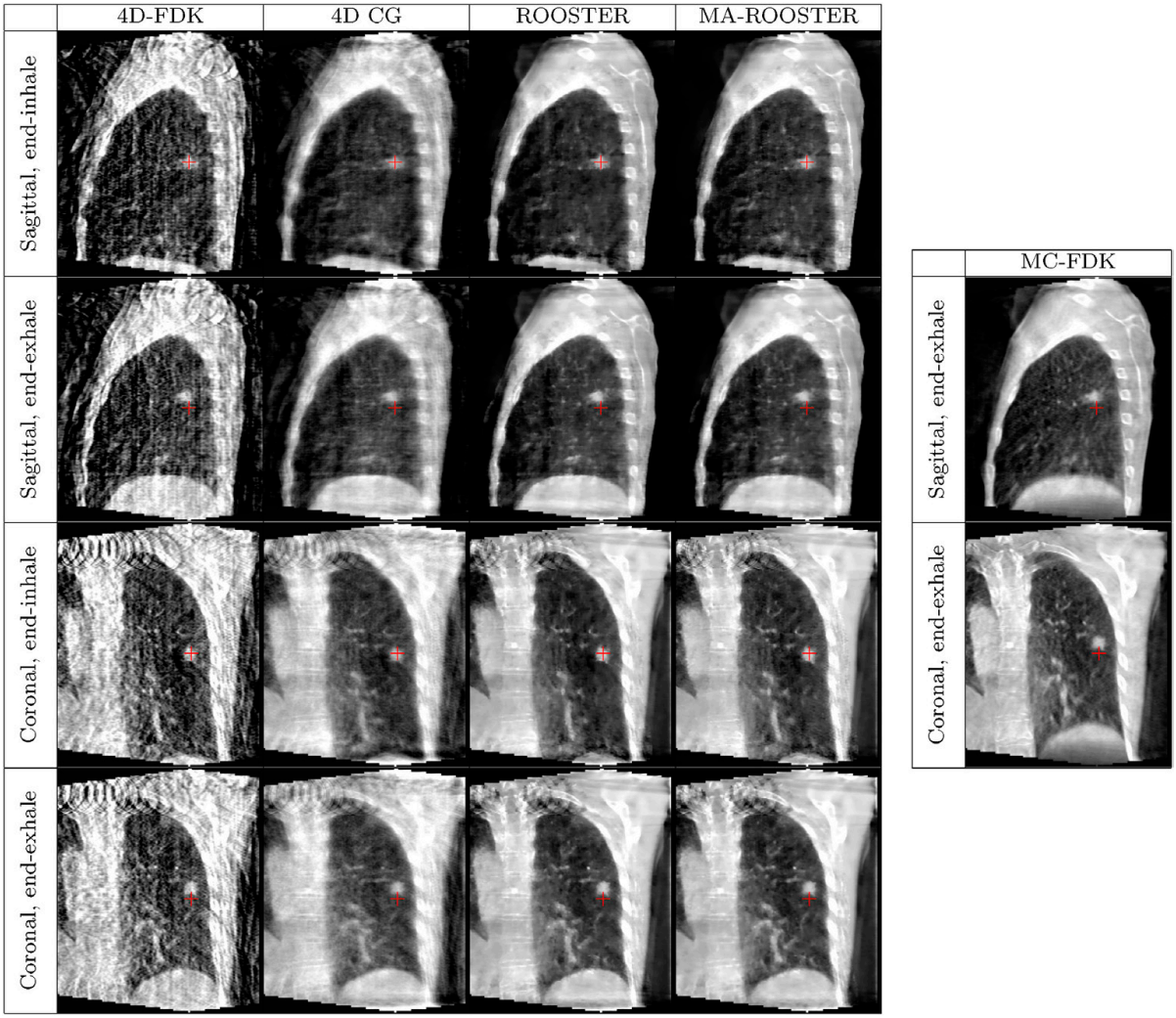

Figure 3.2: Sagittal and coronal slices of 4D cone-beam CT images reconstructed with several methods (FDK, CG, ROOSTER and MA-ROOSTER) and 3D MCFDK. Figure re-printed from [J37].

The image quality of one frame is similar to MCFDK, but we proved that MA-ROOSTER can show changes that MCFDK cannot capture. First, we showed that MA-ROOSTER reconstructs a 4D image which displays a motion different from the prior and closer to the actual motion of the patient. Second, we showed that MA-ROOSTER can recover variations of the tissue densities along the breathing cycle by looking at the average lung density, which is known to be larger at end-exhale than at end-inhale. The pattern of variation was similar to that of the 4D CT used for treatment planning.

3.3 Conclusions

The PhD thesis of Cyril Mory lead to a large effort on 4D iterative reconstruction with applications in cardiology, which was continued during a postdoctoral fellowship with applications in radiotherapy. His efforts lead to state-of-the-art and original algorithms which enriched the RTK [C29]. These algorithms have been evaluated in the recent sparse view reconstruction (SPARE) challenge comparing several such techniques, including MCFDK and MA-ROOSTER, and the

latter was one of the best performing algorithms [J14]. Since MA-ROOSTER is the outcome of many years of work of Cyril Mory on breathing motion compensation, a copy of the corresponding article is provided in chapter A.

We are currently investigating the applications of those techniques to single photon emission computed tomography (SPECT) with Antoine Robert, PhD student co-supervised by David Sarrut and funded by the Kitware company (https://www.kitware.com/). This project opens a completely new field for me, emission tomography, and will allow me to apply the techniques developed for x-ray CT to another modality, SPECT. The collaboration with Kitware is the latest result of my involvement in RTK as Kitware develops its back bone, the insight toolkit (ITK).

4

Region-of-interest reconstruction in the presence of motion

.

The backbone of my research has been tomographic reconstruction for CT since the beginning of my career. However, my PhD supervisors, David Sarrut and Serge Miguet, were not specialists of this field and I have developed external collaborations with a regional group of applied mathematicians, specialists of this topic, mainly led by Rolf Clackdoyle (at the *Laboratoire Hubert Curien (LHC)* in Saint-Étienne at the time, now at the *Techniques de l'Ingénierie Médicale et de la Complexité (TIMC)* laboratory in Grenoble) and Laurent Desbat (at TIMC in Grenoble). The collaboration was initially centered on my PhD subject and led to the main resulting publication [J65], but it was clear that there were other synergies in our works.

Rolf Clackdoyle has been a major actor of new developments in analytical ROI tomography [35]. In ROI tomography, one seeks to reconstruct CT images from laterally truncated projections, i.e., missing data in the direction orthogonal to the axis of rotation. He has co-authored several new algorithms that can analytically handle lateral truncation, which seemed impossible in the previous century. A natural question that arose given our respective investigations was the effect of motion on ROI tomography and how can one correct for it in analytical algorithms. We have co-supervised Jan Hoskovec on this topic from 2013 to 2016, a PhD student funded by the *région Rhône-Alpes*. I present here the main results that we obtained. All results were obtained in 2D on simulated data with a fan-beam geometry.

4.1 Differentiated backprojection

The reconstruction algorithm which has been used is summarized in a few words, without equations. It is based on the *two-step Hilbert transform method* [36] for reconstruction from 2D parallel projections. The key idea is to split the ramp filter (Equation 1.4) in a derivative and a Hilbert filter. Initially, Noo *et al* took the spatial derivative of each 1D projection, backprojected the resulting sinogram and inverted the resulting Hilbert transform in the image space. Taking the derivative is a local operation so truncation is not a problem for this operation. After backprojection of the derivative, also known as the *differentiated backprojection (DBP)*, all points that are seen by the detector at any projection angle on a π arc contain the Hilbert transform of the sought function. Using the (required) knowledge of the envelope of the scanned object, the sought function can be reconstructed along all segments for which the Hilbert transform is known at any point with end points outside the object envelope using the finite inverse Hilbert transform. In other words, all segments with end points outside the object envelope and which are seen by the detector at any projection angle can be reconstructed with this technique.

The work of Jan Hoskovec is based on a subsequent development of Zeng [37] who modified the order of the derivative and the backprojection. Mathematically, this change requires two weighted backprojections, one by the sinus of the projection angle and the other by its cosinus.

The assumption behind the use of this algorithm was that starting with the backprojection would allow to account for motion in the first step while keeping the other steps, the derivative and the finite inverse Hilbert, unchanged.

4.2 ROI reconstruction with motion in the fan-beam

The first approach followed by Jan Hoskovec was limited to object motion which would move the fan-beam at each projection, i.e., the sheaf of x-ray lines intersecting at the source position, to another sheaf of lines intersecting at the same source position, as previously proposed by [12]. Such motion leads to non-rigid motion, potentially impressive as shown in Figure 4.1, but for which a simple resampling of each projection allows to recover the sinogram of a the scanned object at a chosen position.

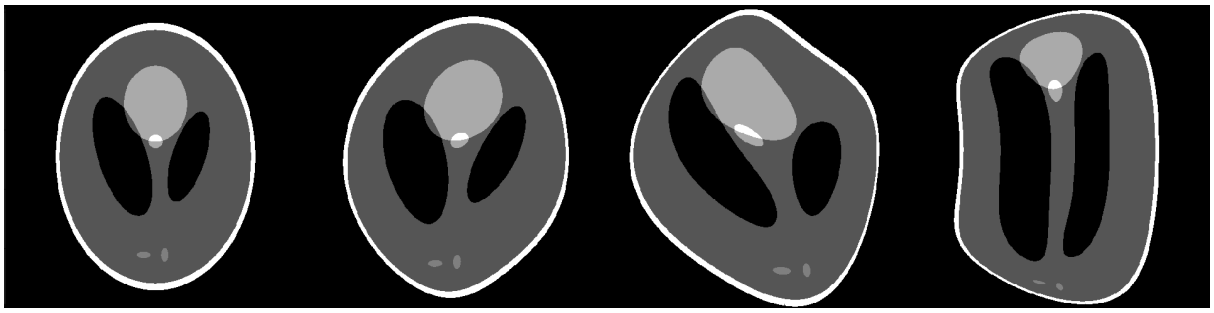

Figure 4.1: Shepp Logan phantom deformed by motion in the fan-beam, as described in section 4.2. Figure re-printed from [C23].

In this work, Jan Hoskovec modified the algorithm of Zeng [37] to compensate for motion during the backprojection of each cone-beam projection. The other steps were kept unchanged and the algorithm can therefore accurately reconstruct any segment with end points outside the object envelope and which is visible in all projections, despite the object motion.

4.3 ROI reconstruction with piecewise linear translations

In a second step [J40], Jan Hoskovec investigated the reconstruction of an object from projections acquired during piecewise translations of the object, as illustrated in the left part of Figure 4.2. This motion might seem simpler since it is rigid, but it modifies the source trajectory and analytical compensation is actually more challenging. The problem can then be reformulated as a static reconstruction with a source trajectory modified by the motion, as illustrated in the right part of Figure 4.2.

The contribution of Jan Hoskovec's work was to analyze both motion and truncation to calculate where all lines are measured, a necessary condition for reconstruction of a region, and to calculate the Hilbert transform in these points. The calculation handles trajectories modified by the motion which are discontinuous due to truncation, unlike previous solutions based on *chord* techniques [38]. The Hilbert transform can then be inverted with existing techniques and the enlargement of the region where the Hilbert transform is known can significantly increase the size of the reconstructible region.

4.4 Conclusions

ROI reconstruction of a moving object has been addressed in two dimensions during the PhD investigations of Jan Hoskovec. The extension to three dimensions has not been addressed

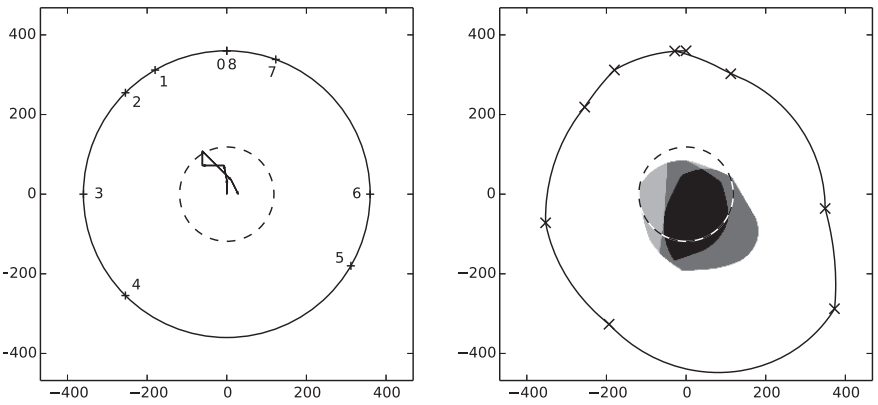

Figure 4.2: Left: source trajectory and motions vectors of an object. Right: corresponding source trajectory in the object frame with a colored partition of space. The points in the black region are always visible in the projections and the Hilbert transform can be computed with conventional DBP from all source positions. The points in the dark gray region are covered by a continuous segment of at least π and their Hilbert transform can be computed with a *chord* technique [38]. In the light gray region, the Hilbert transform can be computed with the method in [J40]. The points in white cannot be reconstructed due to insufficient data. Figure re-printed from [J40].

and is still an open challenge given the complexity of 3D ROI which can be understood by looking at the reconstruction from static helical CT alone, a problem that was also investigated during the postdoctoral fellowship of Fabien Momey with the same collaborators [J34]. Current investigations of Aurélien Coussat, a PhD student who is co-supervised by Jean Michel Létang and me in the context of the same collaboration, address whether equivalent image quality can be obtained with ROI reconstruction of a static object and, if yes, whether dose reduction is possible. Another PhD student, Mathurin Charles, should start in fall 2020 a project co-supervised by Rolf Clackdoyle on ROI reconstruction of a static object using a different approach known as the virtual fan-beam reconstruction.

5 Motion estimation and geometric calibration using DCC

According to [39], DCC, "also known as range conditions, refer to mathematical relationships between projections". They have been used to correct many artifacts which prevent accurate CT reconstruction due to, e.g., beam-hardening and scatter. Rolf Clackdoyle has been actively developping new DCC in the past decade [40, 41, 42, J35, 39]. This chapter describes two contributions using DCC. The first one is the detection of motion, which was investigated in the context of Jan Hoskovec's PhD thesis. The second one is the calibration of the geometry of a micro CT scanner, which was investigated by Jérôme Lesaint, co-supervised by Rolf Clackdoyle and Laurent Desbat, with whom I developed most of his experiments on simulated and real data.

5.1 Motion detection

An interesting set of DCC is the necessary and sufficient DCC for fan-beam projections along a line [40]. These DCC state that "integrals of the fan-beam projections multiplied by a certain function will be a polynomial in the trajectory variable". This source trajectory corresponds to some tomosynthesis systems, but it does not correspond to clinical x-ray CT scanners which use a circular or a helical source trajectory. However, any pair of source positions along any trajectory defines a line and the application of the first order of the DCC, the polynomial of order zero, defines one condition. In [C26], we have studied the use of this DCC for motion detection when the source moves along a line or a circle. This proof-of-concept study has demonstrated both the potential and some limitations of this mathematical tool for this application.

5.2 Geometric calibration

Not long after this initial work, Jérôme Lesaint joined the TIMC laboratory to investigate the use of DCC for auto-calibration [43], i.e., geometric calibration from the measured x-ray projections. Geometric calibration corresponds to the measurement of the source and detector position and orientation for every measured projection. If the source and the detector move similarly from projection to projection, this is equivalent to detecting the rigid motion of the patient. But in most cases, there is no patient motion that corresponds to the sought calibration parameters.

The work of Jérôme Lesaint has lead to the development of DCC for cone-beam CT. One set of DCC [C16, J35] was new but impractical due to its sensitivity to noise. We therefore chose another set for the calibration of a micro CT scanner, previously proposed in [44]. These DCC are calculated from resampled cone-beam projections on a plane parallel to the line defined by a pair of source positions. Each line of this virtual detector measures two fan-beam projections from sources on a parallel line and, as in the previous section, the first order DCC of [40] can be

used. This is illustrated in Figure 5.1. Note that Jérôme Lesaint later derived the DCC in the real detector coordinates [43].

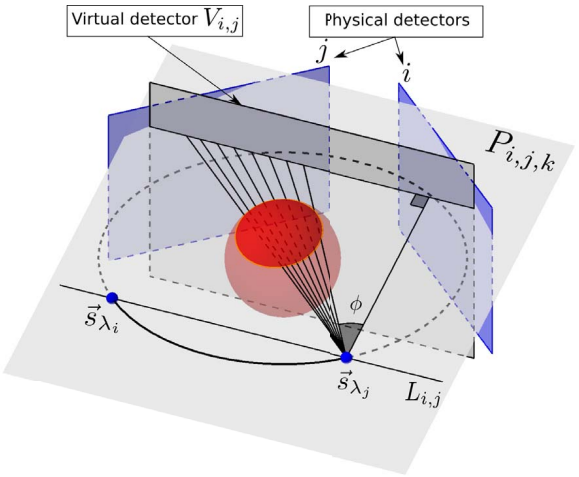

Figure 5.1: Schematic illustration of the resampling onto a virtual detector parallel to the line $L_{i,j}$ defined by two source positions $\vec{s}_{\lambda_i}$ and $\vec{s}_{\lambda_j}$ for the calculation of DCC. Each plane $P_{i,j,k}$ defines one condition. Figure re-printed from [J31].

The DCC can then be used to define a cost function which evaluates to which extent they are verified given a set of geometric calibration parameters. This cost function can then be optimized by finding the set of parameters which best verifies the DCC. In other words, only the dataset in which we are interested is used to geometrically calibrate the system and reconstruct images with good image quality. This strategy has been validated on the system pictured at the bottom right of Figure 1.1. We obtained similar image quality to that obtained with a conventional calibration based on ball bearings. Reconstructed CT images of a sponge sample, before and after auto-calibration, are shown in Figure 5.2.

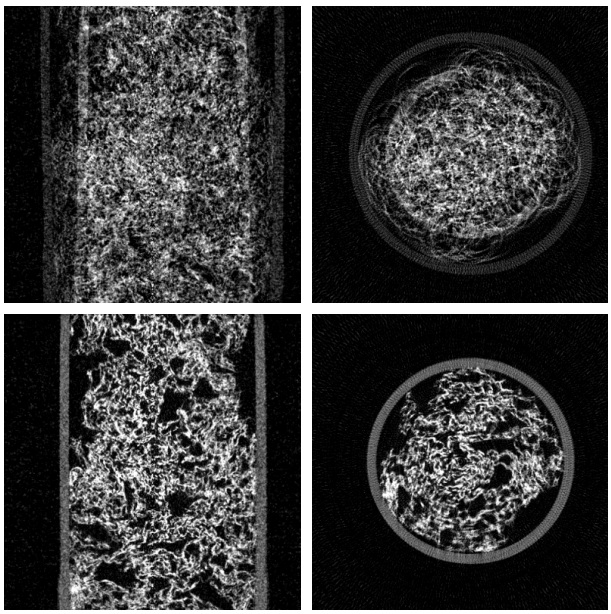

Figure 5.2: Cross-sectional (left) and axial (right) CT slices of a sponge in a tube reconstructed without (top) and with (bottom) auto-calibration based on DCC. The used micro CT scanner is pictured in Figure 1.1. Figure re-printed from [J31].

5.3 Conclusions

The field of DCC has seen many developments in the past few years, from the development of new sets of DCC to their applications to many image corrections. We have demonstrated their potential for motion detection and auto-calibration. Since fall 2019, I am co-supervising with Jean Michel Létang a new PhD student, Mélanie Mouchet, on the use of DCC for respiratory motion correction in conventional (helical) CT after preliminary results during her master [M1]. This new project in collaboration with Siemens nicely connects the different chapters of this first part paving the way to new investigations.

Part II

Spectral computed tomography

6

Image formation in spectral CT

Spectral CT is the collective term for all the technologies which measure and process x-ray projections acquired with more than one x-ray *efficient spectrum*, which is the energy-dependent function obtained by multiplying the source spectrum and the detector response function (both energy-dependent). This may be obtained by using at least two separate sources, by modifying the voltage of one source or by using an energy-resolved detector, as illustrated in Figure 6.1 for dual-energy CT (two efficient spectra). A detailed overview of the main concepts behind image formation in spectral CT is given in chapter B which is partly reused in this chapter to present some of the contributions I co-authored.

Two independent projects have triggered my implication in the development of decomposition and reconstruction algorithms in spectral CT: Dual-Energy X-ray imaging for TargEting Radiotherapy (DEXTER), which funded the PhD thesis of Gloria Vilches Freixas, co-supervised by Jean Michel Létang and me, and Spectral Photon Counting CT (SPCCT), which funded the postdoc fellowships of Cyril Mory and Pierre-Antoine Rodesch. I have also collaborated with the *laboratoire d'électronique des technologies de l'information* (LETI) of the *commissariat à l'énergie atomique et aux énergies alternatives* (CEA), a major actor in the development of photon counting x-ray detectors and who co-funded the PhD of Odran Pivot [S2] with the labex project Physics, Radiobiology, Imaging and Simulation (PRIMES), co-supervised with Jean Michel Létang, Clarisse Fournier and Joachim Tabary, after his master project supervised by Nicolas Ducros, Jean Michel Létang and me [M5].

6.1 Forward problem

Most of the literature is based on the model of Alvarez and Macovski [46] decomposing the attenuation coefficient μ of the object as a linear combination of a few energy-independent and space-independent functions

$$\mu(\boldsymbol{x}, \epsilon) \approx \sum_{m=1}^{\mathrm{M}} a_m(\boldsymbol{x}) f_m(\epsilon) \tag{6.1}$$

with $\boldsymbol{x}$ the 3D position in the object, ϵ the photon energy, M the number of basis functions, a_m the 3D space-dependent (but energy-independent) functions and f_m the energy-dependent (but space-independent) functions. Combining Equation 6.1 with Equation 1.1 and accounting for the effective spectra defines the nonlinear forward problem used in this chapter

$$\hat{y}_{ib} = \int_{\mathbb{R}^+} s_b(\epsilon) \exp\left(- \int_{\mathcal{L}_i} \sum_{m=1}^{\mathrm{M}} a_m(\boldsymbol{x}) f_m(\epsilon) \, \mathrm{d}\ell \right) \mathrm{d}\epsilon \tag{6.2}$$

with $\hat{y}_{ib}$ the expectation of the measures for the i-th detector pixel and the b-th effective spectrum s_b.

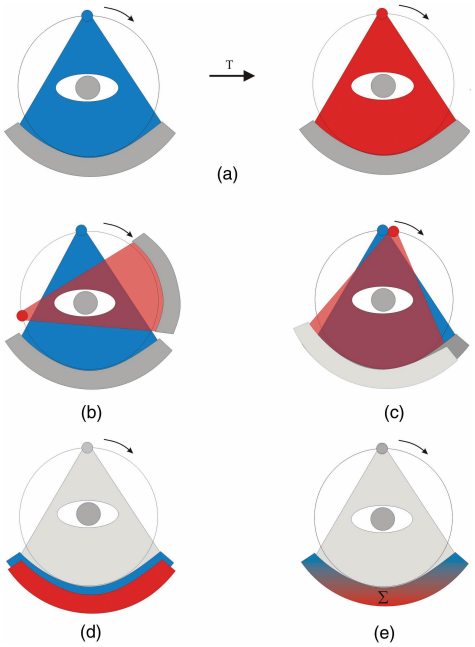

Figure 6.1: Different solutions to acquire dual-energy CT data: (a) two acquisitions with different voltages, (b) two sources, (c) fast kV switching, (d) dual-layer detector and (e) photon counting detector. Figure re-printed from [45].

6.2 Projection-based two-step reconstruction

The first category of solutions assumes that several measurements are available for each pixel of the projections to split the problem in two inverse problems. First, line integrals $A_{im} = \int_{\mathcal{L}_i} a_m(\boldsymbol{x})\,\mathrm{d}\ell$ are decomposed from the measurements using the forward problem

$$\hat{y}_{ib} = \int_{\mathbb{R}^+} s_b(\epsilon) \exp\left(-\sum_{m=1}^{\mathrm{M}} A_{im} f_m(\epsilon)\right) \mathrm{d}\epsilon. \tag{6.3}$$

Then, conventional CT reconstruction can be used to reconstruct the M a_m maps from the M sets of projections $\boldsymbol{A}_m = (A_{1m}, ..., A_{Im})^T$ with $I \in \mathbb{N}$ the number of pixels of the projections.

The first inverse problem, decomposing all values A_{im} from the measures y_{ib}, can be solved separately in each pixel i and is then a small non-linear problem (since M and B are both small). When the spectral model (source spectrum and energy response of each bin) is known, the problem can be solved iteratively by accounting for the Poisson statistics of the photon counting [47, 48]. When the spectral model is not known, one can instead calibrate a polynomial fit of the M unknowns given the B input values from measurements with known thicknesses of materials. Both Odran Pivot [M5] and Gloria Vilches-Freixas [J32] have used this approach for dual-energy ($B = 2$ and $M = 2$) as illustrated in Figure 6.2. Gloria Vilches-Freixas provides a comparison of the two approaches in chapter 5 of her PhD thesis [S3].

The solution is more complex when also decomposing a K-edge material ($M = 3$), e.g., Gadolinium, from more than two energies ($B > 2$), mainly because the problem is more severely ill-conditionned. In [J29], Nicolas Ducros investigated the addition of a spatial regularization in the projection domain and demonstrated a large improvement over the above-mentioned solutions. Figure 6.3 illustrates the improvement over a reference method [48].

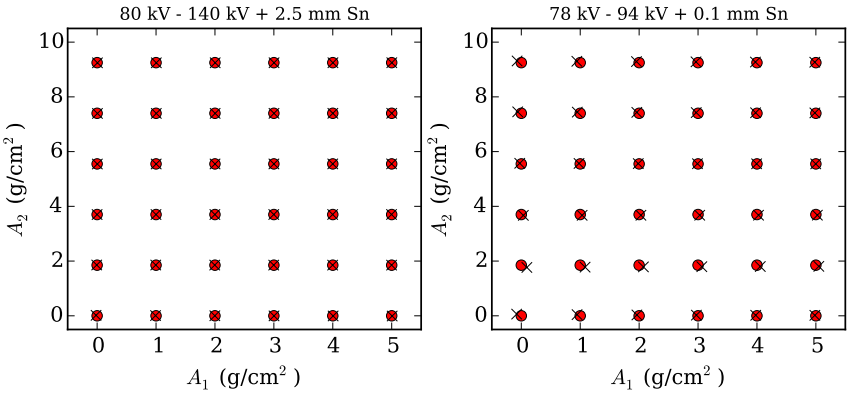

Figure 6.2: Difference between calibration (red points) and a 12-term 4-th order polynomial fit (blue crosses) for deriving basis material thicknesses A_1 and A_2. A different pair of source spectra is shown on each side. Figure re-printed from [S3].

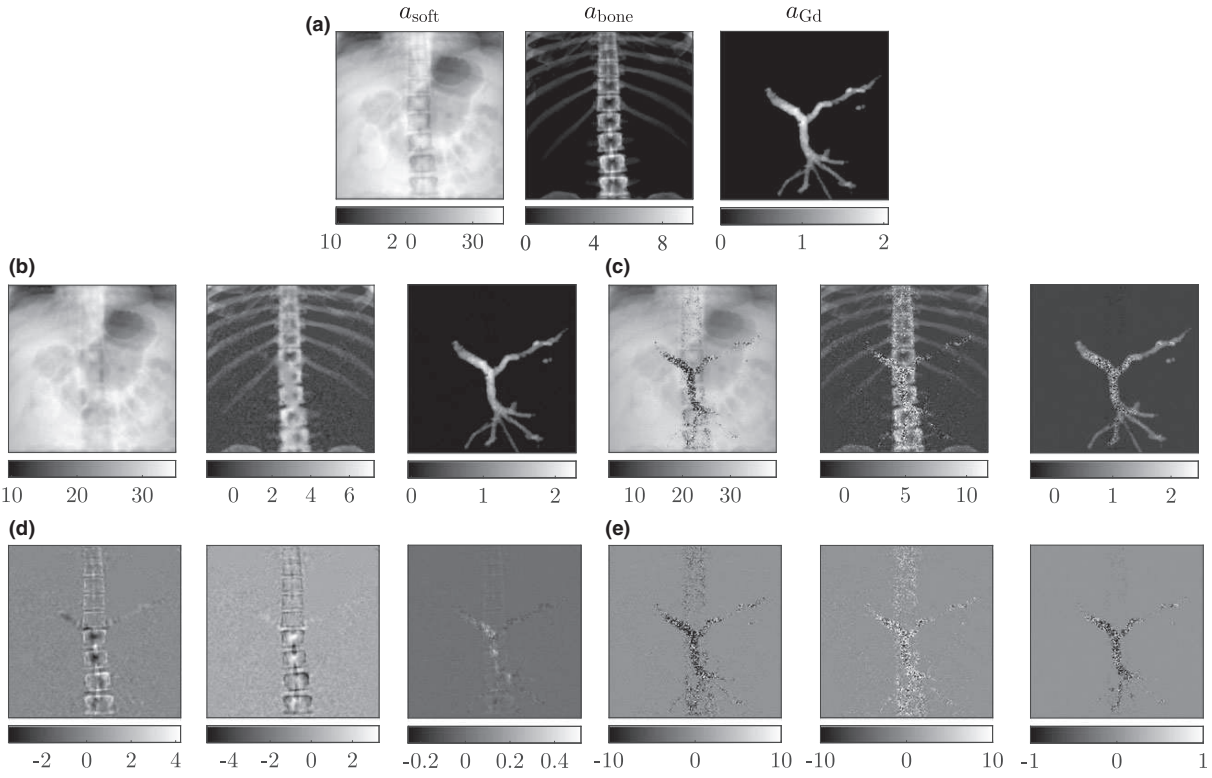

Figure 6.3: Basis material decomposition of (a) a reference radiography made of three materials (soft tissue, bone and gadolinium) with (b) spatial regularization [J29] and (c) no regularization [48]. Figures (d) and (e) are the differences of (a) with (b) and (c), respectively. Figure re-printed from [J29].

6.3 One-step reconstruction

One of the limitations of two-step decomposition is that when $M < B$, some information is necessarily lost after decomposing the projections. Since the problem is ill-conditionned, it seems more adequate to use all the available information to reconstruct the a_m CT images. Cyril Mory has therefore investigated one-step solutions, which directly reconstruct the a_m CT images from the measurements y_{ib}. His work, in the context of a postdoc funded by project SPCCT, aimed at reconstructing $M = 3$ materials from $B = 5$ bins, which corresponds to the characteritics of the prototype photon counting system developed by Philips and installed in Lyon. Cyril Mory has adapted five algorithms [49, 50, 51, 52, 53] to solve this problem and compared them in terms of some image quality metrics and convergence speed [J20]. On a simple numerical test phantom, he found large differences in terms of convergence speed between algorithms (Figure 6.4) with no obvious difference in image quality, even if they did not minimize the exact same cost function.

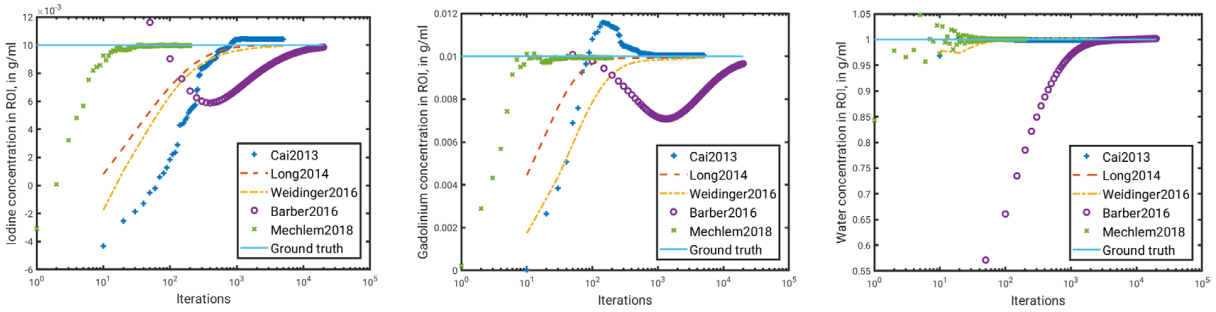

Figure 6.4: Convergence speed of the five one step algorithms compared in [J20] to a common objective, i.e., the reference concentration (horizontal lines) of Iodine (left), Gadolinium (center) and water (right) in selected regions-of-interest. Figure re-printed from [J20].

6.4 Scatter correction in spectral CT

The cone-beam CT scanners presented in Figure 1.1 have large detectors which will capture a large part of scattered radiation. They can all perform two acquisitions with two voltages (Figure 6.1a) and the medPhoton ImagingRing can do fast switching (Figure 6.1c, only in a non-clinical mode). The attenuation of the beam modeled in Equation 1.1 assumes that only the primary radiation is measured. This is a known issue of cone-beam CT and many hardware and software solutions have been proposed to block or correct for scatter. We have actively investigated this issue for mono-energetic acquisitions in collaboration with the public-private partnership ImagX between the université catholique de Louvain (https://uclouvain.be) and the IBA company (https://iba-worldwide.com/). This collaboration led to the development of fast Monte Carlo simulations of scatter using fixed forced detection used, e.g. in [J28] to validate a scatter correction algorithm [J36].

Odran Pivot investigated the correction of scatter for a photon counting system (Figure 6.1e) based on new detectors developed at LETI (Grenoble) during his PhD thesis [S2]. The main idea, based on previous works in single-energy CT [54, 55], is to place a beam modulator with an x-ray attenuation pattern containing high frequencies. Using spectral images of the beam modulator with known objects, e.g., slabs of known materials, one can calibrate a *correction matrix* such that the effect of the beam modulator is compensated for if there is no scatter. The presence of scatter will leave a trace of the beam modulator in the projections images after application of the correction matrix. One can therefore design an algorithm estimating the scatter map which removes the trace of the beam modulator from the scatter-corrected projections. The mask is designed with a high frequency pattern to measure its presence using the norm of the spatial

gradient. The scatter is constrained to be smooth.

Odran Pivot's key innovations are the design of matrices which use the spectral information to compensate for the beam modulator, the use of B-splines, to enforce smoothness and reduce the number of unknowns, and the definition of an appropriate cost function. His algorithm has been validated on both simulated and experimental spectral projections with 8 energy bins. Figure 6.5 shows a result on simulated projections of the International Commission on Radiological Protection (ICRP) adult reference computational phantom. This work has been patented [PA1] before publication [J9].

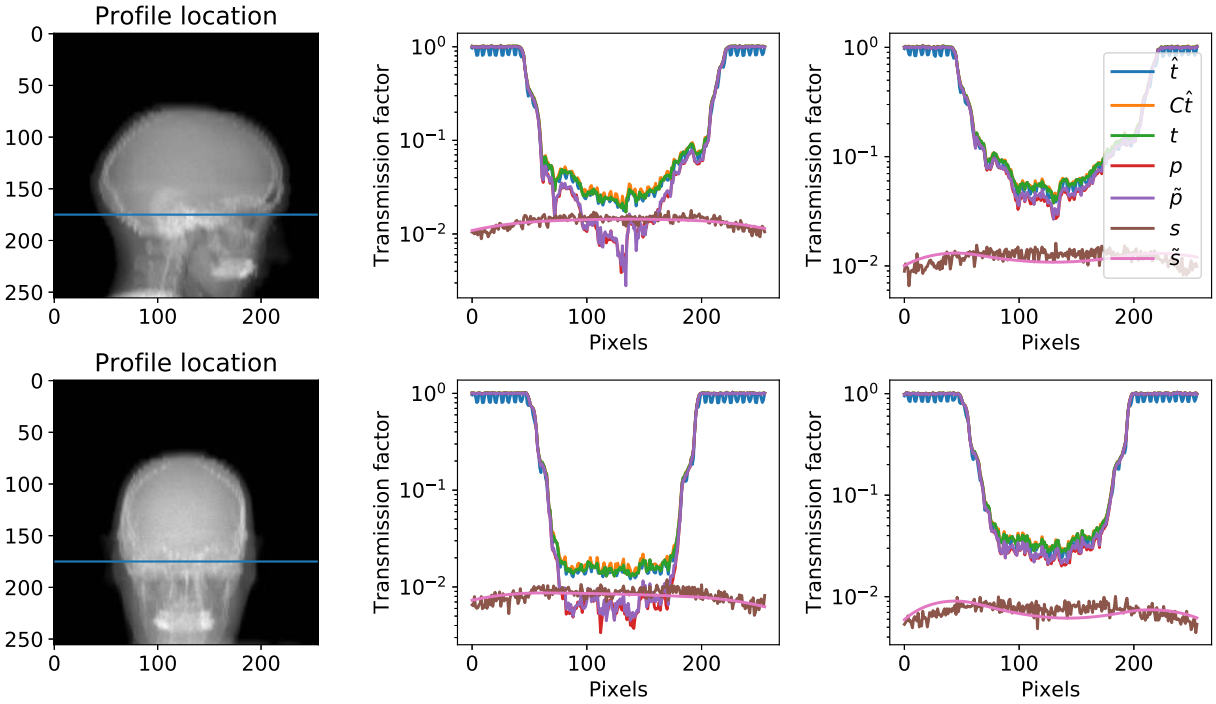

Figure 6.5: Illustration of spectral scatter correction using a beam modulator. Projection profiles of bin 2 (middle) and bin 6 (right) are shown. All profiles are normalized by the profile without object in the beam. The total t (green) is the sum of the primary p (red) and the scatter s (brown). The presence of the modulator modifies the total to $\hat{t}$ (blue) and compensating for the modulator with C still leaves a trace of the modulator due to scatter (orange). The scatter estimation gives the estimate $\tilde{s}$ (pink) and the scatter-corrected projection $\tilde{p}$ (purple). Figure re-printed from [S2].

6.5 Conclusions

Spectral CT has been a very active field of the past decade and the current developments of commercial photon counting CT scanners by the main CT manufacturers is the promise of a bright future. Clinical applications for this technology are under active investigation, e.g., quantification of materials with a K-edge in the diagnostic range as an alternative to SPECT [J15]. Dual-energy CT is already used for proton therapy planning in a few centers and this application is presented in the next chapter.

7 Spectral CT for ion therapy

Ions lose energy while traversing matter until they stop, unlike primary (non-attenuated) photons which keep their initial energy but whose fluence decreases exponentially according to the Beer-Lambert law (Equation 1.1). If one integrates laterally the energy deposited by a beam at a given depth in water, one obtains the depth-dose curves in Figure 7.1 which show that the maximum is deposited at the so-called Bragg peak where most ions stop. This behavior gives a significant advantage to ion therapy over conventional photon therapy as one can adjust the ions energy to deliver the Bragg peak in the targeted tumor. Despite the higher cost compared to conventional photon therapy, many proton therapy centers have been built worldwide to exploit this advantage, e.g., in Orsay, Nice and Caen in France. In Lyon, a large (abandoned) project to build a carbon ion center, *Espace de Traitement Oncologique par Ions Légers Européen* (ETOILE), had motivated many investigations in this field, e.g., on Monte Carlo simulations by my colleagues David Sarrut, Jean Michel Létang and Nicolas Freud at the CLB. Their expertise led to our investigations on ion imaging which are presented in Part III and those presented in this chapter.

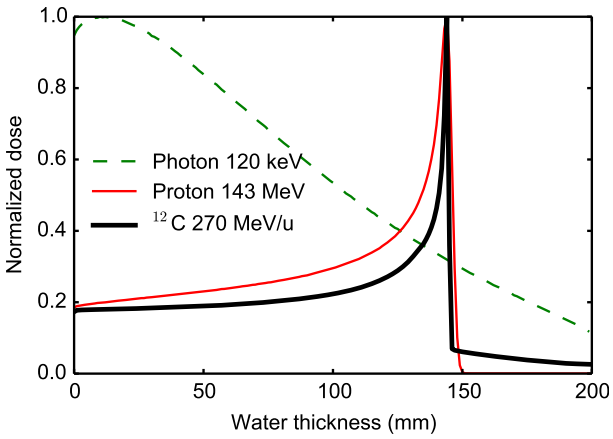

Figure 7.1: Depth dose profile of photons (green), protons (red) and carbon ion (black) in water. Figure re-printed from [S4].

A key challenge in ion therapy is the prediction and the monitoring of the location of the Bragg peak in the patient, also known as the range of the beam. This prediction requires the spatial map of the relative stopping power (RSP) of the patient tissues. The RSP is the ratio of the stopping power of the tissues over that of water, and it can be considered energy-independent, unlike stopping powers [J47]. Currently, ion treatments are planned on x-ray CT images which are converted to RSP using a 1D calibration curve. The uncertainty arising from this conversion is accounted for by adding margins around the target [56]. But several alternative strategies

have been investigated and are still being investigated.

One of the alternatives is spectral CT, based on the intuition that having more information on the patient materials can only improve the prediction of the RSP. Dual-energy CT was first suggested in 2009 [57, 58] and the benefits were theoretically proven not long after [59]. At that time, I was approached by Philipp Steininger and Heinz Deutschmann of the radART institute who were designing a new cone-beam CT scanner, the ImagingRing (Figure 1.1, bottom right), for the Austrian ion treatment center, MedAustron. The ImagingRing is equipped with a source which can switch voltage from projection-to-projection synchronized with a rotating wheel with different filters for each voltage to realize dual-energy CT (Figure 6.1c). This idea led to the DEXTER project which funded the PhD thesis of Gloria Vilches-Freixas on dual-energy cone-beam CT for proton therapy [S3]. This chapter summarizes her developments.

7.1 Dual-energy CT parameters for proton therapy

The DEXTER project started when the ImagingRing (Figure 1.1, top right) was still being developped. Since the project was in partnership with the designers of the ImagingRing, Gloria Vilches-Freixas investigated which voltages and filtrations were the best for the ion therapy application [C15, J32].

In a first step, Gloria Vilches-Freixas designed a method to calibrate a few parameters of the models of the x-ray source spectrum and the energy response of the detector [J38]. The parameters were the anode angle, thicknesses of aluminium and copper in front of the source and the thickness of scintillator in the detector. Several measurements were obtained by measuring the dose with an independent dosimeter (Figure 7.2) and the detector signal with various source voltages and filter thicknesses. The procedure was applied to three scanners, among which the ImagingRing.

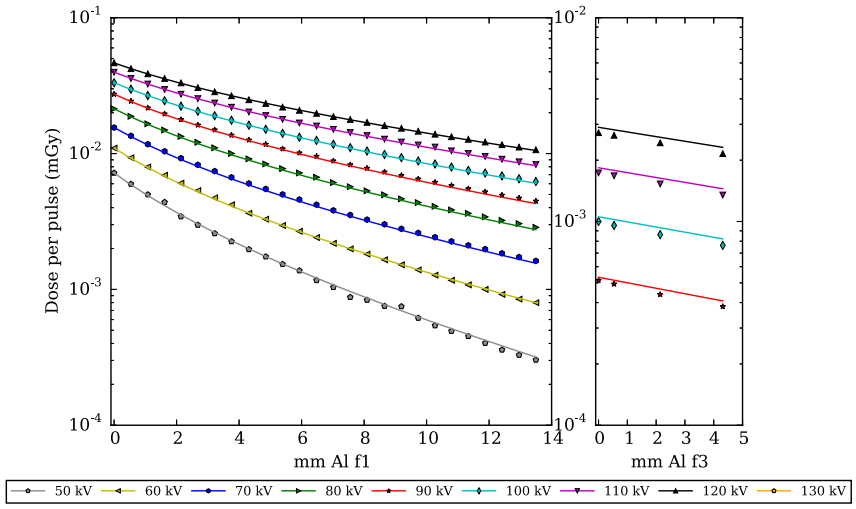

Figure 7.2: Illustration of the procedure for the calibration of the ImagingRing source model. Each point is measured by a dosimeter for a given source voltage and aluminium filtration and the lines depict the fitted source model. Figure re-printed from [J38].

This model was then used to simulate cone-beam projections with various combinations of voltages for the two energies and the thickness of the filter in front of the source for the highest voltage. The study used projection-based two-step decomposition and reconstruction (section 6.2). After reconstruction, the accuracy and the precision of the reconstructed RSP was measured in several materials. The results were found to be mainly dependent on the energy separation between the spectra, which is defined as the difference between the average energies of the two spectra. The accuracy of the RSP was found to be quite insensitive after reaching a

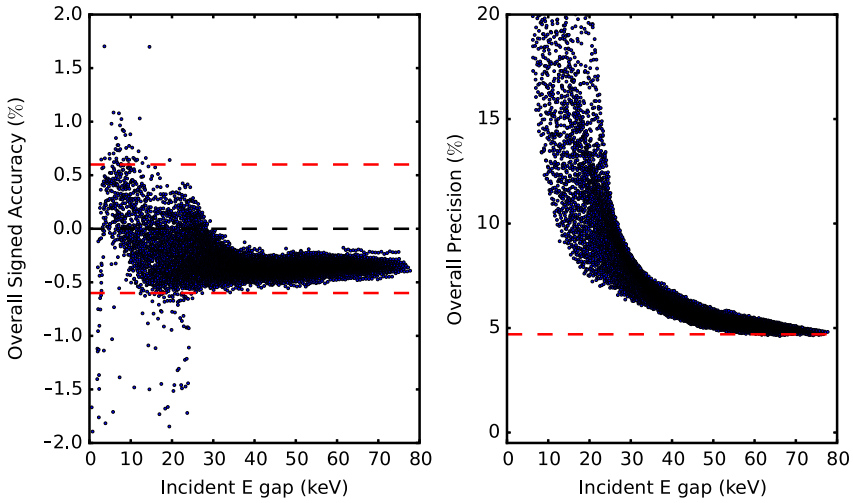

Figure 7.3: Accuracy (left) and precision (right) of the RSP estimated from dual-energy with different energy gaps between spectra obtained by varying the source voltage and the source filtration of the high energy spectrum. Figure re-printed from [J32].

minimum energy separation (Figure 7.3, left) and the optimal combination was actually material-dependent. The precision, on the other hand, improved significantly with increasing energy gap (Figure 7.3, right).

7.2 Comparison between projection-based and image-based spectral decomposition

In parallel to Gloria Vilches-Freixas' PhD, Vicki Trier Taasti was also investigating dual-energy CT for proton therapy in Aarhus (Danemark), but using image-based two-step reconstruction and decomposition, which is explained in chapter B. Therefore, the two PhD students compared the two approaches on simulated data [J30]. The projection-based approach was the Alvarez, Macovski and Kanematsu approach (AMK) developed by Gloria Vilches-Freixas [46, 60] and the three image-based approaches were the Stopping Power Parametrization (SPP) method [61] developed by Vicki Trier Taasti, the Saito and Kanematsu (SK) method [62, 60] and Han's method [63]. The differences between the different approaches were small and not statistically significant, but they indicated a potential advantage for projection-based approaches, with an overall root mean square error of 0.54%, 0.68%, 0.61% and 0.70% for the projection-based, SPP, SK and Han methods, respectively. Figure 7.4 illustrates a similar impact on range errors, i.e., the ability of the reconstructed RSP map to predict the depth of the Bragg peak (Figure 7.1).

7.3 Dual-layer CT for RSP estimation

Another approach was used to estimate the RSP on a commercial scanner, the Philips' IQON installed in Lyon (France), in collaboration with Guillaume Landry of the Ludwig Maximilians university (LMU) in Munich (Germany) [J19]. This scanner is equipped with a dual-layer detector which records two projection images for every x-ray pulse and uses a two-step projection-based approach (section 6.2). In this commercial product, the spectral decomposition is handled by the scanner which only provides mono-energetic CT images. We therefore chose to decompose the images using two mono-energetic CT images based on a combination of their decomposed images (Equation 6.1). An original approach for validation in this article was the comparison with synchrotron CT images acquired on the ID17 beamline of the European Synchrotron Radi-

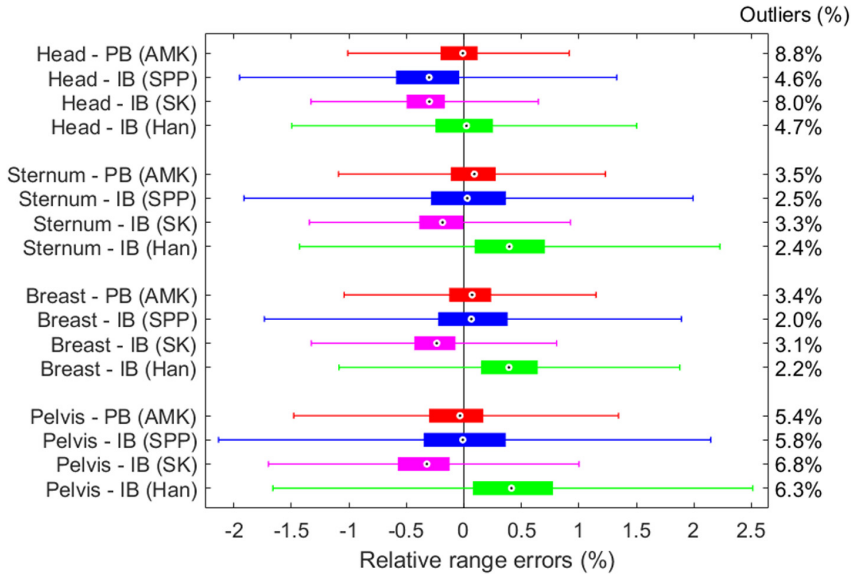

Figure 7.4: Distribution of the range errors assessed on the RSP map estimated from simulated images of the ICRP phantom. Four different axial locations were used (head, sternum, breast and pelvis). The range was assessed by integrating the RSP map through lines in all positions and directions using the Radon transform. Figure re-printed from [J30].

ation Facility (ESRF) with a truly mono-energetic beam (Figure 7.5). Our results demonstrate a root mean squared error of the RSP below 1% despite larger 1.9% for the linear attenuation coefficient, which further validates the dual-energy CT approach for RSP estimation.

7.4 Conclusion

Dual-energy CT for proton therapy has been an active field of research of the past ten years and this chapter presented several contributions of Gloria Vilches-Freixas under the supervision of Jean Michel Létang and me. Another solution to the same problem is proton CT which is presented in the following chapter along with another paper of Gloria Vilches-Freixas combining the two modalities [J24]. Dual-energy CT is now used clinically in a few proton therapy centers and it will probably become the standard for treatment planning. Improvements in image formation, e.g., one-step reconstruction (section 6.3), could play a role in its clinical adoption by improving image quality.

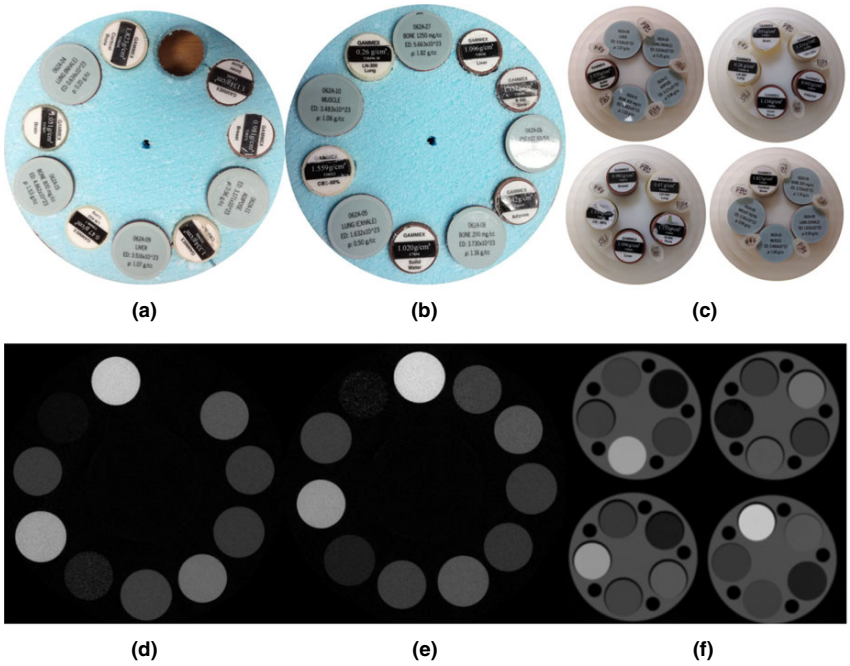

Figure 7.5: . Synchrotron CT images (d,e) and dual-layer CT images (f) at 50 keV of the same inserts with different configurations shown in (a-c). Figure re-printed from [J19].

Part III

Proton computed tomography

8 Energy-loss proton CT

As described in the introduction of chapter 7, my colleagues were interested in proton therapy when I joined the CLB CREATIS group in 2010. In this context, I was quickly introduced to the problem of proton CT reconstruction. Proton CT was originally proposed by Cormack at the same time as x-ray CT [64]. The idea is to use protons with sufficient energy to go through the scanned object or patient. Several experimental works in the 1970s (see [65, 66, 67] for historical reviews) demonstrated the limitations of proton imaging, mainly the poor spatial resolution due to multiple Coulomb scattering (MCS), i.e., the quasi continuous random deflections of protons in matter which cause them to follow slightly curved paths (chapter 7).

The development of proton therapy in the 1990s raised a new interest in proton CT for directly reconstructing the RSP map and improving proton therapy planning. In most of these recent developments, each proton position and direction is measured before and after the patient to estimate the most likely path (MLP) of the proton (Figure 8.1). Nils Krah recently showed [J23] that other integrating approaches, which integrate the information of many protons, like in x-ray CT, will inherently produce images with a poor spatial resolution due to MCS.

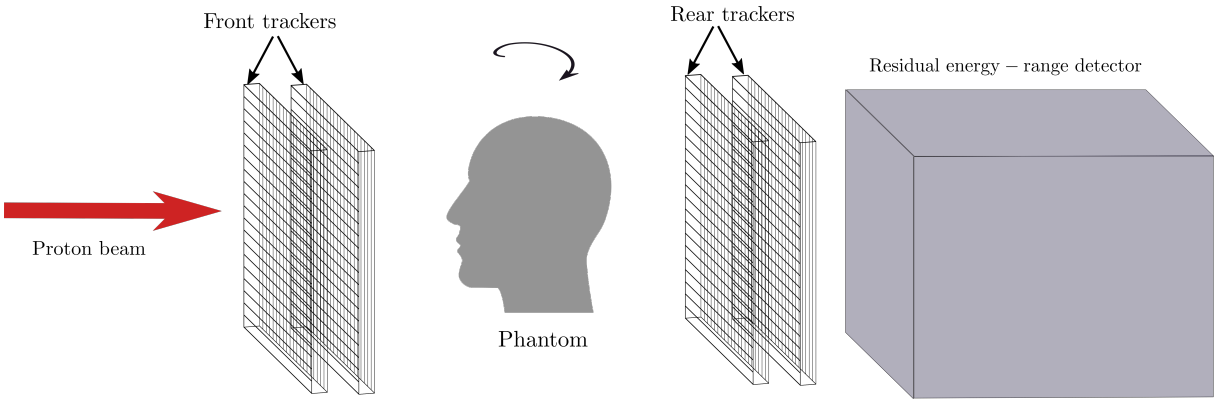

Figure 8.1: Schematic drawing of a list-mode proton CT scanner. Each proton position and direction is measured before and after the patient with pairs of trackers and the residual energy with a calorimeter or a range detector. Figure re-printed from [S1].

The most widely spread approach to proton CT is *energy-loss* proton CT, i.e., linking the energy lost by each proton to both the water-equivalent path length (WEPL) of the proton and the integral of the RSP along the path $\mathbf{\Gamma} \subset \mathbb{R}^3$ of the protons

$$\mathrm{WEPL} \equiv \int_{E_{\mathrm{out}}}^{E_{\mathrm{in}}} \frac{1}{S_{\mathrm{water}}(E)}\,\mathrm{d}E = \int_{t_{\mathrm{in}}}^{t_{\mathrm{out}}} \mathrm{RSP}(\mathbf{\Gamma}(t))\,\mathrm{d}t \tag{8.1}$$

with E_{in} and E_{out} the entrance and exit energies of the proton, S_{water} the energy-dependent proton stopping power in water and t_{in} and t_{out} the entrance and exit times of the proton. In practice, the true (random) proton path $\mathbf{\Gamma} \subset \mathbb{R}^3$ cannot be measured and only the MLP $\hat{\mathbf{\Gamma}}$ is estimated from measures of the entrance and exit positions and directions. The reconstruction of the 3D RSP map from E_{in}, E_{out} and $\hat{\mathbf{\Gamma}}$ for a set of protons, in a *list-mode* approach, is a tomographic reconstruction problem from integrals along curves and I quickly made the connection with motion-compensated CT reconstruction (subsection 1.3.2). However, there was no algorithm for FBP reconstruction along MLP in proton CT, unlike Equation 1.3 for motion-compensated CT which provides an approximate but efficient solution to this problem. I therefore proposed such an algorithm [J57], described in section 8.2, which opened a new field of my investigations with several research projects funding two PhD students (Catherine Therese Quiñones [S4], funded by a ministry grant, and Feriel Khellaf [S1], funded by a *Fondation pour la Recherche Médicale* (FRM) project) and four postdoctoral fellows (Nicolas Arbor and Georges Dedes funded by PRIMES, Nils Krah and Ahmad Addoum funded by the same FRM project). The descriptions of my contributions in this field have been divided in two chapters, the ones directly related to energy-loss proton CT in this chapter and other proton CT modalities in the next one.

8.1 Most likely path of protons

Estimation of the MLP $\hat{\mathbf{\Gamma}}$ of each proton is a prior step of both direct and iterative reconstruction algorithms. The most common solution is to assume that the object is homogeneous and made of water [68, 69] and we have used this approach in most of our developments. In these models, the energy lost by the protons is modeled by a polynomial of order M. In a recent work [J11], Nils Krah demonstrated that under this assumption, the MLP described in [68, 69] is a polynomial of order $M + 3$. The paper also demonstrates how to quickly sample polynomial trajectories for fast Monte Carlo simulations in homogeneous media.

The question of the effect of the homogeneity assumption on the MLP accuracy in heterogeneous objects has been addressed by Feriel Khellaf [J17] by simulating many proton trajectories in simple objects using Gate / Geant4 (Figure 8.2, left). The protons with the same positions and directions, before and after the object, were selected and used to estimate the *real* MLP, i.e., the most likely transverse position at each depth (Figure 8.2, right). The theoretical MLP, given by [69], was always close to the real MLP, even in objects with significant transverse heterogeneities, with a maximum error of 0.41 mm. The maximum difference in an anthropomorphic phantom was 0.13 mm. The transverse heterogeneities have a significant effect on the energy distribution of protons and accounting for this effect will likely have more impact than accounting for heterogeneities in the MLP estimation. All the works presented hereafter use the MLP of Schulte *et al* [69].

8.2 Distance-driven binning

FBP reconstruction from list-mode proton CT data is generally achieved by binning the data in projection images corresponding to a virtual detector plane. In the first approaches, a single plane was used to bin list-mode data. Each pixel of this virtual projection mixes then informations of different protons which have followed different paths, as illustrated in Figure 8.2, and features in-between the source and the plane are blurred. In [J57], we proposed to use the MLP and to bin protons for one source position in several virtual planes instead of one only. By doing so, one computes projection images which have the best spatial resolution for features located in the corresponding plane (Figure 8.3). During FBP reconstruction, one can chose for every source and pixel of the RSP map the projection image which maximizes the spatial resolution. The resulting proton CT image is much better resolved than the ones assuming straight line paths

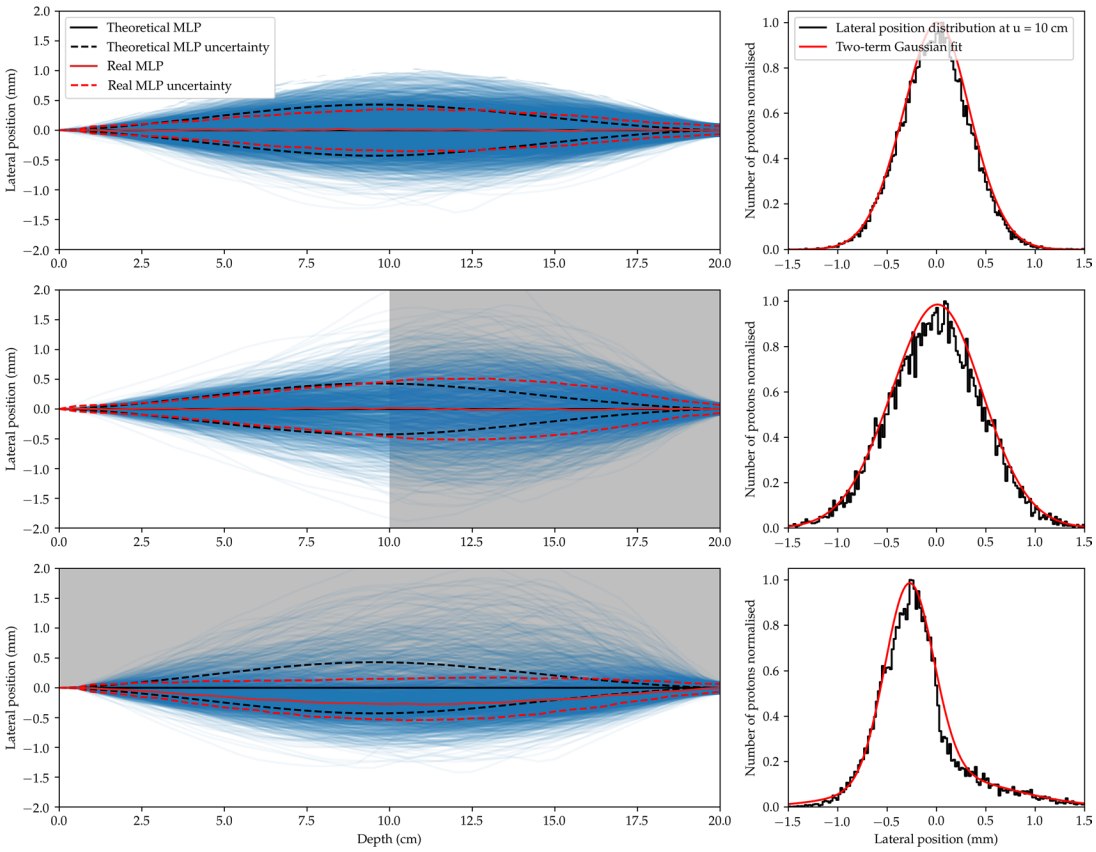

Figure 8.2: MLP estimation for homogeneous (top) and heterogeneous phantoms with a longitudinal heterogeneity (middle) and a transverse heterogeneity (right). The left column illustrates the paths projected on a 2D plane, each blue line representing the path of a proton simulated by Geant4, superimposed on the phantom with water in white and bone in grey. The right column illustrates how the real MLP is estimated, by fitting a two-term Gaussian to all paths at a given depth. Figure re-printed from [J17].

for the protons. This work is fundamental of my involvement in proton CT and a copy of the article is included in chapter C.

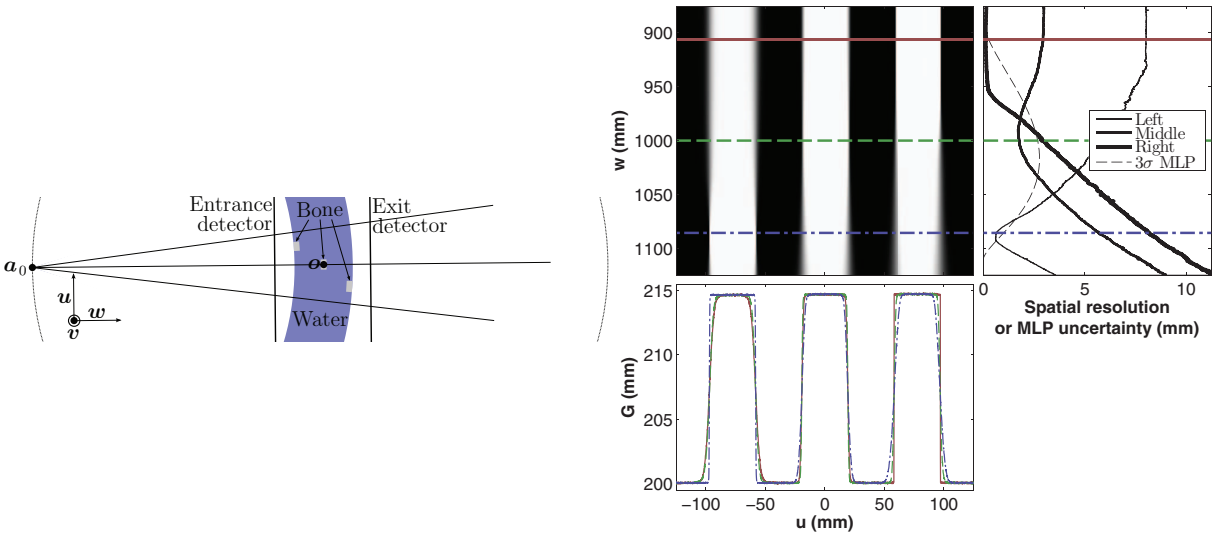

Figure 8.3: Illustration of the distance driven-binning. Without MCS, the left setup would provide a projection made of three rectangular functions. One can observe on the right that MCS actually blurs these rectangular functions and the impact depends on the distance w between the virtual plane and the source. Figures adapted from [J57].

8.3 Two-step reconstruction based on differentiated backprojection

Not long after, another group proposed an alternative approach based on filtering the backprojection [70]. Similarly to the distance-driven binning, their algorithm bins the list-mode data in a 3D image space. However, their space is directly that of the final image and they integrate the binning over the projection angle to obtain the so-called backprojection. The problem is that the backprojection has an infinite support and they provide a first-order correction term for the inevitable approximation. At the same time, Rolf Clackdoyle and I were supervising Jan Hoskovec on Hilbert transform methods for reconstruction (section 4.1) and a differentiated backprojection approach [37] can avoid this issue, as explained in chapter 4. We therefore applied this strategy to proton CT [C19]. The resulting algorithm avoids the additional interpolation required by backprojection after binning since the binning directly occurs on the backprojection grid. An additional advantage is that it can avoid some amount of truncation of the DBP.

8.4 Oblique ramp filtering

A last solution, which was recently investigated by Feriel Khellaf, co-supervised by Jean Michel Létang, Nils Krah and me, is to modify the conventional FBP (ramp filtering of the projections then backprojection), to backproject one projection at a time and apply an oblique ramp filtering before integration over the line orientations [J7]. The main difficulty in the implementation of this algorithm is the discretization of the oblique 2D ramp filter, which was eventually obtained by band-limiting the filter as in the 1D case.

8.5 Comparison between reconstruction algorithms

The developments of the three direct reconstruction algorithms described in the previous sections led to comparative studies.

First, we approached David Hansen, who investigated iterative reconstruction for list-mode proton CT during his PhD and who stated at the International Conference on Translational Research in Radio-Oncology and Physics for Health in Europe (ICTR-PHE) in 2014, attended by George Dedes, that FBP reconstruction accounting for MLP reconstruction was not feasible. We therefore compared the reconstructed images from the same data [J39]. The differences in spatial resolution between the different algorithms (FBP reconstruction using the distance-driven binning and several iterative algorithms) were small, but the computational cost was much lower for the direct FBP reconstruction.

In a separate study [J6], Feriel Khellaf compared the existing direct reconstruction algorithms which use the MLP, i.e., the three methods presented above and two from other groups [70, 71]. A set of reconstructions of the same phantom is provided in Figure 8.4. Using Monte Carlo simulated data, we evaluated the RSP accuracy, the spatial resolution and the computation time. The filtering of the backprojection [70] and the oblique ramp filtering (section 8.4) obtained a slightly better resolution from data simulated with *ideal* trackers (i.e., with infinite spatial resolution), but the differences vanished from realistic data [71] which had a lower spatial resolution. The methods which were better resolved spatially also showed the best RSP accuracy with a mean absolute error of 0.1%. The computation time was dominated by the MLP computation. Since the oblique ramp filtering and the filtering of the backprojection require larger images during reconstruction, the distance-driven binning algorithm (section 8.2) still seems to be the best compromise for the criteria of this study.

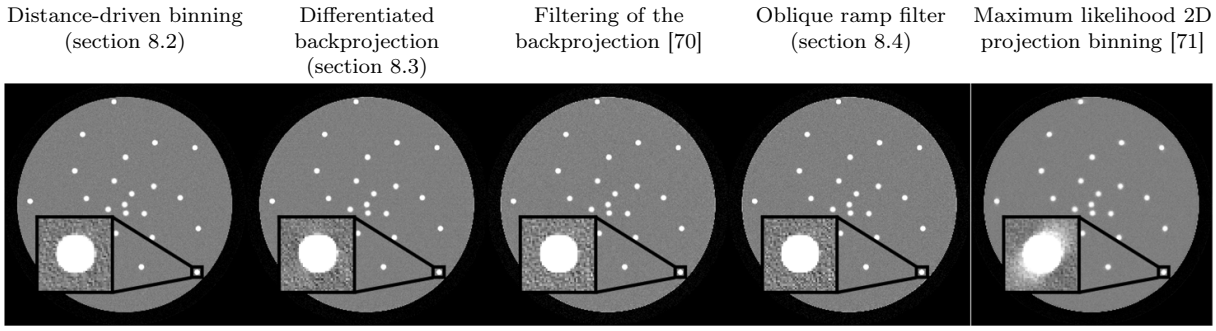

Figure 8.4: Reconstruction of the same resolution phantom from different reconstruction algorithms. Figure adapted from [J6].

8.6 Calibration of x-ray CT numbers to RSP using proton radiography

A major difficulty for practically realizing proton CT is the ability to rotate the proton beam around the patient. That is why it was proposed to measure only a proton radiography, in the direction of the treatment beam, and to use it to automatically determine the conversion curve from x-ray CT numbers to RSP using a prior x-ray CT image. Nils Krah investigated this inverse problem using Monte Carlo simulations [J18], in particular different forward projectors and the need for regularization. The Monte Carlo simulation was based on an initial x-ray CT number to know the ground truth, which would not have been available for a phantom such as the ICRP adult reference computational phantom since, in general, there is no one-to-one mapping between x-ray CT numbers and RSP. The simpler forward projector resulted in similar accuracy as the

Monte Carlo forward projector. The correlation between the unknowns of the problem requires regularization, as illustrated in Figure 8.5.

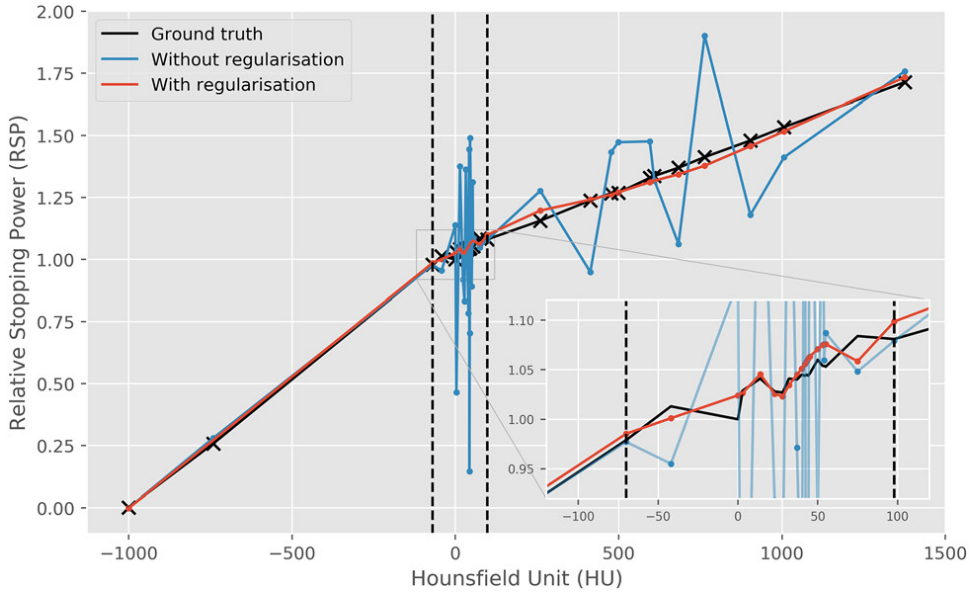

Figure 8.5: CT number to RSP conversion curve determined from a single proton radiography and an x-ray CT image, without (blue) and with (red) regularization). Figure re-printed from [J18].

This work was further developed to apply it to x-ray cone-beam CT [C6]. X-ray cone-beam CT images can now be acquired in some protontherapy rooms and this would provide a solution for imaging the RSP map in the treatment room, without using prior images. X-ray scatter is then a problem and must be partially corrected. With scatter correction, Nils Krah showed that this solution can improve the estimation of the RSP image compared to the planning RSP map which does not account for anatomical changes.

8.7 Mean excitation energy map from energy loss proton CT and dual-energy x-ray CT

Gloria Vilches-Freixas and Catherine Therese Quiñones were PhD students at the same time. Since the former was reconstructing the relative electron density (RED) using dual-energy x-ray CT and the latter was reconstructing the RSP using energy-loss proton CT, we observed that these two maps could be combined to estimate the map of another local property, the mean excitation energy [J24]. Indeed, the Bethe Bloch equation, which can be used to compute the stopping power of ions in a given material at a given energy, depends on two other material properties, the electron density and the mean excitation energy. If one deduces the stopping power and the electron density from energy-loss proton CT and dual-energy x-ray CT, respectively, only the mean excitation energy is left unknown. The technique was assessed using Gate simulations of the ICRP adult reference computational phantom. The proof-of-concept demonstrated the feasibility of the technique (Figure 8.6). However, it was very sensitive to noise because the exponential of the ratio of the two input maps is taken for calculating the map of the mean excitation energy. The slight energy dependence of the RSP [J47] was also a source of inaccuracy. Further investigations would require experimental validation, but the experimental determination of the mean excitation energy is not trivial and the one of water alone is still a subject of discussion.

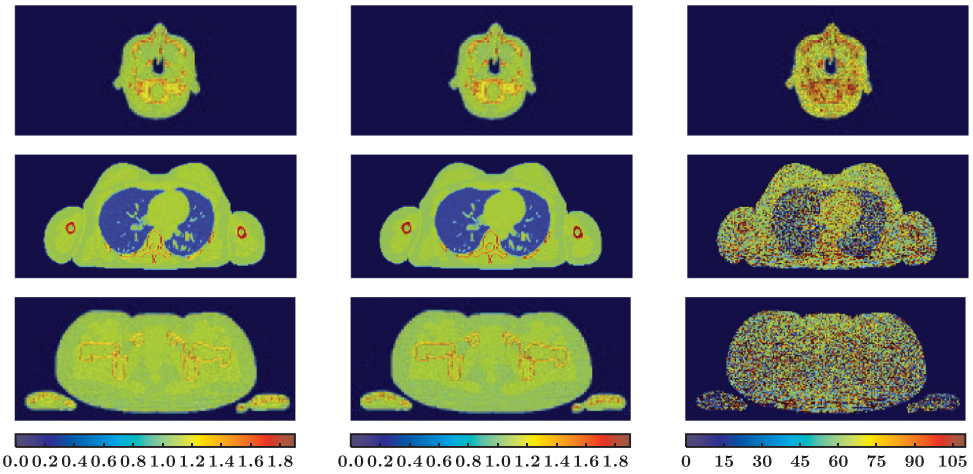

Figure 8.6: RSP (left), RED (middle) and mean excitation energy (right) of the ICRP adult reference computational phantom in the head (top), lungs (middle) and pelvis (bottom) regions. Figure re-printed from [J24].

8.8 Assessment of the clinical relevance of proton CT using Monte Carlo simulations

Proton CT was deemed to be "the ideal way to determine proton RSP distribution inside the patient" [59], but it seemed necessary to assess the difference to x-ray CT. To this end, after some initial developments of George Dedes, Nicolas Arbor simulated x-ray and proton CT images of the ICRP adult reference computational phantom using Gate / Geant4 [J47]. The two scanners were idealized in several ways (no x-ray scatter, perfect proton trackers and energy detector, etc.). X-ray CT was processed as in proton centers, i.e., using a conversion curve from Hounsfield units to RSP. The resulting RSP maps of the phantom in three locations (head, thorax and abdomen) were evaluated in terms of RSP accuracy as well as their ability to predict the range of many small proton pencil beams in different directions and locations. The mean absolute deviation of the latter varied from 0.18 to 2.01 mm for x-ray CT depending on the anatomical site while it was smaller than 0.1 mm for proton CT (Figure 8.7). It was concluded that "under the assumption of a perfect detection system, proton range predictions based on proton CT are therefore both more accurate and more uniform than those based on x-ray CT".

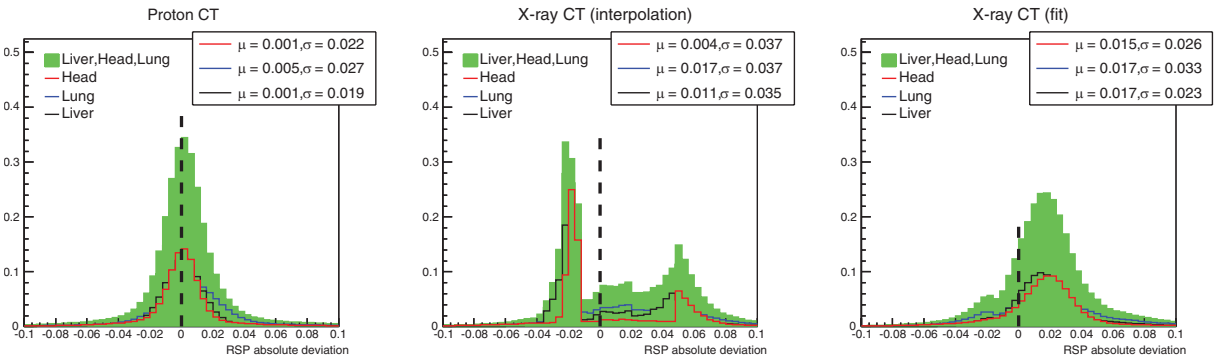

Figure 8.7: Distribution of the range errors measured on RSP maps of the ICRP adult reference computational phantom obtained from simulated x-ray and proton CT images. Two conversion curves from x-ray CT numbers to RSP were used, one using interpolation between a reference phantom and the other from a fit of the same data. Figures adapted from [J47].

8.9 Conclusion

This chapter presented my contributions to the problem of energy-loss proton CT reconstruction. Several algorithms have been proposed since [J57], but our comparative studies indicate that it is still one of the best solutions. Two forms of combination of proton imaging with x-ray CT have also been summarized. We have finally assessed the clinical relevance of proton CT using simulations and found a small but significant improvement over single-energy CT.

George Dedes, who was with us for a few months in 2012 before joining the LMU, continued to evaluate proton CT images with the distance driven binning algorithm and his group (led by Katia Parodi with also the strong involvement of Guillaume Landry) produced many interesting results. First, he compared proton CT to dual-energy CT (chapter 7) using real data acquired on a prototype proton CT scanner. He found a slight advantage of proton over dual-energy CT for plastic inserts mimicking human tissues [J13]. The same group has also been actively investigating RSP resolution of proton CT images reconstructed with the same algorithm [J16, J21]. This work, after some initial proofs of principles [J22, J33], is now used to develop fluence-modulated proton CT images by a PhD student, Jannis Dickmann [J3, J8].

In my opinion, the future of proton CT mainly depends on hardware developments. It is not easy to realize a proton CT scanner which can acquire data sufficiently fast (ideally, with a proton rate around 10 MHz) to make it clinically practical. It also depends on the availability of a gantry or of a rotating chair in the treatment room to realize the tomographic acquisition. If these technical challenges were met, it is my belief that the developments presented in this chapter would be central towards a clinical proton CT scanner.

9 Other proton CT modalities

List-mode proton CT scanners as the one sketched in Figure 8.1 have been developped for reconstructing the RSP map from the measure of the energy loss of each proton. This is not, however, the only possibility. Inspired by the PhD thesis of Cécile Bopp [72, 73, 74], Jean Michel Létang and I supervised the PhD of Catherine Therese Quiñones on attenuation and scattering proton CT [S4]. These three 3D CT images form a 4D image which is multi-modal or, to underline the fact that they are reconstructed from the same measurements, a multi-variate proton CT image. Her work has been continued by two postdocs, Nils Krah and Ahmad Addoum. This chapter describes these investigations and two possibilities to combine energy-loss proton CT with x-ray CT.

9.1 Attenuation proton CT

A majority of the protons go through the patient and one can use the energy loss of each one to reconstruct a proton CT image using Equation 8.1 for the forward model. But there is also a portion of the protons which do not make it through the patient because they encounter inelastic nuclear interactions. As in x-ray CT, one can therefore take the ratio of the number of protons after the patient over the number of protons before the patient, which can be related to the line integral of the inelastic nuclear stopping power map of the scanned object. Unlike the energy-loss proton CT problem (Equation 8.1), for which a line integral is provided by every proton, attenuation proton CT is based on counts for several protons and one must bin the list-mode information. The main contribution of Catherine Therese Quiñones was to adapt the distance driven-binning algorithm (section 8.2) to attenuation proton CT and to characterize the accuracy and the precision of the reconstructed RSP [J42]. The central line of Figure 9.1 and the line profiles in Figure 9.2 illustrate the spatial resolution improvement of the distance-driven binning algorithm over a single distance binning which assumes a straight-line path (SLP). It also illustrates visually the increase in noise for the same imaging dose, which was also demonstrated analytically following the development in [75] for energy-loss proton CT (Figure 9.3). The accuracy of the reconstructed values relies on the assumption that the inelastic nuclear cross section is energy independent, which is only valid above 100 MeV and capping artifacts were observed otherwise.

It is interesting to note the edge-enhancement artefact of SLP images in the bottom line of Figure 9.2. This was attributed to the interplay between MCS and attenuation known as the West-Sherwood effect [76]. Since such images can be acquired by an integrating detector which records a signal proportional to the proton counts, Ahmad Addoum and Nils Krah have investigated how modeling this effect could lead to an improvement of the spatial resolution of such images. The corresponding forward problem mixes the models of attenuation and scattering proton CT (next section). Similarly to projection-based material decomposition in spectral CT

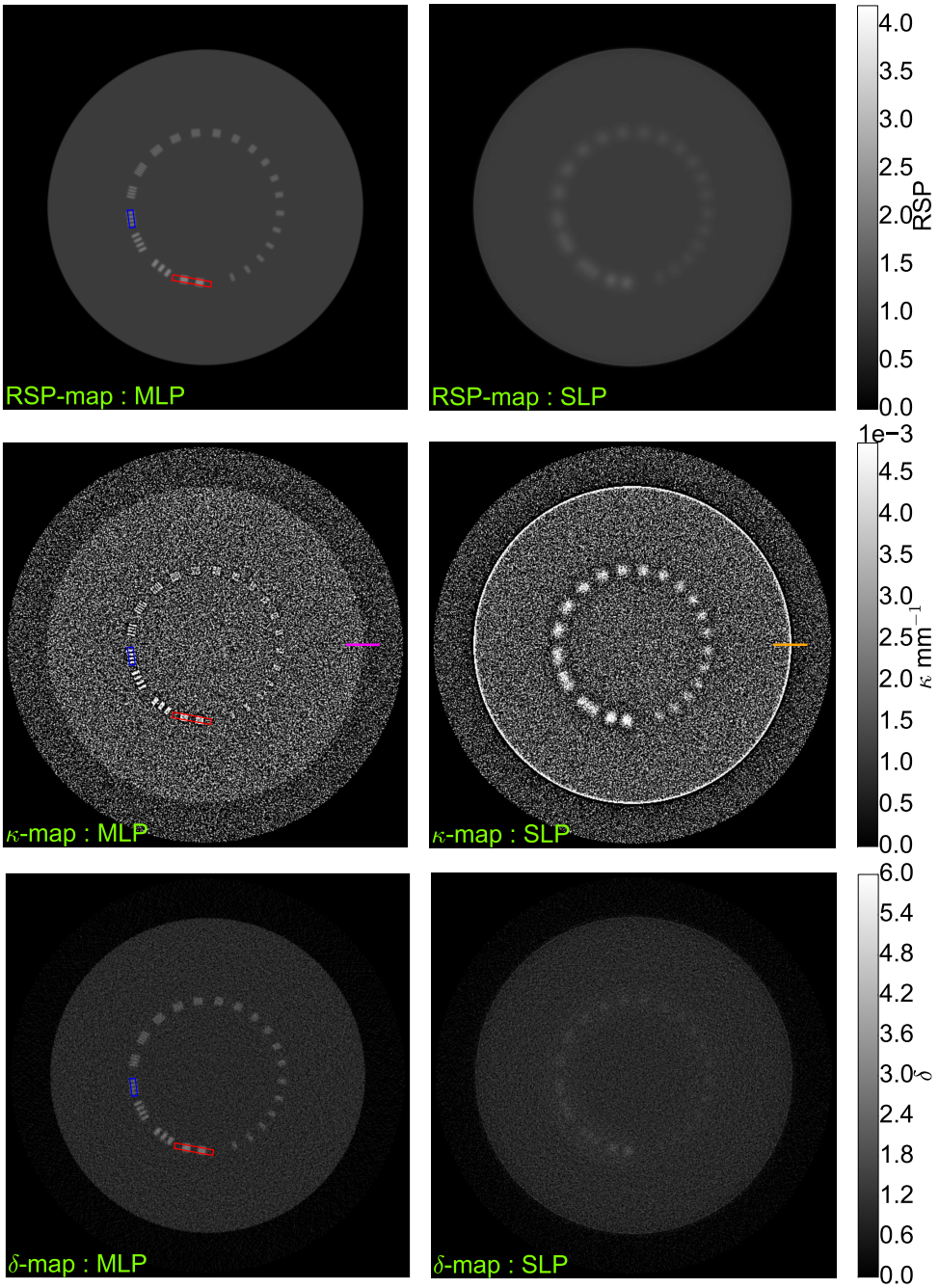

Figure 9.1: Comparison of FBP reconstruction using MLP with the distance-driven binning (left) or conventional FBP reconstructed assuming SLP (right) for energy-loss RSP (top), attenuation κ (middle) and scattering δ (bottom) proton CT. The colored segments and rectangles refer to the location of profiles in Figure 9.2. Figure adapted from [S4].

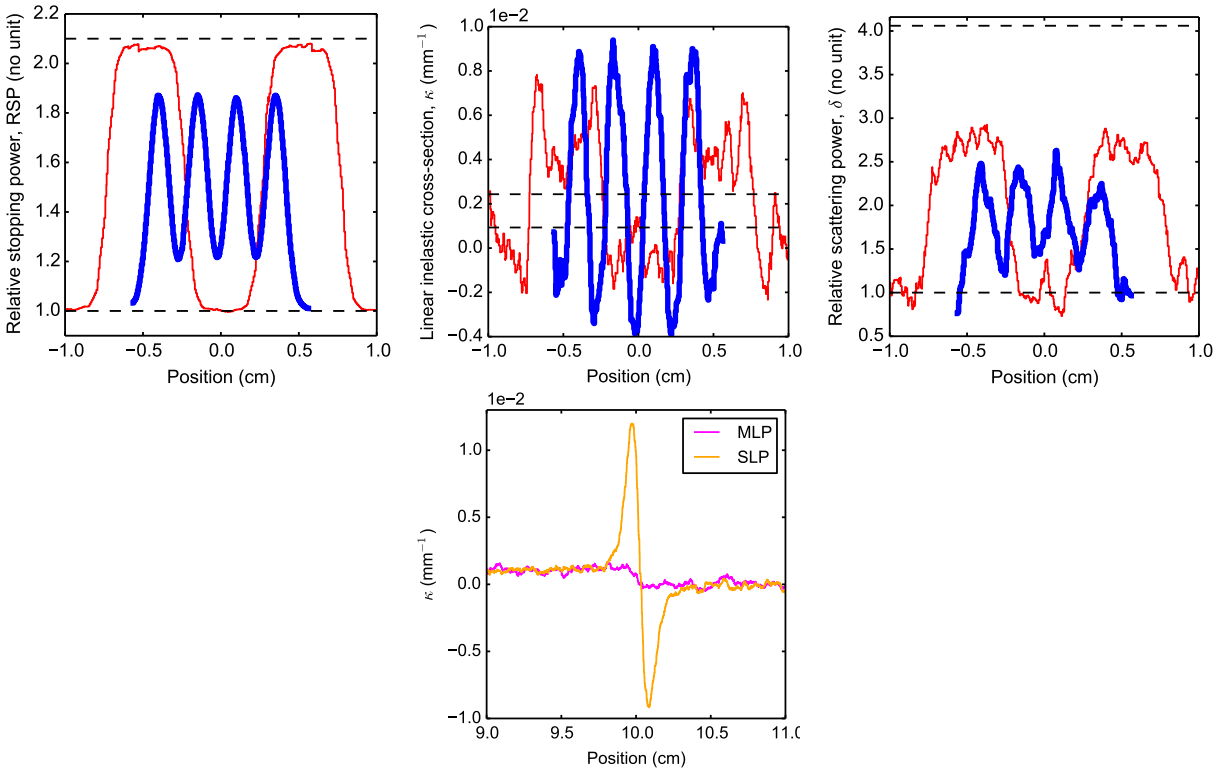

Figure 9.2: Profiles of energy-loss (left), attenuation (middle) and scattering (right) proton CT taken in resolution patterns (top) or at the edge of the cylinder (bottom) of the images in Figure 9.1. The dashed horizontal lines indicate reference values for the materials. Figure adapted from [S4].

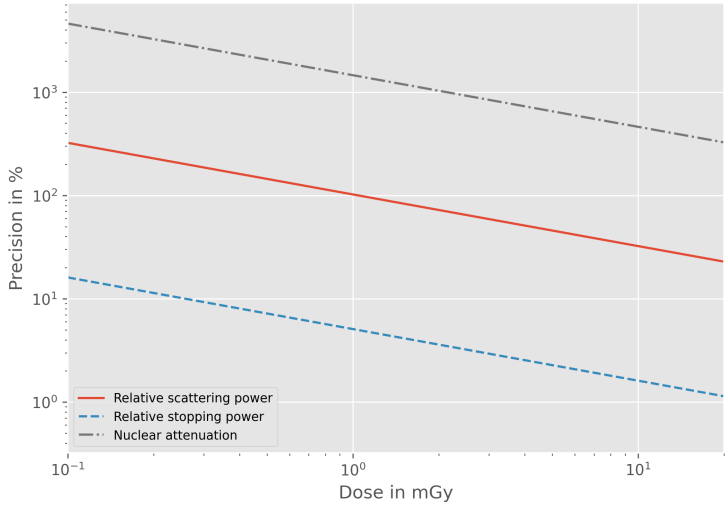

Figure 9.3: Analytically-derived precision as a function of the imaging dose for energy-loss, scattering and attenuation proton CT. Figure courtesy of Nils Krah.

(section 6.2), the inverse problem is non-linear and non-convex. Our first results [A2] indicate that this technique provides a solution for reconstructing scattering proton CT images from integrated data (i.e., not list-mode) with an improvement of the spatial resolution compared to the attenuation image without correction.

9.2 Scattering proton CT

Instead of counting protons, one can estimate how much protons scattered through the object. The amount of MCS depends on the scattering power [77] of the object, which is a function of local material properties (the density and the radiation length) and the proton energy. As for attenuation, estimating the variance of this scattering requires binning the list-mode information and Catherine Therese Quiñones applied the same reconstruction technique. A similar improvement of the spatial resolution was observed (Figure 9.1, bottom line and corresponding profiles in Figure 9.2, right). The noise was also much larger than in energy-loss proton CT, but decreased compared to attenuation proton CT (Figure 9.3). Interestingly, the contrast of scattering powers of two materials (e.g. bone and water) is generally larger than the one of their respective RSP contrast, but the constrast-to-noise ratio is lower due to the noise increase. Unlike the RSP, the scattering power relative to water δ is not energy independent and cupping artefacts were observed in objects which are not essentially made of water.

9.3 Conclusion

This chapter summarized how a single list-mode proton CT dataset can be used to reconstruct other maps than the RSP map: the map of the inelastic nuclear scattering cross section by looking at the beam attenuation and the scattering power map by looking at the spread of the beam. The sets of reconstructed CT images provide a fourth dimension which could be useful to, e.g., better characterize tissues, similarly to what is envisioned for spectral CT (Part II). However, it has been shown that these three quantities are strongly correlated [60] and the much larger noise (Figure 9.3) probably discard clinical use at this stage. There is still one modality which I have never evaluated, the use of the energy straggling as a quantity at the projection level which depends on the traversed tissues. Characterizing this modality as well as any other possibilities would be of interest.

10

Outlook for the future

The purpose of this chapter is to detail on-going activities which have been briefly sketched throughout the manuscript and to develop new projects for future investigations on the foundations of my previous works. I will mainly continue my research in thes three fields presented in the previous chapters but I will also apply my knowledge to other modalities.

10.1 Motion correction in tomography

Despite being as old as tomography, the problem of motion cannot be considered solved. Respiration-correlated CT [78] and cone-beam CT [8] are used clinically but residual artifacts limit their usability. I will therefore continue my developments to further improve image quality of dynamic CT towards the same quality as breathold CT for each time frame. Besides, respiration-correlated tomography is still not in clinical use in other modalities and I aim to apply breathing motion correction techniques to an emission modality, SPECT.

Breathing motion correction in quantitative SPECT

The CREATIS research group at the CLB has developed strong ties to its nuclear medicine department (Lumen, jointly managed by the *Hospices Civils de Lyon*) in the past few years under the leadership of David Sarrut. The motivation for this collaboration is the development of quantitative emission tomography for improving diagnosis as well as targeted radionuclide therapy, a rapidly expanding treatment modality. The collaboration was motivated by David Sarrut's expertise in Monte Carlo simulations for imaging and radiotherapy, which are crucial tools for quantitative SPECT imaging.

A major issue in SPECT of the lungs and the upper abdomen is breathing motion. For example, it "has a large effect on SPECT activity quantitation" of radioembolization according to Bastiaannet *et al* [79]. Motivated by this observation and our respective expertise in simulation of nuclear imaging and motion correction in CT, I am co-supervising Antoine Robert with David Sarrut since December 2018, a PhD student funded by a CIFRE grant of the Kitware company, on the topic of breathing motion correction in SPECT. Kitware is interested in developing its expertise in tomography reconstruction using RTK. A regional project *NucleAr meDicine ImAging with Motion* (NADIAM) is also funding a research engineer for the development of a clinical workflow.

The current investigations focus on data-driven methods which can be applied to patient data retrospectively, i.e., without modification of the clinical protocols. The breathing signal can indeed be extracted from list-mode SPECT data [80] and used to reconstruct 4D SPECT images with state-of-the-art 3D reconstruction techniques for SPECT in each time frame. Breathing motion is then corrected for, but each frame is reconstructed from a subset of the acquired data

and will have a poor signal-to-noise ratio. We will therefore investigate motion compensation strategies similar to those presented in Part I. Simple motion estimation on pairs of projections will be developed first before developing advanced techniques using 2D/3D registration, similar to those described in section 2.3 or in the next section 10.1.

Nuclear medicine has invested a lot in targeted radionuclide therapy and targeted sites moving with breathing will benefit from motion corrected SPECT images. The collaboration with the Lumen group is a promise of a rapid clinical evaluation of the benefit. The group at the CLB gathers the expertise to be a major actor of these developments, including my experience in motion correction in CT.

Estimation of non-cyclic motion from cone-beam projections

My works on motion-compensated cone-beam CT have led me to be convinced that the main bottleneck in image quality is not the reconstruction algorithm but the accuracy of its input, an estimate of the motion during the acquisition. In Part I, the motion is often assumed to be cyclic and this is known to be an approximation. If this condition could be lifted, breathing motion would be further corrected in motion-compensated cone-beam CT images. The framework of Jamie McClelland [26] is particularly attractive to address this problem. It uses one or several surrogate signals describing the irregularity of the motion which are then used to estimate the full motion during the acquisition. We have been collaborating during the master thesis of Pauline Mouchès [M2] and the PhD of Adeyemi Akintonde [C9, A7]. Several problems still need to be solved to be able to estimate the motion on real cone-beam projection images. First, the amplitude of the input breathing signal is used in the chosen model [27], unlike respiration-correlated imaging which only uses its phase. This can be done by extracting the motion of a diaphragm dome [J61], but this is difficult to automate and not robust. Second, the truncation of the cone-beam projections will impact the motion estimation and raise the questions of ROI motion estimation as well as ROI motion-compensated reconstruction. Indeed, accurate estimation of the motion seems impossible out of the field-of-view without prior information and, even in the field-of-view, accurate estimation still needs to be demonstrated. Finally, the motion estimation relies on a prior CT, as in section 2.3, but the effectiveness of alternating between motion estimation and motion-compensated reconstruction could be explored, e.g. following [81] which has only been demonstrated on simplistic simulations.

Data consistency conditions in helical 4D CT

Respiration-correlated 4D CT is clinically used, but it is far from being perfect. Acquired images often suffer from residual motion artifacts, e.g., 90% of the images in [20], and improvement of the image quality of 4D CT images is needed, e.g. for better radiotherapy planning. The cause is not unique, but the main one is also irregular breathing motion. DCC have proven efficient to estimate motion or to calibrate the geometry of a scanner (chapter 5) and Mélanie Mouchet, PhD student funded by a Siemens CIFRE grant and who is co-supervised by Jean Michel Létang and me, is investigating their use for improving the image quality of helical 4D CT. Her on-going works address several methodological challenges. First, there is no literature on DCC for helical CT. The DCC used in [J31] are applicable only for pairs of source projections which are imaging the same part of the object. After identifying pairs of source for which DCC can be computed, Mélanie Mouchet investigates the construction of a graph with source positions as vertices and DCC as edges. Preliminary results indicate that this graph can be used to detect motion between two source positions by calculating the shortest path in the graph: if only a small part of the projections is inconsistent, there should be a "consistent" path between two consistent source positions. Correcting the 4D CT image artifacts will be the purpose of her future investigations, e.g., by better sorting projections prior to the reconstruction of the 4D CT frames by accounting for the DCC discrepancy in an iterative reconstruction algorithm.

This project is a first example of artifact correction using DCC in helical CT. If we can demonstrate efficient motion correction, other artifacts could be corrected for in follow-up projects, e.g., scatter.

Spectral and dynamic five-dimensional (5D) CT

The development of spectral CT will probably trigger the clinical need to combine dynamic and spectral CT. For example, such a combination would be helpful for cardiac imaging with one or more contrast agent(s). Another clinical application is the one which motivated the PhD thesis of Cyril Mory, the segmentation of the infacted region of the myocardium using late enhancement if a C-arm scanner with dual-energy were developed for interventional imaging. Reconstructing energy-resolved and time-resolved images is more complex than treating each dimension separately due to the increase of the number of sought unknowns in the 5D CT image. Reconstructing each frame separately will require enough projection data and the x-ray dose might be detrimental for the patient. Using a motion-compensated strategy combined with a one-step spectral CT reconstruction is ambitious, but it would be a direction of investigations for which I have developed the required skills.

10.2 Region-of-interest CT

I first approached the problem of ROI CT by investigating its combination with a motion of the scanned object (chapter 4). The on-going ANR project *region-of-interest and dose reduction* (ROIdoré) aims at determining whether ROI CT can effectively reconstruct images with the same image quality in the field-of-view as a full field-of-view acquisition and, if yes, whether it leads, as expected, to a reduction of the patient dose. This project raises a variety of theoretical questions which will be first investigated by two PhD students in the coming years.

Differentiated backprojection

Aurélien Coussat, a PhD student co-supervised by Rolf Clackdoyle and me, is currently investigating a first category of ROI algorithm, DBP. The PhD investigations are currently centered on a residual artifact when approaching the border of the field-of-view, which we have also observed with iterative reconstruction [J34], and which breaks the promise of an image quality equivalent to a full field-of-view. Aurélien is more specifically trying to address the problem of the truncated Hilbert transform, which must be solved after DBP when the field-of-view partially overlaps the patient enveloppe. It is known to have a unique and stable solution [82], but an analytical inverse has not been derived yet. With singular value decomposition (SVD), these investigations have clarified the origin of this problem. Initial results [A3, C2] and future investigations aim to reduce or solve it using DBP approaches.

Virtual cone-beam reconstruction

An alternative algorithm for 2D ROI CT is the virtual fan-beam approach [83] which combines the "super short scan" algorithm [84] with a rebinning of the projection data. This algorithm has only been applied to 2D data. Mathurin Charles has obtained a ministry PhD grant to investigate its application to 3D data. The circular source trajectory will be handled first because it seems that one could follow the strategy of the FDK algorithm, i.e., to heuristically apply the 2D algorithm to the acquired cone-beam projections. Adapting the virtual fan-beam algorithm to other source trajectories, e.g., the helical trajectory is desirable, but it is a difficult problem that will be investigated in a separate project in the future.

Image quality

Evaluation of image quality is a central issue of medical imaging. In tomography, simple metrics are used first based on simulated data for which the reference is known, e.g., the root mean square error between a result and a reference. These metrics are insufficient to characterize the quality of an image and a large part of the field is devoted to better assessing image quality, e.g., by modeling observers of the images [85]. The ROIdoré project shall start with simple techniques to measure image quality, but I intend to develop this skill in the future to better demonstrate the clinical potential of my developments.

10.3 Ion CT

Ion CT is not clinically available and the investigations of this field should support the development of clinical scanners and demonstrate the clinical relevance of this technique. Reconstruction is a central component of any CT scanner and previous investigations [J39, J6] suggest that the distance-driven binning algorithm [J57] is a good candidate for a clinical scanner. I also aim at improving the precision and the resolution of reconstructed images.

Time-of-flight ion imaging

Nils Krah has demonstrated that it is mainly the list-mode approach that will reach an acceptable spatial resolution for most clinical objectives [J23]. A challenge for clinical use is the count rate at which current prototypes can operate. For example, one of the most advanced prototypes, developed by an American collaboration, would require a few minutes for acquiring a full ion CT image [86], which seems unacceptable for image-guided ion-therapy. This prototype uses a few calorimeters for measuring the residual energy after the patient [87]. One alternative possibility for designing a clinical scanner is the measure of the time-of-flight of the ions over a known distance after the patient to indirectly measure their residual energy [88]. This alternative strategy would benefit from time-of-flight developments in other modalities, e.g., positron emission tomography (PET) [89]. The current postdoctoral fellowship of Nils Krah, funded by the PhysiCancer project *Ultra-Fast Timing for Online Control of Particle* (CLaRyS-UFT), aims at evaluating time-of-flight for ion CT based on simulations. I am also part of a European collaboration with groups in Germany, Austria and Italy to build a first prototype system with this approach.

Investigation of the dose advantage of proton CT

The main two benefits of proton CT over x-ray CT according to the literature are the improvement of the RSP estimation and the dose reduction. The former has been demonstrated by the investigations of George Dedes and Nicolas Arbor [J47]. The latter has been investigated by Reinhard Schulte *et al* [75], but recent developments [J21, J16] suggest that the contribution of MCS to the image precision has not been accounted for. All studies also neglect spatial resolution in the comparison. In collaboration with LMU, I intend to evaluate the noise in proton and x-ray CT at the same dose and spatial resolution. My intuition is that the dose advantage has been over-estimated, but a careful evaluation based on realistic simulations is required to be conclusive.

Filtering of proton tracks with nuclear interactions

The forward model on which most ion CT reconstruction algorithms relies assumes that the measured ions have only encountered electromagnetic interactions. In practice, a substantial part of the measured ions also encounter nuclear interactions. The literature is very scarce on this subject, but simulations show that it significantly increases image noise and biases the

estimated RSP [69]. Simple strategies can filter out a large part of these proton tracks, but improving this filtering is desirable. Nils Krah and David Sarrut have co-supervised the master internship of Risha Upadhay on the use of machine learning strategies to improve this filtering [90]. The approach is promising, particularly for ions heavier than protons (helium or carbon ions), and should be further developed. Machine learning is a good candidate because the physics is well understood and Monte Carlo simulations can easily generate input data for training a neural network. The main challenge will be the modeling of the detectors in the simulations.

Resolution modeling in ion CT

List-mode ion CT enables the estimation of MLPs, but even perfect detectors cannot estimate the true ion paths. The uncertainty associated to the estimation is known [69], but it is generally not accounted for in the reconstruction. In her last PhD thesis chapter [S1], Feriel Khellaf has demonstrated the possibility to deblur the distance-driven projections, and obtained a significant improvement of the spatial resolution. I believe that we could go further by jointly reconstructing and deblurring the proton CT image. This is a problem similar to resolution modeling in emission tomography [91]. As spatial resolution is the main issue in ion CT, I will investigate such methods for improving it.

Cone-beam CT prior in the reconstruction

Another direction for improving the spatial resolution of ion CT is the one at the origin of the Marie Skłodowska-Curie Individual Fellowship of Nils Krah, *Proton CT reconstruction with a Cone Beam CT prior*. The project idea was to rely on the excellent spatial resolution of cone-beam CT, which can be acquired in some ion treatment room, to obtain spatially resolved and accurate RSP images. Nils Krah proposed an automatic calibration of the cone-beam CT using a proton radiography [C6], which significantly improves the estimate of the RSP map, but one proton radiography cannot resolve all ambiguities [J18]. Using the cone-beam CT in the proton CT reconstruction is a promising alternative [92] which should be further developed in a filtered-backprojection algorithm.

10.4 Spectral CT

Since the clinical introduction of dual energy CT [93], spectral CT has demonstrated its clinical relevance and motivated the investment by the x-ray CT manufacturers in photon counting CT [94]. One can expect the first commercial photon counting scanners in the coming years and CREATIS should have a central role in their developments given our experience on the first clinical Philips prototype in the context of the SPCCT project.

One-step reconstruction

One application of SPCCT is the imaging of contrast media with a K-edge in the diagnostic energy range. However, it seems that its clinical use will be difficult due to the limited sensitivity of the scanner. By jointly decomposing and reconstructing spectral CT images, one-step reconstruction should improve sensitivity and it should therefore be explored. The postdoctoral fellowships of Cyril Mory and Pierre-Antoine Rodesch have led to the comparison of several one-step algorithms on simulated data [J20]. Application to real data has required some corrections to stabilize the convergence with helical data which are incomplete at both ends of the helix [C4]. It should now be possible to validate the benefit in sensitivity on real data acquired on the Philips prototype in Lyon. If a benefit is indeed proven, there will be increased interest in one-step solutions and we will need to make it routinely applicable by improving the computer implementation and investigating better performing optimization algorithms.

Auto-calibration of spectral CT using DCC

Image quality of spectral CT images rely on an accurate description of the forward model, i.e., the effective spectra s_b in Equation 6.2. They are usually determined by prior knowledge of the system such as the source spectra measured with a spectrometer and the detector response measured with monoergetic x-ray sources. But they are not completely stable in time and they need to be adjusted regularly with measurements of the attenuation of known materials. We have even observed that they can slightly drift within one scan with some systems and this drift has a detrimental effect on the image quality of the decomposed spectral CT images. Previous works have demonstrated the ability of DCC to correct for beam-hardening [95, 96]. Motivated by these results and the work of Jérôme Lesaint on auto-calibration of the scanner geometry [43], I intend to investigate auto-calibration of the spectral model using DCC.

Spectral scatter correction without modulation mask

The work of Odran Pivot has demonstrated efficient scatter correction using spectral CT with an attenuation mask in front of the x-ray souce [J9]. Clinical applicability might be difficult because the rotation of the source and the detector around the patient will cause slight movements of the relative position of the mask and the detector. The spectral scatter model based on B-spline could still be used using other techniques, e.g., convolution kernels [97] or DCC [98].

Spectral CT for multimodal x-ray imaging

Like proton imaging, x-ray imaging can image other quantities in addition to the attenuation map: the phase and the dark field maps. They usually require coherent monochromatic sources or optical devices such as grating interferometers which do not meet clinical dose and time constraints. Several teams investigate simpler systems which could be used clinically, e.g., Emmanuel Brun in Grenoble investigates speckle tracking [99]. These efforts will eventually lead to clinical solutions and I intend to enter this field. Initial efforts include my collaboration with Max Langer for the implementation of phase contrast simulation in Gate [J4], the visit of a PhD student, Lina Felsner, from the group of Andreas Maier (Pattern Recognition Lab, Erlangen-Nuremberg, Germany) on the topic of dark field imaging and initial contacts with Emmanuel Brun. My contribution shall be the development of algorithms based on my experience with spectral CT as well as the use of spectral CT for this imaging modalities [100, 101].

10.5 International and local positioning

Different directions for my future investigations have been developed which should be positioned with respect to other groups. I have gained international recognition in the field of image-guided radiotherapy, in particular for the problem of motion in cone-beam CT, so the project on this topic seems natural and is supported by other visible collaborators such as Jamie McClelland (London). The new orientation of my research towards diagnostic CT is possible thanks to the collaboration with Siemens for accessing projection data, a rare possibility given to groups collaborating with constructors (University of Michigan, John Hopkins, etc.). It is even more true for spectral photon counting CT with only a few prototype scanners worldwide. The other new orientation towards emission tomography is the riskiest but there does not seem to be a strong international competition on the topic of motion correction of SPECT for targeted radionuclide radiotherapy. My positioning seems the strongest in proton CT reconstruction where the outcome of my investigations should be the most scrutinized, thanks to collaboration with the main groups (Reinhard Schulte's and Katia Parodi's) in this emerging field.

The project has several local assets. My integration in the group of David Sarrut at the Centre Léon Bérard puts me in an ideal position for the radiotherapy and the nuclear medicine

applications. The efforts of Philippe Douek to develop photon counting CT in Lyon is an asset for spectral CT as well as my collaborations with CEA LETI (Grenoble) who is one of the main developers of counting detectors. On the theoretical side, Rolf Clackdoyle and Laurent Desbat are internationally recognized for their contributions to the field of analytical tomography with famous collaborators, e.g., Frédéric Noo and Michel Defrise. Finally, many works on phase contrast CT originate from ESRF (Grenoble) where Emmanuel Brun (STROBE) and Françoise Peyrin (CREATIS) work.

Conclusion

This thesis has presented my main contributions to the field of CT. Each part has dealt with a fourth dimension, time and energy for x-ray CT and multimodal imaging for proton CT. These contributions have covered several fields such as applied mathematics, computer sciences, particle physics and medical physics. This spectrum of scientific fields demonstrates in my opinion my ability to successfully supervise researchers with a large variety of backgrounds, also thanks to co-supervisors of these fields. I have learned a lot from these collaborations as well as from supervising PhD students and postdoctoral fellows, each one a unique character. Being a supervisor is an art which does not only require scientific qualities but also human ones. I should undoubtedly keep on improving my human skills with new collaborators, be they under my supervision, co-supervisors or mere colleagues.

My numerous co-supervisions have taught me a part of the art of supervision, but my motivation for obtaining my HDR is not the ability to supervise PhD students alone. My co-supervisions have been happy and fruitful. It is more crucial for me to be also allowed to co-supervise PhD students with younger researchers who do not have their HDR yet. I value both the extensive knowledge of experienced researchers and the dynamism of younger ones. So far, I have always been able to chose my research topics thanks to funded projects and to habilitated colleagues interested in investigating these topics with me. I want to continue my developments in the field of CT and this HDR will strengthen my ability to be an independent actor of the field.

References

Personal references

Theses

[T1] **Rit, S.** "Prise en compte du mouvement respiratoire pour la reconstruction d'images tomodensitométriques". PhD thesis. Université Lumière Lyon 2, 2007 (cited on pages 22, 24, 25).

[T2] **Rit, S.** "Analyse d'une séquence d'images par contraste spatio-temporel". MA thesis. Institut National des Sciences Appliquées (INSA), 2004.

Co-supervised PhD theses

[S1] Khellaf, F. "List-mode proton CT reconstruction". PhD thesis. Institut National des Sciences Appliquées (INSA) de Lyon, 2020 (cited on pages 59, 60, 75).

[S2] Pivot, O. "Scatter correction for spectral tomographic imaging". PhD thesis. Institut National des Sciences Appliquées (INSA) de Lyon, 2019 (cited on pages 45, 48, 49).

[S3] Vilches-Freixas, G. "Dual-energy cone-beam CT for proton therapy". PhD thesis. Institut National des Sciences Appliquées (INSA) de Lyon, 2017 (cited on pages 22, 46, 47, 52).

[S4] Quiñones, C. "Proton computed tomography". PhD thesis. Institut National des Sciences Appliquées (INSA) de Lyon, 2016 (cited on pages 51, 60, 67–69).

[S5] Mory, C. "Tomographie cardiaque en angiographie rotationnelle". PhD thesis. Université Claude Bernard Lyon 1, 2014 (cited on pages 22, 31).

[S6] Delmon, V. "Recalage déformable de projections de scanner X à faisceau conique". PhD thesis. Institut National des Sciences Appliquées (INSA) de Lyon, 2013 (cited on pages 22, 23, 28).

Co-supervised Master theses

[M1] Mouchet, M. "Data consistency conditions for improving image quality in x-ray CT". MA thesis. Grenoble INP Phelma, 2019 (cited on page 41).

[M2] Mouches, P. "Rapport de stage ingénieur". MA thesis. INSA Rouen, 2017 (cited on pages 29, 72).

[M3] Cen, Z. "Phase Contrast Simulator on VIP". MA thesis. Institut National des Sciences Appliquées (INSA) de Lyon, 2016.

[M4] Hänsch, A. "Simulation of Misalignments in Propagation-Based X-Ray Phase Tomography". MA thesis. University of Lübeck, 2015.

[M5] Pivot, O. "Développement de la méthode de décomposition par calibration polynomiale pour l'imagerie X bi-énergie". MA thesis. INSA Lyon, 2016 (cited on pages 45, 46).

[M6] Kuijf, H. "Deformable registration of 3D cone-beam CT of lung cancer patients in the presence of anatomical changes". MA thesis. Utrecht University, 2009.

Book chapters

[B1] **Rit, S.**, Mory, C., Noël, P., "Image Formation in Spectral Computed Tomography". In: *Spectral, Photon Counting Computed Tomography*. Ed. by K. Taguchi, I. Blevis, and K. Iniewski. CRC Press, 2020, pp. 355–372 (cited on page 129).

[B2] Sarrut, D., Vandemeulebroucke, J., **Rit, S.,** "4D Modeling and Estimation of Respiratory Motion for Radiation Therapy". In: ed. by Jan Ehrhardt and Christian Lorenz. Springer, 2013. Chap. Intensity-Based Deformable Registration: Introduction and Overview, pp. 103–124 (cited on page 25).

[B3] **Rit, S.**, Sarrut, D., Sonke, J.-J., "4D Modeling and Estimation of Respiratory Motion for Radiation Therapy". In: ed. by Jan Ehrhardt and Christian Lorenz. Springer, 2013. Chap. Respiratory motion correction in cone-beam CT for image-guided radiotherapy, pp. 319–334 (cited on page 23).

Journal articles

[J1] Krah, N., Quiñones, C., Letang, J., **Rit, S.,** "Scattering proton CT". In: *Phys Med Biol* (2020).

[J2] Dedes, G., Dickmann, J., Giacometti, V., **Rit, S.**, Krah, N., Meyer, S., Bashkirov, V., Schulte, R., Johnson, R., Parodi, K., Landry, G., "The role of Monte Carlo simulation in understanding the performance of proton computed tomography". In: *Zeitschrift für Medizinische Physik* (2020).

[J3] Dickmann, J., Sarosiek, C., Rykalin, V., Pankuch, M., **Rit, S.**, Detrich, N., Coutrakon, G., Johnson, R., Schulte, R., Parodi, K., Landry, G., Dedes, G., "Experimental realization of dynamic fluence field optimization for proton computed tomography". In: *Physics in Medicine & Biology* 65.19 (2020), p. 195001 (cited on page 66).

[J4] Langer, M., Cen, Z., **Rit, S.**, Létang, J., "Towards Monte Carlo simulation of X-ray phase contrast using GATE". In: *Opt Express* 28.10 (2020), pp. 14522–14535 (cited on page 76).

[J5] Ayadi, M., Baudier, T., Bouilhol, G., Dupuis, P., Pinho, R., Krason, A., **Rit, S.**, Claude, L., Sarrut, D., "Mid-position treatment strategy for locally advanced lung cancer: a dosimetric study". In: *The British Journal of Radiology* 93.1110 (2020). PMID: 32293191, p. 20190692.

[J6] Khellaf, F., Krah, N., Letang, J.-M., Collins-Fekete, C.-A., **Rit, S.,** "A comparison of direct reconstruction algorithms in proton computed tomography". In: *Phys Med Biol* 65.10 (2020), p. 105010 (cited on pages 63, 74).

[J7] Khellaf, F., Krah, N., Létang, J., **Rit, S.,** "2D directional ramp filter". In: *Phys Med Biol* 65.8 (2020), 08NT01 (cited on page 62).

[J8] Dickmann, J., **Rit, S.**, Pankuch, M., Johnson, R., Schulte, R., Parodi, K., Dedes, G., Landry, G., "An optimization algorithm for dose reduction with fluence-modulated proton CT". In: *Med Phys* 47.4 (2020), pp. 1895–1906 (cited on page 66).

[J9] Pivot, O., Fournier, C., Tabary, J., Létang, J., **Rit, S.,** "Scatter correction for spectral CT using a primary modulator mask". In: *IEEE Trans Med Imag* 39.6 (2020), pp. 2267–2276 (cited on pages 49, 76).

[J10] Pittet, P., Esteves, J., Galvan, J.-M., Lu, G.-N., Blanc, F., Haefeli, G., Hopchev, P., **Rit, S.**, Desbat, L., Ribouton, J., Jalade, P., "SciFi detector and associated method for real-time determination of profile and output factor for small fields in stereotactic radiotherapy". In: *Med Phys* 47.4 (2020), pp. 1930–1939.

[J11] Krah, N., Létang, J.-M., **Rit, S.,** "Polynomial modelling of proton trajectories in homogeneous media for fast most likely path estimation and trajectory simulation." In: *Phys Med Biol* 64 (19 2019), p. 195014 (cited on page 60).

[J12] Niepel, K., Kamp, F., Kurz, C., Hansen, D., **Rit, S.**, Neppl, S., Hofmaier, J., Bondesson, D., Thieke, C., Dinkel, J., Belka, C., Parodi, K., Landry, G., "Feasibility of 4DCBCT-based proton dose calculation: an ex vivo porcine lung phantom study". In: *Z Med Phys* 29.3 (2019), pp. 249–261.

[J13] Dedes, G., Dickmann, J., Niepel, K., Wesp, P., Johnson, R., Pankuch, M., Bashkirov, V., **Rit, S.**, Volz, L., Schulte, R., Landry, G., Parodi, K., "Experimental comparison of proton CT and dual energy X-ray CT for relative stopping power estimation in proton therapy". In: *Phys Med Biol* 64 (16 2019), p. 165002 (cited on page 66).

[J14] Shieh, C.-C., Gonzalez, Y., Li, B., Jia, X., **Rit, S.**, Mory, C., Riblett, M., Hugo, G., Zhang, Y., Jiang, Z., Liu, X., Ren, L., Keall, P., "SPARE: Sparse-view reconstruction challenge for 4D cone-beam CT from a 1-min scan". In: *Med Phys* 46.9 (2019), pp. 3799–3811 (cited on page 34).

[J15] Kochebina, O., Halty, A., Taleb, J., Kryza, D., Janier, M., Sadr, A., Baudier, T., **Rit, S.**, Sarrut, D., "In vivo gadolinium nanoparticle quantification with SPECT/CT". In: *EJNMMI Physics* 6.1 (2019), p. 1 (cited on page 49).

[J16] Dickmann, J., Wesp, P., Rädler, M., **Rit, S.**, Pankuch, M., Johnson, R., Bashkirov, V., Schulte, R., Parodi, K., Landry, G., Dedes, G., "Prediction of image noise contributions in proton computed tomography and comparison to measurements". In: *Phys Med Biol* 64.14 (2019), p. 145016 (cited on pages 66, 74).

[J17] Khellaf, F., Krah, N., Rinaldi, I., Létang, J., **Rit, S.,** "Effects of transverse heterogeneities on the most likely path of protons". In: *Phys Med Biol* 64 (6 2019), p. 065003 (cited on pages 60, 61).

[J18] Krah, N., Patera, V., **Rit, S.**, Schiavi, A., Rinaldi, I., "Regularised patient-specific stopping power calibration for proton therapy planning based on proton radiographic images". In: *Phys Med Biol* 64 (6 2019), p. 065008 (cited on pages 63, 64, 75).

[J19] Landry, G., Dörringer, F., Si-Mohamed, S., Douek, P., Abascal, J., Peyrin, F., Almeida, I., Verhaegen, F., Rinaldi, I., Parodi, K., **Rit, S.,** "Technical Note: Relative proton stopping power estimation from virtual mono-energetic images reconstructed from dual-layer computed tomography". In: *Med Phys* 46.4 (2019), pp. 1821–1828 (cited on pages 53, 55).

[J20] Mory, C., Sixou, B., Si-Mohamed, S., Boussel, L., **Rit, S.,** "Comparison of five one-step reconstruction algorithms for spectral CT". In: *Phys Med Biol* 63 (23 2018), p. 235001 (cited on pages 48, 75).

[J21] Rädler, M., Landry, G., **Rit, S.**, Schulte, R., Parodi, K., Dedes, G., "Two-dimensional noise reconstruction in proton computed tomography using distance-driven filtered back-projection of simulated projections." In: *Phys Med Biol* 63 (21 2018), p. 215009 (cited on pages 66, 74).

[J22] Dedes, G., Johnson, R., Pankuch, M., Detrich, N., Pols, W., **Rit, S.**, Schulte, R., Parodi, K., Landry, G., "Experimental fluence-modulated proton computed tomography by pencil beam scanning". In: *Med Phys* 45 (7 2018), pp. 3287–3296 (cited on page 66).

[J23] Krah, N., Khellaf, F., Letang, J., **Rit, S.**, Rinaldi, I., "A comprehensive theoretical comparison of proton imaging set-ups in terms of spatial resolution." In: *Phys Med Biol* 63 (13 2018), p. 135013 (cited on pages 59, 74).

[J24] Vilches-Freixas, G., Quiñones, C., Létang, J., **Rit, S.,** "Deriving the mean excitation energy map from dual-energy and proton computed tomography". In: *Phys Imag Radiat Oncol* 6 (2018), pp. 20–24 (cited on pages 54, 64, 65).

[J25] Cajgfinger, T., **Rit, S.**, Létang, J., Halty, A., Sarrut, D., "Fixed forced detection for fast SPECT Monte-Carlo simulation". In: *Phys Med Biol* 63 (5 2018), p. 055011.

[J26] Weber, L., Hänsch, A., Wolfram, U., Pacureanu, A., Cloetens, P., Peyrin, F., **Rit, S.**, Langer, M., "Registration of phase-contrast images in propagation-based X-ray phase tomography". In: *J Microsc* 269 (1 2018), pp. 36–47.

[J27] Sarrut, D., Baudier, T., Ayadi, M., Tanguy, R., **Rit, S.,** "Deformable image registration applied to lung SBRT: Usefulness and limitations". In: *Phys Medica* 44 (2017), pp. 108–112 (cited on page 25).

[J28] Zöllner, C., **Rit, S.**, Kurz, C., Vilches-Freixas, G., Kamp, F., Dedes, G., Belka, C., Parodi, K., Landry, G., "Decomposing a prior-CT-based cone-beam CT projection correction algorithm into scatter and beam hardening components". In: *Phys Imag Radiat Oncol* 3 (2017), pp. 49–52 (cited on page 48).

[J29] Ducros, N., Abascal, J.-J., Sixou, B., **Rit, S.**, Peyrin, F., "Regularization of nonlinear decomposition of spectral x-ray projection images". In: *Med Phys* 44 (9 2017), e174–e187 (cited on pages 46, 47).

[J30] Vilches-Freixas, G., Taasti, V., Muren, L., Petersen, J., Létang, J., Hansen, D., **Rit, S.,** "Comparison of projection- and image-based methods for proton stopping power estimation using dual energy CT". In: *Phys Imag Radiat Oncol* 3 (2017), pp. 28–36 (cited on pages 53, 54).

[J31] Lesaint, J., **Rit, S.**, Clackdoyle, R., Desbat, L., "Calibration for Circular Cone-Beam CT Based on Consistency Conditions". In: *IEEE Trans Radiat Plasma Med Sci* 1.6 (2017), pp. 517–526 (cited on pages 22, 40, 72).

[J32] Vilches-Freixas, G., Létang, J., Ducros, N., **Rit, S.,** "Optimization of dual-energy CT acquisitions for proton therapy using projection-based decomposition." In: *Med Phys* 44 (9 2017), pp. 4548–4558 (cited on pages 46, 52, 53).

[J33] Dedes, G., De Angelis, L., **Rit, S.**, Hansen, D., Belka, C., Bashkirov, V., Johnson, R., Coutrakon, G., Schubert, K., Landry, G., Schulte, R., Parodi, K., "Application of fluence field modulation to proton computed tomography for proton therapy imaging". In: *Phys Med Biol* 62 (15 2017), pp. 6026–6043 (cited on page 66).

[J34] Clackdoyle, R., Noo, F., Momey, F., Desbat, L., **Rit, S.,** "Accurate Transaxial Region-of-Interest Reconstruction in Helical CT?" In: *IEEE Trans Radiat Plasma Med Sci* 1.4 (2017), pp. 334–345 (cited on pages 37, 73).

[J35] Clackdoyle, R., Desbat, L., Lesaint, J., **Rit, S.,** "Data Consistency Conditions for Cone-Beam Projections on a Circular Trajectory". In: *IEEE Signal Process Lett* 23.12 (2016), pp. 1746–1750 (cited on page 39).

[J36] Kurz, C., Kamp, F., Park, Y.-K., Zöllner, C., **Rit, S.**, Hansen, D., Podesta, M., Sharp, G., Li, M., Reiner, M., Hofmaier, J., Neppl, S., Thieke, C., Nijhuis, R., Ganswindt, U., Belka, C., Winey, B., Parodi, K., Landry, G., "Investigating deformable image registration and scatter correction for CBCT-based dose calculation in adaptive IMPT". In: *Med Phys* 43.10 (2016), pp. 5635–5646 (cited on page 48).

[J37] Mory, C., Janssens, G., **Rit, S.,** "Motion-aware temporal regularization for improved 4D cone-beam computed tomography". In: *Phys Med Biol* 61.18 (2016), pp. 6856–6877 (cited on pages 32, 33, 105).

[J38] Vilches-Freixas, G., Létang, J., Brousmiche, S., Romero, E., Vila Oliva, M., Kellner, D., Deutschmann, H., Keuschnigg, P., Steininger, P., **Rit, S.,** "Technical Note: Procedure for the calibration and validation of kilo-voltage cone-beam CT models". In: *Med Phys* 43.9 (2016), pp. 5199–5204 (cited on page 52).

[J39] Hansen, D., Sangild Sorensen, T., **Rit, S.,** "Fast reconstruction of low dose proton CT by sinogram interpolation". In: *Phys Med Biol* 61.15 (2016), pp. 5868–5882 (cited on pages 63, 74).

[J40] Hoskovec, J., Clackdoyle, R., Desbat, L., **Rit, S.,** "Exact Fan-Beam Reconstruction With Arbitrary Object Translations and Truncated Projections". In: *IEEE Trans Nucl Sci* 63.3 (2016), pp. 1408–1418 (cited on pages 36, 37).

[J41] **Rit, S.**, Clackdoyle, R., Keuschnigg, P., Steininger, P., "Filtered-backprojection reconstruction for a cone-beam computed tomography scanner with independent source and detector rotations". In: *Med Phys* 43.5 (2016), pp. 2344–2352 (cited on page 24).

[J42] Quiñones, C., Létang, J., **Rit, S.,** "Filtered back-projection reconstruction for attenuation proton CT along most likely paths". In: *Phys Med Biol* 61.9 (2016), pp. 3258–3278 (cited on page 67).

[J43] Wang, L., Sixou, B., **Rit, S.**, Peyrin, F., "Binary tomography reconstruction from few projections with Total Variation regularization for bone microstructure studies". In: *J Xray Sci Technol* 24.2 (2016), pp. 177–189.

[J44] Wang, L., Sixou, B., **Rit, S.**, Peyrin, F., "Binary Tomography Reconstruction From Few Projections With Level-set Regularization Methods For Bone Microstructure Study". In: *International Journal of Tomography and Simulation* 29.1 (2016), pp. 1–17.

[J45] Sixou, B., Wang, L., **Rit, S.**, Peyrin, F., "Binary Tomography Reconstruction with Stochastic Diffusion Based on Level-set and Total Variation Regularization". In: *International Journal of Tomography and Simulation* 29.2 (2016), pp. 1–26.

[J46] Fargier-Voiron, M., Presles, B., Pommier, P., Munoz, A., **Rit, S.**, Sarrut, D., Biston, M.-C., "Evaluation of a new transperineal ultrasound probe for inter-fraction image-guidance for definitive and post-operative prostate cancer radiotherapy". In: *Phys Med* 32 (3 2016), pp. 499–505.

[J47] Arbor, N., Dauvergne, D., Dedes, G., Létang, J., Parodi, K., Quiñones, C., Testa, E., **Rit, S.,** "Monte Carlo comparison of x-ray and proton CT for range calculations of proton therapy beams". eng. In: *Phys Med Biol* 60.19 (2015), pp. 7585–7599 (cited on pages 51, 64, 65, 74).

[J48] Fargier-Voiron, M., Presles, B., Pommier, P., Munoz, A., **Rit, S.**, Sarrut, D., Biston, M.-C., "Ultrasound versus Cone-beam CT image-guided radiotherapy for prostate and post-prostatectomy pretreatment localization". eng. In: *Phys Med* 31.8 (2015), pp. 997–1004.

[J49] Frachon, T., Weber, L., Hesse, B., **Rit, S.**, Dong, P., Olivier, C., Peyrin, F., Langer, M., "Dose fractionation in synchrotron radiation x-ray phase micro-tomography". eng. In: *Phys Med Biol* 60.19 (2015), pp. 7543–7566.

[J50] Wang, M., Sharp, G., **Rit, S.**, Delmon, V., Wang, G., "2D/4D marker-free tumor tracking using 4D CBCT as the reference image". eng. In: *Phys Med Biol* 59.9 (2014), pp. 2219–2233.

[J51] Mory, C., Auvray, V., Zhang, B., Grass, M., Schäfer, D., Chen, S., Carroll, J., **Rit, S.**, Peyrin, F., Douek, P., Boussel, L., "Cardiac C-arm computed tomography using a 3D + time ROI reconstruction method with spatial and temporal regularization". eng. In: *Med Phys* 41.2 (2014), p. 021903 (cited on page 32).

[J52] Fargier-Voiron, M., Presles, B., Pommier, P., **Rit, S.**, Munoz, A., Liebgott, H., Sarrut, D., Biston, M.-C., "Impact of probe pressure variability on prostate localization for ultrasound-based image-guided radiotherapy". In: *Radiother Oncol* 111 (1 2014), pp. 132–137.

[J53] Sarrut, D., **Rit, S.**, Claude, L., Pinho, R., Pitson, G., Bouilhol, G., Lynch, R., "Learning directional relative positions between mediastinal lymph node stations and organs". eng. In: *Med Phys* 41.6 (2014), p. 061905.

[J54] Mory, C., Auvray, V., Zhang, B., Grass, M., Schäfer, D., **Rit, S.**, Peyrin, F., Douek, P., Boussel, L., "Removing streak artifacts from ECG-gated reconstructions using deconvolution". eng. In: *J Xray Sci Technol* 22.2 (2014), pp. 253–270.

[J55] Presles, B., Fargier-Voiron, M., Biston, M.-C., Lynch, R., Munoz, A., Liebgott, H., Pommier, P., **Rit, S.**, Sarrut, D., "Semiautomatic registration of 3D transabdominal ultrasound images for patient repositioning during postprostatectomy radiotherapy". In: *Med Phys* 41.12 (2014), p. 122903.

[J56] Smekens, F., Létang, J., Noblet, C., Chiavassa, S., Delpon, G., Freud, N., **Rit, S.**, Sarrut, D., "Split exponential track length estimator for Monte-Carlo simulations of small-animal radiation therapy". eng. In: *Phys Med Biol* 59.24 (2014), pp. 7703–7715.

[J57] **Rit, S.**, Dedes, G., Freud, N., Sarrut, D., Létang, J., "Filtered backprojection proton CT reconstruction along most likely paths". In: *Med Phys* 40.3, 031103 (2013), p. 031103 (cited on pages 60, 62, 66, 74, 147).

[J58] Delmon, V., **Rit, S.**, Pinho, R., Sarrut, D., "Registration of sliding objects using direction dependent B-splines decomposition". eng. In: *Phys Med Biol* 58.5 (2013), pp. 1303–1314 (cited on pages 25, 27, 28).

[J59] Vandemeulebroucke, J., Bernard, O., **Rit, S.**, Kybic, J., Clarysse, P., Sarrut, D., "Automated segmentation of a motion mask to preserve sliding motion in deformable registration of thoracic CT". eng. In: *Med Phys* 39.2 (2012), p. 1006 (cited on pages 25, 27).

[J60] Bouilhol, G., Ayadi, M., **Rit, S.**, Thengumpallil, S., Schaerer, J., Vandemeulebroucke, J., Claude, L., Sarrut, D., "Is abdominal compression useful in lung stereotactic body radiation therapy? A 4DCT and dosimetric lobe-dependent study". eng. In: *Phys Med* 29.4 (2013), pp. 333–340.

[J61] **Rit, S.**, van Herk, M., Zijp, L., Sonke, J.-J., "Quantification of the variability of diaphragm motion and implications for treatment margin construction". eng. In: *Int J Radiat Oncol Biol Phys* 82.3 (2012), e399–e407 (cited on pages 25, 72).

[J62] **Rit, S.**, Nijkamp, J., van Herk, M., Sonke, J.-J., "Comparative study of respiratory motion correction techniques in cone-beam computed tomography". eng. In: *Radiother Oncol* 100.3 (2011), pp. 356–359.

[J63] Murphy, K. "Evaluation of Registration Methods on Thoracic CT: The EMPIRE10 Challenge". eng. In: *IEEE Trans Med Imaging* 30.11 (2011), pp. 1901–1920.

[J64] Vandemeulebroucke, J., **Rit, S.**, Kybic, J., Clarysse, P., Sarrut, D., "Spatiotemporal motion estimation for respiratory-correlated imaging of the lungs". eng. In: *Med Phys* 38.1 (2011), pp. 166–178 (cited on pages 25–27).

[J65] **Rit, S.**, Sarrut, D., Desbat, L., "Comparison of analytic and algebraic methods for motion-compensated cone-beam CT reconstruction of the thorax". In: *IEEE Trans Med Imaging* 28.10 (2009), pp. 1513–1525 (cited on pages 24, 25, 35).

[J66] **Rit, S.**, Wolthaus, J., van Herk, M., Sonke, J.-J., "On-the-fly motion-compensated cone-beam CT using an a priori model of the respiratory motion". eng. In: *Med Phys* 36.6 (2009), pp. 2283–2296 (cited on page 25).

[J67] **Rit, S.**, Sarrut, D., Boldea, V., Ginestet, C., "Extraction du signal respiratoire à partir de projections cone-beam". In: *Traitement du signal* 23.3–4 (2006), pp. 307–319.

Patents

[PA1] Pivot, O., Fournier, C., Tabary, J., Létang, J., **Rit, S.,** "Procédé de correction d'une image spectrale". 1859368. 2019 (cited on page 49).

Invited conferences

[I1] **Rit, S.** "SP-0240 Breathing motion in cone-beam CT". In: *ESTRO 38 (European SocieTy for Radiotherapy & Oncology)*. Vol. 133. Milan, Italy: Elsevier, 2019, S119–S120.

[I2] **Rit, S.** "4D and motion-compensated cone-beam CT". In: *4D Treatment Planning Workshop*. Groningen, The Netherlands, 2016.

[I3] **Rit, S.** "Motion-compensated Cone-Beam CT for Image-Guided Radiotherapy". In: *SIAM Conference on Imaging Science*. Hong Kong, China, 2014.

[I4] Sarrut, D., Vandemeulebroucke, J., Bouilhol, G., Pinho, R., Delmon, V., **Rit, S.,** "Open source tools for validation of deformable registration". In: *ESTRO 33 (European SocieTy for Radiotherapy & Oncology)*. Vienna, Austria, 2014.

[I5] Sarrut, D., Vandemeulebroucke, J., **Rit, S.,** "Advances in deformable image registration of thoracic 4D CT". In: *ESTRO 29 (European SocieTy for Radiotherapy & Oncology)*. Barcelona, Spain, 2010.

Conference proceeding articles

[C1] Dickmann, J., Sarosiek, C., Coutrakon, G., **Rit, S.**, Detrich, N., Rykalin, V., Pankuch, M., Johnson, R., Schulte, R., Parodi, K., Landry, G., Dedes, G., "Dynamic fluence modulation using proton CT for low–dose imaging in particle therapy". In: *Sixth international conference on image formation in X-ray computed tomography*. Regensburg, Germany, 2020, pp. 642–645.

[C2] Coussat, A., **Rit, S.**, Clackdoyle, R., Defrise, M., Desbat, L., Létang, J., "ROI CT reconstruction combining analytic inversionof the finite Hilbert transform and SVD". In: *Sixth international conference on image formation in X-ray computed tomography*. Bamberg, Germany, 2020, pp. 526–529 (cited on page 73).

[C3] Gindrier, N., Clackdoyle, R., **Rit, S.**, Desbat, L., "Cone-beam reconstruction from n-sin trajectories with transversely-truncated projections". In: *Sixth international conference on image formation in X-ray computed tomography*. Bamberg, Germany, 2020, pp. 46–49.

[C4] Rodesch, P., Si-Mohamed, S., **Rit, S.,** "Spatially varying regularization weights for one-step spectral CT with SQS". In: *Sixth international conference on image formation in X-ray computed tomography*. Bamberg, Germany, 2020, pp. 58–61 (cited on page 75).

[C5] Desbat, L., **Rit, S.**, Clackdoyle, R., Jalade, P., Ribouton, J., Pittet, P., "Geometric tomography for measuring rectangular radiotherapy fields from six projections". In: *2019 IEEE Nuclear Science Symposium and Medical Imaging Conference (NSS/MIC)*. 2019, pp. 1–4.

[C6] Krah, N., **Rit, S.,** "Optimized conversion from CT numbers to proton relative stopping power based on proton radiography and scatter corrected cone-beam CT images". In: *Fully 3D Image Reconstruction in Radiology and Nuclear Medicine*. Vol. 11072. Philadelphia, USA, 2019 (cited on pages 64, 75).

[C7] Mory, C., Brendel, B., Erhard, K., **Rit, S.,** "Generalized least squares for spectral and dual energy CT: a simulation study". In: *Fifth international conference on image formation in X-ray computed tomography*. Salt Lake City, USA, 2018, pp. 98–101.

[C8] Lesaint, J., **Rit, S.**, Clackdoyle, R., Desbat, L., "GCC and FBCC for linear tomosynthesis". In: *Sixth international conference on image formation in X-ray computed tomography*. Salt Lake City, USA, 2018, pp. 114–118.

[C9] Akintonde, A., McClelland, J., Grimes, H., Moinuddin, S., Sharma, R., **Rit, S.**, Thielemans, K., "Data driven cone beam CT motion management for radiotherapy application". In: *Proc. IEEE Nuclear Science Symp. and Medical Imaging Conf. (NSS/MIC)*. 2017, pp. 1–4 (cited on page 72).

[C10] Abascal, J., Ducros, N., **Rit, S.**, Sixou, B., Peyrin, F., "Nonlinear material decomposition for x-ray spectral imaging using a bregman iterative approach". In: *Recherche en Imagerie et Technologies pour la Santé (RITS) 2017*. 2017.

[C11] Ducros, N., Pivot, O., **Rit, S.**, Létang, J., Abascal, J., Boursier, Y., Dupont, M., Morel, C., Peyrin, F., "Imagerie X spectrale: décomposition en base de matériaux par calibration polynomiale". In: *Recherche en Imagerie et Technologies pour la Santé (RITS) 2017*. 2017.

[C12] Ducros, N., Pivot, O., Dupont, M., Kochebina, O., Létang, J., **Rit, S.**, Abascal, J., Peyrin, F., Morel, C., Boursier, Y., "Material decomposition using the PIXSCAN-FLI spectral micro-CT". In: *IEEE Nuclear Science Symposium and Medical Imaging Conference (NSS/MIC)*. Atlanta, USA, 2017, p. 2987.

[C13] Ducros, N., **Rit, S.**, Sixou, B., Peyrin, F., "Non-linear regularized decomposition of spectral x-ray projection images". In: *Fourth international conference on image formation in X-ray computed tomography*. Bamberg, Germany, 2016, 49–52.

[C14] Hoskovec, J., Momey, F., Clackdoyle, R., Desbat, L., **Rit, S.,** "Fan-beam reconstruction under motion and data truncation: mapping analytic and iterative approaches". In: *Fourth international conference on image formation in X-ray computed tomography*. Bamberg, Germany, 2016, pp. 589–592.

[C15] Vilches-Freixas, G., Létang, J., Ducros, N., **Rit, S.,** "Dual-energy CT spectra optimization for proton treatment planning". In: *Fourth international conference on image formation in X-ray computed tomography*. Bamberg, Germany, 2016, pp. 585–588 (cited on page 52).

[C16] Lesaint, J., Clackdoyle, R., **Rit, S.**, Desbat, L., "Two cone-beam consistency conditions for a circular trajectory". In: *Fourth international conference on image formation in X-ray computed tomography*. Bamberg, Germany, 2016, pp. 431–434 (cited on page 39).

[C17] Mory, C., Sixou, B., **Rit, S.,** "4D tomography: an application of incremental constraint projection methods for variational inequalities". In: *GRETSI*. Lyon, France, 2016.

[C18] Mory, C., **Rit, S.,** "Iterative cone beam computed tomography in RTK, the Reconstruction ToolKit". In: *International Conference on the Use of Computers in Radiation Therapy (ICCR)*. 2016.

[C19] **Rit, S.**, Clackdoyle, R., Hoskovec, J., Létang, J., "List-mode proton CT reconstruction using their most likely paths via the finite Hilbert transform of the derivative of the backprojection". In: *Fully 3D Image Reconstruction in Radiology and Nuclear Medicine*. Newport, USA, 2015, pp. 324–327 (cited on page 62).

[C20] Mory, C., **Rit, S.,** "Improving iterative 4D CBCT through the use of motion information". In: *Fully 3D Image Reconstruction in Radiology and Nuclear Medicine*. Newport, USA, 2015, pp. 170–173.

[C21] Mory, C., **Rit, S.,** "4D cone-beam computed tomography using motion-aware regularization". In: *Journées RITS 2015*. 2015, pp. 118–119.

[C22] Presles, B., Fargier-Voiron, M., Alessandrini, M., Biston, M., Pommier, P., **Rit, S.**, Sarrut, D., Liebgott, H., "Realistic Simulations for the Evaluation of Monomodal Registration Algorithms of 3D Pelvic Ultrasound Images". In: *Proc. of International Congress on Ultrasonics (ICU)*. 2015.

[C23] Hoskovec, J., Clackdoyle, R., Desbat, L., **Rit, S.,** "Analytic motion-compensated region-of-interest reconstruction from truncated projections". In: *Proc. IEEE Nuclear Science Symp. and Medical Imaging Conf. (NSS/MIC)*. Seattle, USA, 2014, pp. 1–6 (cited on page 36).

[C24] Langer, M., Frachon, T., Weber, L., Hesse, B., Dong, P., **Rit, S.**, Peyrin, F., "Dose fractionation in X-ray In-line Phase Tomography". In: *IEEE International Symposium on Biomedical Imaging (ISBI'14)*. Vol. In press. 2014.

[C25] **Rit, S.**, Clackdoyle, R., "2D filtered backprojection for fan-beam CT with independent rotations of the source and the detector". In: *Third international conference on image formation in X-ray computed tomography*. 2014, pp. 249–252.

[C26] Clackdoyle, R., **Rit, S.**, Hoskovec, J., Desbat, L., "Fanbeam data consistency conditions for applications to motion detection". In: *Third international conference on image formation in X-ray computed tomography*. 2014, pp. 324–328 (cited on page 39).

[C27] Delmon, V., Vandemeulebroucke, J., Pinho, R., Vila Oliva, M., Sarrut, D., **Rit, S.,** "In-room breathing motion estimation from limited projection views using a sliding deformation model". In: *International Conference on the Use of Computers in Radiation Therapy (ICCR)*. Vol. 489. 1. 2014, p. 012026 (cited on pages 28, 29).

[C28] Bouilhol, G., Ayadi, M., Pinho, R., **Rit, S.**, Sarrut, D., "Motion artifact detection in four-dimensional computed tomography images". In: *Journal of Physics: Conference Series*. Vol. 489. 1. IOP Publishing. 2014, p. 012024 (cited on page 25).

[C29] **Rit, S.**, Vila Oliva, M., Brousmiche, S., Labarbe, R., Sarrut, D., Sharp, G., "The Reconstruction Toolkit (RTK), an open-source cone-beam CT reconstruction toolkit based on the Insight Toolkit (ITK)". In: *J. Phys.: Conf. Ser.* 489 (2014), p. 012079 (cited on pages 21, 33).

[C30] Mory, C., Zhang, B., Auvray, V., Grass, M., Schäfer, D., Peyrin, F., **Rit, S.**, Douek, P., Boussel, L., "Deconvolution for limited-view streak artifacts removal: improvements upon an existing approach". In: *Nuclear Science Symposium and Medical Imaging Conference (NSS/MIC), 2012 IEEE*. 2012, pp. 2370–2373.

[C31] Spinczyk, D., Blanc, R., **Rit, S.**, Sarrut, D., Melodelima, D., "Estimation of respiratory breathing signal from 2D US sequences and 4DCT of the liver". In: *Ultrasonics Symposium (IUS), 2014 IEEE International*. 2014, pp. 2339–2342.

[C32] Blanc, R., Melodelima, D., **Rit, S.**, Rivoire, M., Sarrut, D., "Towards 4DCT-US image fusion for liver motion monitoring". In: *Ultrasonics Symposium (IUS), 2013 IEEE International*. 2013, pp. 817–820.

[C33] **Rit, S.**, Freud, N., Sarrut, D., Létang, J.-M., "Distance-driven binning for proton CT filtered backprojection along most likely paths". In: *Second International Conference on Image Formation in X-Ray Computed Tomography*. Salt Lake City, USA, 2012, pp. 382–385.

[C34] Mory, C., Zhang, B., Auvray, V., Grass, M., Schäfer, D., Peyrin, F., **Rit, S.**, Douek, P., Boussel, L., "ECG-gated C-arm computed tomography using L1 regularization". In: *Signal Processing Conference (EUSIPCO), 2012 Proceedings of the 20th European*. IEEE. 2012, pp. 2728–2732.

[C35] Sarrut, D., Claude, L., **Rit, S.**, Pinho, R., Pitson, G., Lynch, R., "Investigating mediastinal lymph node stations segmentation on thoracic CT following experts guidelines". In: *MICCAI, Proceedings of the First International Workshop on Image-Guidance and Multimodal Dose Planning in Radiation Therapy*. Nice, France, 2012.

[C36] Dedes, G., **Rit, S.**, Dauvergne, D., De Rydt, M., Freud, N., Krimmer, J., Letang, J.-M., Ray, C., Testa, E., "Electron density resolution determination and systematic uncertainties in proton computed tomography (pCT)". In: *Nuclear Science Symposium and Medical Imaging Conference (NSS/MIC), 2012 IEEE*. 2012, pp. 3600–3601.

[C37] Delmon, V., **Rit, S.**, Pinho, R., Sarrut, D., "Direction dependent B-splines decomposition for the registration of sliding objects". In: *Proceedings of the Fourth International Workshop on Pulmonary Image Analysis*. Toronto, Canada, 2011, pp. 45–55.

[C38] Pinho, R., Delmon, V., Vandemeulebroucke, J., **Rit, S.**, Sarrut, D., "Keuhkot: a method for lung segmentation". In: *Proceedings of the Fourth International Workshop on Pulmonary Image Analysis*. Toronto, Canada, 2011, pp. 225–232.

[C39] **Rit, S.**, Pinho, R., Delmon, V., Pech, M., Bouilhol, G., Schaerer, J., Navalpakkam, B., Vandemeulebroucke, J., Seroul, P., Sarrut, D., "VV, a 4D slicer". In: *Proceedings of the Fourth International Workshop on Pulmonary Image Analysis*. Toronto, Canada, 2011, pp. 171–175.

[C40] **Rit, S.**, Kuijf, H., van Kranen, S., van Herk, M., Sonke, J.-J., "Computer assisted analysis of lung tumor regression during radiotherapy". In: *International Conference on the Use of Computers in Radiation Therapy (ICCR)*. Amsterdam, Netherlands, 2010.

[C41] Nijkamp, J., **Rit, S.**, van Herk, M., Sonke, J.-J., "Utilization of 4D-CT and contrast enhanced expiration breath-hold CT for 3D treatment planning of lung tumors". In: *International Conference on the Use of Computers in Radiation Therapy (ICCR)*. 2010.

[C42] **Rit, S.**, van Herk, M., Sonke, J.-J., "Fast distance-driven projection and truncation management for iterative cone-beam CT reconstruction". In: *Fully 3D Image Reconstruction in Radiology and Nuclear Medicine*. Beijing, China, 2009, pp. 49–52.

[C43] **Rit, S.**, Wolthaus, J., van Herk, M., Sonke, J.-J., "On-the-fly motion-compensated cone-beam CT using an a priori motion model". In: *Medical Image Computing and Computer-Assisted Intervention (MICCAI)*. Vol. 5241. New York, USA, 2008, pp. 729–736 (cited on page 25).

[C44] Desbat, L., **Rit, S.**, Clackdoyle, R., Mennessier, C., Promayon, E., Ntalampeki, S., "Algebraic and analytic reconstruction methods for dynamic tomography". In: *Conf Proc IEEE Eng Med Biol Soc*. Lyon, France, 2007, pp. 726–730.

[C45] **Rit, S.**, Sarrut, D., "Cone-beam projection of a deformable volume for motion compensated algebraic reconstruction". In: *Conf Proc IEEE Eng Med Biol Soc*. Lyon, France, 2007, pp. 6544–6547.

[C46] **Rit, S.**, Sarrut, D., Miguet, S., "Gated cone-beam CT imaging of the thorax: a reconstruction study". In: *SPIE Medical Imaging*. Vol. 6510. San Diego, California, USA, 2007, p. 651022.

[C47] **Rit, S.**, Sarrut, D., Ginestet, C., "Comparison of gated and dynamic cone-beam CT reconstruction methods". In: *International Conference on the Use of Computers in Radiation Therapy (ICCR)*. Toronto, Canada, 2007.

[C48] **Rit, S.**, Sarrut, D., Ginestet, C., "Respiratory signal extraction for 4D CT imaging of the thorax from cone-beam CT projections". In: *Medical Image Computing and Computer-Assisted Intervention (MICCAI)*. Vol. 3749. Palm Springs, USA, 2005, pp. 556–563 (cited on page 23).

Abstracts

[A1] Khellaf, F., Krah, N., Létang, J., **Rit, S.,** "A comparison of direct reconstruction algorithms in proton CT". In: *IEEE Nuclear Science Symposium and Medical Imaging Conference (NSS/MIC)*. Manchester, United Kingdom, 2019.

[A2] Addoum, A., Krah, N., Létang, J., **Rit, S.,** "Proton scatter radiography with integration-mode detectors by exploiting the West-Sherwood effect". In: *IEEE Nuclear Science Symposium and Medical Imaging Conference (NSS/MIC)*. Manchester, United Kingdom, 2019 (cited on page 70).

[A3] Coussat, A., **Rit, S.**, Clackdoyle, R., Defrise, M., Desbat, L., Létang, J., "Region-of-interest CT reconstruction using SVD of the truncated Hilbert transform". In: *IEEE Nuclear Science Symposium and Medical Imaging Conference (NSS/MIC)*. Manchester, United Kingdom, 2019 (cited on page 73).

[A4] Robert, A., **Rit, S.**, Jomier, J., Sarrut, D., "Respiration-correlated 4D SPECT reconstruction". In: *IEEE Nuclear Science Symposium and Medical Imaging Conference (NSS/MIC)*. Manchester, United Kingdom, 2019.

[A5] Dickmann, J., Wesp, P., **Rit, S.**, Pankuch, M., Johnson, R., Bashkirov, V., Schulte, R., Parodi, K., Landry, G., Dedes, G., "Understanding image artifacts for a prototype proton computed tomography scanner via Monte Carlo simulations". In: *International Conference on the Use of Computers in Radiation Therapy (ICCR)*. Montreal, Canada, 2019.

[A6] Krah, N., Létang, J., **Rit, S.,** "An analytical method to sample proton trajectories under the influence of multiple Coulomb scattering". In: *International Conference on the Use of Computers in Radiation Therapy (ICCR)*. 2019.

[A7] Akintonde, A., Thielemans, K., Sharma, R., Mouches, P., Mory, C., **Rit, S.**, McClelland, J., "Respiratory motion model derived from CBCT projection data". In: *International Conference on the Use of Computers in Radiation Therapy (ICCR)*. Montreal, Canada, 2019 (cited on pages 29, 72).

[A8] Oger, F., Dupuis, P., Mesny, E., Baudier, T., **Rit, S.**, Tanguy, R., Ayadi, M., "EP-2013 Lung tumor motion based on 4D-CBCT: baseline shift, interfraction amplitude and volume variation". In: *Radiother Oncol* 133 (2019), S1103.

[A9] Clackdoyle, R., **Rit, S.,** "A class of special density functions with matched divergent and parallel projections". In: *IEEE Nuclear Science Symposium and Medical Imaging Conference (NSS/MIC)*. Sydney, Australia, 2018.

[A10] Lesaint, J., Aichert, A., **Rit, S.**, Clackdoyle, R., Desbat, L., "Epipolar consistency conditions: with or without Grangeat?" In: *IEEE Nuclear Science Symposium and Medical Imaging Conference (NSS/MIC)*. Sydney, Australia, 2018.

[A11] Pivot, O., Fournier, C., Tabary, J., **Rit, S.**, Létang, J., "Scatter estimation for spectral CT using a primary modulator mask". In: *IEEE Nuclear Science Symposium and Medical Imaging Conference (NSS/MIC)*. Sydney, Australia, 2018.

[A12] Khellaf, F., Krah, N., Rinaldi, I., Létang, J.-M., **Rit, S.,** "Monte Carlo simulation of the most likely path of protons through a transverse heterogeneity". In: *IEEE Nuclear Science Symposium and Medical Imaging Conference (NSS/MIC)*. Sydney, Australia, 2018.

[A13] Oger, F., Dupuis, P., **Rit, S.**, Tanguy, R., Baudier, T., Ayadi-Zahra, M., "Clinical use of 4D CBCT: ITV volume and amplitude study". In: *Phys Medica* 56 (2018), pp. 1–2.

[A14] Krah, N., Khellaf, F., Létang, J., **Rit, S.**, Rinaldi, I., "Which proton imaging setup should we use in a proton therapy facility?" In: *57th annual conference of the Particle Therapy Co-operative Group (PTCOG)*. Cincinnati, USA, 2018.

[A15] Vilches-Freixas, G., Taasti, V., Hansen, D., Létang, J., Muren, L., Petersen, J., **Rit, S.,** "Stopping power ratio estimation for proton therapy dose calculations using projection- vs. image-based dual-energy CT methods". In: *PTCOG 56 Annual Conference*. Chiba, Japan, 2017.

[A16] Krah, N., Testa, M., **Rit, S.**, Rinaldi, I., "How much can range accuracy in proton therapy be improved through patient specific optimization of the HU-RSP conversion curve?" In: *PTCOG 56 Annual Conference*. Chiba, Japan, 2017.

[A17] Kurz, C., Park, Y., Kamp, F., **Rit, S.**, Winey, B., Sharp, G., Reiner, M., Nijhuis, R., Hansen, D., Ganswindt, U., Thieke, C., Belka, C., Parodi, K., Landry, G., "SU-F-J-186: Enabling Adaptive IMPT with CBCT-Based Dose Recalculation for H&N and Prostate Cancer Patients". In: *American Association of Physicists in Medicine*. Vol. 43. 6. Washington DC, USA: Wiley Online Library, 2016, pp. 3451–3451.

[A18] De Angelis, L., Landry, G., Hansen, D., **Rit, S.**, Belka, C., Dedes, G., Parodi, K., "SU-F-J-214: Dose Reduction by Spatially Optimized Image Quality Via Fluence Modulated Proton CT (FMpCT)". In: *American Association of Physicists in Medicine*. Vol. 43. 6. Washington DC, USA: Wiley Online Library, 2016, pp. 3458–3458.

[A19] Lesaint, J., **Rit, S.**, Clackdoyle, R., Desbat, L., "Calibration of a Micro CT System Based on Data Consistency Conditions". In: *IEEE Nuclear Science Symposium and Medical Imaging Conference (NSS/MIC)*. Strasbourg, France, 2016.

[A20] Quiñones, C., Létang, J., **Rit, S.,** "Scattering proton CT using filtered backprojection along most likely paths". In: *IEEE Nuclear Science Symposium and Medical Imaging Conference (NSS/MIC)*. Strasbourg, France, 2016.

[A21] Clackdoyle, R., Momey, F., Desbat, L., **Rit, S.,** "Accurate Transaxial Region-of-Interest Reconstruction in Helical CT?" In: *IEEE Nuclear Science Symposium and Medical Imaging Conference (NSS/MIC)*. Strasbourg, France, 2016.

[A22] Krah, N., Testa, M., Létang, J.-M., **Rit, S.**, Rinaldi, I., "An Improved Computational Method to Optimize the Stopping Power Calibration Curve for Patient-Specific Proton Therapy Planning". In: *IEEE Nuclear Science Symposium and Medical Imaging Conference (NSS/MIC)*. Strasbourg, France, 2016.

[A23] Hänsch, A., Weber, L., **Rit, S.**, Pacureanu, A., Cloetens, P., Peyrin, F., Langer, M., "Registration of Fresnel diffraction patterns for X-ray phase nanotomography". In: *13th International Conference on X-Ray Microscopy XRM 2016*. Oxford, UK, 2016.

[A24] Fargier-Voiron, M., Pommier, P., **Rit, S.**, Sarrut, D., Biston, M., "EP-1750: Monitoring of intra-fraction prostate motion with a new 4D ultrasound device". In: *ESTRO 35 (European SocieTy for Radiotherapy & Oncology)*. Vol. 119. Turin, Italy: Elsevier, 2016, S819–S820.

[A25] Vilches-Freixas, G., Quinones, C., Létang, J., **Rit, S.,** "Estimation of the ionization potential map from dual-energy CT and proton CT". In: *PTCOG 55 Annual Conference*. Prague, Czech Republic, 2016.

[A26] Vilches-Freixas, G., Létang, J., **Rit, S.,** "EP-1847: Comparison of stopping power estimators from dual-energy computed tomography for protontherapy". In: *ESTRO 35 (European SocieTy for Radiotherapy & Oncology)*. 119. Turin, Italy, 2016, S869.

[A27] Quiñones, C., Létang, J., **Rit, S.,** "Development and characterization of an FBP reconstruction algorithm for proton attenuation CT using most likely paths". In: *IEEE Nuclear Science Symposium and Medical Imaging Conference (NSS/MIC)*. San Diego, California, 2015.

[A28] Vilches-Freixas, G., Létang, J., Presich, K., Steininger, P., **Rit, S.,** "PO-0959: Optimal dose balance between energy levels for material decomposition with dual-energy X-ray CT". In: *3rd ESTRO Forum (European SocieTy for Radiotherapy & Oncology)*. Vol. 115. Barcelona, Spain: Elsevier, 2015, S506–S507.

[A29] **Rit, S.**, Clackdoyle, R., Keuschnigg, P., Steininger, P., "OC-0410: Exact FBP reconstruction for a cone-beam CT scanner with independent rotations of the source and the detector". In: *3rd ESTRO Forum (European SocieTy for Radiotherapy & Oncology)*. Vol. 115. Barcelona, Spain: Elsevier, 2015, S198–S199.

[A30] Mory, C., **Rit, S.,** "PD-0143: 4D cone-beam computed tomography combining total variation regularization and motion compensation". In: *3rd ESTRO Forum (European SocieTy for Radiotherapy & Oncology)*. Vol. 115. Barcelona, Spain: Elsevier, 2015, S68–S69.

[A31] Dedes, G., Asano, Y., Arbor, N., Dauvergne, D., Letang, J., Testa, E., **Rit, S.**, Parodi, K., "SU-EJ-147: Monte Carlo Study of the Precision and Accuracy of Proton CT Reconstructed Relative Stopping Power Maps". In: *3rd ESTRO Forum (European SocieTy for Radiotherapy & Oncology)*. Vol. 42. 6. Barcelona, Spain: American Association of Physicists in Medicine, 2015, pp. 3298–3298.

[A32] Arbor, N., Dauvergne, D., Dedes, G., Létang, J., Parodi, K., Quinones, C., Testa, E., **Rit, S.,** "PD-0139: Monte Carlo evaluation of X-ray and proton CT for the prediction of the range of proton therapy beams". In: *3rd ESTRO Forum (European SocieTy for Radiotherapy & Oncology)*. Vol. 115. Barcelona, Spain: Elsevier, 2015, S66.

[A33] Fargier-Voiron, M., Presles, B., Pommier, P., **Rit, S.**, Sarrut, D., Biston, M., "PO-0987: Ultrasound image guided radiotherapy for prostate cancer using a transperineal probe". In: *3rd ESTRO Forum (European SocieTy for Radiotherapy & Oncology)*. Vol. 115. Barcelona, Spain: Elsevier, 2015, S527.

[A34] Presles, B., Fargier-Voiron, M., Pommier, P., Sarrut, S. R. D., Biston, M.-C., "Two years of experience with the transperineal autoscan system at the Léon Bérard Cancer Center". In: *International Workshop on Ultrasound Guidance in Radiotherapy*. London, UK, 2015.

[A35] Arbor, N., Dauvergne, D., Dedes, G., Letang, J., Quinones, C.-T., Testa, E., **Rit, S.,** "In-Silico Comparison of X-Ray and Proton Computed Tomography for Proton Therapy Dose Simulation with a Full Monte Carlo Treatment Planning". In: *IEEE Nuclear Science Symposium and Medical Imaging Conference (NSS/MIC)*. Seattle, USA, 2014.

[A36] Fargier-Voiron, M., Presles, B., Pommier, P., **Rit, S.**, Munoz, A., Liebgott, H., Sarrut, D., Biston, M., "Impact of probe pressure variability on prostate localization for ultrasound-based image-guided radiotherapy". In: *ESTRO 33 (European SocieTy for Radiotherapy & Oncology)*. Vienna, Austria, 2014.

[A37] **Rit, S.**, Romero, E., Oliva, M. V., Brousmiche, S., Sarrut, D., Létang, J., Freud, N., "PO-0921: Simulation of x-ray images from the planning CT for online correction of scatter in cone-beam CT". In: *ESTRO 33 (European SocieTy for Radiotherapy & Oncology)*. Vol. 111. Vienna, Austria: Elsevier BV, 2014, S115.

[A38] Ayadi-Zahra, M., Bouilhol, G., Krason, A., **Rit, S.**, Dupuis, P., Claude, L., Sarrut, D., "Dosimetric analysis of mid-position vs ITV conformational plans for locally advanced NSCLC. Preliminary results". In: *ESTRO 33 (European SocieTy for Radiotherapy & Oncology)*. Vienna, Austria, 2014.

[A39] Brousmiche, S., Seabra, J., Labarbe, R., Vila Oliva, M., **Rit, S.**, Wikler, D., Lee, J., Teo, K., Orban de Xivry, J., Macq, B., "Design of cone-beam CT for proton therapy gantry". In: *ESTRO 33 (European SocieTy for Radiotherapy & Oncology)*. Vienna, Austria, 2014.

[A40] Wang, M., Sharp, G., **Rit, S.**, Delmon, V., Wang, G., "Improvement of Digitally Reconstructed Radiograph Quality of Thoracic 4D Cone Beam Computed Tomography". In: vol. 40. 6. Indianapolis, Indiana, USA: American Association of Physicists in Medicine, 2013, pp. 411–411.

[A41] Smekens, F., Freud, N., Létang, J., **Rit, S.**, Baldacci, F., Mittone, A., Sarrut, D., "Speeding up Gate/Geant4 for low energy x-ray dose calculation: two Kerma methods". In: *Geant4 2013 International User Conference*. Bordeaux, France, 2013.

[A42] **Rit, S.**, Romero, E., Vila Oliva, M., Smekens, F., Sarrut, D., Létang, J., Freud, N., "Hybrid Monte Carlo / deterministic simulation of X-ray imaging for the correction of scatter in cone-beam computed tomography". In: *Geant4 2013 International User Conference*. Bordeaux, France, 2013.

[A43] **Rit, S.**, Pinho, R., Bouilhol, G., Ayadi, M., Biston, M., Claude, L., Sarrut, D., "Phase II clinical trial comparing mid-position with internal target volume treatment planning". In: *ESTRO 31 (European SocieTy for Radiotherapy & Oncology)*. Barcelona, Spain, 2012.

[A44] Bouilhol, G., **Rit, S.**, Ayadi, M., Sarrut, D., "Margin calculation for temporally asymmetric respiratory motion". In: *ESTRO 31 (European SocieTy for Radiotherapy & Oncology)*. Barcelona, Spain, 2012.

[A45] Van der Reijden, A., Rossi, M., **Rit, S.**, Conijn, S., Belderbos, J., van Herk, M., Remeijer, P., Sonke, J., "First clinical results for motion compensated cone-beam CT (CBCT) in stereotactic ablative radiotherapy (SABR)". In: *ESTRO 31 (European SocieTy for Radiotherapy & Oncology)*. Barcelona, Spain, 2012.

[A46] **Rit, S.**, Nijkamp, J., van Herk, M., Sonke, J.-J., "Comparison of different strategies for respiratory motion correction of cone-beam CT in lung cancer SBRT". In: *ESTRO 31 (European SocieTy for Radiotherapy & Oncology)*. London, United Kingdom, 2011.

[A47] van Herk, M., Mans, A., **Rit, S.**, Nijkamp, J., Sonke, J., "In-vivo analysis of interplay effects due to respiration and respiration irregularities during free-breathing VMAT delivery of SBRT". In: *ESTRO 29 (European SocieTy for Radiotherapy & Oncology)*. Barcelona, Spain, 2010.

[A48] **Rit, S.**, Vandemeulebroucke, J., Sarrut, D., Sonke, J.-J., "B-Spline parametrization of the temporal dimension for respiratory motion estimation". In: *Proceedings of the 29th Annual ESTRO Meeting*. Barcelona, Spain, 2010.

[A49] Chaieb, E. "Etude des paramètres d'acquisition scanner en vue de la réalisation d'une dosimétrie 4D". MA thesis. Université Paul Sabatier Toulouse III, 2006.

[A50] **Rit, S.**, Sarrut, D., Boldea, V., Ginestet, C., "Extraction du signal respiratoire à partir de projections cone-beam du thorax pour l'imagerie TDM 4D en radiothérapie". In: *Journées Scientifiques de la Société Française de Physique Médicale (SFPM)*. Avignon, France, 2005.

[A51] **Rit, S.**, Sarrut, D., Ginestet, C., "Respiratory signal extraction for 4D CT imaging of the thorax from cone-beam CT projections". In: *Proceedings of the 47th Annual ASTRO Meeting*. 2005, S533–S534.

Proceedings

[P1] Beichel, R., Farahani, K., C.Jacobs, Kabus, S., Kiraly, A., Kuhnigk, J.-M., McClelland, J., Mori, K., Petersen, J., **Rit, S.,** eds. *Proceedings of the Sixth International Workshop on Pulmonary Image Analysis*. 2016.

[P2] Peroni, M., Schlaefer, A., Birkfellner, W., Gianoli, C., Knopf, A.-C., McClelland, J., Riboldi, M., **Rit, S.,** eds. *ICART: Imaging and Computer Assistance in Radiation Therapy*. MICCAI workshop. 2015.

[P3] Beichel, R., Bruijne, M., Kabus, S., Kiraly, A., Kitasaka, T., Kuhnigk, J.-M., McClelland, J., Rikxoort, E., **Rit, S.,** eds. *Proceedings of the Fifth International Workshop on Pulmonary Image Analysis*. 2013.

[P4] Birkfellner, W., Mcclelland, J., **Rit, S.**, Schlaefer, A., eds. *Proceedings of the first MICCAI workshop on Image-Guidance and Multimodal Dose Planning in Radiation Therapy*. 2012.

[P5] Beichel, R., Bruijne, M., Ginneken, B., Kabus, S., Kiraly, A., Kuhnigk, J.-M., McClelland, J., Mori, K., Rikxoort, E., **Rit, S.,** eds. *Proceedings of the Fourth International Workshop on Pulmonary Image Analysis*. 2011.

Workshops

[W1] Krah, N., Khellaf, F., Létang, J., **Rit, S.**, Rinaldi, I., "A theoretical comparison of different proton imaging set-ups". In: *The Fourth Loma Linda Workshop*. Loma Linda, USA, 2018.

[W2] Krah, N., Khellaf, F., Létang, J., **Rit, S.**, Rinaldi, I., "A comprehensive theoretical comparison of proton imaging set-ups in terms of spatial resolution". In: *Proton imaging workshop*. Lyon, France, 2018.

[W3] Khellaf, F., Krah, N., Rinaldi, I., Létang, J.-M., **Rit, S.,** "Monte Carlo analysis of the effects of transverse heterogeneities on the most likely path of protons". In: *Proton imaging workshop*. Lyon, France, 2018.

[W4] Kurz, C., Park, Y., Kamp, F., **Rit, S.**, Winey, B., Sharp, G., Reiner, M., Nijhuis, R., Hansen, D., Ganswindt, U., Thieke, C., Belka, C., Parodi, K., Landry, G., "CBCT-based dose calculation to foster adaptive IMPT for H&N and prostate cancer". In: *4D Treatment Planning Workshop*. Groningen, The Netherlands, 2016.

[W5] Rinaldi, I., Rucinski, A., Vilches-Freixas, G., **Rit, S.**, Patera, V., Schiavi, A., Krah, N., "Internal motion tracking based on ion radiographies". In: *4D Treatment Planning Workshop*. Groningen, The Netherlands, 2016.

[W6] Rucinski, A. "Internal motion tracking based on charged secondary proton emission". In: *4D Treatment Planning Workshop*. Groningen, The Netherlands, 2016.

[W7] **Rit, S.** "Elastix, (Plastimatch, NiftyReg)". In: *PRIMES: Journée de rencontre développeurs-utilisateurs recalabe/mouvement*. Lyon, France, 2016.

[W8] **Rit, S.**, Vilches-Freixas, G., Landry, G., Létang, J., "Spectral CT for proton therapy". In: *First photon Counting CT workshop*. Lyon, France, 2015.

[W9] **Rit, S.**, Clackdoyle, R., "2D fan-beam CT with independent source and detector rotation". In: *DROITE Workshop*. Grenoble, France, 2013.

[W10] **Rit, S.**, Romero, E., Vila Oliva, M., Smekens, F., Sarrut, D., Létang, J., Freud, N., "Fixed forced detection for accelerating the simulation of X-ray images with Geant4". In: *Monte Carlo simulation tools for X-ray imaging and fluorescence*. ESRF, Grenoble, France, 2013.

[W11] **Rit, S.** "Distance-driven binning for proton CT filtered backprojection along most likely paths". In: *University College seminar*. London, United Kingdom, 2012.

[W12] Pinho, R., **Rit, S.**, Bouilhol, G., Ayadi, M., Biston, M.-C., Claude, L., Sarrut, D., "Phase II clinical trial comparing Mid-position with internal target volume treatment planning". In: *Journée Médico-Scientifique Centre Léon Bérard*. Lyon, France, 2012.

[W13] Pinho, R., **Rit, S.**, Bouilhol, G., Ayadi, M., Biston, M.-C., Claude, L., Sarrut, D., "Clinical implementation of 4D deformable image registration for the computation of Mid-Position CT images". In: *IGRT Salzburg*. Salzburg, Austria, 2011.

[W14] **Rit, S.** "Distance-driven binning for proton CT filtered backprojection along most likely paths". In: *DROITE Workshop*. Lyon, France, 2012.

[W15] **Rit, S.**, van Herk, M., Zijp, L., Sonke, J.-J., "Quantification of the variability of diaphragm motion and implications for treatment margin construction". In: *Seminar at the Massachusetts General Hospital*. Boston, Massachusetts, USA, 2011.

[W16] **Rit, S.** "Quantification and impact of the variability of the respiratory motion during radiotherapy". In: *CART Research and Education Seminar*. UCSD, San Diego, California, 2010.

Other references

[1] Zeng, G. *Medical Image Reconstruction*. Springer, 2010 (cited on page 21).

[2] Natterer, F. *The mathematics of computerized tomography*. John Wiley & Sons, 1986 (cited on page 21).

[3] Kak, A., Slaney, M., *Principles of computerized tomographic imaging*. IEEE Press, 1988 (cited on page 21).

[4] Vandemeulebroucke, J. "Lung Motion Modelling and Estimation for Image-Guided Radiation Therapy". PhD thesis. Institut National des Sciences Appliquées (INSA) de Lyon, 2010 (cited on pages 22, 23, 28).

[5] McClelland, J., Hawkes, D., Schaeffter, T., King, A., "Respiratory motion models: A review". eng. In: *Med Image Anal* (2012) (cited on page 23).

[6] Kachelriess, M., Sennst, D.-A., Maxlmoser, W., Kalender, W., "Kymogram detection and kymogram-correlated image reconstruction from subsecond spiral computed tomography scans of the heart". In: *Med Phys* 29.7 (2002), pp. 1489–1503 (cited on page 23).

[7] Zijp, L., Sonke, J.-J., van Herk, M., "Extraction of the respiratory signal from sequential thorax cone-beam X-ray images". In: *International Conference on the Use of Computers in Radiation Therapy (ICCR)*. Seoul, Republic of Korea: Jeong Publishing, 2004, pp. 507–509 (cited on pages 23, 29).

[8] Sonke, J.-J., Zijp, L., Remeijer, P., van Herk, M., "Respiratory correlated cone beam CT". In: *Med Phys* 32.4 (2005), pp. 1176–1186 (cited on pages 23, 32, 71).

[9] Schäfer, D., Borgert, J., Rasche, V., Grass, M., "Motion-compensated and gated cone beam filtered back-projection for 3D rotational X-ray angiography". In: *IEEE Trans Med Imaging* 25.7 (2006), pp. 898–906 (cited on pages 23, 24).

[10] Lauritsch, G., Boese, J., Wigstrom, L., Kemeth, H., Fahrig, R., "Towards cardiac C-arm computedtomography". In: *IEEE Trans Med Imaging* 25.7 (2006), pp. 922–934 (cited on page 23).

[11] Roux, S., Desbat, L., Koenig, A., Grangeat, P., "Exact reconstruction in 2D dynamic CT: compensation of time-dependent affine deformations". In: *Phys Med Biol* 49.11 (2004), pp. 2169–2182 (cited on page 24).

[12] Desbat, L., Roux, S., Grangeat, P., "Compensation of some time dependent deformations in tomography". In: *IEEE Trans Med Imaging* 26.2 (2007), pp. 261–269 (cited on pages 24, 36).

[13] Crawford, C., King, K., Ritchie, C., Godwin, J., "Respiratory compensation in projection imaging using a magnification and displacement model". In: *IEEE Trans Med Imaging* 15.3 (1996), pp. 327–332 (cited on page 24).

[14] Feldkamp, L., Davis, L., Kress, J., "Practical cone-beam algorithm". In: *J Opt Soc Am A* 1.6 (1984), pp. 612–619 (cited on pages 24, 31).

[15] Li, T., Koong, A., Xing, L., "Enhanced 4D cone-beam CT with inter-phase motion model". In: *Med Phys* 34.9 (2007), pp. 3688–3695 (cited on page 24).

[16] Boldea, V. "Intégration de la respiration en radiothérapie : apport du recalage déformable d'images". PhD thesis. Université Lumière Lyon 2, 2006 (cited on page 25).

[17] Wolthaus, J., Sonke, J.-J., van Herk, M., Damen, E., "Reconstruction of a time-averaged midposition CT scan for radiotherapy planning of lung cancer patients using deformable registration". In: *Med Phys* 35.9 (2008), pp. 3998–4011 (cited on page 25).

[18] Hemmendorff, M., Andersson, M., Kronander, T., Knutsson, H., "Phase-based multidimensional volume registration". In: *IEEE Trans Med Imaging* 21.12 (2002). Ed. by M.T. Andersson, pp. 1536–1543 (cited on page 25).

[19] Fischer, B., Modersitzki, J., "Ill-posed medicine—an introduction to image registration". In: *Inverse Problems* 24 (2008), p. 034008 (cited on page 25).

[20] Yamamoto, T., Langner, U., Loo, B., Shen, J., Keall, P., "Retrospective analysis of artifacts in four-dimensional CT images of 50 abdominal and thoracic radiotherapy patients". In: *Int J Radiat Oncol Biol Phys* 72.4 (2008), pp. 1250–1258 (cited on pages 25, 72).

[21] Boldea, V., Sharp, G., Jiang, S., Sarrut, D., "4D-CT lung motion estimation with deformable registration: quantification of motion nonlinearity and hysteresis". In: *Med Phys* 35.3 (2008), pp. 1008–1018 (cited on page 25).

[22] Sarrut, D., Delhay, B., Villard, P.-F., Boldea, V., Beuve, M., Clarysse, P., "A comparison framework for breathing motion estimation methods from 4-D imaging". In: *IEEE Trans Med Imaging* 26.12 (2007), pp. 1636–1648 (cited on page 25).

[23] Rueckert, D., Sonoda, L., Hayes, C., Hill, D., Leach, M., Hawkes, D., "Nonrigid registration using free-form deformations: application to breast MR images". eng. In: *IEEE Trans Med Imaging* 18.8 (1999), pp. 712–721 (cited on page 25).

[24] Wu, Z., Rietzel, E., Boldea, V., Sarrut, D., Sharp, G., "Evaluation of deformable registration of patient lung 4DCT with subanatomical region segmentations". In: *Med Phys* 35.2 (2008), pp. 775–781 (cited on pages 26, 27).

[25] Vandemeulebroucke, J., Sarrut, D., Clarysse, P., "Point-validated Pixel-based Breathing Thorax Model". In: *International Conference on the Use of Computers in Radiation Therapy (ICCR)*. Toronto, Canada, 2007 (cited on page 28).

[26] McClelland, J., Modat, M., Arridge, S., Grimes, H., D'Souza, D., Thomas, D., O'Connell, D., Low, D., Kaza, E., Collins, D., Leach, M., Hawkes, D., "A generalized framework unifying image registration and respiratory motion models and incorporating image reconstruction, for partial image data or full images." In: *Phys Med Biol* 62 (11 2017), pp. 4273–4292 (cited on pages 28, 29, 72).

[27] Low, D., Parikh, P., Lu, W., Dempsey, J., Wahab, S., Hubenschmidt, J., Nystrom, M., Handoko, M., Bradley, J., "Novel breathing motion model for radiotherapy". In: *Int J Radial Oncol Biol Phys* 63.3 (2005), pp. 921–929 (cited on pages 29, 72).

[28] Candes, E., Romberg, J., Tao, T., "Robust uncertainty principles: exact signal reconstruction from highly incomplete frequency information". In: *IEEE Trans Inf Theory* 52.2 (2006), pp. 489–509 (cited on page 31).

[29] Bergner, F., Berkus, T., Oelhafen, M., Kunz, P., Pan, T., Grimmer, R., Ritschl, L., Kachelriess, M., "An investigation of 4D cone-beam CT algorithms for slowly rotating scanners". eng. In: *Med Phys* 37.9 (2010), pp. 5044–5053 (cited on page 31).

[30] Boussel, L., Ribagnac, M., Bonnefoy, E., Staat, P., Elicker, B., Revel, D., Douek, P., "Assessment of acute myocardial infarction using MDCT after percutaneous coronary intervention: comparison with MRI". In: *AJR. American journal of roentgenology* 191 (2 2008), pp. 441–447 (cited on page 31).

[31] Momey, F. "Reconstruction en tomographie dynamique par approche inverse sans compensation de mouvement". PhD thesis. Université Jean Monnet de Saint-Étienne, 2013 (cited on page 31).

[32] Rudin, L., Osher, S., Fatemi, E., "Nonlinear total variation based noise removal algorithms". In: *Physica D: Nonlinear Phenomena* 60.1-4 (1992), pp. 259–268 (cited on page 31).

[33] Mory, C., Jacques, L., "A modified 4D ROOSTER method using the Chambolle-Pock algorithm". In: *Fourth international conference on image formation in X-ray computed tomography*. Salt Lake City, USA, 2014, pp. 191–193 (cited on page 32).

[34] Chen, G.-H., Tang, J., Leng, S., "Prior image constrained compressed sensing (PICCS): a method to accurately reconstruct dynamic CT images from highly undersampled projection data sets". eng. In: *Med Phys* 35.2 (2008), pp. 660–663 (cited on page 32).

[35] Clackdoyle, R., Defrise, M., "Tomographic Reconstruction in the 21st Century. Region-of-interest reconstruction from incomplete data." In: *IEEE Signal Process Mag* 27.4 (2010), pp. 60–80 (cited on page 35).

[36] Noo, F., Clackdoyle, R., Pack, J., "A two-step Hilbert transform method for 2D image reconstruction". In: *Phys Med Biol* 49.17 (2004), pp. 3903–3923 (cited on page 35).

[37] Zeng, G. "Image reconstruction via the finite Hilbert transform of the derivative of the backprojection." In: *Med Phys* 34.7 (2007), pp. 2837–2843 (cited on pages 35, 36, 62).

[38] Xia, D., Sidky, E., Yu, L., Zou, Y., Pan, X., "Exact ROI image reconstruction with perturbed source trajectories in C-arm CT". In: *Nuclear Science Symposium Conference Record, 2005 IEEE*. Vol. 4. IEEE. 2005, 4–pp (cited on pages 36, 37).

[39] Clackdoyle, R. "Data Consistency for Linograms and Planograms". In: *IEEE Trans Radiat Plasma Med Sci* PP.99 (2018), p. 1 (cited on page 39).

[40] Clackdoyle, R. "Necessary and Sufficient Consistency Conditions for Fanbeam Projections Along a Line". In: *IEEE Trans Nucl Sci* 60.3 (2013), pp. 1560–1569 (cited on page 39).

[41] Clackdoyle, R., Desbat, L., "Full data consistency conditions for cone-beam projections with sources on a plane". eng. In: *Phys Med Biol* 58.23 (2013), pp. 8437–8456 (cited on page 39).

[42] Clackdoyle, R., Desbat, L., "Data consistency conditions for truncated fanbeam and parallel projections". In: *Med Phys* 42.2 (2015), pp. 831–845 (cited on page 39).

[43] Lesaint, J. "Data consistency conditions in X-ray transmission imaging and their application to the self-calibration problem". Theses. Université Grenoble Alpes, 2018 (cited on pages 39, 40, 76).

[44] Levine, M., Sidky, E., Pan, X., "Consistency conditions for cone-beam CT data acquired with a straight-line source trajectory". In: *Tsinghua Science & Technology* 15.1 (2010), pp. 56–61 (cited on page 39).

[45] Heismann, B., Schmidt, B., Flohr, T., *Spectral computed tomography*. SPIE Press, 2012 (cited on page 46).

[46] Alvarez, R., Macovski, A., "Energy-selective reconstructions in X-ray computerized tomography". eng. In: *Phys Med Biol* 21.5 (1976), pp. 733–744 (cited on pages 45, 53).

[47] Roessl, E., Proksa, R., "K-edge imaging in x-ray computed tomography using multi-bin photon counting detectors". eng. In: *Phys Med Biol* 52.15 (2007), pp. 4679–4696 (cited on page 46).

[48] Schlomka, J., Roessl, E., Dorscheid, R., Dill, S., Martens, G., Istel, T., Bäumer, C., Herrmann, C., Steadman, R., Zeitler, G., Livne, A., Proksa, R., "Experimental feasibility of multi-energy photon-counting K-edge imaging in pre-clinical computed tomography". eng. In: *Phys Med Biol* 53.15 (2008), pp. 4031–4047 (cited on pages 46, 47).

[49] Cai, C., Rodet, T., Legoupil, S., Mohammad-Djafari, A., "A full-spectral Bayesian reconstruction approach based on the material decomposition model applied in dual-energy computed tomography". In: *Med Phys* 40 (11 2013), p. 111916 (cited on page 48).

[50] Long, Y., Fessler, J., "Multi-Material Decomposition Using Statistical Image Reconstruction for Spectral CT". In: *IEEE Trans Med Imag* 33.8 (2014), pp. 1614–1626 (cited on page 48).

[51] Weidinger, T., Buzug, T., Flohr, T., Kappler, S., Stierstorfer, K., "Polychromatic Iterative Statistical Material Image Reconstruction for Photon-Counting Computed Tomography". In: *Int J Biomed Imaging* 2016 (2016), p. 5871604 (cited on page 48).

[52] Foygel Barber, R., Sidky, E., Gilat Schmidt, T., Pan, X., "An algorithm for constrained one-step inversion of spectral CT data". In: *Phys Med Biol* 61.10 (2016), pp. 3784–3818 (cited on page 48).

[53] Mechlem, K., Ehn, S., Sellerer, T., Braig, E., Münzel, D., Pfeiffer, F., Noël, P., "Joint Statistical Iterative Material Image Reconstruction for Spectral Computed Tomography Using a Semi-Empirical Forward Model". In: *IEEE Trans Med Imag* 37 (1 2018), pp. 68–80 (cited on page 48).

[54] Zhu, L., Bennett, N. R., Fahrig, R., "Scatter correction method for X-ray CT using primary modulation: theory and preliminary results." eng. In: *IEEE Trans Med Imaging* 25.12 (2006), pp. 1573–1587 (cited on page 48).

[55] Ritschl, L., Fahrig, R., Knaup, M., Maier, J., Kachelrieß, M., "Robust primary modulation-based scatter estimation for cone-beam CT". In: *Med Phys* 42.1 (2015), pp. 469–478 (cited on page 48).

[56] Paganetti, H. "Range uncertainties in proton therapy and the role of Monte Carlo simulations". eng. In: *Phys Med Biol* 57.11 (2012), R99–117 (cited on page 51).

[57] Beaulieu, L., Bazalova, M., Furstoss, C., Verhaegen, F., "SU-FF-T-408: tissue inhomogeneities in Monte Carlo treatment planning for proton therapy". In: *Med Phys* 36.6Part15 (2009), pp. 2616–2616 (cited on page 52).

[58] Bazalova, M., Zhou, H., Keall, P., Graves, E., "Kilovoltage beam Monte Carlo dose calculations in submillimeter voxels for small animal radiotherapy". eng. In: *Med Phys* 36.11 (2009), pp. 4991–4999 (cited on page 52).

[59] Yang, M., Zhu, X., Park, P., Titt, U., Mohan, R., Virshup, G., Clayton, J., Dong, L., "Comprehensive analysis of proton range uncertainties related to patient stopping-power-ratio estimation using the stoichiometric calibration". eng. In: *Phys Med Biol* 57.13 (2012), pp. 4095–4115 (cited on pages 52, 65).

[60] Kanematsu, N., Inaniwa, T., Koba, Y., "Relationship between electron density and effective densities of body tissues for stopping, scattering, and nuclear interactions of proton and ion beams". eng. In: *Med Phys* 39.2 (2012), pp. 1016–1020 (cited on pages 53, 70).

[61] Taasti, V., Petersen, J., Muren, L., Thygesen, J., Hansen, D., "A robust empirical parametrization of proton stopping power using dual energy CT". In: *Med Phys* 43 (10 2016), p. 5547 (cited on page 53).

[62] Saito, M. "Potential of dual-energy subtraction for converting CT numbers to electron density based on a single linear relationship". eng. In: *Med Phys* 39.4 (2012), pp. 2021–2030 (cited on page 53).

[63] Han, D., Siebers, J., Williamson, J., "A linear, separable two-parameter model for dual energy CT imaging of proton stopping power computation". In: *Med Phys* 43 (1 2016), p. 600 (cited on page 53).

[64] Cormack, A. "Representation of a Function by Its Line Integrals, with Some Radiological Applications". In: *Journal of Applied Physics* 34.9 (1963), pp. 2722–2727 (cited on page 59).

[65] Schulte, R., Penfold, S., "Proton CT for Improved Stopping Power Determination in Proton Therapy". eng. In: *Transactions of the American Nuclear Society* 106.24771877 (2012), pp. 55–58 (cited on page 59).

[66] Poludniowski, G., Allinson, N., Evans, P., "Proton radiography and tomography with application to proton therapy". eng. In: *Br J Radiol* 88.1053 (2015), p. 20150134 (cited on page 59).

[67] Johnson, R. "Review of medical radiography and tomography with proton beams". In: *Reports on progress in physics* 81 (1 2018), p. 016701 (cited on page 59).

[68] Williams, D. "The most likely path of an energetic charged particle through a uniform medium". eng. In: *Phys Med Biol* 49.13 (2004), pp. 2899–2911 (cited on page 60).

[69] Schulte, R. W., Penfold, S. N., Tafas, J. T., Schubert, K. E., "A maximum likelihood proton path formalism for application in proton computed tomography." In: *Med Phys* 35.11 (2008), pp. 4849–4856 (cited on pages 60, 75).

[70] Poludniowski, G., Allinson, N., Evans, P., "Proton computed tomography reconstruction using a backprojection-then-filtering approach". eng. In: *Phys Med Biol* 59.24 (2014), pp. 7905–7918 (cited on pages 62, 63).

[71] Collins-Fekete, C., Brousmiche, S., Portillo, S., Beaulieu, L., Seco, J., "A maximum likelihood method for high resolution proton radiography/proton CT". In: *Phys Med Biol* 61 (23 2016), pp. 8232–8248 (cited on page 63).

[72] Bopp, C., Colin, J., Cussol, D., Finck, C., Labalme, M., Rousseau, M., Brasse, D., "Proton computed tomography from multiple physics processes." eng. In: *Phys Med Biol* 58.20 (2013), pp. 7261–7276 (cited on page 67).

[73] Bopp, C. "The proton as a dosimetric and diagnostic probe". PhD thesis. Université de Strasbourg, 2014 (cited on page 67).

[74] Bopp, C., Rescigno, R., Rousseau, M., Brasse, D., "Quantitative proton imaging from multiple physics processes: a proof of concept". eng. In: *Phys Med Biol* 60.13 (2015), pp. 5325–5341 (cited on page 67).

[75] Schulte, R., Bashkirov, V., Loss Klock, M., Li, T., Wroe, A., Evseev, I., Williams, D., Satogata, T., "Density resolution of proton computed tomography". eng. In: *Med Phys* 32.4 (2005), pp. 1035–1046 (cited on pages 67, 74).

[76] West, D., Sherwood, A., "Proton-scattering radiography". In: *non-destructive testing* 6.5 (1973), pp. 249–257 (cited on page 67).

[77] Gottschalk, B. "On the scattering power of radiotherapy protons". eng. In: *Med Phys* 37.1 (2010), pp. 352–367 (cited on page 70).

[78] Ford, E., Mageras, G., Yorke, E., Ling, C., "Respiration-correlated spiral CT: a method of measuring respiratory-induced anatomic motion for radiation treatment planning". In: *Med Phys* 30.1 (2003), pp. 88–97 (cited on page 71).

[79] Bastiaannet, R., Viergever, M., de Jong, H., "Impact of Respiratory Motion and Acquisition Settings on SPECT Liver Dosimetry for Radioembolization". In: *Med Phys* (2017) (cited on page 71).

[80] Sanders, J., Ritt, P., Kuwert, T., Vija, A., Maier, A., "Fully Automated Data-Driven Respiratory Signal Extraction From SPECT Images Using Laplacian Eigenmaps". In: *IEEE transactions on medical imaging* 35 (11 2016), pp. 2425–2435 (cited on page 71).

[81] Liu, J., Zhang, X., Zhang, X., Zhao, H., Gao, Y., Thomas, D., A, D. L., Gao, H., "5D respiratory motion model based image reconstruction algorithm for 4D cone-beam computed tomography". In: *Inverse Problems* 31.11 (2015), p. 115007 (cited on page 72).

[82] Defrise, M., Noo, F., Clackdoyle, R., Kudo, H., "Truncated Hilbert transform and image reconstruction from limited tomographic data". In: *Inverse problems* 22.3 (2006), p. 1037 (cited on page 73).

[83] Clackdoyle, R., Noo, F., Guo, J., Roberts, J., "Quantitative reconstruction from truncated projections in classical tomography". In: *IEEE Trans Nucl Sci* 51.5 (2004), pp. 2570–2578 (cited on page 73).

[84] Noo, F., Defrise, M., Clackdoyle, R., Kudo, H., "Image reconstruction from fan-beam projections on less than a short scan". In: *Phys Med Biol* 47.14 (2002), pp. 2525–2546 (cited on page 73).

[85] Verdun, F., Racine, D., Ott, J., Tapiovaara, M., Toroi, P., Bochud, F., Veldkamp, W., Schegerer, A., Bouwman, R., Giron, I., Marshall, N., Edyvean, S., "Image quality in CT: From physical measurements to model observers". eng. In: *Phys Med* (2015) (cited on page 74).

[86] Johnson, R., Bashkirov, V., Coutrakon, G., Giacometti, V., Karbasi, P., Karonis, N., Ordoñez, C., Pankuch, M., Sadrozinski, H.-W., Schubert, K., "Results from a Prototype Proton-CT Head Scanner". In: *arXiv preprint arXiv:1707.01580* (2017) (cited on page 74).

[87] Bashkirov, V., Schulte, R., Hurley, R., Johnson, R., Sadrozinski, H.-W., Zatserklyaniy, A., Plautz, T., Giacometti, V., "Novel scintillation detector design and performance for proton radiography and computed tomography". eng. In: *Med Phys* 43.2 (2016), p. 664 (cited on page 74).

[88] Worstell, W., Adams, B., Aviles, M., Bond, J., Cascio, E., Cremer, T., El Fakhri, G., Ertley, C., Foley, M., Grogg, K., Hamel, C., Lu, H.-M., Lyashenko, A., Minot, M., Paganetti, H., Popecki, M., Stochaj, M., "First results developing time-of-flight proton radiography for proton therapy applications". In: *Medical Imaging 2019: Physics of Medical Imaging*. Ed. by Taly Gilat Schmidt, Guang-Hong Chen, and Hilde Bosmans. Vol. 10948. International Society for Optics and Photonics. SPIE, 2019, pp. 101–109 (cited on page 74).

[89] Lecoq, P. "Roadmap toward the 10 ps time-of-flight PET challenge". In: *Phys Med Biol* 65.21 (2020), 21RM01 (cited on page 74).

[90] Upadhay, R. "Explore the use of artificial neural network to filter events in ion computed tomography". MA thesis. Phelma, Grenoble, 2019 (cited on page 75).

[91] Rahmim, A., Qi, J., Sossi, V., "Resolution modeling in PET imaging: Theory, practice, benefits, and pitfalls". In: *Medical Physics* 40.6Part1 (2013), p. 064301 (cited on page 75).

[92] Hansen, D., Petersen, J., Bassler, N., Sørensen, T., "Improved proton computed tomography by dual modality image reconstruction". eng. In: *Med Phys* 41.3 (2014), p. 031904 (cited on page 75).

[93] Flohr, T., McCollough, C., Bruder, H., Petersilka, M., Gruber, K., Süss, C., Grasruck, M., Stierstorfer, K., Krauss, B., Raupach, R., Primak, A., Küttner, A., Achenbach, S., Becker, C., Kopp, A., Ohnesorge, B., "First performance evaluation of a dual-source CT (DSCT) system". In: *Eur Radiol* 16.2 (2006), pp. 256–268 (cited on page 75).

[94] McCollough, C., Leng, S., Yu, L., Fletcher, J., "Dual- and Multi-Energy CT: Principles, Technical Approaches, and Clinical Applications". eng. In: *Radiology* 276.3 (2015), pp. 637–653 (cited on page 75).

[95] Abdurahman, S., Frysch, R., Bismark, R., Melnik, S., Beuing, O., Rose, G., "Beam hardening correction using cone beam consistency conditions". In: *IEEE Transactions on Medical Imaging* 37.10 (2018), pp. 2266–2277 (cited on page 76).

[96] Würfl, T., Hoffmann, M., Aichert, A., Maier, A., Maaß, N., Dennerlein, F., "Calibration-free beam hardening reduction in x-ray CBCT using the epipolar consistency condition and physical constraints". In: *Med Phys* 46 (12 2019), e810–e822 (cited on page 76).

[97] Ohnesorge, B., Flohr, T., Klingenbeck-Regn, K., "Efficient object scatter correction algorithm for third and fourth generation CT scanners". eng. In: *Eur Radiol* 9.3 (1999), pp. 563–569 (cited on page 76).

[98] Abdurahman, S., Frysch, R., Rose, G., "Scatter correction using pair-wise fan beam consistency conditions". In: *Fully 3D Image Reconstruction in Radiology and Nuclear Medicine*. Ed. by Samuel Matej and Scott D. Metzler. Philadelphia, USA: SPIE, 2019 (cited on page 76).

[99] Paganin, D., Labriet, H., Brun, E., Berujon, S., "Single-image geometric-flow x-ray speckle tracking". In: *Phys. Rev. A* 98 (5 2018), p. 053813 (cited on page 76).

[100] Mechlem, K., Sellerer, T., Viermetz, M., Herzen, J., Pfeiffer, F., "Spectral differential phase contrast x-ray radiography". In: *IEEE Transactions on Medical Imaging* 39 (3 2020), pp. 578–587 (cited on page 76).

[101] Sellerer, T., Mechlem, K., Tang, R., Taphorn, K., Pfeiffer, F., Herzen, J., "Dual-energy x-ray dark-field material decomposition". In: (2020) (cited on page 76).

Appendices

A

Article illustrating Part I Motion in cone-beam computed tomography

This appendix contains a copy of [J37]:

Mory, C., Janssens, G., **Rit, S.,** "Motion-aware temporal regularization for improved 4D cone-beam computed tomography". In: *Phys Med Biol* 61.18 (2016), pp. 6856–6877

IOP Publishing | Institute of Physics and Engineering in Medicine Physics in Medicine & Biology

Phys. Med. Biol. **61** (2016) 6856–6877 doi:10.1088/0031-9155/61/18/6856

Motion-aware temporal regularization for improved 4D cone-beam computed tomography

Cyril Mory[1,2], Guillaume Janssens[3] and Simon Rit[2]

[1] iMagX Project, ICTEAM Institute, Université Catholique de Louvain, Louvain-la-Neuve, Belgium
[2] Université de Lyon, CREATIS; CNRS UMR5220; Inserm U1044; INSA-Lyon; Université Lyon 1; Centre Léon Bérard, France
[3] Ion Beam Applications SA, Louvain-La-Neuve, Belgium

E-mail: simon.rit@creatis.insa-lyon.fr

Received 23 February 2016
Accepted for publication 1 July 2016
Published 2 September 2016

Abstract

Four-dimensional cone-beam computed tomography (4D-CBCT) of the free-breathing thorax is a valuable tool in image-guided radiation therapy of the thorax and the upper abdomen. It allows the determination of the position of a tumor throughout the breathing cycle, while only its mean position can be extracted from three-dimensional CBCT. The classical approaches are not fully satisfactory: respiration-correlated methods allow one to accurately locate high-contrast structures in any frame, but contain strong streak artifacts unless the acquisition is significantly slowed down. Motion-compensated methods can yield streak-free, but static, reconstructions. This work proposes a 4D-CBCT method that can be seen as a trade-off between respiration-correlated and motion-compensated reconstruction. It builds upon the existing reconstruction using spatial and temporal regularization (ROOSTER) and is called motion-aware ROOSTER (MA-ROOSTER). It performs temporal regularization along curved trajectories, following the motion estimated on a prior 4D CT scan. MA-ROOSTER does not involve motion-compensated forward and back projections: the input motion is used only during temporal regularization. MA-ROOSTER is compared to ROOSTER, motion-compensated Feldkamp–Davis–Kress (MC-FDK), and two respiration-correlated methods, on CBCT acquisitions of one physical phantom and two patients. It yields streak-free reconstructions, visually similar to MC-FDK, and robust information on tumor location throughout the breathing cycle. MA-ROOSTER also allows a variation of the lung tissue density during the breathing cycle, similar to that of planning CT, which is required for quantitative post-processing.

0031-9155/16/186856+22$33.00

Keywords: tomography, cone-beam, radiotherapy, 4D, motion, thorax

S Online supplementary data available from stacks.iop.org/PMB/61/6856/mmedia

(Some figures may appear in colour only in the online journal)

1. Introduction

State-of-the-art radiotherapy strategies for the treatment of thoracic and upper-abdominal tumors take the patient's breathing motion into account. The clinical workflow is currently the following: the patient first undergoes a four-dimensional (4D) computed tomography (CT) scan, from which doctors determine the treatment plan (Wolthaus *et al* 2008). This plan takes into account, among many parameters, the patient's breathing motion pattern. Treatment is then delivered with a radiotherapy device that can combine a high-energy x-ray beam for tumor treatment and cone-beam CT (CBCT) for pre-treatment imaging, both mounted on the same gantry (Jaffray *et al* 2002). On the treatment day, the patient lies down on the table of the radiotherapy device and a CBCT acquisition can be performed. The CBCT image is used to re-position the table, so as to match the patient position as closely as possible with that of the planning CT. When the CBCT image is reconstructed in three dimensions (3D), it is implicitly assumed that the patient's breathing motion does not change much throughout the treatment and remains close to what it was during the planning 4D CT. Unfortunately, this assumption can be wrong, e.g. if a large tumor shrinks under the effect of radiation, partly restoring the patient's respiratory function. Replacing the 3D with a 4D reconstruction from the same data would allow the clinicians to check whether the patient's breathing motion on the treatment day matches that of the planning CT. If the motions do not match, corrective actions, e.g. re-planning, could be taken, hence improving the radiotherapy.

The methods currently available to reconstruct a CBCT acquisition of a moving object can roughly be divided into four classes:

- Respiration-correlated reconstruction techniques, which reconstruct one 3D frame at a time and concatenate the results to obtain a 4D reconstruction. These techniques include the respiration-correlated versions of the Feldkamp–Davis–Kress (FDK) (Feldkamp *et al* 1984, Sonke *et al* 2005) and simultaneous algebraic reconstruction (Andersen and Kak 1984, Mory *et al* 2014) techniques, as well as 3D regularized reconstruction methods (Leng *et al* 2008, Sidky and Pan 2008, Bergner *et al* 2010). 4D reconstruction techniques that do not perform regularization along time also fall into this category. These methods allow one to accurately locate high-contrast structures throughout the breathing cycle, but each frame has low image quality, due to either streak artifacts, blurring or over-regularization, unless the scanner is slowed down to improve the sampling of cone-beam projections in each 3D frame (Sonke *et al* 2005).
- Classical motion-compensated reconstruction techniques, which use an *a priori* motion estimation (Li *et al* 2007, Rit *et al* 2009a, 2009b, 2011) to back-project along curved trajectories. These methods reconstruct one frame from all projections and yield a static reconstruction, which is only as good as the motion estimation used in the input.
- Joint motion-estimation and motion-compensated reconstruction methods, which estimate the motion directly from the CBCT data (Brehm *et al* 2012, Wang and Gu 2013a, 2013b, Liu *et al* 2015) and perform a motion-compensated reconstruction. The 3D static reconstruction obtained can then be animated with the estimated CBCT motion. These approaches are valid alternatives to the one we propose, although they share a limitation

with the classical motion-compensated reconstruction techniques: the variation of the linear attenuation of lung tissue along the breathing cycle cannot be estimated from such reconstructions.

- Regularized 4D reconstruction techniques, which reconstruct the whole cycle at once, making use of all the projection data, and enforce some similarity between consecutive frames by regularizing along time (Jia *et al* 2010, Ritschl *et al* 2012, Wu *et al* 2012, Mory *et al* 2014).

The proposed method, is halfway between the second and the fourth category. It builds upon the existing reconstruction using spatial and temporal regularization (ROOSTER) and is called motion-aware ROOSTER (MA-ROOSTER). The only change with respect to ROOSTER is that temporal regularization is performed along curved trajectories, following an *a priori* motion estimation computed from the planning 4D CT scan, instead of straight trajectories. In this work, we compare MA-ROOSTER to ROOSTER, to illustrate the benefits of motion-aware over straight regularization, and MA-ROOSTER to motion-compensated FDK (MC-FDK), both with an accurate and an inaccurate *a priori* motion estimation, to prove that MA-ROOSTER indeed shows some robustness to erroneous input motion, while MC-FDK does not. On phantom data, we evaluate the effect of the temporal regularization parameter on the robustness to erroneous input motion, using respiration-correlated reconstructions as references. Then we show reconstruction results with ROOSTER, MA-ROOSTER and MC-FDK on two clinical datasets. Finally, we compare the variations of lung tissue attenuation during the breathing cycle in a MA-ROOSTER reconstruction and in 4D planning CT, and show that they are consistent with each other.

2. Materials and methods

Throughout the paper, we shall use the word ‘frame’ to denote a 3D volume of a 4D sequence. In other contributions, such 3D volumes are often referred to as ‘phases’, but the ‘phase’ also denotes the real number in [0;1], defined as the relative position between two consecutive end-inhales. For simplicity, we shall also refer to ‘the frame representing the patient’s body at phase 50%’ as ‘frame 50%’.

2.1. Respiration-correlated FDK

A 4D reconstruction can be obtained by concatenating 3D respiration-correlated FDK reconstructions (Sonke *et al* 2005, Lu *et al* 2007, Bergner *et al* 2010). The 4D reconstruction contains severe streak artifacts but can serve as a reference to estimate the motion of a high-contrast object like a tumor. Throughout this paper, it is either called respiration-correlated FDK or simply 4D FDK.

2.2. Motion-compensated FDK

The most straightforward approach when a 4D displacement vector field (DVF) is available is to compute a 3D motion-compensated FDK (MC-FDK), performed in this paper as described in (Rit *et al* 2009a, 2009b). It belongs to the ‘classical motion-compensated reconstruction techniques’ described in the introduction. The DVF extracted from the planning CT allows one to warp all frames of the respiratory cycle to the end-exhale frame. By performing an MC-FDK using this DVF, we obtain a motion-compensated 3D reconstruction of the end-exhale frame. The more accurate the DVF, the sharper and better contrasted the reconstruction.

MC-FDK is a 3D reconstruction technique: it reconstructs a single frame, and does not provide any information on the way the tumor actually moves. Therefore, it cannot be used to check whether the patient's breathing motion of the treatment day matches that of the planning CT. We use it in this paper only as a reference for visual comparison to evaluate image quality. Note that with a null DVF, MC-FDK boils down to the blurry static FDK.

2.3. 4D conjugate gradient

The 4D conjugate gradient (CG) method reconstructs a sequence of volumes from a single stack of projections through a convex optimization approach. It consists in minimizing the single-term cost function $\sum_\alpha \left\| R_\alpha S_\alpha f - p_\alpha \right\|_2^2$ by the linear CG algorithm, where

- $\|.\|_2$ is the $\ell 2$ norm.
- α is the projection index.
- f is a 4D sequence of volumes.
- R_α is the forward projection operator at index α. It maps a 3D frame onto a 2D projection image.
- S_α is an interpolator along the time dimension. In this study, S is a linear interpolator. It maps a 3D + time sequence onto a 3D frame, using the respiratory phase of projection α. For example, if f contains ten frames ($f_0, f_1, f_2 ...$) and projection α has been acquired at phase 0.87, then $S_\alpha f = 0.3 f_8 + 0.7 f_9$.
- p_α is the measured projection with index α.

The 4D CG reconstructions are blurry and contain streak artifacts, but provide reliable information on the motion of objects that are not hidden by the streaks, e.g. large tumors or high-contrast structures. The ROOSTER method builds upon 4D CG, adding some regularization steps.

2.4. The ROOSTER method

ROOSTER is a recent iterative reconstruction method alternating between several optimization goals (Mory *et al* 2014). It assumes that a motion mask, i.e. a rough segmentation of the region where movement is expected to occur, is available. As motion can occur outside the lungs, since the rib cage and the abdomen move during breathing, we used the motion mask extracted from the 4D planning CT (Vandemeulebroucke *et al* 2012), dilated by morphological operations in order to include the ribs. ROOSTER consists in solving the following five subproblems at each iteration of the main loop:

- Minimizing the data-attachment term $\sum_\alpha \left\| R_\alpha S_\alpha f - p_\alpha \right\|_2^2$, by 4D CG.
- Enforcing positivity, by setting all negative voxels of f to zero.
- Removing motion where it is not expected to occur, by averaging along time outside the motion mask.
- Enforcing the spatial gradient's sparsity in each frame using 3D total variation (TV) denoising.
- Enforcing the temporal gradient's sparsity for each spatial position, by one-dimensional (1D) TV denoising along time.

Each supbroblem's output is used as the input for the next subproblem. This constitutes one iteration of the main loop, the output of which is fed back to the CG minimizer for the next iteration.

TV denoising is here intended in its convex optimization sense, i.e. applying TV denoising on f_{noisy} yields $f_{\text{denoised}} = \arg\min_u \left\|u - f_{\text{noisy}}\right\|_2^2 + \gamma TV(u)$, where parameter γ controls the strength of the TV regularization (the higher, the stronger the regularization). In convex optimization literature, TV denoising is also referred to as the 'proximal operator' of TV (Boyd and Ye 2011). ROOSTER makes use of 3D TV for spatial denoising of each frame (with strength parameter γ_{space} and of 1D temporal TV for temporal denoising between frames (with strength parameter γ_{time}). They are defined as follows:

$$TV_{\text{space}}(u) = \|\sqrt{(\nabla_x u)^2 + (\nabla_y u)^2 + (\nabla_z u)^2}\,\|_1 \tag{1}$$

and similarly

$$TV_{\text{time}}(u) = \|\nabla_t u\|_1 \tag{2}$$

where $\nabla_x, \nabla_y, \nabla_z$ and ∇_t are the gradient operators along the spatial axes x, y, z and along the time axis t, respectively, and $\|.\|_1$ is the $\ell 1$ norm. In both spatial 3D and temporal 1D TV denoising, the minimization is performed by the basis pursuit dequantization algorithm (Jacques *et al* 2010).

2.5. Motion-active ROOSTER

Through a breathing cycle, a given spatial location can contain tissues within a large range of linear attenuation coefficients, e.g. lung tissues and blood vessels. In this case, regularization along time as performed in ROOSTER enforces similarity between unrelated objects. As a result, it can smooth away the small moving structures and the high-intensity structures of one frame can partially spread out to the previous and next frames. The diaphragm, small structures in the lungs and lung tumors seem to gradually fade from one position to another, while they should have sharp edges and a distinct position on every frame. This effect can partly be explained by noting that, while TV is often said to favor piecewise-constant functions, the 1D TV of a monotonic function is exactly the same as the 1D TV of a step function with the same lower and upper bounds. 1D TV therefore favors piecewise-monotonic functions, not only piecewise-constant functions. When used to regularize along time, it can cause the above-described blurring effect between consecutive frames. To tackle this issue, one could try to find a better regularizer along time than 1D TV, e.g. based on the $\ell 0$ norm of the temporal gradient. In the MA-ROOSTER algorithm, we have chosen to circumvent the problem by bending the regularization trajectories, so as to follow the moving structures.

As explained in the introduction, lung cancer patients undergo a 4D CT at the beginning of the radiotherapy, on which their treatment is planned. From the 4D planning CT, a 4D DVF can be estimated, which maps the end-exhale frame to each other frame. The method by which the DVF estimation is performed has little importance for MA-ROOSTER, only the DVF itself matters. Since this *a priori* motion estimation is available, we propose improving ROOSTER by performing temporal regularization along curved trajectories following the motion. This is illustrated in figure 1. Note that it is mathematically equivalent, but much easier to implement, to first warp all frames onto the end-exhale frame by 'backward mapping' (see chapter 10.2 of Moeslund (2012)), and then to apply straight regularization along time on the warped sequence. The regularized frames must then be inverse-warped to their original phase (see section 2.6). Note that trilinear interpolation-based image warping is a linear process, and can therefore be described by a matrix. To describe the MA-ROOSTER temporal regularization in a formal way, assuming that we reconstruct a sequence f of ten frames, let

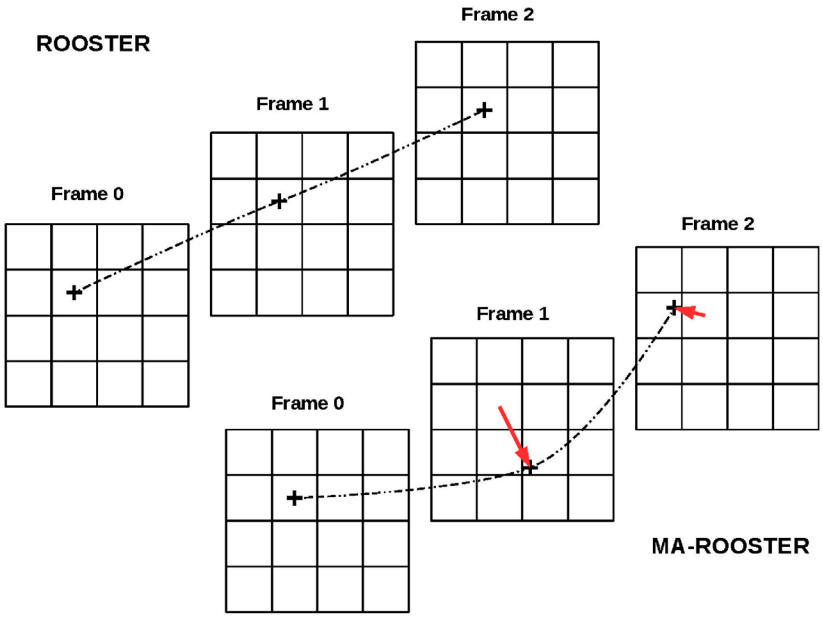

Figure 1. Illustration of the voxel selection for temporal regularization. Top: the behavior of ROOSTER, select in each frame the voxel that is located at a fixed spatial position. Bottom: behavior of MA-ROOSTER, follow the trajectory of the voxel, given by the input DVF. The red arrows are the vectors of the input DVF.

- N be the number of voxels in a 3D frame.
- $f_{\text{noisy}} = \begin{pmatrix} f_0 \\ \vdots \\ f_9 \end{pmatrix}$ be the sequence to regularize, with $f_j \in \mathbb{R}^N, j \in \{0..9\}$ the individual frames
- $W = \begin{pmatrix} W_0 & & 0 \\ & \ddots & \\ 0 & & W_9 \end{pmatrix}$ be the 4D warping operator, with $W_j : \mathbb{R}^N \to \mathbb{R}^N, j \in \{0..9\}$ the 3D warping operators for each frame.
- $Wf_{\text{noisy}} = \begin{pmatrix} W_0 f_0 \\ \vdots \\ W_9 f_9 \end{pmatrix}$ be the warped sequence (each 3D frame in f is warped independently).
- D_{time} be the TV denoising along time operator (note that D_{time} is not linear).
- $D_{\text{time}}(Wf_{\text{noisy}})$ be the denoised warped sequence.

Then $f_{\text{denoised}} = W^{-1} D_{\text{time}}(Wf_{\text{noisy}})$ is the denoised and inverse-warped sequence, which will be used as input for the next main loop iteration of MA-ROOSTER.

An inverse DVF can only be obtained when the DVF is diffeomorphic (Arsigny *et al* 2006). And even when a diffeomorphic DVF and its inverse are available, the associated warping operators are not the exact inverse of one another, because of interpolation errors. Since inverting W in reasonable time is impossible, we will always use the warping operator associated with the inverse DVF, which from a strict linear algebra standpoint is an approximation of W^{-1}. Nevertheless, by an abuse of notation, we will write W^{-1} to denote it. Details on how to mitigate the effects of using an imperfect W^{-1} are given in section 2.6. Note that a null DVF

results in $W = W^{-1} = I$, i.e. in temporal regularization along straight lines as in ROOSTER. ROOSTER can therefore be seen as a specific case of MA-ROOSTER with a null DVF. Intuitively, this means that MA-ROOSTER should yield better results than ROOSTER as soon as the DVF is better than null, even when it does not perfectly describe the real displacement.

The temporal regularization enforces a trade-off between the motion present in the projection data and the one described by the input DVF. It discourages deviating too far from the input motion, but does not prevent it. MA-ROOSTER is thus expected to show some robustness to motion estimation inaccuracies. The temporal regularization also discourages variations in lung tissue attenuation during the breathing cycle, but does not prevent them. The attenuation of lung tissue in MA-ROOSTER reconstructions is therefore expected to vary slowly throughout the breathing cycle, as a result of the air and blood flows in the lungs.

2.6. Inverse warping

Some motion estimation methods, including the one we used, provide two so-called 'inverse-consistent' DVFs (Christensen and Johnson 2001, Janssens *et al* 2011, Wang and Gu 2013b). Let W and W^{-1} be their associated warping operators. They are approximately the inverse of each other. In practice, $\hat{f} = W^{-1}Wf$ is a blurry approximation of f, since it has undergone two trilinear interpolations, one contained in W, the other one in W^{-1}. With a small trick, however, the blurring can be limited. We compute f_{denoised} as follows:

$$\begin{aligned} f_{\text{denoised}} &\approx W^{-1}D_{\text{time}}(Wf_{\text{noisy}}) \\ &\approx W^{-1}(D_{\text{time}}(Wf_{\text{noisy}}) - Wf_{\text{noisy}} + Wf_{\text{noisy}}) \\ &= W^{-1}(D_{\text{time}}(Wf_{\text{noisy}}) - Wf_{\text{noisy}}) + f_{\text{noisy}} \end{aligned} \tag{3}$$

In equation (3), $D_{\text{time}}(Wf_{\text{noisy}}) - Wf_{\text{noisy}}$ is the correction brought by regularization along time to Wf_{noisy}. Restricting the approximate inverse warping by W^{-1} to that correction allows one to avoid blurring f_{noisy}.

MA-ROOSTER can also handle the case where only a single DVF is available, i.e. the motion estimation method used does not provide the inverse DVF. The inverse warping in that case relies on convex optimization, and has been described in Mory and Rit (2015).

2.7. Metrics

Since the main purpose of MA-ROOSTER is to provide a 4D reconstruction on which tumor motion can be measured, we have designed a quantitative metric to measure tumor motion. A secondary objective is to yield a reconstruction that is close, in terms of 'image quality', to what doctors are used to in 3D (i.e. FDK), and which contains as few streak artifacts as possible, so as not to hamper visual interpretation. This secondary objective being both quite vague and extremely difficult to quantify with metrics, in particular on patient data (McCollough *et al* 2012), we have chosen to leave it to visual evaluation.

The motion of tumors throughout the breathing cycle was measured as follows:

- A small region of interest (ROI) containing the full trajectory of the tumor was delineated manually. The ROI is static, and in any frame the whole tumor is inside the ROI.
- Each frame was cropped to keep only the ROI. A translation-only motion was estimated between each cropped frame and the end-exhale cropped frame, using the open-source software Elastix, with the mean squared difference as a similarity measure, and a pyramid of four resolutions.

- The Euclidian norm of the obtained 3D translation vector was computed and is reported in graphs (see figures 4, 6, 8, 10 and 12).

2.8. Table subtraction

FDK can be used to reconstruct any voxel contained in the field of view, independent of the others. The reconstructed volume can therefore be a small part of the attenuating object. Optimization-based tomography methods, on the other hand, require the reconstructed volume to fully contain the object (Ziegler *et al* 2008). In other words, the reconstructed volume should be large enough so that any object appearing in the measured projections lies inside it. If this requirement is not met, overshoot appears on the borders of the reconstructed volume, which then causes streak artifacts once back-projected, and the reconstruction quickly diverges. In some radiation therapy centers, patients lie in a stereotactic body frame (SBF), which is typically much larger than them. Setting the reconstructed volume to be large enough to contain the SBF could increase the computation time and memory footprint by a factor of 4 or more, which is unacceptable for MA-ROOSTER. The SBF therefore has to be removed from the projections before reconstruction. To this end, we performed a static 3D reconstruction of the full volume (patient + SBF + table), masked out the patient, forward projected through the residual 3D volume (SBF + table) and subtracted the result from the original projections. The corrected projections were then used for reconstruction. This simple pre-processing, very close to the one proposed in Ziegler *et al* (2008), proved sufficient to reconstruct a volume as small as possible, containing only the patient, without generating overshoot and streak artifacts.

2.9. Physical phantom data

Since the patient's breathing motion of the day can differ from the one estimated on the 4D planning CT, it is important to evaluate whether MA-ROOSTER can handle inexact input motion information, and how errors in its input DVF, extracted from the 4D planning CT, propagate to the 4D CBCT reconstruction. MA-ROOSTER should theoretically show some robustness to such errors. To evaluate this robustness, we performed reconstructions with both underestimated and overestimated DVFs.

Acquisitions were performed on a 4D thorax phantom built at the Université Catholique de Louvain (UCL), and shown on figure 2. The phantom's diaphragm has a controllable motion period and amplitude, and can be stopped at specific positions. An insert was added close to the diaphragm, simulating a small tumor. The figures focus on slices extracted from the end-exhale phase, but each MA-ROOSTER reconstruction is a 4D sequence of eight volumes of size $244 \times 284 \times 308$, with isotropic 1 mm voxel size, representing the whole breathing cycle. We performed two dynamic acquisitions with either an 18 mm or a 9 mm amplitude in diaphragm motion on the cranio–caudal axis, and ten fixed acquisitions, with the 'diaphragm' at the following positions : 0, 2, 4, 6, 8, 10, 12, 14, 16 and 18 mm. The fixed acquisitions were reconstructed with the FDK algorithm (Feldkamp *et al* 1984), then arranged in two sequences to simulate 4D planning CTs. The first sequence was $\{0, 2, 4, 6, 8, 10, 8, 6, 4, 2\}$ and the second $\{0, 2, 4, 6, 8, 10, 12, 14, 16, 18, 16, 14, 12, 10, 8, 6, 4, 2\}$. From each of these fake 4D CT sequences, a pair of inverse-consistent DVFs was estimated using the method described in Janssens *et al* (2011). MA-ROOSTER's implementation can handle DVFs of an arbitrary number of frames (not necessarily the same as the number of reconstructed frames in f), by interpolating along time if required. The DVF-pair extracted from the first sequence describes a 10 mm amplitude motion, whereas the one extracted from the second sequence describes an 18 mm amplitude motion.

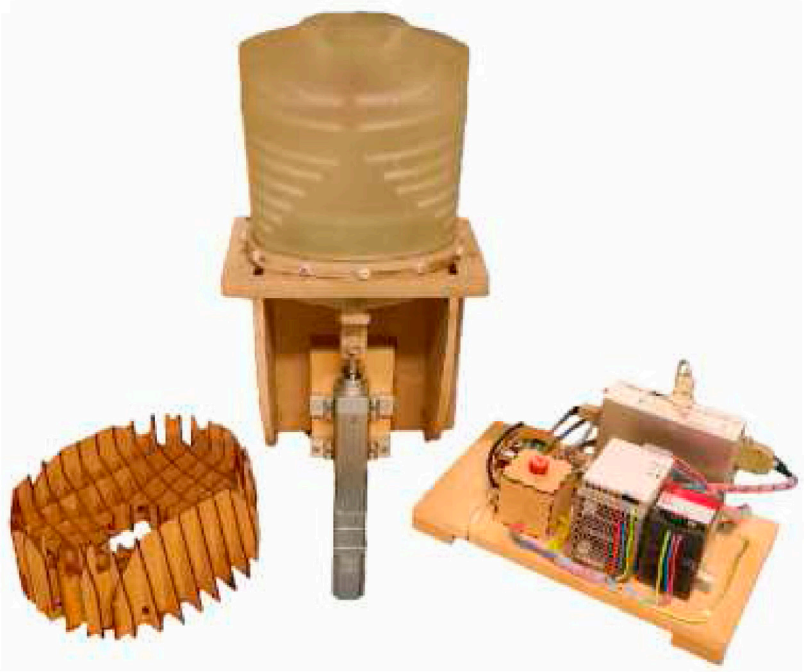

Figure 2. Photograph of the 4D thorax phantom. From left to right: support grid, actual thorax phantom with its hydraulic cylinder and electronic control board.

Note that these are the amplitudes for the motion of the diaphragm. The motion of the insert we placed on top of the diaphragm is of slightly lower amplitude, and the motion of the structures near the neck is of much lower amplitude, since the lungs are made of compressible foam.

Three experiments were conducted:

- Reconstructing the acquisition with 18 mm amplitude motion using the 18 mm amplitude DVF (correct motion).
- Reconstructing the acquisition with 18 mm amplitude motion using the 10 mm amplitude DVF (underestimated motion).
- Reconstructing the acquisition with 9 mm amplitude motion using the 18 mm amplitude DVF (overestimated motion).

In both ROOSTER and MA-ROOSTER, the γ_{time} parameter controls the trade-off between the attachment to the projection data and the attachment to the input DVF: $\gamma_{\text{time}} = 0$ means no regularization along time, i.e. the motion in the reconstruction is only the result of the motion in the projection data (desirable), but it also means a lot of streak artifacts (not desirable). On the other hand, $\gamma_{\text{time}} = +\infty$ means no streaks (desirable), but a strict attachment to the input DVF (not desirable). In the case of ROOSTER, the input DVF is null, so $\gamma_{\text{time}} = +\infty$ means no motion. Setting γ_{time} to obtain robustness to errors in the input DVF and high image quality, i.e. good contrast, sharp structures and few streaks, therefore requires a few trials. In radiotherapy, the primary goal of a 4D CBCT is to determine the real motion of the tumor, so for this application γ_{time} should be set to a small value, even if it means leaving some streaks in the image. In addition to evaluating the robustness of MA-ROOSTER to erroneous input motion information, the results presented in this section suggest a way to determine a suitable γ_{time} experimentally: acquire or generate projections of a moving phantom with known motion, perform several reconstructions with incorrect input motion and different values of γ_{time}, and

choose a value sufficiently low to yield robustness to erroneous input motion. In each experiment, four different values of γ_{time} were tested.

2.10. Clinical data

2.10.1. 4D planning CT. For both patients, the planning CT, from which the 4D DVF was extracted, has been acquired on a brilliance big bore 16-slice 4D CT scanner (Philips Medical Systems, Cleveland, OH). Each frame of this 4D CT is a $512 \times 512 \times 170$ voxel volume, with a voxel size of $0.88 \times 0.88 \times 2$ mm (the last dimension is the cranio–caudal axis). As with the phantom, for each patient a pair of inverse-consistent DVFs was estimated on the 4D planning CT using the method described in Janssens *et al* (2011).

2.10.2. CBCT data. Two CBCT acquisitions performed on different patients were reconstructed. Each one contains approximately 635 projections, each made of 512×512 pixels of size 0.8×0.8 mm. They have been acquired on an Elekta Synergy CBCT, along a 360 degrees trajectory, at 5.48 frames per second, using an off-center detector (Cho *et al* 1996) to enlarge the field of view. All 4D methods were set to reconstruct the respiratory cycle as a sequence of ten volumes. The size of the reconstructed volumes depends on the patient's size. It was $220 \times 280 \times 370$ voxels for patient 1, and $285 \times 270 \times 307$ voxels for patient 2, both with isotropic voxels of $1\,\text{mm}^3$.

2.10.3. Parameters. In both ROOSTER and MA-ROOSTER, γ_{space} was set to the same value as for the phantom study, i.e. $\gamma_{\text{space}} = 0.000\,05$. An animated GIF sequence available in the supplementary material shows that $\gamma_{\text{space}} = 0.0001$ leads to over-regularization (stacks.iop.org/PMB/61/6856/mmedia). As a rule of thumb, a regularization parameter should be set to the highest value that does not cause adverse effects, so we have set $\gamma_{\text{space}} = 0.000\,05$, which is close to the limit. γ_{time} was set to the value taken from the phantom study, to obtain robustness to erroneous input motion and limited streak artifacts removal, i.e. $\gamma_{\text{time}} = 0.0002$. The supplementary material also contains an animated GIF sequence showing the results obtained with a large number of different γ_{time} parameters (patient2_gamma_time.gif). Two other animated GIF sequences, with the same layout as figures 9 and 11, show the reconstructions of patients 1 and 2 through a full breathing cycle (patient1.gif and patient2.gif, respectively).

2.10.4. Reference. On clinical data, no ground truth of the DVF is available. The DVF estimated on the 4D planning CT may not be an accurate estimate of the patient's breathing motion on treatment days, especially if morphological changes, e.g. tumor shrinkage or atelectasis evolution, have occurred in the meantime. As a workaround, we propose using two respiration-correlated reconstructions, 4D FDK and 4D CG, as references for the motion of high-contrast structures (the low-contrast ones are either blurred or hidden by under-sampling artifacts). Since we extracted similar motion information from both of these unregularized reconstructions, we have assumed that this motion information was cross-validated and trustworthy.

3. Results

3.1. On a physical phantom

3.1.1. Correct motion. Figure 3 shows ROOSTER, MA-ROOSTER and MC-FDK reconstructions of the phantom with four different values of γ_{time}. The acquisition was performed with 18 mm amplitude motion, and the DVF used for the MA-ROOSTER and MC-FDK

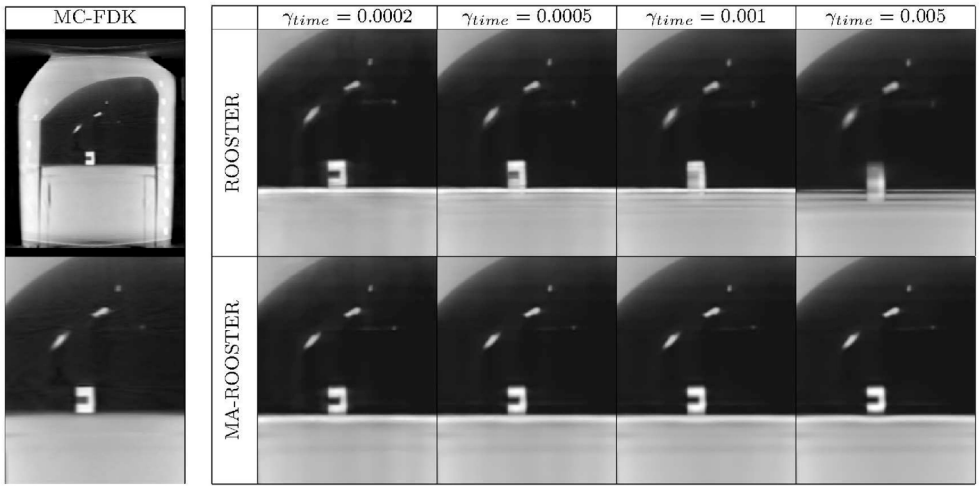

Figure 3. MC-FDK (full volume and zoom in), ROOSTER and MA-ROOSTER (zoom in) reconstructions of the UCL 4D phantom, with several values of the temporal regularization parameter. The real motion amplitude is 18 mm, and so is the motion amplitude in the input DVF.

reconstructions represents that motion. Note that ROOSTER does not make use of the DVF. When γ_{time} is high, MA-ROOSTER yields sharper results that ROOSTER, which is not surprising given the additional information it has made use of. Also, the MA-ROOOSTER and MC-FDK reconstructions have comparable image quality: when the input DVF is accurate, both MA-ROOSTER and MC-FDK perform well.

Figure 4 contains two graphs which show the amplitude of the insert's motion measured in the MA-ROOSTER reconstructions (on the left) and in the ROOSTER reconstructions (on the right), as well as on the 4D-FDK reconstruction (on both). The ideal profile, i.e. the one that shows perfect robustness to erroneous input motion information, is the dotted black line of the 4D-FDK. In this case, with various values of γ_{time}, the insert's position in the MA-ROOSTER reconstructions does not differ from the reference position by more than 1 mm. On the other hand, as γ_{time} increases, the motion amplitude in the ROOSTER reconstruction decreases: a higher γ_{time} means a stricter attachment to the input DVF, which for ROOSTER consists in null motion.

3.1.2. Underestimated motion. Figure 5 shows ROOSTER, MA-ROOSTER and MC-FDK reconstructions of the phantom with four different values of γ_{time}. The acquisition was performed with 18 mm amplitude motion, and the DVF used for the MA-ROOSTER and MC-FDK reconstructions only represents 10 mm amplitude motion. Since ROOSTER does not make use of the DVF, the ROOSTER results are the same as in figure 3. When γ_{time} is high, MA-ROOSTER still yields sharper results than ROOSTER, which confirms that MA-ROOSTER should yield better results than ROOSTER as soon as the DVF is closer to the real motion than a null DVF (see section 2.5). With a small value of γ_{time}, MA-ROOOSTER yields a much sharper reconstruction than MC-FDK: correctly tuned, MA-ROOSTER shows some robustness to errors in the DVF, while MC-FDK does not.

Figure 6 shows the amplitude of the insert's motion measured in the MA-ROOSTER reconstructions and in a 4D-FDK reconstruction. With a small value of γ_{time}, both ROOSTER and MA-ROOSTER yield an accurate reconstruction of the motion pattern. With higher values of γ_{time}, both methods tend to a stricter attachment to their input DVF. Since the one

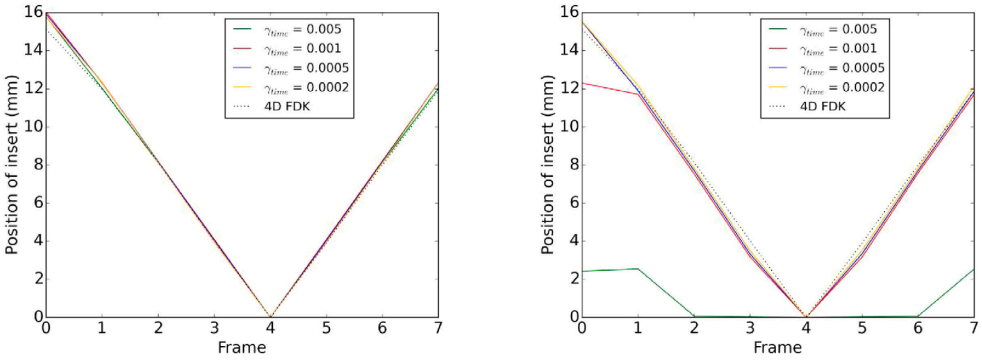

Figure 4. Detected position of the moving insert in the MA-ROOSTER reconstructions (on the left) and in the ROOSTER reconstructions (on the right) with correct input motion. The 4D FDK is used as a reference.

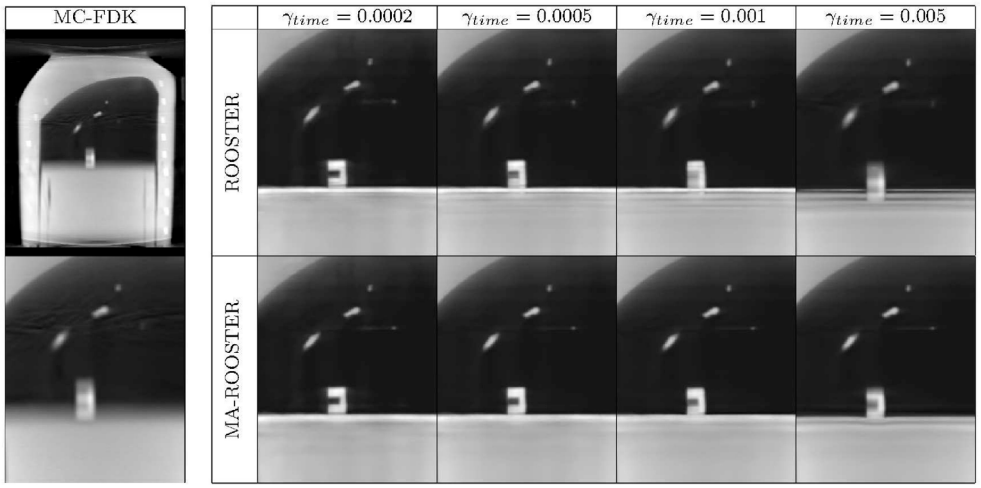

Figure 5. ROOSTER, MA-ROOSTER and MC-FDK reconstructions of the UCL 4D phantom, with several values of the temporal regularization parameter. The real motion amplitude is 18 mm, but the input DVF only models 10 mm amplitude motion.

used in MA-ROOSTER is closer to reality than the null motion assumed by ROOSTER, MA-ROOSTER performs better in that case.

3.1.3. Overestimated motion. Figure 7 shows ROOSTER, MA-ROOSTER and MC-FDK reconstructions of the phantom with four different values of γ_{time}. The acquisition was performed with 9 mm amplitude motion, and the DVF used for the MA-ROOSTER and MC-FDK reconstructions represents 18 mm amplitude motion. Again, ROOSTER does not make use of the DVF, but the ROOSTER results are different from those in figures 3 and 5 since the projection data have changed. This time, even with γ_{time} high, there is no clear ranking between MA-ROOSTER, which assumes a motion of amplitude 18 mm, and ROOSTER, which assumes a motion of amplitude 0 mm (the real motion amplitude is 9 mm). This observation is consistent with the statement in section 2.5: if the MA-ROOSTER's input DVF is not a better estimate of the real motion than a null DVF, there is

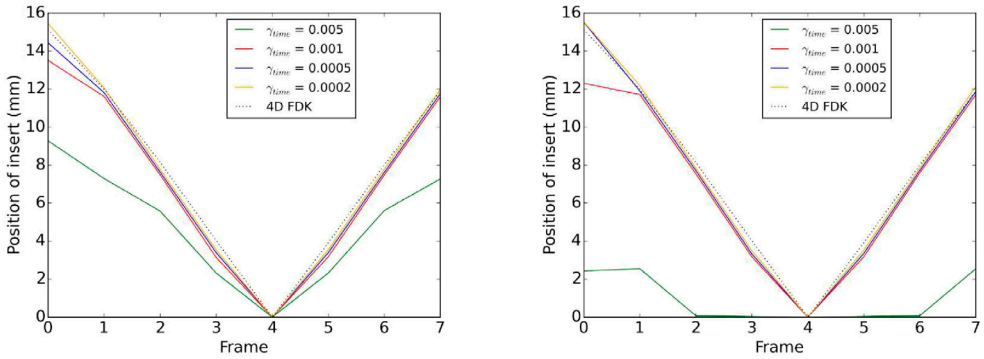

Figure 6. The detected position of the moving insert in the MA-ROOSTER reconstructions (on the left) and in the ROOSTER reconstructions (on the right) with underestimated input motion. The 4D FDK is used as a reference.

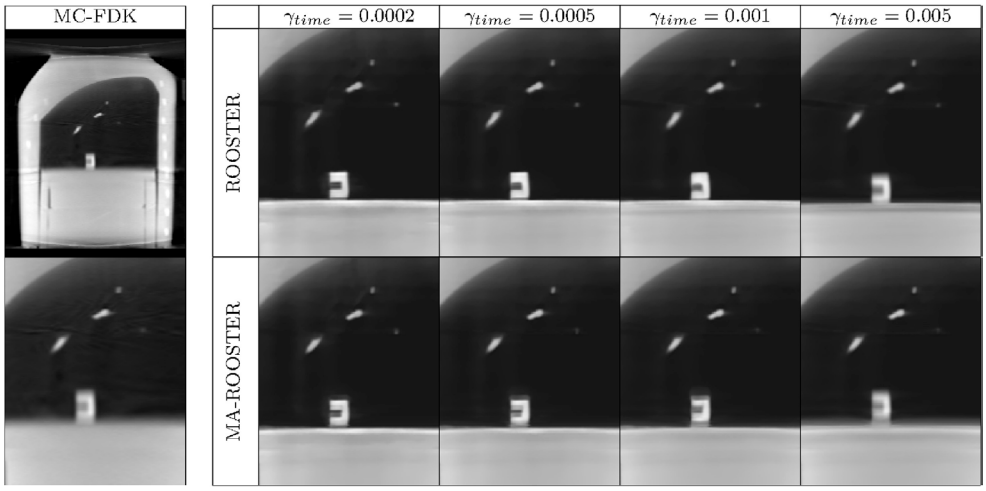

Figure 7. ROOSTER, MA-ROOSTER and MC-FDK reconstructions of the UCL 4D phantom, with several values of the temporal regularization parameter. The real motion amplitude is 9 mm, but the input DVF models 18 mm amplitude motion.

no reason why MA-ROOSTER should yield better results than ROOSTER. Similarly, as in figure 5, with a small value of γ_{time} MA-ROOOSTER yields a much sharper reconstruction than MC-FDK.

Figure 8 shows the amplitude of the insert's motion measured in the MA-ROOSTER reconstructions and in a 4D-FDK reconstruction. The ROOSTER results allow one to locate the tumor more precisely than MA-ROOSTER ones. In this case, assuming an overestimated motion (MA-ROOSTER) is worse than assuming null motion (ROOSTER). Such a situation, however, is very unlikely to occur in a clinical context.

3.2. On patients

As explained in section 2.5, the temporal regularization enforces a trade-off between the motion present in the projection data and the one described by the input DVF. Since in

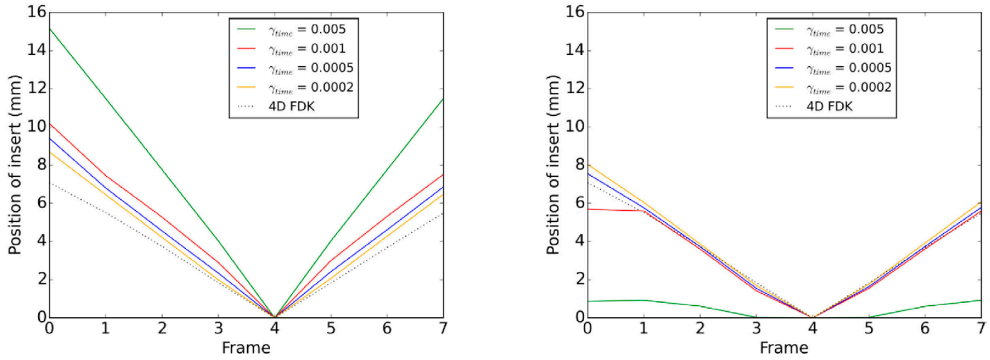

Figure 8. Detected position of the moving insert in the MA-ROOSTER reconstructions (on the left) and in the ROOSTER reconstructions (on the right) with overestimated input motion. The 4D FDK is used as a reference.

radiotherapy one of the the primary goals of 4D CBCT is to compare the breathing motion of the treatment day with that of the planning CT, we recommend seting γ_{time} to stick to the motion of the projection data. From the phantom study, $\gamma_{\text{time}} = 0.0002$ seems the safest choice, and $\gamma_{\text{time}} = 0.0005$ would be 'strong but acceptable' regularization. We have chosen $\gamma_{\text{time}} = 0.0002$. In other applications where motion evaluation is less critical, e.g. cardiac road-mapping (Knecht *et al* 2008), γ_{time} could be set to a higher value.

3.2.1. Patient 1. Figure 9 shows sagittal and coronal slices of the reconstructions obtained using 4D FDK, 4D CG, ROOSTER and MA-ROOSTER on patient 2, at the end-inhale (rows 1 and 3) and end-exhale (rows 2 and 4) phases. MC-FDK should show the end-exhale since the reference image of the DVF is the end-exhale. The small moving structures in the lungs are better contrasted in the MA-ROOSTER reconstruction than in the ROOSTER one, in particular on the end-inhale frame.

In terms of the contrast and sharpness of small structures, MA-ROOSTER does much better than 4D CG and 4D FDK, but still has some streaks that are absent from the MC-FDK (e.g. around the ribs). We recall that the MC-FDK is used only as a reference for image quality, since it cannot provide information on the motion on the treatment day.

Figure 10 shows the tumor motion throughout the breathing cycle, measured as described in section 2.7. Mostly, it is cranio–caudal motion, but in some patients (not here) the tumor may also undergo high-amplitude antero–posterior motion. The reference motion amplitude, i.e. the difference between tumor position at end-inhale and end-exhale, measured on both unregularized 4D reconstructions, differs from the one estimated on the planning CT by 2 to 3 mm. In both the ROOSTER and MA-ROOSTER reconstructions the tumor position is at maximum 1 mm away from the references.

Artifacts can be observed on the diaphragm and liver of patient 1 at end-exhale, in MA-ROOSTER reconstructions. In the corresponding area on the MC-FDK, the region is darker than clinically expected. These artifacts have the same profound cause, namely that in some phases the motion compensation leads outside the field of view. The difference between the nature of the artifacts arise from the different ways motion compensation is performed in the two methods. In MA-ROOSTER, all frames are warped to a single one and regularization along time is performed on the warped frames. For some frames, this warping implies forward or backward mapping outside the field of view, right in the cone-beam artifacts, which 'brings in' cone-beam artifacts. These are then spread out to the other frames through regularization

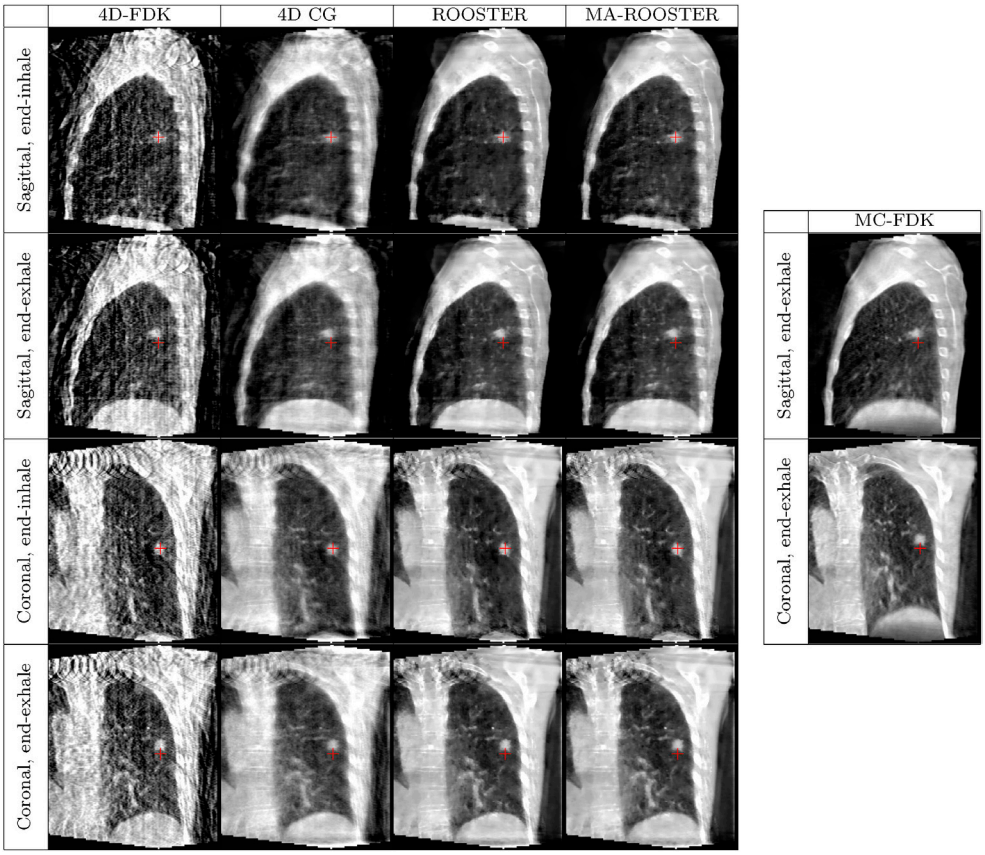

Figure 9. Slices through reconstructions of patient 1. Left panels (from left to right): 4D-FDK, 4D CG, ROOSTER and MA-ROOSTER. Right panels: MC-FDK of the end-exhale phase. The red cross marks a fixed spot, approximately at the center of the tumor in the end-inhale position, to ease visual evaluation of the motion's amplitude.

along time. In MC-FDK, when the DVF points outside the field of view, the projection data is assumed to be null. Fewer back-projected rays reach the inside of the FOV, which results in an attenuation that is lower than expected. Patient 1 also has metal artifacts, visible mostly in the coronal view, caused by a tracheotomy device. Note that cone-beam artifacts can also be observed at the top of the reconstruction of both patients, although these do not interfere with motion compensation.

3.2.2. Patient 2. Figure 11 shows sagittal and coronal slices of the reconstructions obtained using 4D FDK, 4D CG, ROOSTER and MA-ROOSTER on patient 2, in end-inhale (rows 1 and 3) and end-exhale (rows 2 and 4) phases. MC-FDK shows the end-exhale.

The comparison with ROOSTER yields the same results as for patient 1. On this patient, however, MA-ROOSTER achieves a slightly higher contrast than MC-FDK on small structures, especially below the tumor in the sagittal view, but has a slightly lower contrast on the tumor itself. Even with the red cross as a reference spot, it is difficult to notice a change in motion amplitude between the various methods. However, this time, the motion estimation results are clearly in favor of MA-ROOSTER, as shown in figure 12, which is similar to figure 10 but for patient 2. The reference motion amplitude, measured on both

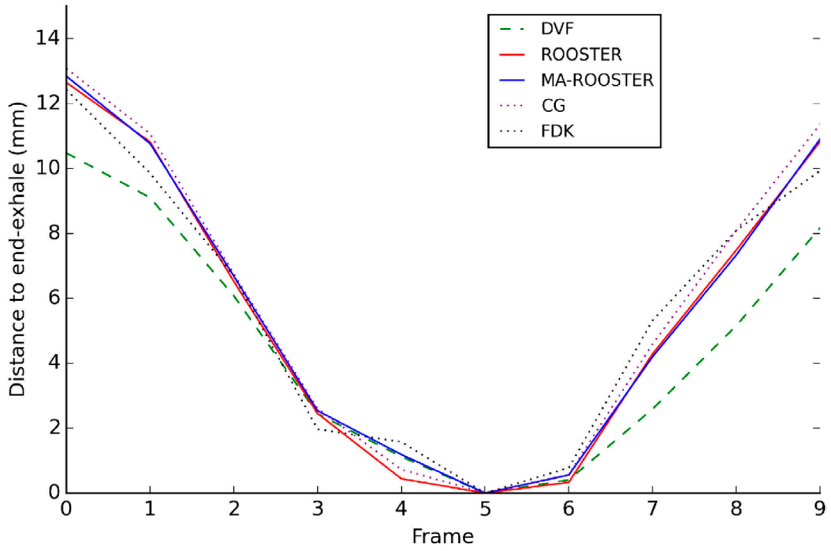

Figure 10. Distance to end-exhale position (in mm) estimated around the tumor on several 4D reconstructions of patient 1, and computed from the DVF.

unregularized 4D reconstructions, is 4 mm larger than the one estimated on the planning CT. The discrepancy between tumor position in the ROOSTER reconstruction and in the references reaches 3 mm at end-exhale, while it remains within 1 mm throughout the cycle in the MA-ROOSTER result. Again, this tends to prove that MA-ROOSTER is robust to inaccuracies of the input DVF.

3.2.3. Linear attenuation coefficients of lung tissue. An interesting feature of MA-ROOSTER is that it allows a variation of the linear attenuation coefficients of lung tissue throughout the respiratory cycle. To measure this variation, we warped all frames onto frame 50% and summed the attenuation of all voxels contained in the mask shown on figure 13. This was performed on the planning CT images and the MA-ROOSTER reconstructions. Since the planning CT images are in Hounsfield units (HU), a small calculation is necessary to make sure that the HUs and linear attenuation coefficients are supposed to follow the same variations. For a position $\mathbf{x}$ and a phase p,

$$\begin{aligned} \mathrm{HU}(\mathbf{x},p) &= \frac{\mu(\mathbf{x},p)-\mu_{\mathrm{air}}}{\mu_{\mathrm{water}}-\mu_{\mathrm{air}}}\times 1000 - 1000 \\ \mathrm{HU}(\mathbf{x},p)+1000 &\approx \frac{\mu(\mathbf{x},p)}{\mu_{\mathrm{water}}}\times 1000, \quad \text{since } \mu_{\mathrm{air}}\approx 0. \end{aligned} \tag{4}$$

The ratio between attenuation in frame p and in frame 50% is

$$\frac{\mu(\mathbf{x},p)}{\mu(\mathbf{x},50\%)} = \frac{\mathrm{HU}(\mathbf{x},p)+1000}{\mathrm{HU}(\mathbf{x},50\%)+1000}. \tag{5}$$

The ratios between the sum of voxel values in frame p and in frame 50% should therefore be the same in the planning CT expressed in 'HU + 1000' and in the MA-ROOSTER reconstruction. Figure 14 shows these ratios throughout the breathing cycle on patient 1. The mean attenuation in lung tissue in MA-ROOSTER reconstructions follows the same trend as in the 4D CT reconstruction.

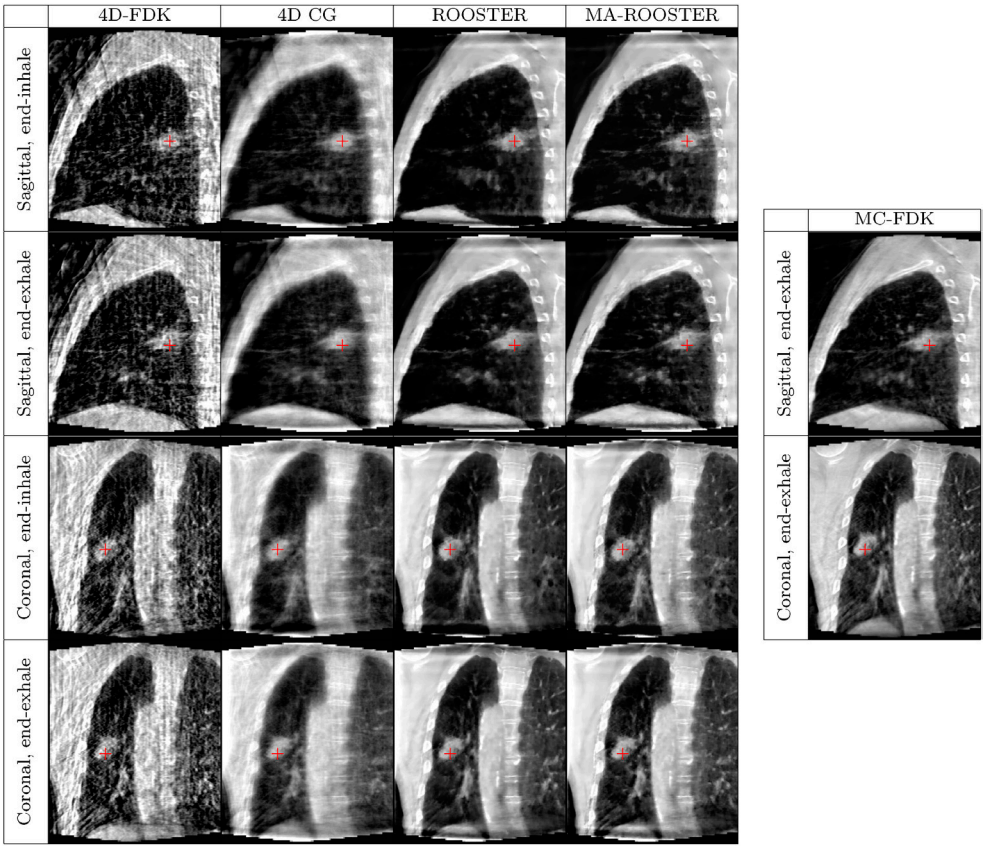

Figure 11. Slices through reconstructions of patient 2. Left panels (from left to right): 4D-FDK, 4D CG, ROOSTER and MA-ROOSTER. Right panels: MC-FDK of the end-exhale phase. The red cross marks a fixed spot, approximately at the center of the tumor in end-inhale position, to ease visual evaluation of the motion's amplitude.

4. Discussion

4.1. Comparison to ROOSTER and MC-FDK

MA-ROOSTER outperforms ROOSTER when the DVF used is closer to the real motion than a null DVF. MA-ROOSTER also outperforms MC-FDK when the DVF does not exactly represent the motion of the day, since it corrects for some of the DVF's inaccuracies. For real image-guided radiation therapy (IGRT) cases, any sensible motion estimation on the planning CT, even a rough one, will usually be a better estimate of the motion of the day than nothing. On the other hand, even if the motion estimation on the planning CT is perfect, it is impossible to know *a priori* whether or not it represents accurately the motion of the day. Therefore, for real IGRT cases, MA-ROOSTER is likely to provide more reliable reconstructions than both ROOSTER and MC-FDK.

With respect to the classical approach used in 'motion-compensated' tomography, which consists in bending the forward and back-projection trajectories, motion-aware regularization is a new way to make use of an existing motion estimation. The additional parameter to tune, γ_{time}, is to be seen more as an additional degree of freedom than as an additional burden, since

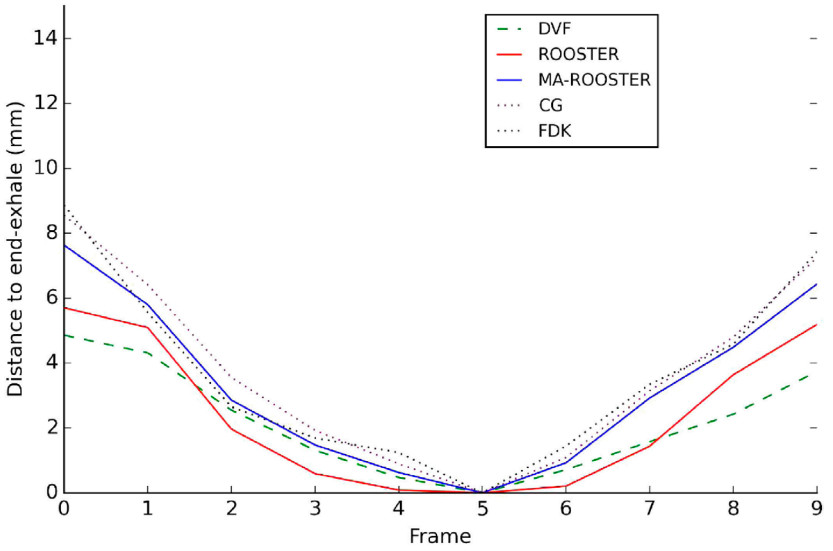

Figure 12. Distance to end-exhale position (in mm) estimated around the tumor on several 4D reconstructions of patient 2, and computed from the DVF.

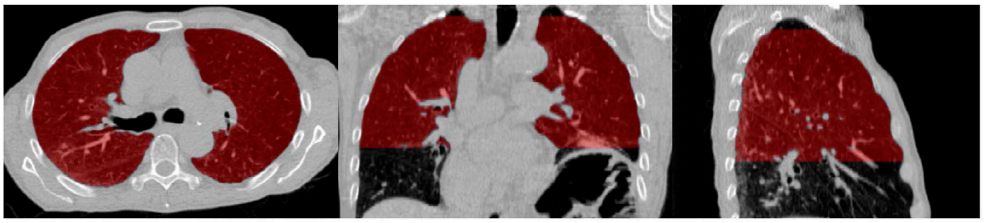

Figure 13. Mask used to measure attenuation variation in lung tissue, shown on frame 50% of the planning CT.

setting $\gamma_{\text{time}} = +\infty$ yields results very similar (although not theoretically identical) to motion-compensated ones.

Other denoising methods exist which could be described as 'motion-aware', e.g. temporal non-local means (TNLM) (Tian *et al* 2011), since in regularizing between consecutive frames they assume that the underlying structures may have moved. TNLM does not require an input DVF, but is computationally more demanding than MA-ROOSTER. In addition, the implicit motion it uses is likely to be very irregular, and therefore not a proper description of the real motion.

4.2. Phantom studies

It is very unusual, in a clinical context, to have such a large discrepancy in the motion amplitude between the planning CT and the CBCT as the ones we used in the phantom study: when anatomical changes occur that are likely to alter the patient's breathing amplitude, doctors usually order a re-planning of the treatment on a new 4D planning CT. Our phantom experiments are therefore quite extreme cases (Seppenwoolde *et al* 2002, Rit *et al* 2012). On real data, we expect the planning CT's motion to be closer to the motion of the day.

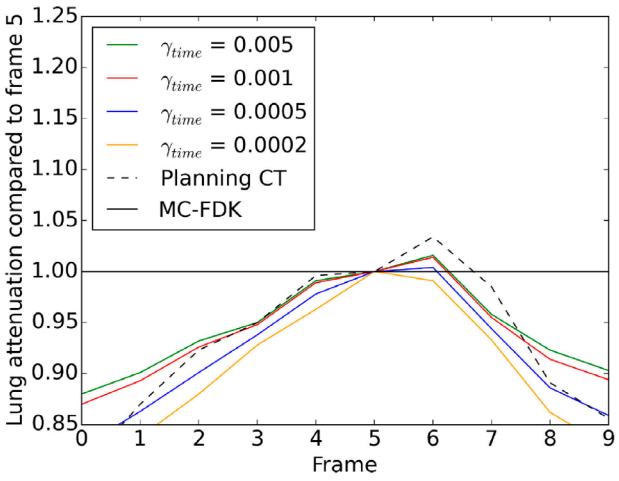

Figure 14. Ratio between the mean attenuation in lungs in a given frame and in frame 50%, in the planning CT and MA-ROOSTER reconstructions of the CBCT data. MC-FDK is shown to recall that it cannot describe such variations.

4.3. Variation of lung tissue attenuation during the respiratory cycle

While it is clear that lung tissue should not have a constant attenuation over time (Guerrero *et al* 2006), it is hard to say how this attenuation should vary. We restricted ourselves to pointing out that the variation of attenuation observed in the MA-ROOSTER reconstructions is consistent with that of the planning CT, as shown on figure 14. This feature of MA-ROOSTER could prove important in applications that require quantitative CBCT, e.g. (Bernchou *et al* 2015).

4.4. Other applications

In interventional cardiology, an accurate 4D reconstruction of the patient's beating heart would allow functional analysis such as left ventricle ejection fraction measurement, detection of hypo- or a-kynesia of some myocardium segments, and road-mapping for numerous interventions like electrophysiology or aortic valve replacement. But many interventional cardiology procedures do not require a 4D CT scan, therefore no DVF is available. For patients who did undergo a 4D CT before their 4D CBCT, MA-ROOSTER could be tested on 4D cardiac CBCT data.

Since MA-ROOSTER has been proved to correct for some of the input DVF's inaccuracies, further work could involve estimating a new DVF from the MA-ROOSTER reconstruction, and performing a second MA-ROOSTER with this new DVF as the input.

4.5. Convergence

Neither ROOSTER nor MA-ROOSTER come with a convergence proof. Furthermore, as each iteration of the main loop is rather long, the stopping criterion is not based on some convergence measurement, but on the number of iterations. Although ROOSTER and MA-ROOSTER behave well in practice for the cases we have studied, there is no theoretical guarantee that they converge, nor that the solution they yield at convergence is more desirable than their output after ten iterations. An animated GIF sequence has been added

to the supplementary material which follows the reconstructed image through 100 iterations (patient2_iterations.gif). Ten iterations seems to be a good choice, since when the number of iterations rises no major image quality improvement is observable, and some dark and bright dots appear. These dots are presumably caused by imperfect inverse warping, which causes some voxels to be modified by temporal regularization when they should not.

Observations on the convergence of ROOSTER, involving the theory of non-expansive mappings, can be found in Mory *et al* (2014). As each step of ROOSTER can be expressed as a proximal mapping, an algorithm similar to ROOSTER can be obtained by minimizing a carefully chosen cost function with the Chambolle–Pock method (Chambolle and Pock 2011). Such an attempt can be found in Mory and Jacques (2014), but the resulting algorithm proved impractical because of its slow initial convergence. Future work includes transforming ROOSTER and MA-ROOSTER into efficient proximal algorithms.

4.6. Regularization

Spatial TV regularization has been shown to be better suited to phantom images than to real clinical data (Mory *et al* 2012), as it favors piecewise-constant images. The spatial TV denoising step could be replaced with some wavelet-based denoising. Finding better-suited regularizers and implementing them efficiently is also part of the future work on MA-ROOSTER.

4.7. Computational cost

The reconstructions were performed on an Intel Xeon E5-2620 CPU with 12 cores, equipped with an nVidia GTX780 GPU, running OpenSuse 13.1. All three methods were implemented using the Reconstruction ToolKit (RTK) (Rit *et al* 2013), an open source C++ software based on the Insight ToolKit' (ITK). With this set-up, the total reconstruction time with MA-ROOSTER for patient 1 is 21 min, divided as follows: 4D CG optimization took 17 min, spatial TV denoising 45 s, warping 80 s, inverse warping 100 s and the other operations can be neglected. When the motion estimation method used on the planning CT only yields a single 4D DVF (instead of two inverse-consistent 4D DVFs), MA-ROOSTER uses an iterative procedure to perform the inverse warping, which increases the duration of that step to 19 min, while all the other execution times remain the same.

4.8. Implementation

All the reconstruction methods used in this paper (4D-FDK, MC-FDK, 4D CG, ROOSTER and MA-ROOSTER) have been implemented in the RTK library (http://openrtk.org/), an open-source software based on ITK. RTK is available to anyone, documented, and we provide help on how to compile, use and modify the code through a mailing list open to everyone, as well as via a wiki (http://wiki.openrtk.org/). A page on the RTK wiki specifically describes how to use ROOSTER and MA-ROOSTER (http://wiki.openrtk.org/index.php/RTK/Examples/4DROOSTERReconstruction) and contains links to the data of both patients (4D planning CT, projections, geometry, respiratory signal and DVFs), as well as the command lines to reproduce the results on patients. The phantom data (projections, geometry, simulated respiratory signal and DVFs) can be made available on request. The implementation of the method we used to compute the 4D DVFs from the 4D planning CT (Janssens *et al* 2011), on the other hand, is not open source. Note that MA-ROOSTER can use DVFs generated by any motion estimation method, and that how the motion estimation is performed is beyond the scope of the present paper.

5. Conclusion

The proposed method, MA-ROOSTER, yields a reconstruction that is visually close to MC-FDK, while being robust to motion estimation inaccuracies. MA-ROOSTER appears as an excellent trade-off between the MC-FDK technique (which provides high-quality 3D images, but from which one cannot retrieve the motion of the day nor the attenuation variation due to the flows of air and blood in the lungs) and unregularized 4D reconstruction techniques (from which one can estimate the motion of the day of large structures, but which have poor image quality).

Acknowledgments

The authors would like to thank Sébastien Brousmiche and Guillaume Janssens for their help in performing the acquisitions on the phantom. This research work has been partially funded by the iMagX project. iMagX is a public partnership between UCL and IBA funded by the Walloon region under convention number 1017266 and 1217662, and by grant ANR-12-BS01-0018 (DROITE project).

References

Andersen A H and Kak A C 1984 Simultaneous algebraic reconstruction technique (SART): a superior implementation of the art algorithm *Ultrason. Imaging* **6** 81–94

Arsigny V *et al* 2006 A log-Euclidean framework for statistics on diffeomorphisms *Medical Image Computing and Computer-Assisted Intervention* (*Lecture Notes in Computer Science* vol 4190) ed R Larsen *et al* (Berlin: Springer) pp 924–31

Bergner F *et al* 2010 An investigation of 4D cone-beam CT algorithms for slowly rotating scanners *Med. Phys.* **37** 5044

Bernchou U *et al* 2015 Prediction of lung density changes after radiotherapy by cone beam computed tomography response markers and pre-treatment factors for non-small cell lung cancer patients *Radiother. Oncol.* **117** 17–22

Boyd S and Ye Y 2011 *Foundations and Trends in Optimization* (New York: Dover)

Brehm M *et al* 2012 Self-adapting cyclic registration for motion-compensated cone-beam CT in image-guided radiation therapy *Med. Phys.* **39** 7603–18

Chambolle A and Pock T 2011 A first-order primal-dual algorithm for convex problems with applications to imaging *J. Math. Imaging Vis.* **40** 120–45

Cho P S, Rudd A D and Johnson R H 1996 Cone-beam CT from width-truncated projections *Comput. Med. Imaging Graph.* **20** 49–57

Christensen G E and Johnson H J 2001 Consistent image registration *IEEE Trans. Med. Imaging* **20** 568–82

Feldkamp L A, Davis L C and Kress J W 1984 Practical cone-beam algorithm *J. Opt. Soc. Am.* A **1** 612–9

Guerrero T *et al* 2006 Dynamic ventilation imaging from four-dimensional computed tomography *Phys. Med. Biol.* **51** 777–91

Jacques L, Hammond D K and Fadili J 2010 Dequantizing compressed sensing: when oversampling and non-Gaussian constraints combine (arXiv:0902.2367v4)

Jaffray D A *et al* 2002 Flat-panel cone-beam computed tomography for image-guided radiation therapy *Int. J. Radiat. Oncol. Biol. Phys.* **53** 1337–49

Janssens G *et al* 2011 Diffeomorphic registration of images with variable contrast enhancement *Int. J. Biomed. Imaging* **2011** 891585

Jia X *et al* 2010 4D computed tomography reconstruction from few-projection data via temporal non-local regularization *Medical Image Computing and Computer-Assisted Intervention* (*Lecture Notes in Computer Science* vol 6361) ed T Jiang *et al* (Berlin: Springer) pp 143–50

Knecht S *et al* 2008 Computed tomography-fluoroscopy overlay evaluation during catheter ablation of left atrial arrhythmia *Europace* **10** 931–8

Leng S *et al* 2008 High temporal resolution and streak-free four-dimensional cone-beam computed tomography *Phys. Med. Biol.* **53** 5653–73
Li T, Koong A and Xing L 2007 Enhanced 4D cone-beam CT with inter-phase motion model *Med. Phys.* **34** 3688
Liu J *et al* 2015 5D respiratory motion model based image reconstruction algorithm for 4D cone-beam computed tomography *Inverse Problems* **31** 115007
Lu J *et al* 2007 Four-dimensional cone beam CT with adaptive gantry rotation and adaptive data sampling *Med. Phys.* **34** 3520
McCollough C H *et al* 2012 Achieving routine submillisievert CT scanning: report from the summit on management of radiation dose in CT *Radiology* **264** 567–80
Moeslund T B 2012 *Introduction to Video and Image Processing: Building Real Systems and Applications* (Berlin: Springer)
Mory C and Jacques L 2014 A modified 4D ROOSTER method using the Chambolle–Pock algorithm *Proc. 3rd Int. Conf. on Image Formation in X-ray Computed Tomography (Salt Lake City, USA) pp* 191–3 (http://ucair.med.utah.edu/CTmeeting/ProceedingsCTMeeting2014.pdf)
Mory C and Rit S 2015 Improving iterative 4D CBCT through the use of motion information *Proc. of Fully 3D 2015 (Newport, Rhode Island, USA)*
Mory C *et al* 2012 ECG-gated C-arm computed tomography using L1 regularization *Proc. 20th European Signal Processing Conf.* pp 2728–32
Mory C *et al* 2014 Cardiac C-arm computed tomography using a 3D+ time ROI reconstruction method with spatial and temporal regularization *Med. Phys.* **41** 021903
Rit S *et al* 2009a On-the-fly motion-compensated cone-beam CT using an *a priori* model of the respiratory motion *Med. Phys.* **36** 2283–96
Rit S, Sarrut D and Desbat L 2009b Comparison of analytic and algebraic methods for motion-compensated cone-beam CT reconstruction of the thorax *IEEE Trans. Med. Imaging* **28** 1513–25
Rit S *et al* 2011 Comparative study of respiratory motion correction techniques in cone-beam computed tomography *Radiother. Oncol.* **100** 356–9
Rit S, van Herk M, Zijp L and Sonke J J 2012 Quantification of the variability of diaphragm motion and implications for treatment margin construction *Int. J. Radiat. Oncol. Biol. Phys.* **82** e399–407
Rit S, Vila Oliva M, Brousmiche S, Labarbe R, Sarrut D and Sharp G C 2013 The Reconstruction RoolKit (RTK), an open-source cone-beam CT reconstruction toolkit based on the Insight ToolKit (ITK). *Proc. Int. Conf. on the Use of Computers in Radiation Therapy*
Ritschl L *et al* 2012 Iterative 4D cardiac micro-CT image reconstruction using an adaptive spatio-temporal sparsity prior *Phys. Med. Biol.* **57** 1517–25
Seppenwoolde Y *et al* 2002 Precise and real-time measurement of 3D tumor motion in lung due to breathing and heartbeat, measured during radiotherapy *Int. J. Radiat. Oncol. Biol. Phys.* **53** 822–34
Sidky E Y and Pan X 2008 Image reconstruction in circular cone-beam computed tomography by constrained, total-variation minimization *Phys. Med. Biol.* **53** 4777–807
Sonke J J *et al* 2005 Respiratory correlated cone beam CT *Med. Phys.* **32** 1176
Tian Z *et al* 2011 Low-dose 4DCT reconstruction via temporal nonlocal means *Med. Phys.* **38** 1359–65
Vandemeulebroucke J *et al* 2012 Automated segmentation of a motion mask to preserve sliding motion in deformable registration of thoracic CT *Med. Phys.* **39** 1006–15
Wang J and Gu X 2013a High-quality four-dimensional cone-beam CT by deforming prior images *Phys. Med. Biol.* **58** 231
Wang J and Gu X 2013b Simultaneous motion estimation and image reconstruction for 4D cone-beam CT *Med. Phys.* **40** 101912
Wolthaus J W *et al* 2008 Comparison of different strategies to use four-dimensional computed tomography in treatment planning for lung cancer patients *Int. J. Radiat. Oncol. Biol. Phys.* **70** 1229–38
Wu H *et al* 2012 Spatial-temporal total variation regularization for 4D-CT reconstruction *Proc. SPIE* **8313** 83133J
Ziegler A, Nielsen T and Grass M 2008 Iterative reconstruction of a region of interest for transmission tomography *Med. Phys.* **35** 1317

B

Book chapter illustrating Part II Spectral computed tomography

This appendix contains a copy of [B1]:

Rit, S., Mory, C., Noël, P., "Image Formation in Spectral Computed Tomography". In: *Spectral, Photon Counting Computed Tomography.* Ed. by K. Taguchi, I. Blevis, and K. Iniewski. CRC Press, 2020, pp. 355–372

19 Image Formation in Spectral Computed Tomography

Simon Rit[1], *Cyril Mory*[1], *and Peter B. Noël*[2]
[1]Univ Lyon, INSA-Lyon, Université Claude Bernard Lyon 1, UJM-Saint Etienne, CNRS, INSERM, CREATIS, Centre Léon Bérard, Lyon, France
[2]Department of Radiology, Perelman School of Medicine, University of Pennsylvania, Philadelphia, Pennsylvania, USA

CONTENTS

19.1 Image-Based Decomposition 358
19.2 Projection-Based Decomposition 359
19.2.1 Decomposition into Material Projections 359
19.2.2 Tomographic Reconstruction 361
19.3 One-Step Inversion 362
19.3.1 Forward Problem and Cost Function 363
19.3.2 Minimization 363
19.4 Regularization 364
19.5 Image Quality Issues Specific to Spectral CT 366
19.6 Conclusion 367
References 367

Spectral Computed Tomography (CT) can perform "color" x-ray detection; for example, photon-counting detectors can discriminate the energy of individual x-ray photons and divide them into several predefined energy bins, thereby providing a spectral analysis of the transmitted x-ray beam. By measuring the x-ray attenuation in two or more distinct energy bins, one can gain information about the elemental composition of an object, making it possible via material decomposition to distinguish between different materials, such as contrast agents and different types of tissues, in a single CT scan. This concept of spectral CT is based on the x-ray attenuation differences of various materials when simultaneously exposed by a spectrum of x-ray photons (which are emitted in a wide spectral range by a standard x-ray tube). Attenuation differences reflect the differences in material interactions with low- and high-energy photons, mainly Compton scatter and photoelectric effects in the diagnostic energy range. Interaction of x-rays with matter is described by the linear attenuation coefficient μ of an object, which depends on the three-dimensional (3D) position $\boldsymbol{x}$ in space and the one-dimensional (1D) energy ϵ of incident photons. The photon fluence Φ after the object of a monoenergetic pencil beam is described by the Beer-Lambert law:

$$\Phi = \Phi_0 \exp\left(-\int_{\mathcal{L}} \mu(\boldsymbol{x}, \epsilon) \mathrm{d}\ell \right) \tag{19.1}$$

with ϵ the beam energy, Φ_0 the initial beam fluence, and $\mathcal{L}$ the line corresponding to the beam.

Conventional CT scanners acquire a single sinogram, mixing all photons regardless of their energy. Reconstruction algorithms for single-energy CT either neglect the energy dependency of the incident beam or use corrections for multi-energy effects known as beam hardening [8], for example

by assuming that a single material composes the object in the field-of-view [7]. Spectral CT scanners employ a variety of strategies to acquire multiple sinograms representative of different energy segments of the incoming spectra [38]. The purpose of this chapter is to present specific algorithmic solutions required to utilize this additional energy dimension in combination with conventional and advanced tomographic reconstruction algorithms.

The central goal of spectral processing steps is to reconstruct not only a 3D μ map at a given (effective) energy, but a four-dimensional (4D) μ for the energy range measured with two to five energy discrimination measurements provided by a spectral CT scanner. A simplified model becomes necessary and many contributions (also presented in this chapter) are based on a model proposed by Alvarez and Macovski [4]. This paradigm describes μ as a linear combination of a few energy-independent and space-independent functions, which they note:

$$\mu(\boldsymbol{x},\epsilon) \approx \sum_{m=1}^{\mathrm{M}} a_m(\boldsymbol{x}) f_m(\epsilon) \tag{19.2}$$

with $\boldsymbol{x}$ the 3D position in the object, M the number of basis functions, a_m the 3D space-dependent (but energy-independent) functions, and f_m the energy-dependent (but space-independent) functions. Two approaches have been proposed for the f_m functions and a_m volumes in human tissue. Both methods only require $\mathrm{M} = 2$ basis functions. One is to assume that the object attenuates x-rays as if it was composed of two materials, for example, water and bone [23]. The function f_m is then the mass-attenuation coefficient of material m, which solely depends on the energy, and the volume a_m is a map of the concentration of material m. The other approach proposes that image contrast is based on an x-ray particle model describing the physical interaction of photoelectric absorption and Compton scattering. The function f_m then approximates the energy dependence of the phenomenon m, and the volume a_m is a map of the cross-section for that type of interaction. In addition to the two functions to represent human materials, there can be additional components in the basis to represent non-human elements ($\mathrm{M} > 2$), for example, contrast materials having a K-absorption edge in the diagnostic energy range [57, 82]. Without loss of generality, we will refer to f_m as material-specific CT maps in the following sections.

The x-ray source of a CT scanner is polychromatic and characterized by an energy spectrum. Similarly, the signal measured by the detector is a function of the energies of impinging photons. The impinging spectrum is not equivalent to the measured one because the measurements can be distorted while the signal is picked up from the detector and processed by complex electronics. The ratio of the spectrum collected with a detector over the impinging spectrum is called a detector response function or pulse height distribution. These two energy functions can be merged into an *effective spectrum*, which is the product of the source spectrum and the detector response function. The concept of an effective spectrum can describe any spectral system, whether several effective spectra are acquired by using different source spectra, for example, with different source voltages, by using two detectors with different responses, for example, with different sensitive materials, or by using different energy thresholds for photon-counting detectors. Figure 19.1 illustrates the effective spectra of different systems.

Plugging the model of the linear attenuation coefficient (Equation 19.2) into the Beer-Lambert law (Equation 19.1) and accounting for the polychromatism of the effective spectra leads to the forward model of the inverse problem studied in this chapter

$$\hat{y}_{ib} = \int_{\mathbb{R}^+} s_b(\epsilon) \exp\left(-\int_{\mathcal{L}_i} \sum_{m=1}^{\mathrm{M}} a_m(\boldsymbol{x}) f_m(\epsilon) \mathrm{d}\ell \right) \mathrm{d}\epsilon \tag{19.3}$$

with $\hat{y}_{ib}$ the expectation of the measures for the i-th detector pixel and the b-th effective spectrum s_b (b stands for energy bin in photon counting systems). The goal of this inverse problem is to estimate

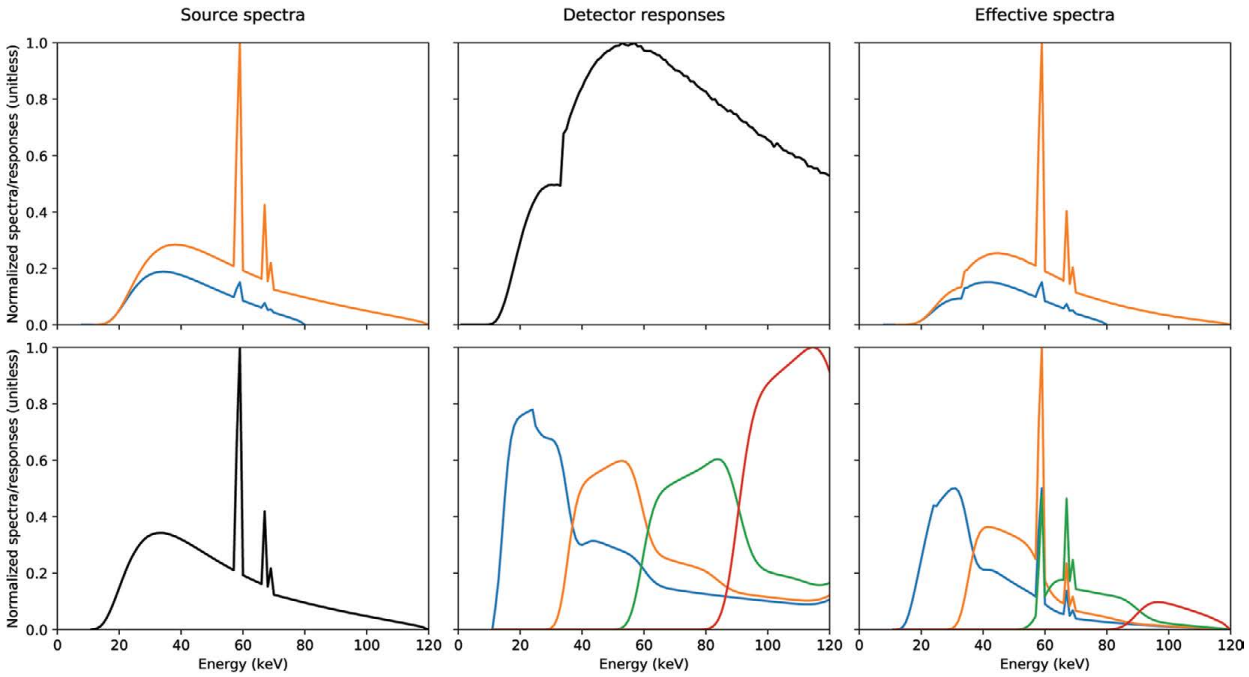

FIGURE 19.1 Examples of source spectra (left), detector responses (middle), and effective spectra (right), for a fast-switching x-ray source with an energy-integrating detector with a CsI scintillator (top, data from system #2 in [81]) and a photon-counting system with four energy bins (bottom, data from [16]).

the unknown material images $\boldsymbol{a}$ from measures $\boldsymbol{y}$. The effective spectra s can be estimated independently, before using the algorithms presented in this chapter [17, 40, 67]. The energy functions f are chosen based on the model in Equation 19.2. This forward model only accounts for the attenuation of primary rays and neglects scatter, pile-up, charge sharing, and other complex effects, unless those can be taken into account in the effective spectrum.

The following three sections introduce the main classes of spectral CT reconstruction algorithms (Figure 19.2): image-based and projection-based, which perform decomposition into

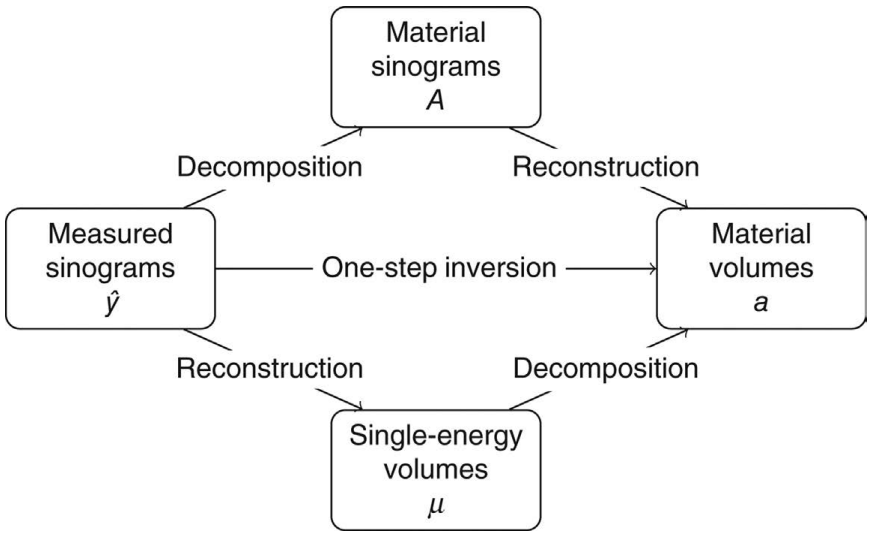

FIGURE 19.2 The three classes of inversion methods described in this chapter are image-based decomposition (bottom row, Section 19.1), projection-based decomposition (top row, Section 19.2), and one-step inversion (Section 19.3).

materials and tomographic reconstruction separately, and are therefore referred to as "two-step" methods, and one-step inversion, which merges both decomposition and reconstruction into a single inverse problem. The final sections describe possible regularizers for these ill-posed inverse problems and potential image quality issues specific to spectral CT decomposition and reconstruction.

19.1 IMAGE-BASED DECOMPOSITION

Image-based decomposition was initially developed for exploiting two (or more) CT acquisitions obtained at different tube-voltages on a conventional CT scanner [6]. With distinct spectra at different voltages, the resulting CT slices display energy dependent differences. Image-based decomposition assumes that the b-th single-energy CT represents the attenuation coefficient at a given (effective) energy e_b, which is true with monoenergetic CT acquisitions at a synchrotron [79], by reconstructing from the log-transformed projections $\ln(s_b(e_b)/y_{ib})$, or with the use of an efficient beam hardening correction. Under this assumption, the CT image $\mu(\cdot, e_b)$ of the b-th effective spectrum is, according to Equation 19.2, a linear combination of the sought space-dependent functions a_m and the energy-dependent functions f_m. Combining the measurements, one obtains at each spatial position $\boldsymbol{x}$ a small linear system of equations with as many equations as CT images:

$$\mu(\boldsymbol{x}) = \boldsymbol{F}\boldsymbol{a}(\boldsymbol{x}) \tag{19.4}$$

with

$$\mu(\boldsymbol{x}) = \begin{bmatrix} \mu(\boldsymbol{x}, e_1) \\ \mu(\boldsymbol{x}, e_2) \\ \vdots \\ \mu(\boldsymbol{x}, e_{\mathrm{B}})) \end{bmatrix}, \quad \boldsymbol{F} = \begin{bmatrix} f_1(e_1) & f_2(e_1) & \dots & f_{\mathrm{M}}(e_1) \\ f_1(e_2) & f_2(e_2) & \dots & f_{\mathrm{M}}(e_2) \\ \vdots & \vdots & \ddots & \vdots \\ f_1(e_{\mathrm{B}}) & f_2(e_{\mathrm{B}}) & \dots & f_{\mathrm{M}}(e_{\mathrm{B}}) \end{bmatrix} \quad \text{and} \quad \boldsymbol{a}(\boldsymbol{x}) = \begin{bmatrix} a_1(\boldsymbol{x}) \\ a_2(\boldsymbol{x}) \\ \vdots \\ a_{\mathrm{M}}(\boldsymbol{x}) \end{bmatrix}. \tag{19.5}$$

Given its small size, this system can easily be solved, for example, with the Moore-Penrose pseudoinverse (which is the inverse of $\boldsymbol{F}$ if $\boldsymbol{F}$ is invertible). Moreover, since there is no spatial dependence of $\boldsymbol{F}$, this (pseudo-)inverse can be computed once for all voxels if the effective energy of the input CT images is known. Otherwise, it can be directly calibrated using materials with known linear attenuation properties. Image-based decomposition can be combined with regularization, for example to reduce noise [14, 15, 49, 76]. A simulated example using monochromatic spectra is provided in Figure 19.3.

The simplicity of image-based decomposition makes it an attractive solution. It is also extensively used in applications where access to raw data/sinograms is not available, as demonstrated in radiotherapy applications [80]. Another advantage compared to projection-based inversions is that there is no need to have projections acquired with the same geometry (source and detector positions and orientations) for all effective spectra, as is, for example, the case when two different x-ray sources are used for the acquisition of different spectra. The input CT images must still be perfectly registered, and this is true for all algorithms presented here. Even if two (or more) CT acquisitions could easily be acquired on any clinical CT scanner with different voltages, patient motion, for example, through breathing, reduces significantly the quality of spectral results. Another significant drawback of image-based decomposition is the impact of beam hardening when using conventional x-ray sources. Inaccuracies of beam hardening correction will have a direct influence on the result [71]. Advanced beam hardening correction

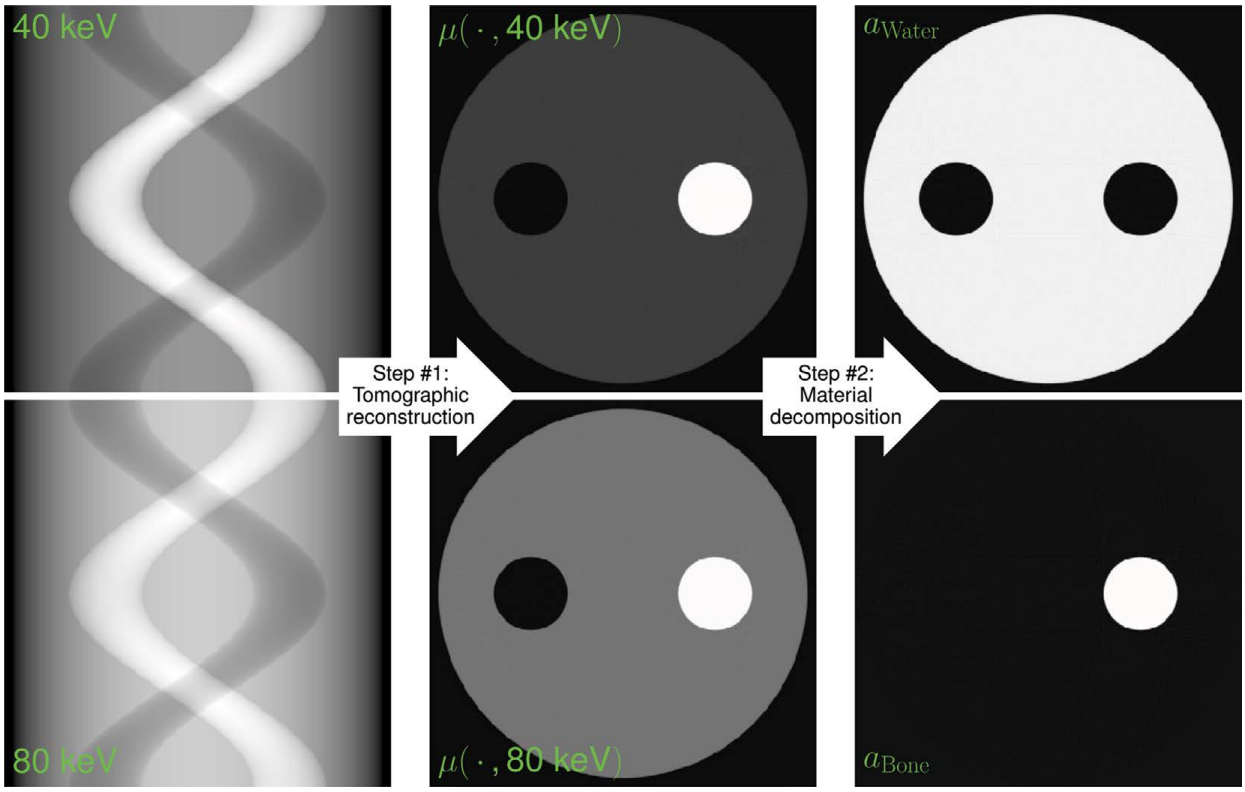

FIGURE 19.3 Left: noiseless simulated dual-energy log-transformed sinograms using monochromatic irradiations at 40 keV (top) and 80 keV (bottom). Middle: corresponding single-energy volumes g_b. Right: decomposed volumes a_m. The object is made of a liquid water component (top right) and cortical bone (bottom right). The linear attenuation coefficients used for the simulation are those of ICRP retrieved from x-ray lib [64], that is, $\mu_{\text{water}}(40\ \text{keV}) = 0.27\,\text{cm}^{-1}, \mu_{\text{water}}(80\ \text{keV}) = 0.18\,\text{cm}^{-1}, \mu_{\text{water}}(40\ \text{keV}) = 1.19\,\text{cm}^{-1}$ and $\mu_{\text{bone}}(80\ \text{keV}) = 0.41\,\text{cm}^{-1}$.

algorithms require the knowledge of the linear attenuation coefficients of the materials in the field-of-view, for example, by relying on the same model as Equation 19.2 [8]. Image-based decomposition is therefore simple because it forwards the complexity of Equation 19.3 from the decomposition to the beam hardening correction. The difficulty therefore lies in the latter and has lead to the development of algorithms, which correct for beam hardening in the image domain while decomposing by using a different model than Equation 19.2 [34]. Another approach, intermediate with one-step inversion (section 19.3), projects the current estimate to iteratively correct for beam hardening [35].

19.2 PROJECTION-BASED DECOMPOSITION

Projection-based methods perform first the decomposition in projection space before reconstructing material-specific CT maps (Figure 19.2).

19.2.1 Decomposition into Material Projections

Decomposition into material-specific projections aims to determine, for each pixel of the multi-energy sinogram, the corresponding line integral through the spatial maps a_m. For example, if the object consists of two materials as in Figure 19.3 and the basis functions f_m are the corresponding linear attenuation coefficients of the materials, the aimed decomposed data will be the sinogram

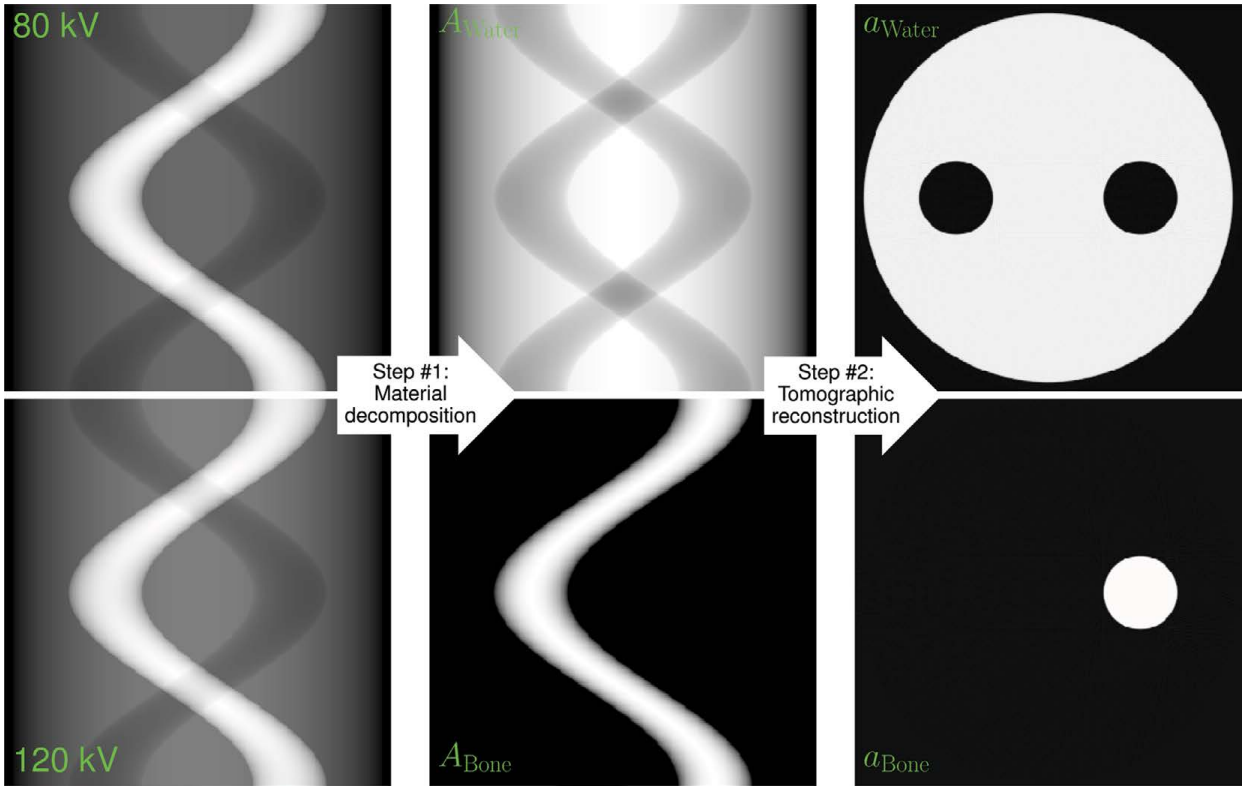

FIGURE 19.4 Left: noiseless simulated dual-energy sinograms of the object in Figure 19.3 using the 80 kV (top) and 120 kV (bottom) spectra and the detector response shown on top of Figure 19.1. Middle: decomposed sinograms A_m using projection-based decomposition with μ_{water} and μ_{bone} as basis functions f_m. Right: decomposed volumes a_m. The object is the same as in Figure 19.3.

of each material, as illustrated in Figure 19.4. Formally, Equation 19.3 is modified by inverting the order of the integral over the line $\mathcal{L}_i$ and the discrete sum over the M basis functions. Projection-based decomposition then utilizes the forward model:

$$\hat{y}_{ib} = \int_{\mathbb{R}^+} s_b(\epsilon) \exp\left(-\sum_{m=1}^{\mathrm{M}} A_{im} f_m(\epsilon) \right) \mathrm{d}\epsilon \tag{19.6}$$

with the unknowns $A_{im} = \int_{\mathcal{L}_i} a_m(\boldsymbol{x}) \mathrm{d}\ell$ corresponding to the i-th line integral through a_m. This decomposition yields a set $\boldsymbol{A}$ of M sinograms (one per basis function), which can each be reconstructed to obtain one volume per material. Similarly to the image-based problem, decomposing the acquired sinograms $\boldsymbol{y}$ into material-specific sinograms $\boldsymbol{A}$ is a small problem when processed pixel-by-pixel, with M unknowns to find from B measurements. However, the exponential function causes the problem to be non-linear and the (weighted) least squares data fidelity term is non-convex [1].

In their seminal paper [4], Alvarez and Macovski proposed to approximate the logarithm of the expectation of the measures $\hat{\boldsymbol{y}}$ by a P-th order polynomial of the A_{im}:

$$\ln \hat{y}_{ib} \simeq \sum_{p_1 + p_2 + \ldots + p_{\mathrm{M}} \leq \mathrm{P}} \alpha_{p_1 p_2 \ldots p_{\mathrm{M}}} A_{i1}^{p_1} A_{i2}^{p_2} \ldots A_{i\mathrm{M}}^{p_{\mathrm{M}}} \tag{19.7}$$

with $\{p_1,\ldots,p_M\}$ the exponents and $\alpha_{p_0 p_1 \ldots p_M}$ the coefficients of the polynomial. Another solution is to directly approximate the inversion by a polynomial [28]:

$$A_{im} \simeq \sum_{q_1+q_2+\ldots+q_B \leq P} \beta_{q_1 q_2 \ldots q_B} \left(\ln \hat{y}_{i1}\right)^{q_1} \left(\ln \hat{y}_{i2}\right)^{q_2} \ldots \left(\ln \hat{y}_{iB}\right)^{q_B} \tag{19.8}$$

with $\{q_1,\ldots,q_B\}$ the exponents and $\beta_{q_0 q_1 \ldots q_B}$ the coefficients of this other polynomial. Both methods are very efficient solutions, probably best suited to dual-energy decomposition with two basis functions ($B = M = 2$). In any case, they are only approximations of Equation 19.6 or its inverse. The accuracy of this approximation can be improved by increasing the polynomial order P, but it also degrades the stability of the decomposition. Already in [4], the authors did not use all nine possible monomials and later studies suggested a rationale for adequately selecting a subset of monomials [29]. If the effective spectra s are known, the coefficients of the polynomials can be computed to best approximate the forward model, as $\boldsymbol{F}$ in image-based decomposition (Equation 19.4). Otherwise, one can directly calibrate the polynomial coefficients without estimating s by taking projections through multiple combinations of basis material layers with known thicknesses as, for example, in the calibration phantom of [2].

In 2008, in order to deal with three materials and four energy bins, Roessl *et al.* proposed to solve the problem in the maximum likelihood sense [57, 62], that is, to determine which are the most likely A_{im} given the measured y_{ib}. To maximize the log-likelihood, they used the Nelder-Mead downhill simplex method [47], which is a zero order optimization algorithm for convex problems, that is, which does not need the gradient of the cost function with respect to the optimized variables. Under standard clinical x-ray exposure, the statistical noise on y_{ib} results in very noisy decomposed sinograms, which must be filtered to become usable, as illustrated in Figure 19.5.

Brendel *et al.* [5] proposed to improve Roessl's optimization using the iterative coordinate descent. They also introduced spatial regularization in their minimization problem to limit noise in decomposed sinograms: in addition to being in agreement with the measured photon counts, the decomposed material line integrals in a pixel i must be similar to those in the neighboring pixels. However, regularizing in the projection domain is unusual and it can negatively impact the reconstructed images if it is inadequately chosen or weighted. Similar approaches based on solving an inverse problem include the work of Ducros *et al.* [16] and Abascal *et al.* [1] solving a weighted least-squares problems using a Gauss-Newton algorithm and an iterative Bregman scheme. The latter authors also used the Kullbac-Leibler divergence [21], which is more adapted to Poisson noise distributions and should lead to a result similar to the maximum likelihood approach of [57, 62].

Intermediate solutions between the polynomial models (Equations 19.7 and 19.8) and the full non-linear model (Equation 19.6) have been tailored for the case of more measurements than basis functions [2, 3, 26, 27, 41, 94]. Another approach is to use machine learning to solve this complex but small problem, for example, by using a neural network [93].

A significant advantage of projection-based decomposition over image-based decomposition (section 19.1) is that it does not suffer from beam hardening because the material maps $\boldsymbol{f}$ are energy-independent. However, it can only be applied if the measurements for different spectra are acquired with the same geometry, which is the case for dual-layer detectors and spectral photon-counting detectors but not for dual-source systems or fast-switching x-ray sources. For dual-source or fast-switching systems, one solution is to interpolate the sinograms to have corresponding measurements, but this step could limit the accuracy. Performing several successive acquisitions with different spectra on a standard CT is in theory feasible, but just like with image-based methods, patient motion is then a concern.

19.2.2 Tomographic Reconstruction

None of the methods presented in subsection 19.2.1 makes any assumption on how the material sinograms are reconstructed once they have been decomposed. In fact, any tomographic reconstruction

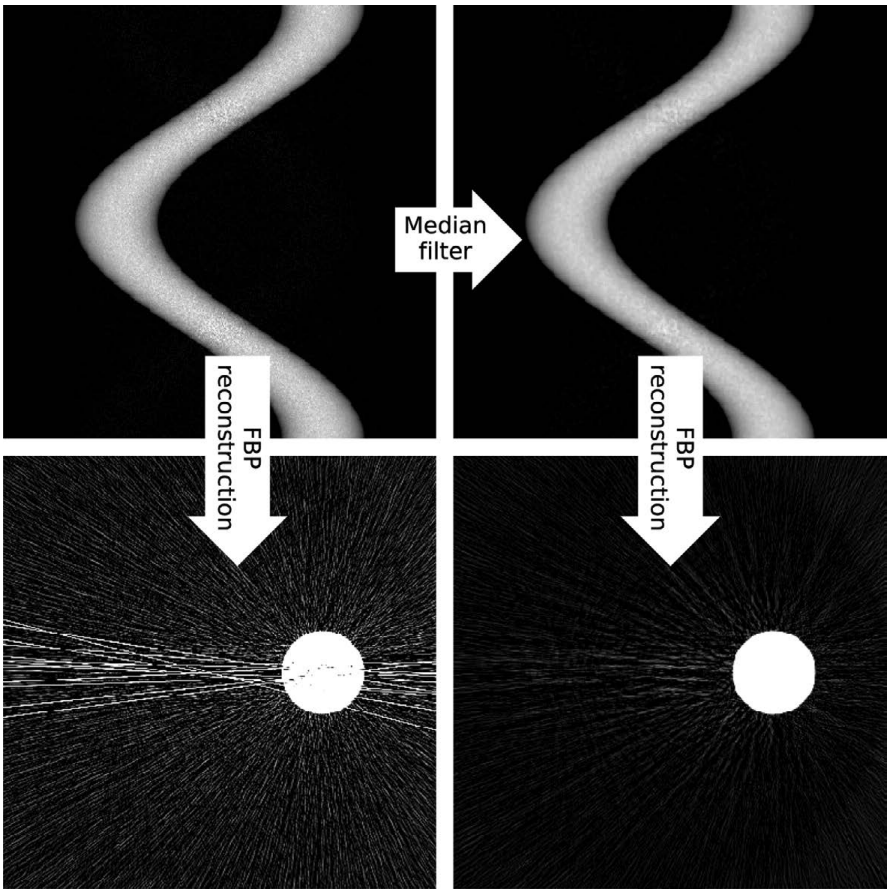

FIGURE 19.5 Sinogram of the bone (top) and its reconstruction (bottom) for the same object as Figure 19.4 with an additional solution of 1 mg/mL gadolinium filling the left hole of the water component. Data simulated using the 5-bin spectral model of the Philips small animal prototype in Lyon [65] corrupted with Poisson noise. The projection-based decomposition is the algorithm of Roessl *et al.* [57, 62] with the three-material basis $\boldsymbol{f} = \{\mu_{\text{Water}}, \mu_{\text{Bone}}, \mu_{\text{Gadolinium}}\}$. Images reconstructed with a filtered backprojection reconstruction. The right sinogram resulted from a median filter to remove outliers. Outliers are in the low-count area, for rays that traverse both the bone and the gadolinium (see other reconstructions in Figure 19.6).

method can be used, including filtered backprojection algorithms. However, the decomposition is sensitive to noise and it is natural to account for this noise in an iterative reconstruction algorithm. A first solution is to use an estimate of the variance of the decomposed sinograms in a weighted least squares algorithm [61]. The material decomposition process also induces anti-correlated noise between the different materials [22], which suggests the use of reconstruction techniques that also account for covariances [60]. Variances and covariances can be estimated using the Cramér-Rao lower bound [56]. Sawatzky *et al.* [59] and Mory *et al.* [43] proposed such an approach. The core idea of these methods is that minimizing the usual least-squares data-attachment term yields the best linear unbiased estimator (BLUE) only when all data samples are uncorrelated and have equal variance. In all other cases, the BLUE is obtained by minimizing a generalized least squares (GLS) term, which involves the inverse of the covariance matrix of the noise. Although GLS is formally simple, it is computationally much more demanding since all material-specific CT maps f_m must be reconstructed simultaneously. It is not clear yet whether the improvement in image quality is worth the increased computational complexity [43].

19.3 ONE-STEP INVERSION

One-step methods generate material maps $\boldsymbol{a}$ straight from recorded photon counts $\boldsymbol{y}$. Similar to projection-based decomposition (section 19.2), these methods can rely, for example, on the forward model in Equation 19.3, but with the advantage of not requiring matching projections

(similar to image-based decomposition section 19.1). It also circumvents the fundamental drawback of all two-step approaches: the first step may introduce errors, which cannot be compensated for in the second step. An excellent illustration of this latter problem is the presence of outliers in sinograms decomposed with non-regularized projection-based methods [57, 62]: as the decomposition process is non-linear, it may strongly amplify the statistical noise on the photon counts, resulting in some pixels with entirely incorrect values for the line integral. Reconstructing without first removing these outliers yields material-specific CT maps dominated by powerful streak artifacts (Figure 19.5).

19.3.1 Forward Problem and Cost Function

Most one-step reconstruction methods apply an identical forward model, which is the equivalent to Equation 19.3 except that the two integrals (over the energies ϵ and the line positions ℓ) are discretized. Note, there is no analytical solution to this problem. Discretizing the line integral is the basis of most iterative single-energy CT reconstruction algorithms and despite being posed as a linear inverse problem, single-energy iterative CT is computationally expensive, which partly explains why manufacturers have only recently started implementing it in commercial CT scanners [50]. One-step spectral CT is even more computationally expensive: with the same number of pixels and voxels, the number of measurements is multiplied by the number B of effective spectra (second index of $\boldsymbol{y}$) and the number of unknowns is multiplied by the number M of basis energy functions (second index of $\boldsymbol{a}$), plus the inverse problem is non-linear.

In the literature, the cost functions are constructed from different terms to solve this problem. For the data-attachment, the most widespread approach is to maximize the likelihood of observing the measurements $\boldsymbol{y}$, given the material-specific CT volumes $\boldsymbol{a}$ under the assumption that the measurements are corrupted by Poisson noise [18, 33, 40, 75, 83]. Other methods minimize a weighted-least squares data-attachment term, computed either on the photon counts [77] or on the ratio between photon counts and photon counts if there had been no attenuation [9, 12]. For the regularization, various conventional options have been considered: positivity [12, 33], total-variation [9, 18], or a similar measure based on the spatial gradient [33, 40, 77, 83].

19.3.2 Minimization

Given the size and non-linearity of the one-step inversion problem, the primary challenge is to minimize the cost function. Almost every method uses a different algorithm to solve its cost function and the landscape of solutions strongly resembles that of single-energy CT.

Several works attempt to adapt methods developed for single-energy CT, which assume a linear problem. Zhao *et al.* [92] linearize the cost function and use an algebraic reconstruction technique (ART) [19]. Li *et al.* [30] do the same using filtered backprojection reconstruction. Cai *et al.* [9] used a non-linear conjugate gradient. Chen *et al.* [12] used a heuristic non-convex adaptation of ASD-POCS [66]. Rodesch *et al.* [54] adapted the maximum likelihood polychromatic algorithm of De Man *et al.* [36].

Several works [33, 40, 83] used separable quadratic surrogates (SQS). The surrogate is a tool for *optimization transfer* [25], which aims at accelerating the minimization of the cost function. Formally, the function $\Phi_{\boldsymbol{x}_0} : \mathbb{R}^N \to \mathbb{R}$ is a surrogate of the cost function $\Psi : \mathbb{R}^N \to \mathbb{R}$ at $\boldsymbol{x}_0 \in \mathbb{R}^N$ if and only if $\Phi_{\boldsymbol{x}_0}$ is above Ψ on $\mathbb{R}^N$, and tangent to Ψ at $\boldsymbol{x}_0$, that is,

$$\begin{cases} \Phi_{\boldsymbol{x}_0}(\boldsymbol{x}) \geq \Psi(\boldsymbol{x}) & \forall \boldsymbol{x} \in \mathbb{R}^N, \\ \Phi_{\boldsymbol{x}_0}(\boldsymbol{x}_0) = \Psi(\boldsymbol{x}_0) & \text{and} \\ \Phi'_{\boldsymbol{x}_0}(\boldsymbol{x}_0) = \Psi'(\boldsymbol{x}_0). \end{cases} \tag{19.9}$$

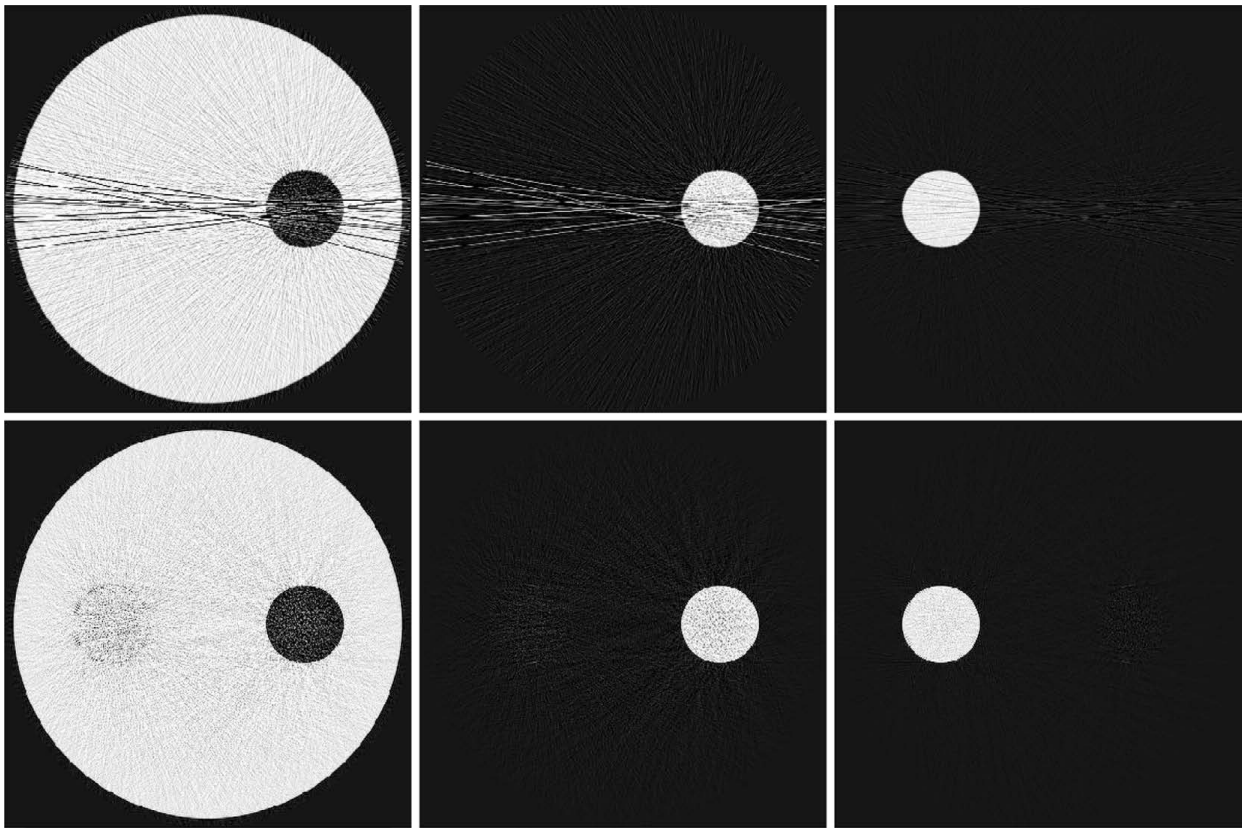

FIGURE 19.6 Projection-based (top, algorithm of [57, 62] combined with filtered-backprojection reconstruction) and one-step reconstruction (bottom, 500 iterations of the algorithm of [40] without subsets and without regularization) using the spectral model and the object described in Figure 19.5. From left to right: water, bone, and gadolinium maps. The grayscale is ±10% around the target concentration of each material.

It is separable if the contribution to Φ of one or a few unknowns can be separated from the ones of the other unknowns. The advantage is that the minimization can be split into many subproblems, each with one or a few unknowns, which can be solved in one iteration of Newton's algorithm, if these subproblems are quadratic. For spectral CT reconstruction, the existing SQS allows solving a subproblem with M unknowns per pixel [33, 40, 83]. Two SQS have been derived in the literature for one-step reconstruction [33, 83], but the inequality in Equation 19.9 is only demonstrated for the one in [33]. Since the problem is non-convex, SQS minimization would retrieve a local minimum if the initialization is not adequately chosen [33].

Some algorithms address the non-convexity using a primal-dual metric algorithm. Foygel Barber *et al.* developed the *Mirrored Convex/Concave Optimization for Nonconvex Composite Functions* (MOCCA) [18, 63], a primal-dual scheme derived from the Chambolle-Pock algorithm [11]. Tairi *et al.* [75] used a variable-metric primal algorithm [13].

Several of these algorithms have been compared in [44] on a simulated test case (three-material decomposition from a 5-bin photon-counting detector). All the algorithms converged to a visually similar solution, but there were substantial differences in convergence speed. Figure 19.6 demonstrates the potential benefit of one-step reconstruction, but it is clear that further research is required before one-step reconstruction can be routinely applied in a spectral CT scanner.

19.4 REGULARIZATION

The problem of decomposition and reconstruction for spectral CT is an ill-posed inverse problem, as is tomographic reconstruction alone [46]. Regularization is therefore required to obtain satisfying results.

In two-step decomposition algorithms, the regularization may be applied to each of the two steps, as pointed out in sections 19.1 and 19.2. Regularizing the first step is probably mandatory in both cases: this is well-known for tomographic CT reconstruction, the first step of image-based methods, and it empirically seems to be the case in projection-based decomposition (Figure 19.5), although this may depend on the number M of basis functions and the number B of effective spectra. The choice of the regularization and its strength is sensitive because it will impact the inputs of the second step. Inverting the decomposition in one step alleviates this difficulty.

There are many options for the regularization of spectral CT. As pointed out in section 19.2, only a small number of studies have suggested to regularize the decomposition of projections [1, 5, 16]. In general, the regularization is rather applied to the CT maps, that is, in the image domain. Any regularization used in tomographic reconstruction may be applied to each volume independently, for example, total variation (TV) [18, 63] or a differentiable approximation of TV [33, 40, 78, 83] (Figure 19.7), the $\ell 1$-norm of wavelets coefficients [87] or the $\ell 0$-norm of dictionaries [91]. Several such regularizers have been compared for spectral CT in [58].

Some authors have suggested to assume that the material-specific CT maps share the same structures and developed regularizations to take advantage of this similarity to improve the results. Similar strategies have been developed for dual-modality imaging such as anatomical priors from CT used in positron emission tomography (PET) reconstruction [52]. Total nuclear variation is a generalization of TV to multi-channel images, which was proposed for this specific goal [53]. Like TV, it favors a piecewise constant volume for each material, but it also favors volumes where edges have the same location and orientation. Several other multi-channel regularizers have been applied to spectral CT data [24, 48, 86].

A final class of regularization is the use of constraints to overcome a larger number of material-specific CT maps than energy measurements (M > B) [31–33, 42, 89]. Additional constraints are

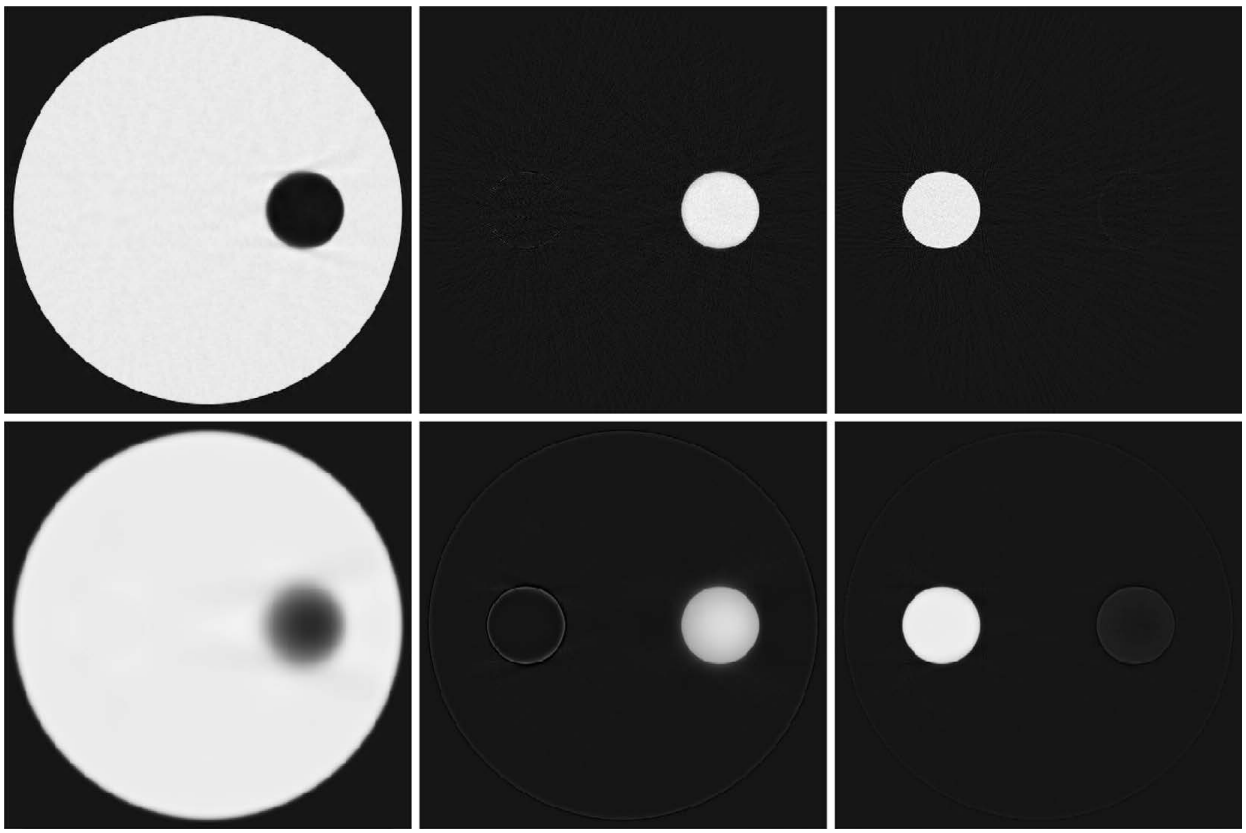

FIGURE 19.7 Effect of regularization on one-step reconstruction [40] from the same data as in Figure 19.6. The regularizer is Green's approximation of TV [20] on each material-specific CT map. The number of iterations was increased to 1000 to reach (visual) convergence. The regularization weights (one per material-specific CT map) have been first chosen to be maximum without visible cross-talk (top) and 100 times larger each (bottom). The grayscale is the same as in Figure 19.6.

added to those in Equation 19.4 or Equation 19.6 by assuming some predefined properties of the scanned materials based on volume and/or mass preservation between the sum of each material-specific CT maps and the mixture. These techniques have been applied in all types of inversions, image-based [31, 32, 42], projection-based [89], and one-step [33].

19.5 IMAGE QUALITY ISSUES SPECIFIC TO SPECTRAL CT

Spectral CT scanners can reconstruct regular CT-like volumes: the photon counts obtained from a spectral CT acquisition can be either fed to one of the spectral CT reconstruction methods described above, yielding material-specific maps, or merged back together into a single sinogram and reconstructed, generating a regular-CT volume (e.g., in Hounsfield Units, HU). Although they are reconstructed from identical input data, it turns out that material-specific CT volumes are typically much noisier than their HU counterpart. The two fundamental reasons for this phenomenon are: reconstructing several volumes instead of a single one reduces the amount of measured photons used per voxel, which results in higher noise (which can be compensated for by increasing the radiation exposure), and the non-linear decomposition process amplifies the noise.

With the introduction of photon-counting detectors into clinical routine, one can expect to see a reduction in detector pixel sizes [69, 84]. The increase in spatial resolution will extend the diagnostic range of CT imaging, for example, in the visualization of fine structures in the lung or along coronary arteries with stents [37, 65, 68]. In those cases, the high-resolution acquisition enables an improved sampling of high-frequency features and reduces noise aliasing [51]. However, for sections without fine details, a high-frequency noise will significantly reduce the image quality. In the future, it will be essential to incorporate these new circumstances into the image reconstruction and to optimize it through algorithmic solutions still to be developed. On this note, the additional energy dimension provides an increased amount of information, which can be utilized to denoise spectral images. The data can be utilized following strategies like prior image constraints [90] or dictionaries [39, 85] (section 19.4).

Additionally, material volumes are subject to decomposition errors, commonly referred to as "cross-talk": materials can appear in the wrong material-specific CT volumes. The severity of cross-talk depends on how much the materials' attenuation profiles differ from each other (the more similar they are, the stronger the cross-talk) and on how much noise is present in the photon counts (the noisier the data, the stronger the cross-talk). In one-step inversion methods, regularization can also cause cross-talk: regularizing one material creates discrepancies between the estimated photon counts and the measured ones, which are compensated by adding or removing some amount of another material. This effect is particularly intense on the borders of structures when a strong spatial regularization is applied, as illustrated in Figure 19.7.

Ring artifacts are a very common artifact in any type of CT imaging and can have a variety of sources. In conventional CT, if one detector element is out of calibration, the reading of this element may consistently be incorrect. As a consequence, the later reconstructed CT slice will be affected by rings. As photon-counting detectors are highly complex and sensitive compared to conventional detectors, a dedicated calibration needs to be performed. While this spectral technology, as well as calibration methods, are still under development, rings that may appear after reconstruction can be removed to a large degree by classical ring removal algorithms [45, 88]. Regarding rings or other artifacts, it is essential to understand that the current hardware does not represent an ideal detector. Novel sensor material (imperative for photon-counting CT), along the lines of cadmium telluride and cadmium zinc telluride, come with technical challenges which can be addressed by hardware as well as software solutions. Pile-up and spectral distortions are two of the main effects, which reduce the quality of spectral data from photon-counting detectors. Several investigators have developed techniques to model those shortcomings with different software-based techniques [10, 55, 70, 72–74]. These achievements represent an ideal opportunity to overcome some of those hardware shortcomings but they still need to be integrated in the image formation algorithms described in this chapter.

19.6 CONCLUSION

Spectral CT systems, especially systems equipped with a spectral photon-counting detector, are a promising development for the clinical routine. Many benefits concerning the diagnostic range have been discussed, which include low-dose, high-resolution, quantitative, and K-edge imaging. First prototype systems [69, 84] have been installed and have demonstrated benefits along the same lines. At the same time, one has to realize that this development comes with challenges, which translate into non-ideal imaging performances. The harmonization between hardware and software will significantly aid the process of overcoming those current shortcomings. In this chapter, we presented algorithmic solutions, which address a wide range of possible spectral CT implementations and the challenges that come along with each of them. In three sections, we introduced the main classes of spectral CT reconstruction algorithms: image-based and projection-based, which perform decomposition into materials and tomographic reconstruction separately and are therefore referred to as "two-step" methods, and one-step inversion, which merges both decomposition and reconstruction into a single inverse problem. For the coming years, while spectral CT will fully translate into the clinical routine, further algorithmic developments will be necessary to improve, for example, the sensitivity, to constantly extend the diagnostic range of CT imaging.

REFERENCES

1. J.F.P.J. Abascal, N. Ducros, and F. Peyrin. Nonlinear material decomposition using a regularized iterative scheme based on the Bregman distance. *Inverse Probl*, 34:124003, October 2018.
2. R.E. Alvarez. Estimator for photon counting energy selective x-ray imaging with multibin pulse height analysis. *Med Phys*, 38(5):2324–2334, May 2011.
3. R.E. Alvarez. Efficient, non-iterative estimator for imaging contrast agents with spectral x-ray detectors. *IEEE Trans Med Imaging*, 35(4):1138–1146, April 2016.
4. R.E. Alvarez and A. Macovski. Energy-selective reconstructions in x-ray computerized tomography. *Phys Med Biol*, 21(5):733–744, September 1976.
5. B. Brendel, F. Bergner, K. Brown, and T. Koehler. Penalized likelihood decomposition for dual layer spectral CT. In *Fourth international conference on image formation in X-ray computed tomography*, pages 41–44, Bamberg, Germany, 2016.
6. R.A. Brooks. A quantitative theory of the Hounsfield unit and its application to dual energy scanning. *J Comput Assist Tomogr*, 1(4):487–493, October 1977.
7. R.A. Brooks and G. Di Chiro. Beam hardening in x-ray reconstructive tomography. *Phys Med Biol,* 21(3):390–398, May 1976.
8. T.M. Buzug. *Computed Tomography: From Photon Statistics to Modern Cone-Beam CT.* Springer Science & Business Media, 2008.
9. C. Cai, T. Rodet, S. Legoupil, and A. Mohammad-Djafari. A full-spectral bayesian reconstruction approach based on the material decomposition model applied in dual-energy computed tomography. *Med Phys*, 40:111916, November 2013.
10. J. Cammin, J. Xu, W.C. Barber, J.S. Iwanczyk, N.E. Hartsough, and K. Taguchi. A cascaded model of spectral distortions due to spectral response effects and pulse pileup effects in a photon-counting x-ray detector for CT. *Med Phys*, 41(4):041905, March 2014.
11. A. Chambolle and T. Pock. A first-order primal-dual algorithm for convex problems with applications to imaging. *J Math Imaging Vis*, 40(1):120–145, May 2011.
12. B. Chen, Z. Zhang, E.Y. Sidky, D. Xia, and X. Pan. Image reconstruction and scan configurations enabled by optimization-based algorithms in multispectral CT. *Phys Med Biol*, 62:8763–8793, November 2017.
13. E. Chouzenoux, J.-C. Pesquet, and A. Repetti. Variable metric forward–backward algorithm for minimizing the sum of a differentiable function and a convex function. *J Optimiz Theory App*, 162(1):107–132, July 2014.
14. Q. Ding, T. Niu, X. Zhang, and Y. Long. Image-domain multi-material decomposition for dual-energy CT based on prior information of material images. *Med Phys*, 45(8):3614–3626, May 2018.
15. X. Dong, T. Niu, and L. Zhu. Combined iterative reconstruction and image-domain decomposition for dual energy CT using total-variation regularization. *Med Phys*, 41(5):051909, April 2014.

16. N. Ducros, J.F.P.-J. Abascal, B. Sixou, S. Rit, and F. Peyrin. Regularization of nonlinear decomposition of spectral x-ray projection images. *Med Phys*, 44:e174–e187, September 2017.
17. S. Ehn, T. Sellerer, K. Mechlem, A. Fehringer, M. Epple, J. Herzen, F. Pfeiffer, and P.B. Noël. Basis material decomposition in spectral CT using a semi-empirical, polychromatic adaption of the Beer-Lambert model. *Phys Med Biol*, 62:N1–N17, January 2017.
18. R. Foygel Barber, E.Y. Sidky, T. Gilat Schmidt, and X. Pan. An algorithm for constrained one-step inversion of spectral CT data. *Phys Med Biol*, 61(10):3784–3818, May 2016.
19. R. Gordon, R. Bender, and G.T. Herman. Algebraic reconstruction techniques (ART) for three-dimensional electron microscopy and x-ray photography. *J Theor Biol*, 29(3):471–481, December 1970.
20. P.J. Green. Bayesian reconstructions from emission tomography data using a modified EM algorithm. *IEEE Trans Med Imaging*, 9(1):84–93, March 1990.
21. T. Hohweiller, N. Ducros, F. Peyrin, and B. Sixou. Spectral CT material decomposition in the presence of Poisson noise: A Kullback–Leibler approach. *IRBM*, 38(4):214–218, 2017. Research in Imaging and Health TechnologieS 2017 (RITS 2017).
22. W.A. Kalender, E. Klotz, and L. Kostaridou. An algorithm for noise suppression in dual energy CT material density images. *IEEE Trans Med Imaging*, 7(3):218–224, September 1988.
23. W.A. Kalender, W.H. Perman, J.R. Vetter, and E. Klotz. Evaluation of a prototype dual-energy computed tomographic apparatus. I. Phantom studies. *Med Phys*, 13:334–339, May 1986.
24. D. Kazantsev, J.S. Jørgensen, M.S. Andersen, W.R.B. Lionheart, P.D. Lee, and P.J. Withers. Joint image reconstruction method with correlative multi-channel prior for x-ray spectral computed tomography. *Inverse Probl*, 34(6):064001, April 2018.
25. K. Lange, D.R. Hunter, and I. Yang. Optimization transfer using surrogate objective functions. *J Comput Graph Stat*, 9(1):1–20, March 2000.
26. O. Lee, S. Kappler, C. Polster, and K. Taguchi. Estimation of basis line-integrals in a spectral distortion-modeled photon counting detector using low-order polynomial approximation of x-ray transmittance. *IEEE Trans Med Imaging*, 36(2):560–573, February 2017.
27. O. Lee, S. Kappler, C. Polster, and K. Taguchi. Estimation of basis line-integrals in a spectral distortion-modeled photon counting detector using low-rank approximation-based x-ray transmittance modeling: K-edge imaging application. *IEEE Trans Med Imaging*, 36(11):2389–2403, November 2017.
28. L.A. Lehmann, R.E. Alvarez, A. Macovski, W.R. Brody, N.J. Pelc, S.J. Riederer, and A.L. Hall. Generalized image combinations in dual KVP digital radiography. *Med Phys*, 8(5):659–667, September 1981.
29. J.-M. Letang, N. Freud, and G. Peix. Signal-to-noise ratio criterion for the optimization of dual-energy acquisition using virtual x-ray imaging: Application to glass wool. *J Electron Imaging*, 13(3):436–449, July 2004.
30. M. Li, Y. Zhao, and P. Zhang. Accurate iterative FBP reconstruction method for material decomposition of dual energy CT. *IEEE Trans Med Imaging*, 38(3):802–812, March 2019.
31. Z. Li, S. Leng, L. Yu, Z. Yu, and C.H. McCollough. Image-based material decomposition with a general volume constraint for photon-counting CT. *Proceedings of SPIE–the International Society for Optical Engineering*, 9412, 2015.
32. X. Liu, L. Yu, A.N. Primak, and C.H. McCollough. Quantitative imaging of element composition and mass fraction using dual-energy CT: Three-material decomposition. *Med Phys*, 36:1602–1609, May 2009.
33. Y. Long and J.A. Fessler. Multi-material decomposition using statistical image reconstruction for spectral CT. *IEEE Trans Med Imaging,* 33(8):1614–1626, August 2014.
34. C. Maass, M. Baer, and M. Kachelriess. Image-based dual energy CT using optimized precorrection functions: A practical new approach of material decomposition in image domain. *Med Phys*, 36:3818–3829, August 2009.
35. C. Maass, E. Meyer, and M. Kachelriess. Exact dual energy material decomposition from inconsistent rays (MDIR). *Med Phys*, 38:691–700, February 2011.
36. B. De Man, J. Nuyts, P. Dupont, G. Marchal, and P. Suetens. An iterative maximum-likelihood polychromatic algorithm for CT. *IEEE Trans Med Imaging*, 20:999–1008, October 2001.
37. M. Mannil, T. Hickethier, J. von Spiczak, M. Baer, A. Henning, M. Hertel, B. Schmidt, T. Flohr, D. Maintz, and H. Alkadhi. Photon-counting CT: High-resolution imaging of coronary stents. *Invest Radiol*, 53:143–149, March 2018.
38. C.H. McCollough, S. Leng, L. Yu, and J.G. Fletcher. Dual- and multi-energy CT: Principles, technical approaches, and clinical applications. *Radiology*, 276(3):637–653, September 2015.

39. K. Mechlem, S. Allner, S. Ehn, K. Mei, E. Braig, D. Münzel, F. Pfeiffer, and P.B. Noël. A post-processing algorithm for spectral CT material selective images using learned dictionaries. *Biomed Phys Eng Express*, 3(2):025009, February 2017.
40. K. Mechlem, S. Ehn, T. Sellerer, E. Braig, D. Münzel, F. Pfeiffer, and P.B. Noël. Joint statistical iterative material image reconstruction for spectral computed tomography using a semi-empirical forward model. *IEEE Trans Med Imaging*, 37(1):68–80, January 2018.
41. K. Mechlem, T. Sellerer, S. Ehn, D. Münzel, E. Braig, J. Herzen, P.B. Noël, and F. Pfeiffer. Spectral angiography material decomposition using an empirical forward model and a dictionary-based regularization. *IEEE Trans Med Imaging*, 37(10):2298–2309, October 2018.
42. P. Mendonca, P. Lamb, and D. Sahani. A flexible method for multi-material decomposition of dual-energy CT images. *IEEE Trans Med Imaging*, 33(1):99–116, January 2014.
43. C. Mory, B. Brendel, K. Erhard, and S. Rit. Generalized least squares for spectral and dual energy CT: a simulation study. In *Sixth international conference on image formation in X-ray computed tomography*, pages 98–101, Salt Lake City, USA, 2018.
44. C. Mory, B. Sixou, S. Si-Mohamed, L. Boussel, and S. Rit. Comparison of five one-step reconstruction algorithms for spectral CT. *Phys Med Biol*, 63:235001, November 2018.
45. B. Münch, P. Trtik, F. Marone, and M. Stampanoni. Stripe and ring artifact removal with combined Wavelet–Fourier filtering. *Optics Express*, 17:8567–8591, May 2009.
46. F. Natterer. *The Mathematics of Computerized Tomography*. John Wiley & Sons, 1986.
47. J.A. Nelder and R. Mead. A simplex method for function minimization. *The Computer Journal,* 7(4):308–313, January 1965.
48. S. Niu, G. Yu, J. Ma, and J. Wang. Nonlocal low-rank and sparse matrix decomposition for spectral CT reconstruction. *Inverse Probl*, 34, February 2018.
49. T. Niu, X. Dong, M. Petrongolo, and L. Zhu. Iterative image-domain decomposition for dual-energy CT. *Med Phys*, 41(4):041901, April 2014.
50. X. Pan, E.Y. Sidky, and M. Vannier. Why do commercial CT scanners still employ traditional, filtered back-projection for image reconstruction? *Inverse Probl*, 25:1230009, January 2009.
51. A. Pourmorteza, R. Symons, A. Henning, S. Ulzheimer, and D.A. Bluemke. Dose efficiency of quarter-millimeter photon-counting computed tomography: First-in-human results. *Invest Radiol*, 53:365–372, June 2018.
52. J. Qi and R.M. Leahy. Iterative reconstruction techniques in emission computed tomography. *Phys Med Biol*, 51:R541–R578, August 2006.
53. D.S. Rigie and P.J. La Rivière. Joint reconstruction of multi-channel, spectral CT data via constrained total nuclear variation minimization. *Phys Med Biol*, 60(5):1741–1762, February 2015.
54. P.-A. Rodesch, V. Rebuffel, C. Fournier, F. Forbes, and L. Verger. Spectral CT reconstruction with an explicit photon-counting detector model: A one-step approach. *Medical Imaging 2018: Physics of Medical Imaging*, 10573: 1057353. International Society for Optics and Photonics, 2018.
55. E. Roessl, H. Daerr, and R. Proksa. A fourier approach to pulse pile-up in photon-counting x-ray detectors. *Med Phys*, 43:1295–1298, March 2016.
56. E. Roessl and C. Herrmann. Cramér-Rao lower bound of basis image noise in multiple-energy x-ray imaging. *Phys Med Biol*, 54:1307–1318, March 2009.
57. E. Roessl and R. Proksa. K-edge imaging in x-ray computed tomography using multi-bin photon counting detectors. *Phys Med Biol*, 52(15):4679–4696, August 2007.
58. M. Salehjahromi, Y. Zhang, and H. Yu. Comparison study of regularizations in spectral computed tomography reconstruction. *Sens Imaging*, 19, March 2018.
59. A. Sawatzky, Q. Xu, C.O. Schirra, and M.A. Anastasio. Proximal ADMM for multi-channel image reconstruction in spectral x-ray CT. *IEEE Tran Med Imaging,* 33(8):1657–1668, August 2014.
60. C.O. Schirra, B. Brendel, M.A. Anastasio, and E. Roessl. Spectral CT: A technology primer for contrast agent development. *Contrast Media Mol Imaging*, 9(1):62–70, January 2014.
61. C.O. Schirra, E. Roessl, T. Koehler, B. Brendel, A. Thran, D. Pan, M.A. Anastasio, and R. Proksa. Statistical reconstruction of material decomposed data in spectral CT. *IEEE Tran Med Imaging,* 32(7):1249–1257, July 2013.
62. J.P. Schlomka, E. Roessl, R. Dorscheid, S. Dill, G. Martens, T. Istel, C. Bäumer, C. Herrmann, R. Steadman, G. Zeitler, A. Livne, and R. Proksa. Experimental feasibility of multi-energy photon-counting K-edge imaging in pre-clinical computed tomography. *Phys Med Biol*, 53(15):4031–4047, August 2008.
63. T. Schmidt, R. Foygel Barber, and E. Sidky. A spectral CT method to directly estimate basis material maps from experimental photon-counting data. *IEEE Tran Med Imaging*, 36(9):1808–1819, April 2017.

64. T. Schoonjans, A. Brunetti, B. Golosio, M. Sanchez del Rio, V.A. Solé, C. Ferrero, and L. Vincze. The xraylib library for x-ray–matter interactions. Recent developments. *Spectrochim Acta B*, 66(11-12):776–784, November 2011.
65. S. Si-Mohamed, D. Bar-Ness, M. Sigovan, D.P. Cormode, P. Coulon, E. Coche, A. Vlassenbroek, G. Normand, L. Boussel, and P. Douek. Review of an initial experience with an experimental spectral photon-counting computed tomography system. *Nucl Instrum Meth A*, 873:27–35, November 2017.
66. E.Y. Sidky and X. Pan. Image reconstruction in circular cone-beam computed tomography by constrained, total-variation minimization. *Phys Med Biol*, 53(17):4777–4807, September 2008.
67. E.Y. Sidky, L. Yu, X. Pan, Y. Zou, and M. Vannier. A robust method of x-ray source spectrum estimation from transmission measurements: Demonstrated on computer simulated, scatter-free transmission data. *J Appl Phys*, 97(12):124701, June 2005.
68. R. Symons, Y. De Bruecker, J. Roosen, L. Van Camp, T.E. Cork, S. Kappler, S. Ulzheimer, V. Sandfort, D.A. Bluemke, and A. Pourmorteza. Quarter-millimeter spectral coronary stent imaging with photon-counting CT: Initial experience. *J Cardiovasc Comput*, 12(6):509–515, November 2018.
69. K. Taguchi. Energy-sensitive photon counting detector-based x-ray computed tomography. *Radiol Phys Technol*, 10:8–22, March 2017.
70. K. Taguchi, E.C. Frey, X. Wang, J.S. Iwanczyk, and W.C. Barber. An analytical model of the effects of pulse pileup on the energy spectrum recorded by energy resolved photon counting x-ray detectors. *Med Phys*, 37:3957–3969, August 2010.
71. K. Taguchi, T. Itoh, M.K. Fuld, E. Fournie, O. Lee, and K. Noguchi. "X-Map 2.0" for edema signal enhancement for acute ischemic stroke using non-contrast-enhanced dual-energy computed tomography. *Invest Radiol*, 53:432–439, July 2018.
72. K. Taguchi, C. Polster, O. Lee, K. Stierstorfer, and S. Kappler. Spatio-energetic cross talk in photon counting detectors: Detector model and correlated Poisson data generator. *Med Phys,* 43:6386, December 2016.
73. K. Taguchi, K. Stierstorfer, C. Polster, O. Lee, and S. Kappler. Spatio-energetic cross-talk in photon counting detectors: Numerical detector model (PcTK) and workflow for CT image quality assessment. *Med Phys*, 45:1985–1998, May 2018.
74. K. Taguchi, M. Zhang, E.C. Frey, X. Wang, J.S. Iwanczyk, E. Nygard, N.E. Hartsough, B.M.W. Tsui, and W.C. Barber. Modeling the performance of a photon counting x-ray detector for CT: Energy response and pulse pileup effects. *Med Phys*, 38:1089–1102, February 2011.
75. S. Tairi, S. Anthoine, C. Morel, and Y. Boursier. Simultaneous reconstruction and separation in a spectral CT framework with a proximal variable metric algorithm. In *Sixth international conference on image formation in X-ray computed tomography*, pages 32–35, Salt Lake City, USA, 2018.
76. S. Tao, K. Rajendran, C.H. McCollough, and S. Leng. Material decomposition with prior knowledge aware iterative denoising (MD-PKAID). *Phys Med Biol*, 63:195003, September 2018.
77. S. Tilley II, M. Jacobson, Q. Cao, M. Brehler, A. Sisniega, W. Zbijewski, and J.W. Stayman. Penalized-likelihood reconstruction with high-fidelity measurement models for high-resolution cone-beam imaging. *IEEE Trans Med Imaging*, 37(4):988–999, April 2018.
78. S. Tilley II, W. Zbijewski, J.H. Siewerdsen, and J.W. Stayman. A general CT reconstruction algorithm for model-based material decomposition. *Proceedings of SPIE–The International Society for Optical Engineering*, 10573, March 2018.
79. M. Torikoshi, T. Tsunoo, M. Sasaki, M. Endo, Y. Noda, Y. Ohno, T. Kohno, K. Hyodo, K. Uesugi, and N. Yagi. Electron density measurement with dual-energy x-ray CT using synchrotron radiation. *Phys Med Biol*, 48(5):673–685, March 2003.
80. W. van Elmpt, G. Landry, M. Das, and F. Verhaegen. Dual energy CT in radiotherapy: Current applications and future outlook. *Radiother Oncol*, 119(1):137–144, April 2016.
81. G. Vilches-Freixas, J.M. Létang, S. Brousmiche, E. Romero, M. Vila Oliva, D. Kellner, H. Deutschmann, P. Keuschnigg, P. Steininger, and S. Rit. Technical note: Procedure for the calibration and validation of kilo-voltage cone-beam CT models. *Med Phys*, 43(9):5199–5204, 2016.
82. X. Wang, D. Meier, K. Taguchi, D.J. Wagenaar, B.E. Patt, and E.C. Frey. Material separation in x-ray CT with energy resolved photon-counting detectors. *Med Phys*, 38:1534–1546, March 2011.
83. T. Weidinger, T.M. Buzug, T. Flohr, S. Kappler, and K. Stierstorfer. Polychromatic iterative statistical material image reconstruction for photon-counting computed tomography. *Int J Biomed Imaging*, 2016:5871604, 2016.
84. M.J. Willemink, M. Persson, A. Pourmorteza, N.J. Pelc, and D. Fleischmann. Photon-counting CT: Technical principles and clinical prospects. *Radiology*, 289:293–312, November 2018.

85. W. Wu, Y. Zhang, Q. Wang, F. Liu, P. Chen, and H. Yu. Low-dose spectral CT reconstruction using image gradient $\ell 0$–norm and tensor dictionary. *Appl Math Model*, 63:538–557, 2018.
86. W. Wu, Y. Zhang, Q. Wang, F. Liu, F. Luo, and H. Yu. Spatial-spectral cube matching frame for spectral CT reconstruction. *Inverse Probl*, 34(10):104003, 2018.
87. Q. Xu, A. Sawatzky, M.A. Anastasio, and C.O. Schirra. Sparsity-regularized image reconstruction of decomposed K-edge data in spectral CT. *Phys Med Biol*, 59(10):N65–N79, May 2014.
88. L. Yan, T. Wu, S. Zhong, and Q. Zhang. A variation-based ring artifact correction method with sparse constraint for flat-detector CT. *Phys Med Biol*, 61(3):1278–1292, February 2016.
89. L. Yu, X. Liu, and C.H. McCollough. Pre-reconstruction three-material decomposition in dual-energy CT. *Medical Imaging 2009: Physics of Medical Imaging*, 7258: 72583V. International Society for Optics and Photonics, 2009.
90. Z. Yu, S. Leng, Z. Li, and C.H. McCollough. Spectral prior image constrained compressed sensing (spectral PICCS) for photon-counting computed tomography. *Phys Med Biol*, 61:6707–6732, September 2016.
91. B. Zhao, H. Ding, Y. Lu, G. Wang, J. Zhao, and S. Molloi. Dual-dictionary learning-based iterative image reconstruction for spectral computed tomography application. *Phys Med Biol*, 57:8217–8229, December 2012.
92. Y. Zhao, X. Zhao, and P. Zhang. An extended algebraic reconstruction technique (E-ART) for dual spectral CT. *IEEE Trans Med Imaging*, 34(3):761–768, March 2015.
93. K.C. Zimmerman and T.G. Schmidt. Experimental comparison of empirical material decomposition methods for spectral CT. *Phys Med Biol*, 60(8):3175–3191, April 2015.
94. Y. Zou and M.D. Silver. Analysis of fast kV-switching in dual energy CT using a pre-reconstruction decomposition technique. *Medical Imaging 2008: Physics of Medical Imaging*, 6913: 691313. International Society for Optics and Photonics, 2008.

C

Article illustrating Part III Proton computed tomography

This appendix contains a copy of [J57]:

Rit, S., Dedes, G., Freud, N., Sarrut, D., Létang, J., "Filtered backprojection proton CT reconstruction along most likely paths". In: *Med Phys* 40.3, 031103 (2013), p. 031103

Filtered backprojection proton CT reconstruction along most likely paths

Simon Rit,[a] George Dedes, Nicolas Freud, David Sarrut, and Jean Michel Létang
Université de Lyon, CREATIS, CNRS UMR5220, Inserm U1044, INSA-Lyon, Université Lyon 1, Centre Léon Bérard, 69008 Lyon, France

(Received 28 July 2012; revised 7 October 2012; accepted for publication 11 October 2012; published 28 February 2013)

Purpose: Proton CT (pCT) has the potential to accurately measure the electron density map of tissues at low doses but the spatial resolution is prohibitive if the curved paths of protons in matter is not accounted for. The authors propose to account for an estimate of the most likely path of protons in a filtered backprojection (FBP) reconstruction algorithm.
Methods: The energy loss of protons is first binned in several proton radiographs at different distances to the proton source to exploit the depth-dependency of the estimate of the most likely path. This process is named the distance-driven binning. A voxel-specific backprojection is then used to select the adequate radiograph in the distance-driven binning in order to propagate in the pCT image the best achievable spatial resolution in proton radiographs. The improvement in spatial resolution is demonstrated using Monte Carlo simulations of resolution phantoms.
Results: The spatial resolution in the distance-driven binning depended on the distance of the objects from the source and was optimal in the binned radiograph corresponding to that distance. The spatial resolution in the reconstructed pCT images decreased with the depth in the scanned object but it was always better than previous FBP algorithms assuming straight line paths. In a water cylinder with 20 cm diameter, the observed range of spatial resolutions was $0.7 - 1.6$ mm compared to $1.0 - 2.4$ mm at best with a straight line path assumption. The improvement was strongly enhanced in shorter 200° scans.
Conclusions: Improved spatial resolution was obtained in pCT images with filtered backprojection reconstruction using most likely path estimates of protons. The improvement in spatial resolution combined with the practicality of FBP algorithms compared to iterative reconstruction algorithms makes this new algorithm a candidate of choice for clinical pCT. © *2013 American Association of Physicists in Medicine*. [http://dx.doi.org/10.1118/1.4789589]

Key words: proton computed tomography, proton CT, filtered backprojection, most likely path

I. INTRODUCTION

Proton computed tomography (pCT) has been considered very early in the history of CT (Ref. 1) with a continuous development until the beginning of the 1980s. Its investigation was then slowed down because the ratio between benefits and cost was too low compared to photon CT scanners but the development of proton therapy has triggered new studies on pCT scanners.[2–4]

pCT could indeed improve proton therapy compared to current clinical practice since it could reduce the uncertainty of the proton therapy planning due to the lack of accuracy in the proton stopping power of tissues computed from photon CT images.[5,6] This uncertainty contributes to the range uncertainty margin which is between 2.5% + 1 mm and 3.5% + 3 mm depending on the hospital.[7] It would be reduced with pCT since the proton stopping power is better characterized with protons than photons. Another potential benefit is the reduction of the imaging dose compared to photon CT (Refs. 8 and 9) since the energy loss of every proton can be measured and provides information about the patient tissues, while measurement of the probability of interactions of photons with tissues requires a large number of photons. Finally, pCT is an additional modality which could have its own advantages for improving the diagnostic.[10]

pCT has one major drawback compared to photon CT, its lack of spatial resolution. Indeed, protons traversing matter undergo multiple deflections due to multiple Coulomb scattering, resulting in curved trajectories and blurred proton radiographs.[11] Many research initiatives of the past decade have focused on this issue and it has been proposed to track each proton individually using pairs of position-sensitive detectors before and after the scanned object.[3,4,12] The measured positions are used to estimate the most likely path of each individual proton which has proven efficient to improve spatial resolution using Monte Carlo simulations.[9,13–15]

The estimation of the most likely path of each proton resolves in a curve. The pCT reconstruction problem, therefore, relates to the inversion of the generalized Radon transform where one integrates the sought pCT image over a family of curves. This problem has already been studied in motion-compensated CT reconstruction.[16] There is still no exact analytical inversion for curved lines, it is only known how to compensate for a motion that preserves the straightness of integration lines.[17] However, approximate algorithms based

on voxel-specific backprojection have proven efficient to increase spatial resolution.[18,19]

Most likely paths have only been used in pCT reconstruction algorithms to select the protons having straight trajectories in a filtered backprojection (FBP) algorithm[8] or in iterative reconstruction algorithms.[20,21] However, FBP algorithms with most likely paths would be desirable in clinical practice to improve spatial resolution with a practical algorithm, similar to what has been developed for motion-compensated CT.[22] In this paper, we propose a practical FBP algorithm for pCT reconstruction using the curved most likely path of each proton based on voxel-specific backprojections with an intermediate binning step to handle the acquired list-mode data.

II. METHOD

II.A. pCT reconstruction problem

Protons lose most of their energy via electromagnetic inelastic collisions if they do not undergo nuclear interactions. The local energy loss $\mathrm{d}E$ at a point of space $\boldsymbol{x} \in \mathbb{R}^3$ is given by

$$-\frac{\mathrm{d}E}{\mathrm{d}x}(\boldsymbol{x}) = \eta(\boldsymbol{x})S(I(\boldsymbol{x}), E(\boldsymbol{x})), \tag{1}$$

where $\eta : \mathbb{R}^3 \to \mathbb{R}$ is the relative electron density with respect to a reference medium (water in this study), $S : \mathbb{R}^2 \to \mathbb{R}$ is the proton stopping power in the reference medium given by the Bethe-Bloch equation[23] which, under realistic simplifications,[24] only depends on $I : \mathbb{R}^3 \to \mathbb{R}$, the tissue-specific ionization potential, and $E : \mathbb{R}^3 \to \mathbb{R}$, the energy of the proton crossing the tissue. The ionization potential I varies moderately in human tissues and has a limited effect on S so, in pCT, it is typically approximated to that of water, i.e., $I(\boldsymbol{x}) = I_{\text{water}} = 78\,\text{eV},\ \forall \boldsymbol{x} \in \mathbb{R}^3$ in our simulations. Under this assumption, integrating Eq. (1) leads to the line integral

$$\int_{\boldsymbol{\Gamma}_i} \eta(\boldsymbol{x})\mathrm{d}l = \int_{E_i^{out}}^{E_i^{in}} \frac{\mathrm{d}E}{S(I_{\text{water}}, E)} \tag{2}$$

with $i \in \mathbf{I} \subset \mathbb{N}$ the index of tracked protons, $\boldsymbol{\Gamma}_i(t) \in \mathbb{R}^3$ the curved trajectory of the proton, function of time $t \in \mathbb{R}$, and E_i^{in} and E_i^{out} the energies of the proton at the entrance and exit detectors. Finding η from E_i^{in}, E_i^{out} and an estimate $\hat{\boldsymbol{\Gamma}}_i(t) \in \mathbb{R}^3$ of the path $\boldsymbol{\Gamma}_i$ for a set $\mathbf{I}$ of protons is the pCT reconstruction problem.

The energy integral is defined as $G : \mathbb{R}^2 \to \mathbb{R}$ to simplify notations in the following with

$$G(E_i^{in}, E_i^{out}) = \int_{E_i^{out}}^{E_i^{in}} \frac{\mathrm{d}E}{S(I_{\text{water}}, E)}. \tag{3}$$

In practice, the incident energy E_i^{in} of a monoenergetic proton beam would be assumed to be known, the exit energy could be measured with, e.g., a calorimeter detector, and the energy loss in air would be neglected.

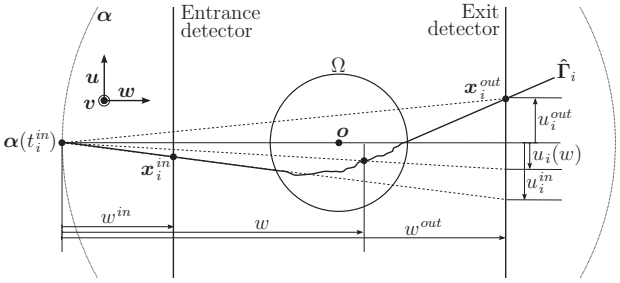

FIG. 1. Schematic top view of the pCT scanner used in this study. The signed distances w^{out}, w^{in}, w and u_i^{out}, u_i^{in}, $u_i(w)$ are used in Eqs. (6)– (8), respectively. The effect of multiple Coulomb scattering in the object has purposely been exaggerated for the sake of the clarity of the scheme.

II.B. pCT scanner for most likely path estimation

Proton path estimation is a crucial problem in pCT reconstruction because it directly influences the spatial resolution.[11] Several solutions have been proposed to the problem of most likely path (MLP) estimation.[9,13,14] These recent works on MLP estimation rely on pCT scanners[3,4] which are able to track the position and the direction of each proton, before and after traversing the object.

We assumed a similar cone-beam pCT scanner in this study with a proton source following a circular trajectory $\boldsymbol{\alpha}(t) \in \mathbb{R}^3$ around the axis defined by the isocenter $\boldsymbol{o} \in \mathbb{R}^3$ and the unit axis $\boldsymbol{v} \in \mathbb{R}^3$ (Fig. 1). 2D tracking detectors were positioned before and after the scanned object to record the entrance and exit positions and directions of each proton noted

$$\begin{cases} \boldsymbol{x}_i^{in} &= \boldsymbol{\Gamma}_i(t_i^{in}) \\ \boldsymbol{x}_i^{out} &= \boldsymbol{\Gamma}_i(t_i^{out}) \\ \dot{\boldsymbol{x}}_i^{in} &= \dfrac{\mathrm{d}\boldsymbol{\Gamma}_i(t_i^{in})}{\mathrm{d}t} \\ \dot{\boldsymbol{x}}_i^{out} &= \dfrac{\mathrm{d}\boldsymbol{\Gamma}_i(t_i^{out})}{\mathrm{d}t} \end{cases} \tag{4}$$

with $t_i^{in}, t_i^{out} \in \mathbb{R}$ the times at which proton i crosses the entrance and exit tracking detectors, respectively. We define the unit vectors $\boldsymbol{u}, \boldsymbol{w} : \mathbb{R}^3 \to \mathbb{R}^3$ depending on the source position, with $\boldsymbol{w}(\boldsymbol{\alpha}(t)) = -\boldsymbol{\alpha}(t)/\|\boldsymbol{\alpha}(t)\|_2$ and $\boldsymbol{u}(\boldsymbol{\alpha}(t)) = \boldsymbol{v} \times \boldsymbol{w}(\boldsymbol{\alpha}(t))$ to dispose of a 3D Cartesian coordinate system $\{\boldsymbol{u}, \boldsymbol{v}, \boldsymbol{w}\}$ in the frame of reference of the source/detector pair. $\boldsymbol{u}$ and $\boldsymbol{v}$ therefore define the orientation of the detectors and $\boldsymbol{w}$ the main beam direction. We also assumed that the convex hull of the object $\Omega \subset \mathbb{R}^3$ was known which can practically be measured with a surface scanner or an initial reconstruction without MLPs.

The algorithm proposed in this work is applicable to any MLP estimation $\hat{\boldsymbol{\Gamma}}_i$ from the convex hull Ω and the list-mode proton data E_i^{in}, $\boldsymbol{x}_i^{in}$, $\dot{\boldsymbol{x}}_i^{in}$, E_i^{out}, $\boldsymbol{x}_i^{out}$, and $\dot{\boldsymbol{x}}_i^{out}$.

II.C. Distance-driven binning

Our objective is to adapt existing filtered backprojection algorithms for pCT reconstruction. Previous filtered backprojection algorithms for pCT have binned list-mode proton data

in virtual proton radiographs and we recall first this binning process. Let $j \in \mathbf{J} \subset \mathbb{Z}^2$ be a set of spatial indices corresponding to a grid of pixels of the exit tracking detector and $h : \mathbb{R}^2 \to \mathbb{R}$ their indicators,

$$h_j(\boldsymbol{y}) = \begin{cases} 1 & \text{if } \boldsymbol{y} \in \mathbb{R}^2 \text{ is in pixel } j, \\ 0 & \text{else.} \end{cases} \tag{5}$$

It is assumed that the pCT scanner operates in a step-and-shoot mode with gantry rotations only during beam-off time to have, during beam-on times, a discrete number of source positions $\boldsymbol{a}_p \in \mathbb{R}^3$, $p \in \mathbf{P} = \{1, ..., P\}$ with $P \in \mathbb{N}$ the number of source positions. The list-mode proton data are partitioned in subsets $\mathbf{I}_p \subset \mathbf{I}$ of protons emitted from the same source position. We define the binning of list-mode data for each source position in virtual proton radiographs sampled at the exit detector as

$$g^{out}_{j,p} = \frac{\sum_{i\in\mathbf{I}_p} h_j\left(u^{out}_i, v^{out}_i\right) G\left(E^{in}_i, E^{out}_i\right)}{\sum_{i\in\mathbf{I}_p} h_j\left(u^{out}_i, v^{out}_i\right)} \tag{6}$$

with the distances u^{out}_i and v^{out}_i relative to $\boldsymbol{a}_p = \boldsymbol{\alpha}(t^{in}_i)$ in the $\{\boldsymbol{u}, \boldsymbol{v}, \boldsymbol{w}\}$ system (Fig. 1),

$$\begin{cases} u^{out}_i = \left(\boldsymbol{x}^{out}_i - \boldsymbol{a}_p\right) \cdot \boldsymbol{u}(\boldsymbol{a}_p), \\ v^{out}_i = \left(\boldsymbol{x}^{out}_i - \boldsymbol{a}_p\right) \cdot \boldsymbol{v}. \end{cases}$$

Repeating this operation for each of the P source positions, one obtains a typical set of P projection images that has already been used in standard filtered-backprojection algorithms for pCT reconstruction assuming a straight proton path between $\boldsymbol{a}_p$ and $\boldsymbol{x}^{out}_i$.[8,24–26]

We observe that this principle can be extended, and we propose to do another binning using the entrance positions $\boldsymbol{x}^{in}_i$ to bin list-mode proton data on the exit detector assuming a straight proton path going through $\boldsymbol{a}_p$ and $\boldsymbol{x}^{in}_i$, i.e.,

$$g^{in}_{j,p} = \frac{\sum_{i\in\mathbf{I}_p} h_j\left(u^{in}_i, v^{in}_i\right) G\left(E^{in}_i, E^{out}_i\right)}{\sum_{i\in\mathbf{I}_p} h_j\left(u^{in}_i, v^{in}_i\right)} \tag{7}$$

with the distances (Fig. 1),

$$\begin{cases} u^{in}_i = \dfrac{w^{out}}{w^{in}}\left(\boldsymbol{x}^{in}_i - \boldsymbol{a}_p\right) \cdot \boldsymbol{u}(\boldsymbol{a}_p), \\ v^{in}_i = \dfrac{w^{out}}{w^{in}}\left(\boldsymbol{x}^{in}_i - \boldsymbol{a}_p\right) \cdot \boldsymbol{v}, \\ w^{in} = \left(\boldsymbol{x}^{in}_i - \boldsymbol{a}_p\right) \cdot \boldsymbol{w}(\boldsymbol{a}_p), \\ w^{out} = \left(\boldsymbol{x}^{out}_i - \boldsymbol{a}_p\right) \cdot \boldsymbol{w}(\boldsymbol{a}_p). \end{cases}$$

The ratio w^{out}/w^{in} is the constant magnification from the entrance to the exit detection plane produced by a cone-beam with apex $\boldsymbol{a}_p$ to obtain the coordinates on the exit flat panel. Therefore, if protons were traveling in straight lines, $g^{in}_{j,p}$ and $g^{out}_{j,p}$ would be equal and their actual differences are due to multiple Coulomb scattering.

We extend the binning to any distance from the source and propose the concept of distance-driven binning, given by

$$g_{j,p}(w) = \frac{\sum_{i\in\mathbf{I}_p} h_j(u_i(w), v_i(w)) G(E^{in}_i, E^{out}_i)}{\sum_{i\in\mathbf{I}_p} h_j(u_i(w), v_i(w))} \tag{8}$$

with the distances illustrated in Fig. 1,

$$\begin{cases} u_i(w) = \dfrac{w^{out}}{w}(\hat{\boldsymbol{\Gamma}}_i(t_{i,w}) - \boldsymbol{a}_p) \cdot \boldsymbol{u}(\boldsymbol{a}_p), \\ v_i(w) = \dfrac{w^{out}}{w}(\hat{\boldsymbol{\Gamma}}_i(t_{i,w}) - \boldsymbol{a}_p) \cdot \boldsymbol{v}. \end{cases}$$

Here, $t_{i,w}$ is the time at which proton i crosses the plane parallel to the detectors at distance $w \in \mathbb{R}$ from the source, i.e., $(\hat{\boldsymbol{\Gamma}}_i(t_{i,w}) - \boldsymbol{a}_p) \cdot \boldsymbol{w}(\boldsymbol{a}_p) = w$. Equation (8) is the extension of Eqs. (6) and (7) to any distance w using the most likely path $\hat{\boldsymbol{\Gamma}}_i$ of proton i to interpolate intermediate positions between entrance and exit positions $\boldsymbol{x}^{in}_i$ and $\boldsymbol{x}^{out}_i$; it is indeed an interpolation process since $g_{j,p}(w^{out}) = g^{out}_{j,p}$ and $g_{j,p}(w^{in}) = g^{in}_{j,p}$. It was our hypothesis that accounting for the distance from the source to the binning plane allows improvement of the spatial resolution of objects located in that plane in the binned proton radiographs. This hypothesis has been validated in the first simulation.

In practice, $g_{j,p}$ is computed at a finite number of distances in the $\boldsymbol{w}$ direction, trilinear interpolation is used between the samples and we obtain a 4D sinogram $g : \mathbb{R}^3 \times \mathbf{P} \to \mathbb{R}$ instead of the conventional 3D sinogram, e.g., $g^{in}, g^{out} : \mathbb{R}^2 \times \mathbf{P} \to \mathbb{R}$. The optimal distance between samples $g_{j,p}$ in the $\boldsymbol{w}$ direction depends on the curvature of most likely paths, i.e., on the spatial straggling of protons due to multiple Coulomb scattering.

II.D. Distance-driven backprojection

The use of the distance-driven binning requires the modification of existing FBP algorithms. In this study, we adapted the Feldkamp–Davis–Kress (FDK) algorithm.[27] The 2D weighting and filtering of projection images in the FDK algorithm is not modified but repeated at every depth w; we note $\tilde{g}_p : \mathbb{R}^3 \to \mathbb{R}$ the filtered projection acquired at source position $\boldsymbol{a}_p$. A voxel-specific backprojection is used to select the adequate distance w, leading to the reconstruction formula

$$\eta(\boldsymbol{x}) = \sum_{p\in\mathbf{P}} \Delta\theta_p \left(\frac{\|\boldsymbol{o} - \boldsymbol{a}_p\|_2}{w(\boldsymbol{a}_p, \boldsymbol{x})}\right)^2 \times \tilde{g}_p\left(u(\boldsymbol{a}_p, \boldsymbol{x}), v(\boldsymbol{a}_p, \boldsymbol{x}), w(\boldsymbol{a}_p, \boldsymbol{x})\right) \tag{9}$$

with

$$\begin{cases} u(\boldsymbol{a}_p, \boldsymbol{x}) = \dfrac{w^{out}}{w(\boldsymbol{a}_p, \boldsymbol{x})}\left((\boldsymbol{x} - \boldsymbol{a}_p) \cdot \boldsymbol{u}(\boldsymbol{a}_p)\right), \\ v(\boldsymbol{a}_p, \boldsymbol{x}) = \dfrac{w^{out}}{w(\boldsymbol{a}_p, \boldsymbol{x})}\left((\boldsymbol{x} - \boldsymbol{a}_p) \cdot \boldsymbol{v}\right), \\ w(\boldsymbol{a}_p, \boldsymbol{x}) = (\boldsymbol{x} - \boldsymbol{a}_p) \cdot \boldsymbol{w}(\boldsymbol{a}_p), \end{cases}$$

and $\Delta\theta_p \in \mathbb{R}$ the angle weighting resulting from the discretization of the integral on the gantry angles. Equation (9) is similar to the standard FDK reconstruction formula except for the use of 3D projection images instead of 2D projection images where the last dimension is related to the distance to the source $w(\boldsymbol{a}_p, \boldsymbol{x})$. It is worth noting that both the backprojection and its FDK weighting depend on $w(\boldsymbol{a}_p, \boldsymbol{x})$.

The proposed algorithm is an approximate algorithm which takes advantage of improved spatial resolutions in proton radiographs during voxel-specific backprojection. One can observe that if the pixel indicators h were Dirac delta functions and if there was a single proton per indicator, using Eqs. (8) and (9) without filtering would simply backproject the proton energy integral G along the most likely proton path. The intermediate distance-driven binning is to allow the filtering of the FDK algorithm.

II.E. Simulations

The algorithm was implemented using RTK, an open-source reconstruction toolkit.[33] The evaluation was carried out on Monte Carlo simulations using GATE v6.2,[28] an end-user software using the Geant4 toolkit v4.9.5.p01.[29] Electromagnetic and hadronic interactions of primary and secondary protons were simulated, both in the air and in simulated objects. The `G4BraggModel` below 2 MeV and the `G4BetheBlochModel` beyond were used for inelastic electromagnetic interactions. The `G4UrbanMscModel95` described multiple scattering. Inelastic hadronic interactions with target nuclei were modeled using the `G4BinaryCascade` for protons with energies higher than 170 MeV, while the `G4PreCompound` was used for lower energies. Elastic hadronic interactions of protons were simulated with `G4HadronElastic`. The precalculated table of the stopping power and the particle range during Geant4 initialization were binned in the range of 0.1 keV to 10 GeV in a total number of 350 bins. The transportation step was 1 mm.

An ideal pCT scanner was simulated: a 200 MeV monoenergetic point source was placed at distance $\|\boldsymbol{o} - \boldsymbol{a}_p\| = 100$ cm from the isocenter and the characteristics (E_i^{in}, E_i^{out}, $\boldsymbol{x}_i^{in}$, $\dot{\boldsymbol{x}}_i^{in}$, $\boldsymbol{x}_i^{out}$, and $\dot{\boldsymbol{x}}_i^{out}$) of protons traversing the planes $w^{in} = 89$ cm and $w^{out} = 111$ cm were recorded. The measurements were exact, i.e., assumed perfect detectors, and the envelope Ω of each scanned object was also assumed to be perfectly known.

Standard 3σ cuts on energy and angle were applied to discard secondary protons produced by nuclear interactions.[24] Since it is not possible to measure in reality the exact path of each proton, the most likely path of each proton was estimated using its characteristics (position, direction, and energy) recorded at each of the two detectors. We used straight paths outside Ω and curved paths in Ω according to the maximum likelihood formalism of Schulte *et al.*[14] We closely followed their work for the parametrization of the estimation of the most likely paths.

The simulations used the materials properties defined in Geant4 based on the databases of the *National Institute of Standards and Technology* (NIST), including modifications with respect to NIST based on experiments, e.g., I_{H_2O} which equals 78 eV instead of 75 eV since Geant4 v4.9.3. In both Eq. (3) and the most likely path estimation, the object was assumed to be homogeneous and made of water. The energy integral G [Eq. (3)] was computed numerically with 100 eV bins.

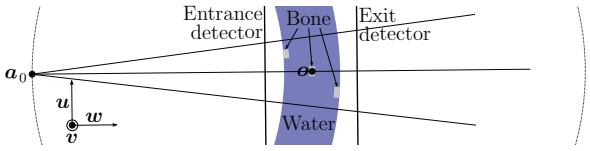

FIG. 2. Drawing of the setup of simulation 1.

II.E.1. Simulation 1

The first simulation was designed to provide the reader with insights into the effect of the distance-driven binning by looking at a single projection image only, i.e., $P = 1$. We centered a spherical shell of water with radii 90 and 110 cm around the proton source, therefore placing the isocenter in the middle of the water layer (Fig. 2). Three spherical bone inserts with identical solid angles were placed in the water sphere with regular radii from the source ($90 - 92$, $99 - 101$, and $108 - 110$ cm). Since all objects are portions of hollow spheres centered on the source position $\boldsymbol{a}_1$, the projection image for particles travelling along straight lines crossing the source would be a rectangular function with one rectangle per insert. The flux of protons through the plane $(\boldsymbol{o}, \boldsymbol{w})$ was uniform and equal to 648 000 protons $\cdot$ mm^{-2}, allowing distance-driven binning in a fine lattice with $0.1 \times 2 \times 0.1$ mm^3 spacing of $2500 \times 1 \times 2500$ samples in the $\{\boldsymbol{u}, \boldsymbol{v}, \boldsymbol{w}\}$ coordinate system.

II.E.2. Simulation 2

The second simulation was designed to measure the spatial resolution in reconstructed images relative to the depth of inserts in the object. Several aluminium cylinders with ø5 mm were regularly placed along a spiral in a large water cylinder with ø20 cm (Fig. 3). The total flux of protons was equal to the one of simulation 1 but $P = 720$ projection images were simulated which gave a proton flux of 900 protons $\cdot$ mm^{-2} $\cdot$ projection^{-1}. The projection images were binned in a lattice with $0.5 \times 1 \times 0.5$ mm^3 spacing of $500 \times 2 \times 500$ samples. Only the central slice $(\boldsymbol{o}, \boldsymbol{v})$ of the pCT image was reconstructed to avoid the cone-beam artifacts which are only encountered in other slices and depend on the scanned object.[27,30] The resolution of reconstructed images was $2100 \times 1 \times 2100$ voxels with 0.1 mm isotropic spacing. In addition to the proposed reconstruction formula [Eq. (9)], the standard FDK algorithm was used with the sinograms binned before ($w = 90$ cm) and after ($w = 110$ cm) the objects, respectively.

II.E.3. Simulation 3

The third phantom is a phantom used to measure the spatial resolution of clinical CT scanners, the CTP528 high-resolution module of the Catphan phantom (The Phantom Laboratory, Salem, NY). The module consists in various resolution gauges made of 2 mm-thick aluminium sheets placed on a ø10 cm circle in a ø20 cm water cylinder (Fig. 4). The parameters were the same as the ones of simulation 2.

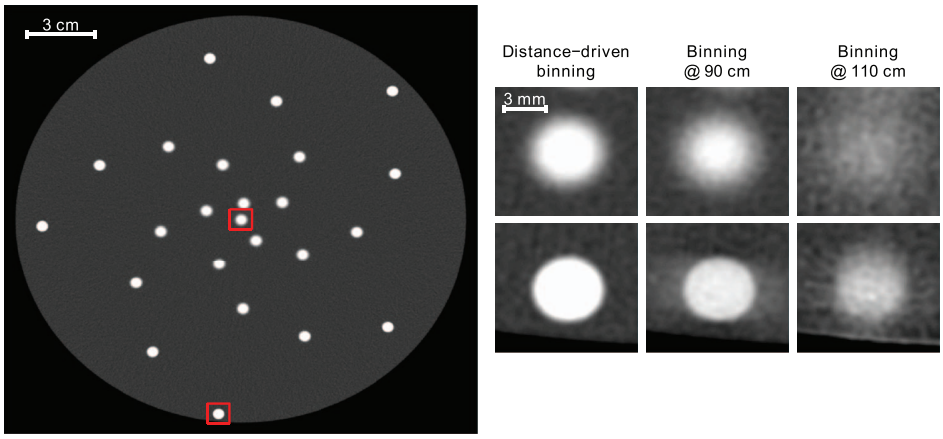

FIG. 3. Simulation 2. Central slice of the pCT reconstruction with distance-driven binning (left) and zooms on the central (right, top line) and peripheric (right, bottom line) inserts indicated with squared boxes. Gray-level range: [0.7, 2]. The first column of zoomed images were obtained with the proposed algorithm and the second and third columns were obtained with the standard FDK algorithm using sinograms binned according to the position of protons at 90 cm (entrance of the phantom) and 110 cm (exit of the phantom) from the source, respectively.

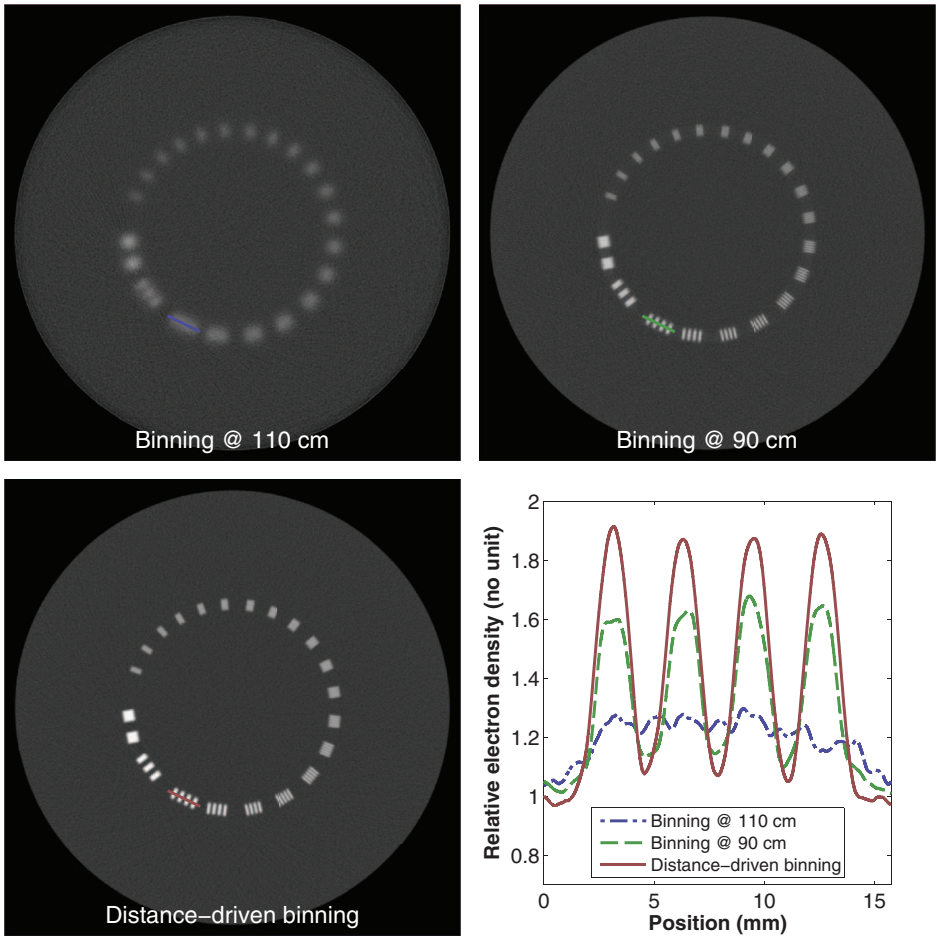

FIG. 4. Simulation 3, full scan. (Top-left) central axial slice of the standard FDK reconstruction using the 2D set of projection images $g(110\,\text{cm})$ binned according to the position of protons at the exit of the object. Gray-level range: [0.7, 2]. (Top-right) idem with the sinogram $g(90\,\text{cm})$ at the entrance of the object. (Bottom-left) distance-driven FDK reconstruction using the complete set of 3D projections g. (Bottom-right) profile along the three segments drawn on each slice.

II.E.4. Spatial resolution

The spatial resolution was quantified by measuring the edge response of the inserts with the distance required for the edge response to rise from 10% to 90%.[31] Higher values mean lower spatial resolution.

III. RESULTS

III.A. Simulation 1

Figure 5 illustrates the distance-driven binning in the projection space. The effect of multiple Coulomb scattering depended on the distance to the source and the position of the inserts. The edges of the bone inserts were the sharpest at the distance w in the sinogram which corresponds to their location in space, i.e., at the level of each line profile (Fig. 5, bottom). The loss of sharpness increased with the distance to their location (Fig. 5, right). The best spatial resolution was obtained for the right insert, which was the closest to the entrance, whereas the worst spatial resolution was obtained for the middle insert which is the one at the isocenter. This is related to the performances of the most likely path estimation, illustrated with the 3σ error envelope (Fig. 5, top-right, dashed curve) which increases with depth in the object, the increase being higher on the exit side ($w < 1000$ mm) than on the entrance side ($w > 1000$ mm). η for water and bone are 1 and 1.77, respectively, so the minimum and maximum of the profiles should be 200 and 215.3 mm [Eq. (3)]. The minimum is accurate but the maximum is slightly underestimated due to the use of the $I_{H_2O} = 78$ eV ionization potential of water instead of the $I_{Bone} = 92$ eV ionization potential of bone.

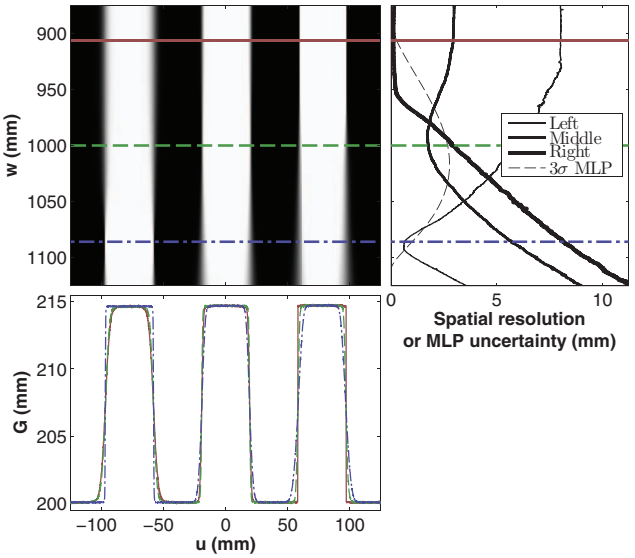

FIG. 5. Simulation 1. 2D slice of the binned 3D projection image (top-left) with the three profiles at the distance corresponding to the center of each insert (bottom-left) and the 10%–90% distance of each insert relative to the distance w to quantify the spatial resolution (top-right, solid lines). The top-right plot also displays the 3σ uncertainty of the MLP of protons with entrance and exit positions and directions along the central ray $\boldsymbol{a}_p\boldsymbol{o}$ (dashed line) computed using Eq. (27) of Schulte's derivation of the most likely path (Ref. 14). The 10%–90% distance was measured on each side of the inserts but the minimum of the two distances is plotted for each insert. The right, middle and left inserts are located at $90-92$, $99-101$, and $108-110$ cm from the source, respectively.

III.B. Simulation 2

The spatial resolution in the reconstructed pCT images can be visually observed in Fig. 3. The spatial resolution was not spatially uniform and gradually degrading from the periphery to the center of the phantom. Zooms on two pCT images reconstructed with the standard FDK algorithms are provided for comparison. The binning $g(110\,\text{cm})$, which uses the positions of protons after the object as provided by proton radiographs, gives the worst spatial resolution. The binning $g(90\,\text{cm})$, which uses the position of protons before the object, improves the spatial resolution but the distance-driven binning g [Eq. (8)] with the proposed reconstruction formula [Eq. (9)] was visually better.

The depth-dependence and the improved spatial resolution were quantified by looking at the 10%–90% distance of the edge profile of each aluminium insert (Fig. 6). Each 4 mm profile was obtained by averaging 360 radial profiles with equal angular spacing taken from the center of each insert. The range of spatial resolutions were $0.7-1.6$, $1.0-2.4$, and $2.2-3.2$ mm for the distance-driven binning, the binning $g(90\,\text{cm})$ and the binning $g(110\,\text{cm})$, respectively. Note that the inserts were not large enough for accurately measuring spatial resolutions greater than 1.5 mm due to the influence of the opposite side, which explains the noisy pattern of, e.g., $g(110\,\text{cm})$. The relative electron density η was accurately reconstructed for water ($\eta_{H_2O} = 1$) but that of aluminium was underestimated ($\eta_{Al} = 2.34$), probably because of the ionization potential assumption in Eq. (3) ($I_{Al} = 166$ eV).

III.C. Simulation 3

The improvement on spatial resolution was confirmed using simulations of a real phantom designed to measure the spatial resolution of photon CT scanners (Fig. 4). Profiles are provided through the pattern corresponding to $3\,\text{lp}\cdot\text{cm}^{-1}$. The spatial resolution improved with the distance binning compared to the spatial resolution of reconstruction using the original FDK algorithm with binning using the proton positions before and after the object (Fig. 4, bottom left vs two top slices). Among the two reconstructions with the original FDK algorithm, the binning before the object had a better spatial resolution.

The effect is emphasized when only a subset of projection images is used which corresponds to a short scan (Fig. 7). Parker weighting[32] was used to account for the short scan in each reconstruction of Fig. 7.

IV. DISCUSSION

We have proposed an algorithm to use curved most likely paths in a pCT filtered backprojection algorithm [Eq. (9)]. Our

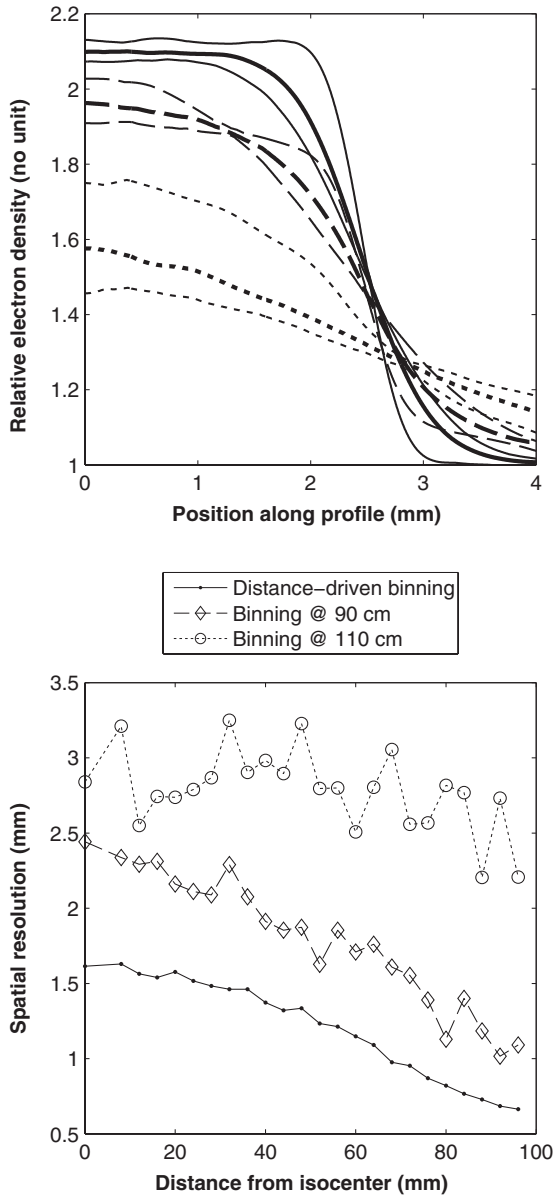

FIG. 6. Simulation 2. Quantification of the spatial resolution of each insert of Fig. 3. (Top) median (thick line) and 5/95-centile (thin lines) of the 24 average profiles. (Bottom) spatial resolution quantified with the 10%–90% distance of the edge profile of each edge insert relatively to the insert distance to the isocenter.

solution uses a distance driven binning in order to improve the spatial resolution in proton radiographs (Fig. 2). During backprojection, the spatial position of each voxel is translated to a distance to the source and the corresponding radiograph in the binned radiographs is used so that the sharpest binning is selected for objects at the voxel location. The improvement of the spatial resolution in projection images is propagated to the reconstructed pCT images and substantial improvement has been observed compared to other pCT images reconstructed with the original FDK algorithm (Figs. 3, 4, 6, and 7).

A side observation of this study is that existing FBP algorithms are more efficient with binning using proton positions before they enter the scanned object than proton positions after they exit the scanned object, the latter binning corresponding to what is obtained with real proton radiographs without proton tracking before the exit detector.[2] This difference is due to the higher energy of protons before they enter the object: since the effect of multiple Coulomb scattering increases with energy loss, the difference between their path and a straight line will gradually increase and the exit position is the worst position to estimate the straight line.[11] The substantial improvement obtained by tracking the protons before the object might be sufficient in some cases, for example, when the observed inserts are not at the center of the object and a full scan is performed, as is the case in Fig. 4. If the improvement is not sufficient or if short scan acquisitions are used, our algorithm further increases the spatial resolution at the cost of a tracking detector after the scanned object in addition to the detector for measuring the residual energy (Fig. 1).

Several choices have been made in the implementation of the proposed algorithm which could be modified to further improve the image quality. First, we have used voxel indicators for the binning [Eq. (5)] but more advanced basis functions could be used to allow, e.g., bilinear splitting during binning. Another potential improvement is the use of more robust estimators than the average during binning [Eq. (8)], e.g., the median, to eliminate outliers such as protons which underwent hadronic collisions. Finally, we could also allow binning of one proton through several source positions as it has been proposed in the parallel geometry.[21] These potential improvements have, however, a computational cost which was deemed prohibitive in the context of this study where a high proton flux was used. They might be required in the context of low dose pCT. Faster reconstruction could also be obtained by tuning the spacing of the samples of the distance-driven binning in the $\boldsymbol{w}$ direction. We have used the same spacing as in the $\boldsymbol{u}$ direction, to enforce fine sampling of the most likely path, but the spacing could be optimized to reduce computational cost (Fig. 2)

This FBP algorithm is as approximate as other FBP algorithms used in pCT since there is no exact solution for curved trajectories. We observed an improved spatial resolution without apparent loss in density resolution (Figs. 3 and 4) because the algorithm only modifies high frequencies of the sinogram without modifying low frequencies (Fig. 5). The algorithm is inspired by our experience in approximate motion compensated FBP reconstruction where limited differences have been observed with iterative reconstruction.[19] In the future, we intend to compare the proposed algorithm with existing pCT iterative algorithms to study their relative performances in terms of spatial and density resolutions at several levels of imaging doses.

It has been reported that FBP algorithms provide good density resolution compared to iterative algorithms such as algebraic reconstruction algorithms.[21] In our simulations, we observed that the electron density of water was accurately reconstructed but the electron density of aluminum inserts was systematically underestimated (Figs. 3 and 4). We believe that

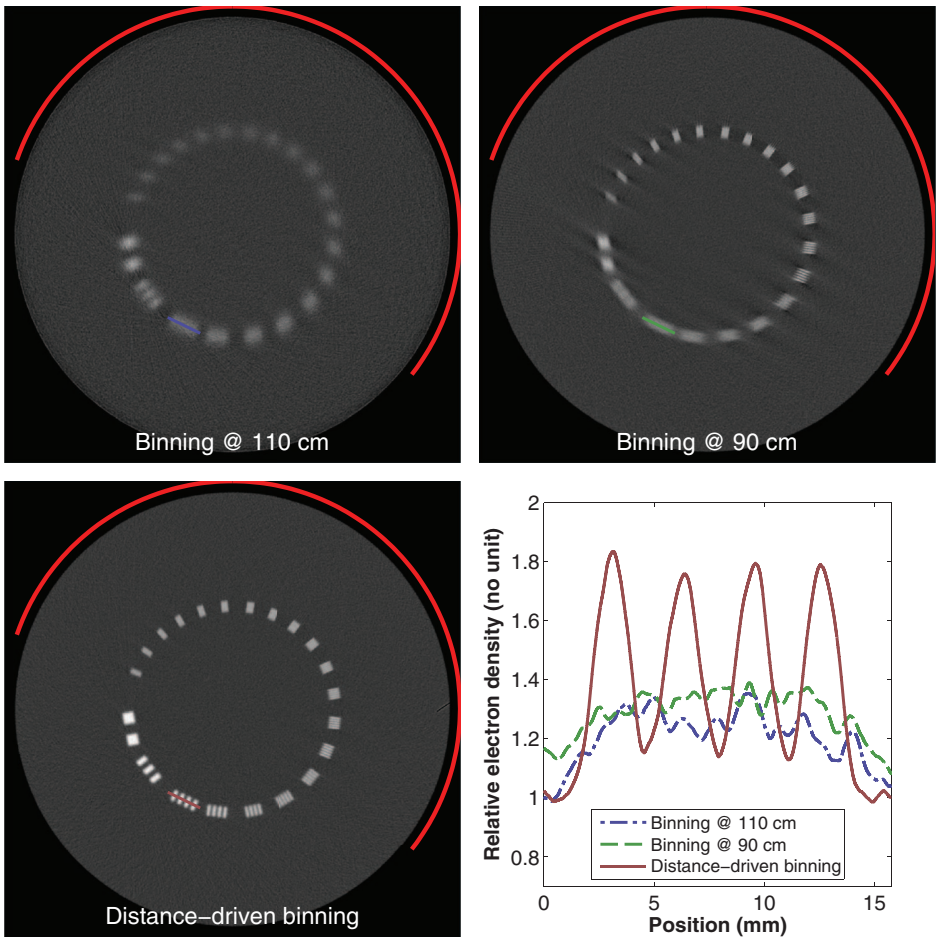

FIG. 7. Simulation 3, short scan. Idem as Fig. 4 with an additional circle arc indicating the angular coverage of the source trajectory with a down-scaled diameter for illustration purposes (ø20.5 cm on the figure instead of ø200 cm in reality).

the approximation of the ionization potential to that of water in Eq. (2) is the cause of this inaccuracy since the problem already arises in the projection space in simulation 1. We are currently investigating this with an extensive study on density resolution, also including the simulation of more realistic beam lines and detectors.

The phantoms simulated in this study were almost homogeneous and essentially made of water. These properties have been used in the most likely path estimation as in many past studies on pCT, but are unrealistic for patient imaging. We have planned on evaluating the impact of assuming an homogeneous target on the spatial resolution of patient pCT images. If inhomogeneities were prohibitively degrading spatial resolution, they could still be accounted for in Schulte's bayesian framework[14] using, e.g., a first pCT image reconstructed without most likely path estimation to roughly estimate the tissues map.

The major advantage of our algorithm over iterative pCT algorithms is faster on-the-fly reconstruction. These assets could become essential for their use in proton therapy treatment rooms when the reconstructed image is required to check the patient anatomy prior to starting the treatment. In this context, a short scan could also potentially reduce the acquisition time and the imaging dose, for which the use of most likely paths seems crucial (Fig. 7).

V. CONCLUSION

We have developed a filtered-backprojection pCT reconstruction algorithm that takes advantage of the estimation of the most likely path of protons. Improvement in the spatial resolution has been observed on Monte Carlo simulations compared to existing straight-line approximations. The improvement in spatial resolution combined with the practicality of FBP algorithms compared to iterative reconstruction algorithms makes this new algorithm a candidate of choice for clinical pCT.

ACKNOWLEDGMENTS

This work was supported by the grant ProTom (ITMO Cancer et Technologie in the Plan Cancer 2009–2013 program), the LabEX PRIMES (ANR) and the Lyric grant INCa-4664.

[a]Author to whom correspondence should be addressed. Electronic mail: simon.rit@creatis.insa-lyon.fr

[1]A. Cormack, "Representation of a function by its line integrals, with some radiological applications," J. Appl. Phys. **34**, 2722–2727 (1963).
[2]U. Schneider *et al.*, "First proton radiography of an animal patient," Med. Phys. **31**, 1046–1051 (2004).
[3]R. Schulte *et al.*, "Conceptual design of a proton computed tomography system for applications in proton radiation therapy," IEEE Trans. Nucl. Sci. **51**, 866–872 (2004).
[4]V. Sipala *et al.*, "PRIMA: An apparatus for medical application," Nucl. Instrum. Methods Phys. Res. A **658**, 73–77 (2011).
[5]B. Schaffner and E. Pedroni, "The precision of proton range calculations in proton radiotherapy treatment planning: Experimental verification of the relation between CT-HU and proton stopping power," Phys. Med. Biol. **43**, 1579–1592 (1998).
[6]M. Yang *et al.*, "Comprehensive analysis of proton range uncertainties related to patient stopping-power-ratio estimation using the stoichiometric calibration," Phys. Med. Biol. **57**, 4095–4115 (2012).
[7]H. Paganetti, "Range uncertainties in proton therapy and the role of Monte Carlo simulations," Phys. Med. Biol. **57**, R99–117 (2012).
[8]G. Cirrone *et al.*, "Monte Carlo evaluation of the filtered back projection method for image reconstruction in proton computed tomography," Nucl. Instrum. Methods Phys. Res. A **658**, 78–83 (2011).
[9]D. Wang *et al.*, "Bragg peak prediction from quantitative proton computed tomography using different path estimates," Phys. Med. Biol. **56**, 587–599 (2011).
[10]N. Depauw and J. Seco, "Sensitivity study of proton radiography and comparison with kV and MV x-ray imaging using Geant4 Monte Carlo simulations," Phys. Med. Biol. **56**, 2407–2421 (2011).
[11]U. Schneider and E. Pedroni, "Multiple Coulomb scattering and spatial resolution in proton radiography," Med. Phys. **21**, 1657–1663 (1994).
[12]H.-W. Sadrozinski *et al.*, "Development of a head scanner for proton CT," Nucl. Instrum. Methods Phys. Res. A **699**, 205–210 (2013).
[13]D. Williams, "The most likely path of an energetic charged particle through a uniform medium," Phys. Med. Biol. **49**, 2899–2911 (2004).
[14]R. W. Schulte *et al.*, "A maximum likelihood proton path formalism for application in proton computed tomography," Med. Phys. **35**, 4849–4856 (2008).
[15]B. Erdelyi, "A comprehensive study of the most likely path formalism for proton-computed tomography," Phys Med Biol **54**, 6095–6122 (2009).
[16]A. Katsevich, "An accurate approximate algorithm for motion compensation in two-dimensional tomography," Inverse Probl. **26**, 065007 (2010).
[17]L. Desbat *et al.*, "Compensation of some time dependent deformations in tomography," IEEE Trans. Med. Imaging **26**, 261–269 (2007).
[18]C. Ritchie *et al.*, "Correction of computed tomography motion artifacts using pixel-specific back-projection," IEEE Trans. Med. Imaging **15**, 333–342 (1996).
[19]S. Rit *et al.*, "Comparison of analytic and algebraic methods for motion-compensated cone-beam CT reconstruction of the thorax," IEEE Trans. Med. Imaging **28**, 1513–1525 (2009).
[20]T. Li *et al.*, "Reconstruction for proton computed tomography by tracing proton trajectories: A Monte Carlo study," Med. Phys. **33**, 699–706 (2006).
[21]S. Penfold, "Image reconstruction and Monte Carlo simulations in the development of proton computed tomography for applications in proton radiation therapy," Ph.D. thesis, Centre for Medical Radiation Physics, University of Wollongong, 2010.
[22]S. Rit *et al.*, "On-the-fly motion-compensated cone-beam CT using an a priori model of the respiratory motion," Med. Phys. **36**, 2283–2296 (2009).
[23]J. Beringer *et al.* (Particle Data Group), "Review of particle physics," Phys. Rev. **D86**, 010001 (2012).
[24]R. Schulte *et al.*, "Density resolution of proton computed tomography," Med. Phys. **32**, 1035–1046 (2005).
[25]K. Hanson *et al.*, "Computed tomography using proton energy loss," Phys. Med. Biol. **26**, 965–983 (1981).
[26]P. Zygmanski *et al.*, "The measurement of proton stopping power using proton-cone-beam computed tomography," Phys. Med. Biol. **45**, 511–528 (2000).
[27]L. Feldkamp *et al.*, "Practical cone-beam algorithm," J. Opt. Soc. Am. A **1**, 612–619 (1984).
[28]S. Jan *et al.*, "GATE V6: A major enhancement of the GATE simulation platform enabling modelling of CT and radiotherapy," Phys. Med. Biol. **56**, 881–901 (2011).
[29]S. Agostinelli *et al.*, "Geant4-a simulation toolkit," Nucl. Instrum. Methods Phys. Res. A **506**, 250–303 (2003).
[30]S. Mori *et al.*, "Properties of the prototype 256-row (cone beam) CT scanner," Eur. Radiol. **16**, 2100–2108 (2006).
[31]S. W. Smith, *The Scientist and Engineer's Guide to Digital Signal Processing* (California Technical Publishing, San Diego, CA, 1997).
[32]D. Parker, "Optimal short scan convolution reconstruction for fanbeam CT," Med. Phys. **9**, 254–257 (1982).
[33]See http://www.openrtk.org for recontruction toolkit (RTK).

D

Résumé français

Ce mémoire d'habilitation à diriger les recherches (HDR) résume l'ensemble de mes contributions depuis mon recrutement au Centre National de la Recherche Scientifique (CNRS) et mon affection au Centre de Recherche En Acquisition et Traitement de l'Image pour la Santé (CREATIS) en janvier 2010, en se focalisant plus particulièrement sur mes contributions en tant qu'encadrant de doctorants ou post-doctorants. Le mémoire est divisé en trois parties : la prise en compte du mouvement en tomodensitométrie (TDM) conique par rayons X, la TDM spectrale et la TDM proton, chacune de ces problématiques permettant l'obtention d'une image TDM quadridimensionnelle (4D). Ces parties sont précédées d'un curriculum vitæ et suivies d'une conclusion, d'une liste de références personnelles et de trois annexes contenant chacune une publication en lien avec une des parties.

Prise en compte du mouvement en TDM conique par rayons X

Le mouvement en tomodensitométrie conique était mon sujet de doctorat et de post-doctorat et j'ai naturellement commencé par poursuivre ces investigations.

J'ai d'abord participé aux travaux de doctorat de Jef Vandemeulebroucke sur l'estimation de mouvement en TDM conique pour la reconstruction compensée en mouvement. Ses travaux ce sont d'abord attachés à prendre en compte la continuité temporelle du mouvement lors de son estimation à partir d'une image TDM 4D. Dans un second temps, il s'est intéressé à l'estimation automatique de la localisation de la plèvre pour prendre en compte la discontinuité spatiale du mouvement induite par le glissement de la plèvre. Ces travaux ont été approfondis par Vivien Delmon qui a proposé une modélisation B-spline de ce glissement permettant de garantir la continuité du mouvement dans la direction orthogonale au glissement. Pour finir, ces modèles de mouvement ont été utilisés par les deux doctorants pour estimer le mouvement à partir de projections rayons X coniques et reconstruire une image TDM tridimensionnelle (3D) avec compensation du mouvement respiratoire.

Une seconde catégorie de solutions pour prendre en compte le mouvement respiratoire est la reconstruction itérative 4D régularisée. Ces travaux ont été principalement menés par Cyril Mory, durant sa thèse et son post-doctorat. Sa thèse portait sur le mouvement cardiaque en TDM conique. Ses travaux ont permis le développement d'un algorithme de reconstruction itératif 4D comportant une régularisation spatiale et temporelle, *RecOnstructiOn using Spatial and TEmporal Regularization* (ROOSTER). L'algorithme a été enrichi au cours d'un post-doctorat portant sur le mouvement respiratoire pour devenir *motion-aware ROOSTER* (MA-ROOSTER) et tenir compte d'une estimation du mouvement lors de la régularisation temporelle.

Les travaux de thèse de Jan Hoskovec ont porté sur la combinaison du problème de mouvement et de données manquantes en TDM. Ses recherches ont porté sur l'algorithme de rétroprojection de la dérivée des projections qui permet de résoudre en partie ce problème quand

l'objet scanné est statique. Elles ont abouti à la prise en compte de mouvements spécifiques, dont les mouvements rigides par morceaux, et d'étudier la reconstructibilité suivant les données manquantes et le mouvement.

Jan Hoskovec s'est également intéressé aux conditions de rang, qui sont des conditions mathématiques qui sont censées être respectées par les projections. Il a montré que le mouvement peut généralement être détecté par ces conditions. Par la suite, j'ai participé à l'encadrement de Jérôme Lesaint qui s'est intéressé à ces mêmes conditions pour la calibration géométrique de scanners TDM.

TDM spectrale

La TDM spectrale est le terme regroupant les technologies permettant d'acquérir des images rayons X avec différents spectres polychromatiques effectifs (bi-énergie, comptage, etc...).

Je me suis d'abord intéressé à la formation d'image en TDM spectrale. Il y a différentes catégories de solutions pour ce problème. Les solutions en deux étapes décomposent d'abord les projections mesurées en projections d'éléments d'une base dite de décomposition, par exemple en projections de quelques matériaux, avant application d'une reconstruction tomographique conventionnelle. Au cours de sa thèse, Gloria Vilches-Freixas a étudié les méthodes polynomiales qui approximent le problème ou sa solution par une fonction polynomiale. Nicolas Ducros s'est intéressé aux méthodes itératives régulariées pour la décomposition. Par la suite, Cyril Mory a étudié les méthodes en une seule étape, qui sont nettement plus complexes à mettre en œuvre. Une étude comparative a permis de dégager la méthode la plus efficace pour notre problème parmi les méthodes en une étape existantes. Enfin, Odran Pivot s'est intéressé au cours de son doctorat à la correction du rayonnement diffusé en TDM spectrale en utilisant un masque atténuant la fluence de la source de rayons X.

Une des applications cliniques envisagées de la TDM spectrale est l'estimation du pouvoir d'arrêt des protons, sujet de doctorat de Gloria Vilches-Freixas. Ses recherches ont porté sur la modélisation spectrale de scanners coniques ainsi que sur l'influence de paramètres d'acquisition (tensions haute et basse, filtration de la haute énergie) sur l'estimation du pouvoir d'arrêt des protons. Elle a enfin comparé différentes stratégies de décompositions pour cette estimation.

TDM proton

La dernière partie porte sur la TDM proton, une modalité d'imagerie qui connait un regain d'intérêt avec le développement de la thérapie proton car elle peut reconstruire directement le pouvoir d'arrêt proton à partir de la mesure de la perte d'énergie des protons. Je me suis intéressé à cette modalité car le problème posé par les scanners modernes est une intégrale le long d'une ligne courbe, tout comme la reconstruction avec compensation de mouvements non-rigides. J'ai proposé un algorithme de reconstruction de type rétroprojection filtrée permettant de prendre en compte ces lignes courbes. Par la suite, le doctorat de Feriel Khellaf a permis de proposer d'autres solutions directes à ce même problème. Ces différentes solutions ont été comparées aux algorithmes de la littérature. L'intérêt pour la thérapie proton a été évalué par deux post-doctorants, Georges Dedes et Nicolas Arbor, à partir de simulations Monte Carlo réalistes.

La thèse de Catherine Therese Quiñones a porté sur la reconstruction d'images TDM proton autres que l'estimation du pouvoir d'arrêt : la TDM proton d'atténuation et la TDM proton de diffusion. Ces travaux ont été prolongés par deux post-doctorants, Nils Krah et Ahmad Addoum.

Le mémoire se conclut par quelques perspectives liées essentiellement à mes projets en cours ainsi que par ma motivation à obtenir mon HDR, principalement la possibilité de co-encadrer des thèses avec d'autres chercheurs ne l'ayant pas encore ainsi que, si besoin, pouvoir encadrer des doctorants de manière indépendante.